AFOSR-TR-97
0335

July 31, 1997

FINAL REPORT

Cross Disciplinary Materials Research Program

at the

Materials Research Center of the
University of Pittsburgh

Sponsored By
Air Force Office of Scientific Research
AFOSR F49620-95-1-0167

Principal Investigators

F.S. Pettit
Materials Science and
Engineering Dept.
School of Engineering

J.T. Yates, Jr.
Department of Chemistry
College of Arts and Sciences

University of Pittsburgh
Pittsburgh, PA 15261

Period Covered

February 1, 1995 - April 30, 1997

REPORT DOCUMENTATION PAGE

Form Approved
OMB No. 0704-0188

1. AGENCY USE ONLY (Leave blank)

2. REPORT DATE 07/31/97

3. REPORT TYPE AND DATES COVERED Final 02/01/95 to 04/30/97

4. TITLE AND SUBTITLE
Final Report
Cross-Disciplinary Materials Research Program

5. FUNDING NUMBERS
F49620-95-1-0167
10 U.S.C. 2358
C 213/00

6. AUTHOR(S)
F.S. Pettit, J.T. Yates, Jr.
University of Pittsburgh

7. PERFORMING ORGANIZATION NAME(S) AND ADDRESS(ES)
University of Pittsburgh
350 Thackeray Hall
Pittsburgh, PA 15260

8. PERFORMING ORGANIZATION REPORT NUMBER

9. SPONSORING/MONITORING AGENCY NAME(S) AND ADDRESS(ES)
AFOSR/NA
110 Duncan Avenue, Suite B-115
Bolling AFB DC, 20332-0001

10. SPONSORING/MONITORING AGENCY REPORT NUMBER
F49620-95-10167

11. SUPPLEMENTARY NOTES

12a. DISTRIBUTION/AVAILABILITY STATEMENT
Approved for public release;
distribution unlimited.

19971002 144

13. ABSTRACT (Maximum 200 words)

This Final Report describes the research progress in the Cross-Disciplinary Materials Program at the University of Pittsburgh during the period February 1, 1995 through April 30, 1997. Research has been undertaken in three technical areas; High Performance Materials, Optoelectronics, and Catalysis. The projects in High Performance Materials include studies on the oxidation of superalloys, coatings, TiAl and other intermetallics, the thermoprocessing of near gamma-TiAl, the wear of diamond films and monitoring diamond growth with UV Raman Spectroscopy, the modeling of blending and the modeling of adhesion of polymers, and the attempt to remove sulfur from liquid metals. The Optoelectronics projects are concerned with multi-quantum well devices, polymerized crystalline colloidal arrays to be developed for laser eye protection, synthesis of non-linear metallo-organic compounds, determination of carrier concentration in n-type 4H and 6HSiC, and an electron beam method for growing epitaxial SiC. The Catalysis projects are involved with a new automotive catalyst for decomposition of NO_x, studies of the dechlorination of chlorofluorocarbons, the synthesis of new transition metal compounds for catalysts, and the results of using hydroxyapatite and fluorohydroxyapatite for decomposition of nerve gas.

14. SUBJECT TERMS
High Performance Materials, Optoelectronics, Catalysis, Diamond, Quantum Well Structures, Nonlinear Optical Materials, SiC, NO_x Decomposition, Dechlorination, Superalloys, Coatings

15. NUMBER OF PAGES 205

16. PRICE CODE

17. SECURITY CLASSIFICATION OF REPORT	18. SECURITY CLASSIFICATION OF THIS PAGE	19. SECURITY CLASSIFICATION OF ABSTRACT	20. LIMITATION OF ABSTRACT
UNCLASSIFIED	UNCLASSIFIED	UNCLASSIFIED	UL

GENERAL INSTRUCTIONS FOR COMPLETING SF 298

The Report Documentation Page (RDP) is used in announcing and cataloging reports. It is important that this information be consistent with the rest of the report, particularly the cover and title page. Instructions for filling in each block of the form follow. It is important to ***stay within the lines*** to meet ***optical scanning requirements.***

Block 1. Agency Use Only *(Leave blank)*.

Block 2. Report Date. Full publication date including day, month, and year, if available (e.g. 1 Jan 88). Must cite at least the year.

Block 3. Type of Report and Dates Covered. State whether report is interim, final, etc. If applicable, enter inclusive report dates (e.g. 10 Jun 87 - 30 Jun 88).

Block 4. Title and Subtitle. A title is taken from the part of the report that provides the most meaningful and complete information. When a report is prepared in more than one volume, repeat the primary title, add volume number, and include subtitle for the specific volume. On classified documents enter the title classification in parentheses.

Block 5. Funding Numbers. To include contract and grant numbers; may include program element number(s), project number(s), task number(s), and work unit number(s). Use the following labels:

C	- Contract	PR	- Project
G	- Grant	TA	- Task
PE	- Program Element	WU	- Work Unit Accession No.

Block 6. Author(s). Name(s) of person(s) responsible for writing the report, performing the research, or credited with the content of the report. If editor or compiler, this should follow the name(s).

Block 7. Performing Organization Name(s) and Address(es). Self-explanatory.

Block 8. Performing Organization Report Number. Enter the unique alphanumeric report number(s) assigned by the organization performing the report.

Block 9. Sponsoring/Monitoring Agency Name(s) and Address(es). Self-explanatory.

Block 10. Sponsoring/Monitoring Agency Report Number. *(If known)*

Block 11. Supplementary Notes. Enter information not included elsewhere such as: Prepared in cooperation with...; Trans. of...; To be published in.... When a report is revised, include a statement whether the new report supersedes or supplements the older report.

Block 12a. Distribution/Availability Statement. Denotes public availability or limitations. Cite any availability to the public. Enter additional limitations or special markings in all capitals (e.g. NOFORN, REL, ITAR).

- **DOD** - See DoDD 5230.24, "Distribution Statements on Technical Documents."
- **DOE** - See authorities.
- **NASA** - See Handbook NHB 2200.2.
- **NTIS** - Leave blank.

Block 12b. Distribution Code.

- **DOD** - Leave blank.
- **DOE** - Enter DOE distribution categories from the Standard Distribution for Unclassified Scientific and Technical Reports.
- **NASA** - Leave blank.
- **NTIS** - Leave blank.

Block 13. Abstract. Include a brief *(Maximum 200 words)* factual summary of the most significant information contained in the report.

Block 14. Subject Terms. Keywords or phrases identifying major subjects in the report.

Block 15. Number of Pages. Enter the total number of pages.

Block 16. Price Code. Enter appropriate price code *(NTIS only)*.

Blocks 17. - 19. Security Classifications. Self-explanatory. Enter U.S. Security Classification in accordance with U.S. Security Regulations (i.e., UNCLASSIFIED). If form contains classified information, stamp classification on the top and bottom of the page.

Block 20. Limitation of Abstract. This block must be completed to assign a limitation to the abstract. Enter either UL (unlimited) or SAR (same as report). An entry in this block is necessary if the abstract is to be limited. If blank, the abstract is assumed to be unlimited.

TABLE OF CONTENTS

I. EXECUTIVE SUMMARY

This final report describes the progress that has been made on the Cross-Disciplinary Materials Research Program at the University of Pittsburgh over the period of the AFOSR Grant F49620-95-1-0167 which extended from February 1, 1995 through April 30, 1997. During this period emphasis has been placed upon performing multidisciplinary research in the thrust areas of high performance materials, optoelectronics and catalytic materials. Emphasis has also been placed upon interactions with industry to encourage technology transfer. Over the duration of this grant 31 faculty from the Departments of Chemistry, Physics, Chemical Engineering, Electrical Engineering, and Materials Science and Engineering have worked on 24 projects in the three principal thrust areas. These investigations involved 35 graduate students and 4 postdoctoral students. Approximately 74 papers have been published or submitted for publication. A monthly industrial seminar has been used to stimulate interactions between MRC faculty and industry representatives. Finally, near the end of this first year of this grant, a two day materials symposium entitled "Frontiers in Materials Science - 1995" was held at the University of Pittsburgh to identify important materials research areas and to stimulate university-industry interactions.

In the following section, brief summaries are presented of the 24 research projects that were worked upon during the duration of this grant.

High Performance Materials

- Professor Meier's investigations on the adherence of alumina scales to superalloys and to coatings on superalloys have been directed at measurement of residual stresses in these scales after oxidation by using x-ray diffraction techniques. Residual stresses were measured insitu at temperature. Substantial growth stresses were observed as well as some stress relief of growth and thermally induced stresses. The residual stresses at room temperature in these scales were larger for isothermal oxidation compared to cyclic oxidation which indicates more stress relief during the latter type of test.

- Professor Birks' group is attempting to reduce the sulfur concentration in superalloys to less than 1 ppm during liquid phase melting. Reactions of sulfur with CaO and Y_2O_3 coatings on crucibles have not been successful. Experiments using Y_2O_3 crucibles have shown that the sulfur concentration is reduced but not to the desired levels. Additional work is planned using Y_2O_3 crucibles to improve this technique of sulfur removal from alloys.

- The oxidation of titanium matrix composites reinforced with SiC has been studied by Professor Pettit at temperatures between 500°C to 900°C in air, oxygen and in these two gases with controlled amounts of water vapor. Mechanisms accounting for the effects of these gases on oxidation have been developed and documented. It has also been shown that alloy compositions such as Ti-22Al-23Nb (at %) do not have a sufficient oxidation resistance to be used long periods of time above 600°C without a protective coating.

- Professor DeArdo's group is studying the effect of thermomechanical (TMP) processing on the structure-property relationship of the near gamma TiAl alloys. The goal is to produce a fine grain lamellar microstructure via TMP at high temperatures. Progress has been made in identifying how a number of processing parameters influence the lamellar microstructure.

- Professor Meier and his students have continued investigations on the oxidation of TiAl and $MoSi_2$. The adverse effect of air on the selective oxidation of aluminum in TiAl has been explained by showing that nitride formation prevents the development of continuous layers of Al_2O_3. Pesting of $MoSi_2$ has also been shown to result from accelerated oxidation at temperatures between 500° to 600°C in combination with defects in the $MoSi_2$ (e.g. cracks) which are formed during processing.

- Investigations on the oxidation and wear of diamond films has been continued by Professor Pettit. The temperature and pressure dependencies of the linear oxidation rate constants have been determined and shown to be consistent with adsorption and dissociation of oxygen as the rate controlling process in the oxidation reaction. It has also been shown that wear of diamond films occur by fracturing and chipping of the film. The diamond does not transform to carbon during machining of nonferrous alloys. The effects caused by machining of ferrous alloys have also been studied and the wear of diamond coatings has been shown to occur via chemical reaction of the diamond with iron.

- Professor Asher and his students have successfully installed a UV-laser in a diamond film growth unit at Westinghouse Science and Technology Center. This laser has been used to determine the perfection of diamond in situ as the film is being deposited.

- Professor Lindt's group has obtained an exact solution to the problem of instability of two sheets of miscible Newtonian fluids undergoing simple shear flow. They have also integrated the previous fragmented knowledge of coalescence and breakup of liquid bodies into a novel framework of differential population balances. Both findings provide a rational basis based on first principles for the design and blending of high performance polymer blends.

- Professor Balaz's group have developed theoretical computer models to predict the behavior of copolymers as they bond onto interfaces. The results provide guidelines for developing regular distinct patterns on surfaces, for creating films, for tailoring the permeability of the surfaces and systems, and for adhesion.

- Professor Blacherè installed a dual arm and parallel beam collimator accessories for the x-ray diffraction machine. These new accessories allow residual stress measurements on thin films, in particular on high temperature oxide films on turbine blade materials. These new accessories have been used to measure residual strains in thin oxides and in other films. These measurements have been performed at room temperature as well as at temperatures of 1000° and 1100°C. Three publications on this technique are currently in press.

- Professor Stoehr's group has shown that forced fluid flows during the casting of an aluminum alloy-SiC composite can affect segregation, especially when the phases have considerable differences in density. Significant segregation and redistribution of SiC and

Si particles were observed at all stirring rates. The formation of a concentration gradient of the particles at the minimum stirring rate gave way to a homogeneous distribution at moderate rates, and at higher rates inhomogeneous distributions returned with the formation of particle denuded, hot tear regions and cracks. The most homogeneous region, almost without any formation of denuded regions, was obtained at 100 rpm.

- Professor Beckman's research on attempting to generate microcellular polymeric materials has been successful in preparing both low bulk density and low cell sizes. These results show that certain polymers processes operated at appropriate conditions can have a bulk density as low as 0.12 g/cc and cell sizes of less than 10 microns.

Opto-electronics

- Professor Langer's group has refined the design of multi-quantum well (MQW) systems with defined optical properties (index of refraction and electric field dependence of the index). The analytical theory is complete and may be used to predict the necessary conditions for reflectivity as a function of applied electric field, wavelength, and angle of incidence. The length of the interferometer may now be made shorter with no loss in properties. Growth of new metal/GaAs MQW composites has begun.

- Professor Asher has developed approaches to add linear polymers to gels to increase the response rate for shrinking and swelling.

- Professors Cooper and Hopkins have discovered a new route to W(0) nitrosoaryl complexes in which both the metal center and organic functionality's can act as donor groups to a ligand based acceptor. The synergistic effects of these two donor centers on the optical properties of the complex are under investigation.

- Professor Yates' group has constructed an ultrahigh vacuum system for the growth of SiC films by bombarding adsorbed methylsilane (CH_3SiH_3) with low energy electrons. The deposited films are then analyzed by XPS, AES, ELS, LEED and TPD. The SiC films grown to-date on Si(100) crystals are amorphous. Similar methods were used to grow SiO_2 films. This work has shown that low energy electrons can be used with chemical vapor deposition to produce thin films with unique properties. Three publications have been accepted.

- Professor Gravé's group has designed samples and experiments for observing optically induced domain switching in two different configurations (unipolar and bipolar samples). They have modified and acquired the equipment necessary for the measurements and characterization.

- Professor Beratan's group has developed several inverse design strategies for constrained and unconstrained optimization of molecular properties. Rather than creating a new material and then determining what are its properties, they are developing a new theoretical strategy to instruct the synthetic chemist as to what molecular structure should be synthesized in order to optimize a certain property. Applications to linear and non-linear optical properties were pursued.

- Significant advances in the basic theory required for modeling colloid crystal arrays are being made in Professor Coalson's group. They have carried out large scale molecular dynamics simulations of these systems in order to assess their stability under external stress (e.g. intense localized heating). During the past year they have devised a simple analytical model of the pressure exerted by a colloidal crystal due to electrostatic repulsion between members of the array.

- Professor Choyke has constructed an apparatus for performing Hall effect and capacitance - voltage (CV) measurements between 90 and 800K. The overall goal is to establish under which circumstances CV and Hall measurements correspond, and how the material characteristics proper to SiC influence both. This work has focussed upon the significance of the Hall scattering effect that perturbs Hall measurements.

Catalysis

- Professor Hall's group has discovered a new durable catalyst for lean-burn automotive catalytic converters. This new catalyst, iron-containing zeolite (FeZSM-5), can use unburned hydrocarbons to reduce NOx to NO_2 in the presence of excess O_2, H_2O, CO_2 and SO_2. This new catalyst is remarkable because it can operate in an oxygen rich atmosphere, it is inexpensive compared to the Pt catalysts, and does not steam poison like the copper-containing zeolite catalysts. The prototype FeZSM-5 catalyst has operated for over 2,500 hrs in a 20% H_2O and 150 ppm SO_2 atmosphere. The 2,500 hrs is equivalent to 100,000 miles at 40 mph, which is the federal mandate for automotive catalysts. A patent application has been filed, publications have been submitted to two journals, oral presentations have and are being made, and automotive companies are being contacted.

- Professor Eror leads the group looking for an effective catalyst for nerve gas destruction. Tests have been conducted on substrates of hydroxyapatite (HA) and fluorohydroxyapatite (FHA) using the nerve gas simulant, dimethylmethyl phosphonate (DMMP). Tests showed that platinized substrates were more effective than non-platinized substrates, however both HA and FHA were subject to poisoning.

- Professor Cooper's group has been developing an improved understanding of mechanistic steps for important catalytic sequences. Mechanistic studies have established that alkylidene/alkyl insertion in a tungstenocene complex occurs by a migratory mechanism in which the alkyl group moves from the metal to the electrophilic unsaturated carbon.

- Professor d'Itri and her group are investigating the hydrodechlorination of chlorofluorocarbons by palladium supported by different substrates of Al_2O_3. They have shown that for early time on stream both the Al_2O_3 and the Pd metal participate in the reaction. However after longer times, only the metal participates. There is the possibility that carbene coupling reactions are occurring. If proven, this would allow the conversion of chlorinated compounds into high value compounds such as olefins.

II. INTRODUCTION

The Cross-Disciplinary Materials Research Program has been sponsored by the U.S. Air Force Office of Scientific Research (AFOSR) and is being administered through the Materials Research Center (MRC). The MRC is dedicated to interdisciplinary research for advancing the state-of-the-art in materials science. The Materials Research Center (MRC) was established in October, 1991, at the University of Pittsburgh through the cooperative efforts of the School of Engineering, the College of Arts and Sciences, and the U.S. Air Force Office of Scientific Research (AFOSR) (Figure 1). The MRC supports research in the departments of Chemistry, Physics, Materials Science and Engineering, Electrical Engineering, and Chemical and Petroleum Engineering. The Co-Directors for the MRC are Professor Fred S. Pettit (Materials Science and Engineering Dept.) and Professor John T. Yates, Jr. (Chemistry Department). The MRC is currently funding research in the areas of high performance materials, optoelectronics, and catalysts (Figure 1).

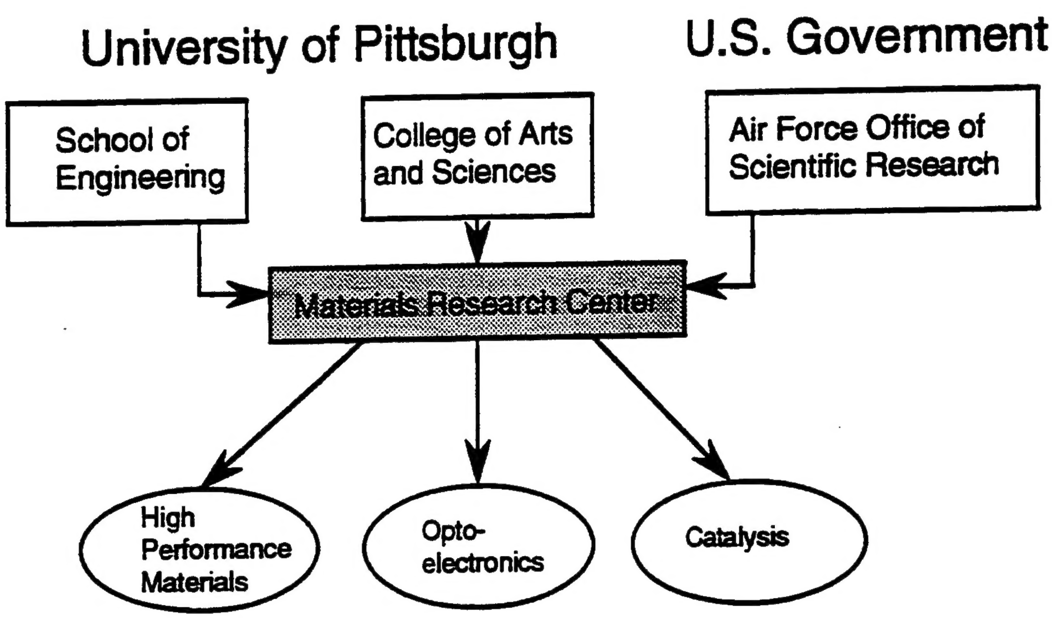

Figure 1. The Materials Research Center was formed by the combined efforts of the School of Engineering, the College of Arts and Sciences, and the AFOSR.

The three technical thrust areas of the MRC are coordinated by scientific area directors as shown in Figure 2. Emphasis has been placed upon cross-disciplinary research and technology transfer. The technical topics that have been studied in the scientific area of high performance materials are shown in Figure 3 along with the companies involved in the technology transfer. The topical area of research and the organizations involved in the technology transfer for optoelectronics and catalyst scientific areas are presented in Figures 4 and 5, respectively.

This final report describes the progress during the period of February 1, 1995 through April 30, 1997. The highlights and key accomplishments are presented first, and then the details of the individual research programs are described. The final sections describe the internal and external interactions of the MRC.

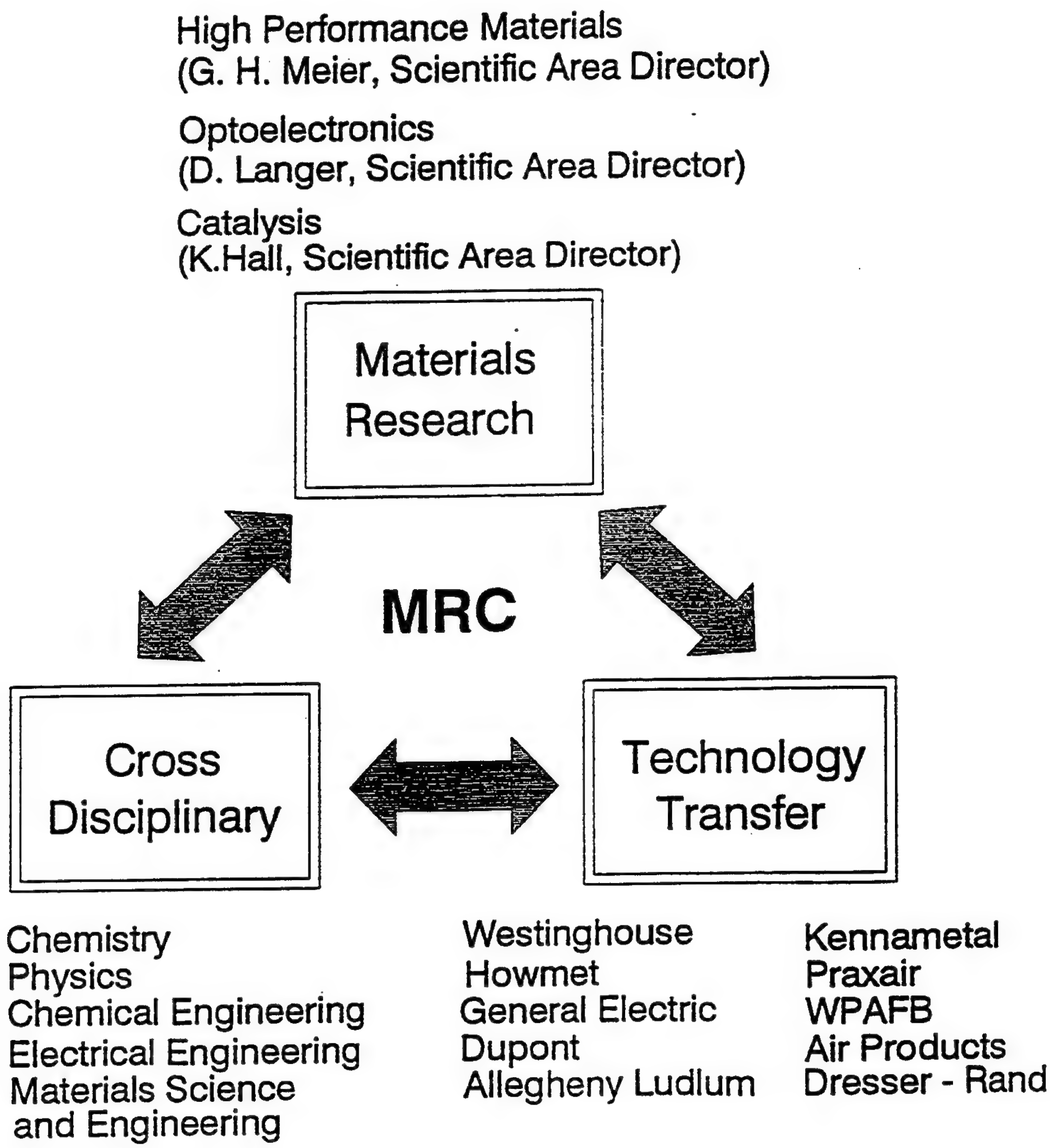

Figure 2. Schematic diagram to show organization of MRC.

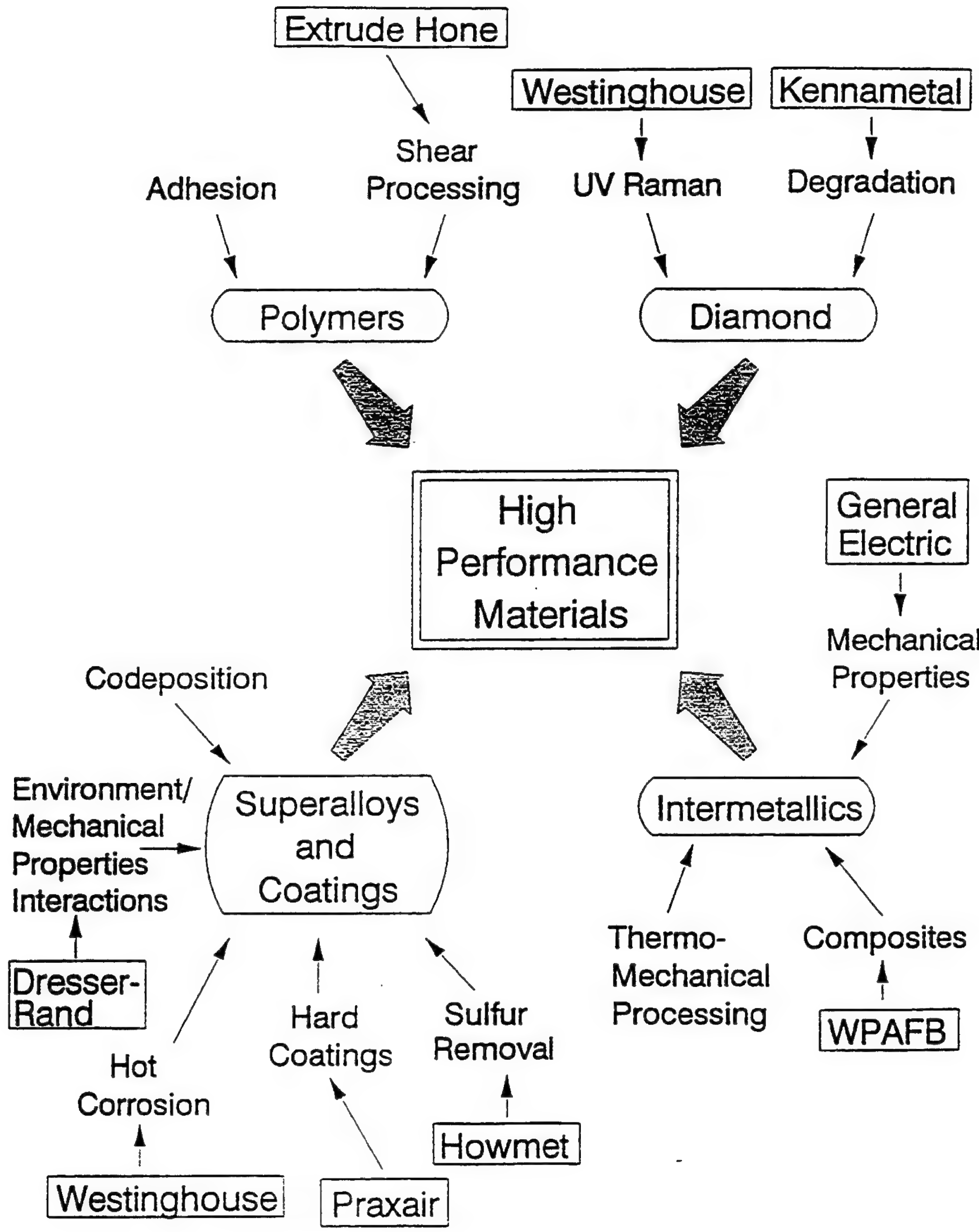

Figure 3. Schematic diagram to show the topics emphasized under High Performance Materials

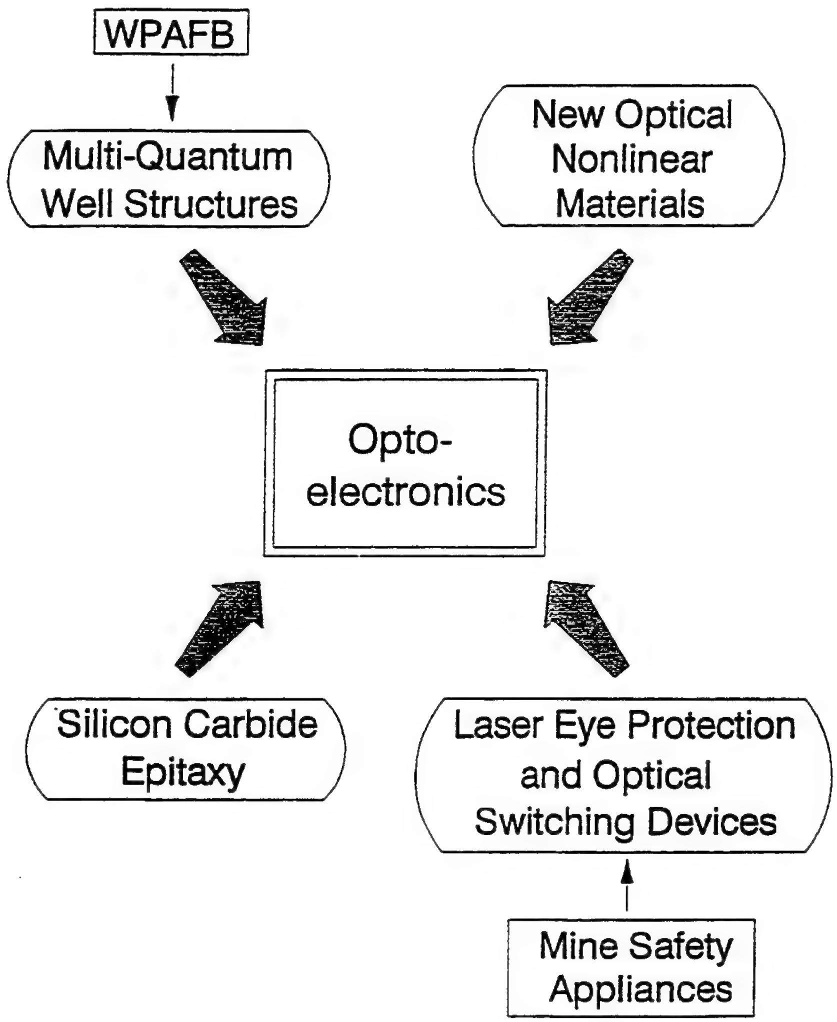

Figure 4. Schematic to show topics emphasized under Optoelectronics.

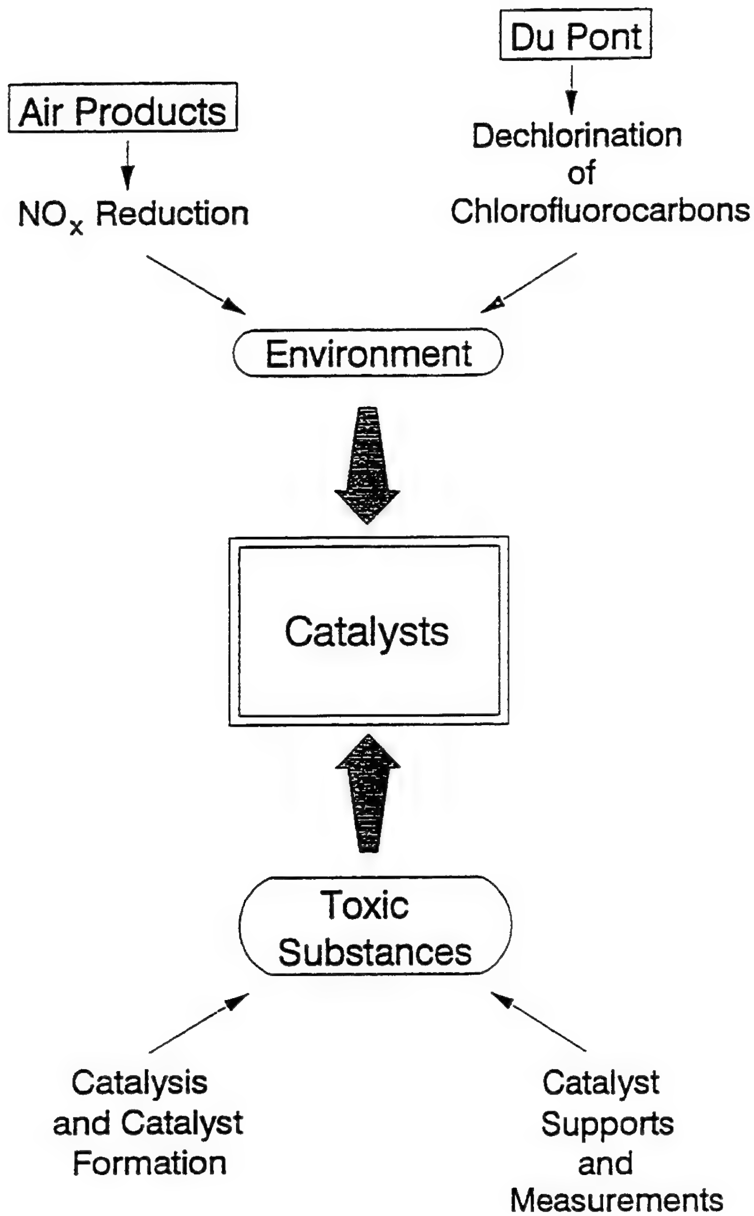

Figure 5. Schematic to show topics emphasized under Catalysts.

III. HIGHLIGHTS AND KEY ACCOMPLISHMENTS

There have been many highlights achieved during the period of this grant. The key accomplishments are listed below. The details are given in section IV, Technical Progress Report.

- A two-day symposium, "Frontiers in Materials Science - 1995" was chaired by Dr. John T. Yates Jr. and featured twelve distinguished speakers on topics covering the field of materials science. This symposium was attended by over 168 participants from universities, industry and government.

- A capability has been established to measure the residual stresses in oxide scales by using X-ray diffraction. These stresses can be measured both at room temperature and at temperatures up to 1100°C in air. Measurements of this type are extremely valuable in accounting for the effects of reactive elements on the adherence of alumina scales to alloys.

- The adverse effects of nitrogen in air on the oxidation of the intermetallic TiAl have been shown to be caused by TiN formation at the oxide-alloy interface which prevents the development of a protective layer of alumina on this intermetallic.

- Pesting of $MoSi_2$ has been shown to be caused by accelerated oxidation of this intermetallic at 500°-600°C, where a continuous scale of SiO_2 cannot be developed, in combination with processing defects such as cracks in the intermetallic.

- A UV laser has been installed in a diamond film growth unit and measured in-situ spectra of the growing diamond films. This type of apparatus has the potential for controlling diamond film perfection during deposition.

- The wear of diamond films on carbide inserts during machining of aluminum-silicon alloys has been shown to occur by fracturing and not by oxidation nor transformation to nondiamond species.

- The oxidation behavior of titanium base matrix alloys for composites has been studied at temperatures between 500° to 900°C in oxygen, air and water vapor. The alloy with the composition Ti-22Al-23Nb, which contains the orthorhombic phase in addition to α_2 and β, develops oxide scales in which transport is controlled by diffusion through Nb_2O_5 and it cannot be used uncoated at temperatures above 600°C.

- An exact solution to the problem of instability of two sheets of miscible Newtonian fluids undergoing simple shear flow has been developed. It is proposed that the well established linear perturbation theory leading by definition to an integer power polynomial in wavenumber for the complex wave velocity is incorrect.

- Guidelines have been established for creating self-healing polymeric coatings, as well as patterned films for opto-electronic applications. The conditions that drive polymers to form patterned films on solid surfaces have been isolated and the effects of molecular

structure or chemical environment on the formation, size and shape of the patterns within the film have been determined.

- Fluid flow in multiphase castings has been examined and it has been shown that forced flows can result in increased segregation, especially when the phases have considerable differences in density as is true for aluminum alloy-silicon carbide cast composite material.

- Using the "swell/quench" method in supercritical CO_2, materials have been generated with both low bulk density and low cell sizes. Preliminary results have shown that certain polymers can be processed to have a bulk density as low as 0.12 g/cc and cell sizes of less than 10 microns.

- The design of multiple quantum well systems with defined optical properties has been refined. A new concept has been developed which allows the length of the interferometer to be shortened with the incorporation of two Y-branches without an increase of losses.

- A convenient new route to W(O) nitrosoaryl complexes by nitrosation of acrylate complexes has been developed. This results in unprecedented insertion of NO into a W-aryl bond, to give a nitrosoaryl complex which cannot be prepared by conventional approaches.

- A stable automotive NO_X catalyst has been discovered which functions in oxygen rich environments without poisoning by steam or SO_2. A patent application has been filed.

- It has been shown that low energy electrons may be used to enhance the growth rate of semiconductor films under chemical vapor deposition conditions. Hence, such films may be deposited under conditions that results in structural characteristics capable of yielding unique properties.

- New switchable optical diffractors are being developed based upon controlling light diffraction from mesocopic periodicities in matter.

IV. TECHNICAL PROGRESS REPORT

IV.A HIGH PERFORMANCE MATERIALS

IV.A.1 Superalloys and Coatings

Principal Investigator: Professor G. H. Meier
Materials Science and Engineering Department
University of Pittsburgh

Other Faculty Participants: Dr. N. Birks
Materials Science and Engineering Department
University of Pittsburgh

Dr. J. R. Blachère
Materials Science and Engineering Department
University of Pittsburgh

Dr. F. S. Pettit
Materials Science and Engineering Department
University of Pittsburgh

Students: Mr. C. Barshick
Mr. F. Dethorey
Mr. C. Sarioglu
Mr. C. Stinner

IV.A.1.1 INTRODUCTION

High temperature alloys, depending on the application, must withstand conditions of isothermal and cyclic oxidation, corrosion by impurities in the exposure environment, and particle erosion. In cases where the alloys are not sufficiently resistant to the exposure conditions they must be coated. This project is focussed on the resistance of Ni-base superalloys and high temperature Fe-base alloys to this type of degradation and the use of coatings for protection. The particular objectives are the following.

1. Improve understanding of the factors which affect the adherence of protective alumina films to high-temperature Ni- and Fe-base alloys.

2. Establish the conditions for the formation of Cr-Al diffusion coatings on Ni-base superalloys.

3. Develop the degradation mechanisms of nitride-coated superalloys under combined erosion/oxidation conditions.

4. Develop mechanisms for the synergistic effects of mechanical loading and corrosive environments on degradation of superalloys.

IV.A.1.2. ACCOMPLISHMENTS AND SIGNIFICANCE

Substantial progress has been made in all four areas. Two Senior Projects were completed in 1996 and two Ph.D theses will be completed in Summer 1997. A number of papers have been published or submitted and a number of formal and informal interactions have been developed. These interactions include companies such as Praxair, Dresser-Rand, Howmet, GE Aircraft Engines, and Westinghouse. Collaboration has also been continued with NASA Lewis Research Center and the Max-Planck-Institut für Metallforschung (Stuttgart). Finally, the work on alumina adherence has been coupled with the MRC project on stress measurement in thin films (J. R. Blachere P.I.) with excellent results. The following is a summary of the accomplishments in the various areas.

Alumina Adherence to Ni-base and Fe-base Alloys

State-of-the-art superalloys and Fe-Cr-Al alloys are useful for high temperature applications, in large part, because they form protective alumina surface films by the selective oxidation of aluminum from the alloy. The adherence of the alumina to the alloy is crucial to maintaining oxidation resistance, particularly under thermal cycling conditions. It is now well established that small additions of reactive elements, such as yttrium, hafnium, and cerium, substantially improve the adherence of alumina films to alloy substrates[1]. While the effects produced by the reactive elements are widely known the mechanisms whereby they improve adherence are not completely understood. Over the last fifty years a number of mechanisms have been proposed. These include: reactive elements acting as vacancy sinks to suppress void formation at the alloy/oxide interface[2,3], formation of oxide pegs at the alloy/oxide interface[4], alteration of the growth mechanism of the oxide resulting in reduced growth stresses[5], reactive element segregation to the alloy/oxide interface to form a graded seal[6] or otherwise strengthen the alloy/oxide bond[7], increased oxide plasticity[8], and reactive elements tieing up sulfur in the alloy to prevent it from segregating to the alloy/oxide interface and weakening an otherwise strong bond[9,10]. The importance of the latter mechanism has been illustrated in experiments where hydrogen annealing of nickel-base single crystals[11,12] and FeCrAl alloys[13] lowered the sulfur contents to very low levels and resulted in dramatic improvements in the adherence of alumina films to the alloys. The work in this project is focussed on developing a quantitative description of the process of oxide spalling and how it is influenced by the presence of sulfur and reactive elements. This involves measuring the stresses generated both during oxide formation and specimen cooling, observing the processes of stress relaxation by deformation of the alloys, and the structure of the alloy oxide interface. It has been shown that one can quantitatively predict what concentration of a particular reactive metal is required to alleviate the effects of a given concentration of sulfur impurity.

Figure 1 shows the effect of reactive element additions on the cyclic oxidation of FeCrAl in air at 1100°C. The undoped alloy shows an initial mass gain followed by a mass loss, resulting from spallation of a protective alumina film, followed by a large mass gain, resulting from the rapid growth of iron-containing oxides. All of the doped alloys exhibit small positive mass gains for the duration of the experiment[13].

The alumina film which developed on undoped FeCrAl during isothermal or cyclic oxidation was highly convoluted and spalled from the alloy over most of the surface. The alloy substrate exhibits large smooth areas where the oxide had lost contact at the oxidation temperature, Figure 2. The alumina spallation and the accompanying Al depletion from the alloy, result in formation of thick Fe-rich oxides during cyclic oxidation. Figure 3 shows the cross-section of alumina formed on the Y-doped FeCrAl which showed no separation from the substrate and was generally planar except for a very few regions (not shown) where internal oxidation had occurred. Figure 4 shows the cross-section of alumina formed on the Ti-doped alloy during cyclic oxidation. The oxide is adherent to the substrate with no interfacial voids but the oxide and alloy surface have undergone substantial deformation. These convolutions which were observed in the first 48 hours of cyclic oxidation were not found after isothermal oxidation for 50 hours at 1150°C or 300 hours at 1100°C which means that thermal stresses, in addition to growth stresses, must play a role in their development.

Figure 1 also shows the effect of desulfurization of FeCrAl. This specimen shows small positive mass gains comparable to those for the doped alloys. The oxides was adherent with no interfacial voids but exhibited convolutions, similar to those on the Ti-doped alloy, in the regions where alloy grain boundaries intersected the alloy/scale interface.

The different behavior of Ti-doped FeCrAl (relative to that of Y-doped FeCrAl), which involves suppression of interfacial voids and greatly improved adherence but does not prevent convolutions has been investigated further. Figure 5 shows cross-section TEM micrographs of the alumina formed after 1 hour and 6 hours at 1100°C. After 1 hour the oxide is approximately 500nm thick and contains equiaxed grains which are approximately 200nm in diameter. Numerous triangular-shaped voids were observed where oxide grain boundaries intersect the alloy/scale interface. After 6 hours the scale consists of columnar grains which have grown underneath the initally-formed equiaxed zone. The alloy/oxide interface has become facetted but no interfacial voids could be observed to remain. Careful STEM measurements on the 6-hour scale indicated segregation of approximately 0.8 monolayer of Ti to the alloy/scale interface but no Ti segregation to the alumina grain boundaries. Therefore, one source of the difference between Y- and Ti-doping appears to be the lack of segregation to alumina grain boundaries compared to the extensive segregation of Y reported in several studies[14-16].

Additionally the residual stress in the scale on Ti-doped FeCrAl after isothermal and cyclic oxidation at 1100°C was measured by XRD. (The details of the various XRD techniques will be presented in a later section of this report.) Assuming a biaxial stress and a homogeneous elastic medium the strain in a direction ϕ along the surface of the film for an inclination (tilt) φ of the selected (h,k,l) plane with respect to the surface of the film is:

$$(\epsilon_3)_{\phi\psi}=\frac{d_{\phi\psi}-d_o}{d_o}=\frac{1+\nu}{E}\sigma_\phi \sin^2\psi-\frac{\nu}{E}(\sigma_1+\sigma_2) \qquad (1)$$

Here, $(\epsilon_3)_{\phi\psi}$ is the average strain in the direction ϕ along the normal to the diffracting planes {h,k,l} which have a tilt ψ; $d_{\phi\psi}$ is the d-spacing of these planes and d_o is the unstrained value; the stresses σ_1 and σ_2 are normal stresses in the direction of orthogonal axes S_1 and S_2 defined parallel to the film surface; σ_ϕ is the normal stress parallel to the surface of the film and making

an angle ϕ with S_1; and ν and E are the Poisson's ratio and Young's modulus of the film, respectively. The stress along the direction ϕ is obtained from the slope of a plot of $\sin^2\psi$ vs $d_{\phi\psi}$-d_o/d_o. The $d_o$used was the value of $d_{\phi\psi}$ at $\psi=0$. This practice is known to introduce negligible error[17] and partially corrects for solid solution effects. The data of Figure 6 were obtained for two values of ϕ, 0 and 90°. The positive and negative tilts for each orientation give sets of points which fit well on a straight line demonstrating the reproducibility of the measurements and good linearity of the data. This linearity suggests that the assumptions for equation (1) are met and that there are no substantial stress gradients through the scale. The slope of the plot for the isothermally oxidized specimen gives a stress value of 4400 MPa (compression) in the alumina layer. A significant result in Figure 6 is that the slope of the plot is lower for cyclic oxidation conditions giving a stress of 3400 MPa (compression). These results indicate that a part of the thermal stress is being relaxed on each cycle during cooling by deformation of the substrate

The results of cyclic oxidation experiments for the Ni-base single crystal alloys at 1100°C are presented in Figure 7. The oxidation resistance of the untreated alloys is in the order 1487 > 1484 > 1480 which suggests that doping with 0.1Hf improves adherence but that combined doping with 0.1Hf + 0.1Y is more effective. Unfortunately an alloy doped only with Y was not available.

Sulfur removal improved the cyclic oxidation resistance of both 1480 and 1484. These results support the observations that sulfur removal improves the alumina adherence to alloys which do not contain reactive elements (1480). However, the improvement for 1484, which contains Hf, indicates that the sulfur removal somehow makes the Hf more effective. Whether this effect will occur for an alloy containing Y is not yet clear.

Figure 7 also indicates a dependence on specimen thickness for the desulfurized PWA 1480. The hydrogen anneal improved the adherence for the 3.0 mm thick specimen but not to the extent for the 0.3 mm thick specimen. This implies a limitation on the section thickness which can be desulfurized in the solid state[18].

Figure 8 shows the results of cyclic oxidation experiments performed in air at 1100°C on polycrystalline Ni-base alloys having the same bulk composition as single-crystal PWA 1484 but containing various sulfur contents. These data indicate that, for this alloy, there is a critical sulfur content between 3 and 8 ppm below which adherent scales are formed. Comparison with data for PWA 1480, in Figure7, indicates that either the 0.1 wt%Hf in the polycrystalline specimens containing 1 and 3 ppm lowers the the content of sulfur which is free to diffuse to the alloy/oxide interface to below 0.1ppm or it provides a beneficial effect in addition to sulfur-gettering.

Figure 9 shows the oxide scale formed on the polycrystalline alloy containing 1ppm sulfur after 2453 hours of cyclic oxidation. The oxide scale consists of an α-alumina layer (4 μm thick) between a transient oxide layer and an Al-depleted substrate (10-20 μm) layer. The oxide scale was adherent to the substrate during cyclic oxidation. The oxide layer on the alloy containing 45 ppm sulfur was not adherent and spalled extensively as shown in the cross-section micrograph in Figure 10. More rapidly-growing oxides, such as NiO and $Ni(Al,Cr)_2O_4$, formed

on the surface of the alloy and during cyclic oxidation these oxides spalled from the surface resulting in large weight losses, as shown in Figure 8.

The residual stress in the alumina layer on PWA 1484 after 24 hours isothermal oxidation at 1100°C was measured to be 4050 Mpa (compression). Experiments are continuing to determine how this value is influenced by oxidation time, sulfur content and reactive element content and hot-stage XRD is being used to determine the contribution of growth stress to the overall residual stress.

Desulfurization by hydrogen annealing was also found to improve the adherence of alumina to NiAl. The improvement in adherence was associated with a substantial reduction in the number of interfacial voids for the desulfurized specimen. However, the void formation was not completely suppressed as it was for the desulfurized FeCrAl specimens.

Cr/Al Diffusion Coatings on Superalloys

The aluminizing of Ni-base alloys via the pack-cementation process has been a commerically viable process for many years[19]. In recent years the plating of Pt on the substrate prior to aluminizing has been used to produce "platinum-aluminide" coatings[20]. This type of coating has resulted in improved cyclic oxidation resistance and reduced interdiffusion with the substrate.

Currently, the improvement in hot corrosion resistance imparted to Ni-Al alloys by Cr additions has resulted in research efforts aimed at codepositing Cr and Al in aluminide coatings. The simultaneous codeposition of Al and Cr via the pack cementation process, using pure elemental powders, is, however, difficult. The large difference in the thermodynamic stabilities of the Al and Cr halides causes Al-halide species to predominate in the pack atmosphere[21]. However, by employing binary chromium-aluminum (Cr-Al) master alloys, the high relative Al halide vapor pressures can be moderated. This is the result of the fact that chromium-rich master alloys exhibit negative deviations from ideality and the activity of Al in the master alloy can be reduced by several orders of magnitude. The reduced thermodynamic activity of Al, results in generation of lower vapor pressures for the otherwise favored halide species (e.g., $AlCl$, $AlCl_2$ etc.). Therefore comparable Al and Cr vapor pressures result. Thus, provided a suitable activator and binary master alloy is chosen, the codeposition of Cr and Al into Ni base materials is possible. Rapp and Bianco[22-24] have used this approach to form coatings containing as much as 13 at% Cr in β-NiAl on Ni-base superalloys and have shown them to have greater hot corrosion resistance at 900°C than aluminide coatings without the Cr modification[24]. Da Costa et al[25,26] have achieved Cr concentrations as high as 40 at% using Cr-rich masteralloys and multiple activators ($NaCl+NH_4Cl$).

Work in this project is directed at studying how the pack variables, such as the amount and composition of the source alloy and the activator, affect the composition and morphology of Cr-aluminide coatings on Ni-base alloys. It has been found that codeposition of Cr and Al is possible with a single activator, that the most promising activator is NH_4Cl, and that the Cr concentration in the coating increases as the amount of NH_4Cl in the pack is increased. Figure 11 indicates that the equilibrium partial pressure of $CrCl_2$ increases as the amount of NH_4Cl is increased while the partial pressures of $AlCl$ and $AlCl_2$ decrease. thus making the pack more

chromizing. Additionally, for a given concentration of Cr in the master alloy, the Cr concentration in the coating increases as the amount of masteralloy is decreased. This effect results from both thermodynamic and kinetic factors. Figure 12 shows that, as the amount of master alloy is decreased, the aluminum chloride pressures decrease relative to the chromium chloride pressures leading to more chromizing conditions. In addition, as the amount of master alloy is decreased, the master alloy particles are more readily depleted of coating elements. Because the master alloy is rich in chromium this also leads to more chromizing conditions. Maps which define the types of coatings produced by various deposition conditions have been prepared. Figure 13 shows such maps for NH_4Cl-activated packs with master alloys containing 95Cr-5Al and 90Cr-10Al. The maps show the range of deposition conditions which produce aluminizing conditions, chromizing conditions, and codeposition. The numbers in parentheses refer to an "above pack" arrangement for which an organic coating was applied to the specimen prior to coating to separate the pack material from the coating. Examples of the coatings corresponding to the codeposition region of the map are shown in Figure 14 for Ni-270 and Figure 15 for PWA 1484.

Erosion/Oxidation of Nitride Coatings on Superalloys

Under some conditions superalloys are subjected to the combined effects of oxidation and particle erosion. In these cases coatings, which can withstand both forms of degradation are required. In this project the behavior of hard nitride (TiN, CrN) coatings on IN718 substrates is being studied. It has been found that the TiN coatings are more resistant to room temperature erosion because of their higher hardness compared to CrN. However, as the temperature is increased the oxidation of the coatings interacts with the erosion such that at 800°C the CrN coating is more resistant because it has greater resistance to oxidation. The mechanisms of material removal from the coatings at the various temperatures is currently being studied.

IV.A.1.3 SUMMARY

Substantial progress has been made in understanding the factors which affect the generation of stresses in alumina scales on Fe- and Ni-base alloys and how these stresses lead to spalling of the oxide and/or deformation of the alloy. The conditions for the formation of Cr-Al diffusion coatings on Ni-base alloys have been made more quantitative. The degradation mechanisms of nitride-coated superalloys under combined erosion/oxidation conditions have been clarified.

IV.A.1.4. REFERENCES

1. D.P. Whittle and J. Stringer, Phil. Trans. Roy. Soc. Lond., A295, 309 (1980).
2. J. Stringer, Met. Rev., 11, 113 (1966).
3. J. K. Tien and F. S. Pettit, Met. Trans., 3, 1587 (1972).
4. E. J. Felten, J. Electrochem. Soc., 108, 490 (1961)
5. F. A. Golightly, F. H. Stott, and G. C. Wood, Oxid. Met., 10, 163 (1976).
6. H. Pfeiffer, Werkst. Korros., 8, 574 (1957).
7. J. E. McDonald and J. G. Eberhardt, Trans. TMS-AIME, 233, 512 (1965).
8. J. E. Antill and K. A. Peakall, J. Iron Steel Inst., 205, 1136 (1967).

9. A. W. Funkenbusch, J. G. Smeggil, and N. S. Bornstein, Met. Trans., 16A, 1164 (1985).
10. J. G. Smeggil, A. W. Funkenbusch, and N. S. Bornstein, Met. Trans., 17A, 923 (1986).
11. B. K. Tubbs and J. K. Smialek, "Effect of Sulfur Removal on Scale Adhesion to PWA 1480" Symposium on Corrosion and Particle Erosion at High Temperatures, eds. V. Srinivasan and K. Vedula, TMS, 1989, p.459.
12. R. V. McVay, P. Williams, G. H. Meier, F. S. Pettit, and J. L. Smialek, "Oxidation of Low Sulfur Single Crystal Nickel-Base Superalloys", Superalloys 1992, S. D. Antolovich, R. W. Stusrud, R. A. MacKay, D. L. Anton, T. Khan, R. D. Kissinger, and D. L. Klarstrom eds., p. 807, TMS (1992).
13. M. C. Stasik, F. S. Pettit, and G. H. Meier, A. Ashary, and J. L. Smialek, Scripta Met. et Mater., 31, 1645 (1994).
14. T. A. Ramanarayanan, M. Raghavan, and R. Petrovic-Luton, J. Electrochem. Soc. 131 (1984) 923
15. B. A. Pint, J. R. Martin, and L. W. Hobbs, Oxid. Metals 39 (1993) 167
16. E. Schumann, Oxid. Metals 43 (1995) 157.
17. J. C. Nayan and J. B. Cohen, “Residual Stresses”, Springer Verlag (1987)
18. G. H. Meier, F. S. Pettit, and J. L. Smialek, Materials and Corrosion 46 (1995) 232
19. G. W. Goward and L. W. Cannon: “Pack Cementation Coatings for Superalloys: A Review of History, Theory, and Practice”, Paper 87-GT-50, Gas Turbine Conf., ASME, 1987.
20. J. S. Smith and D. H. Boone: “Platinum Modified Aluminides-Present Status”, Paper 90-GT-319, Gas Turbine and Aeroengine Congress, ASME, 1990.
21. S. C. Kung and R. A. Rapp: Oxid. Met., 32, 89 (1989).
22. R. Bianco and R. A. Rapp: J. Electrochem. Soc., 140, (1993) 1181.
23. R. Bianco and R. A. Rapp: in High Temperature Materials Chemistry-V, W. B. Johnson and R. A. Rapp Eds., The Electrochem. Soc., 1990 p. 211.
24. R. Bianco, R. A. Rapp and J. L. Smialek: J. Electrochem. Soc., 140, (1993) 1191.
25. W. Da Costa, B. Gleeson and D. J. Young: J. Electrochem. Soc., 141, (1994) 1464.
26. W. Da Costa, B. Gleeson and D. J. Young: J. Electrochem. Soc., 141, (1994)2690.

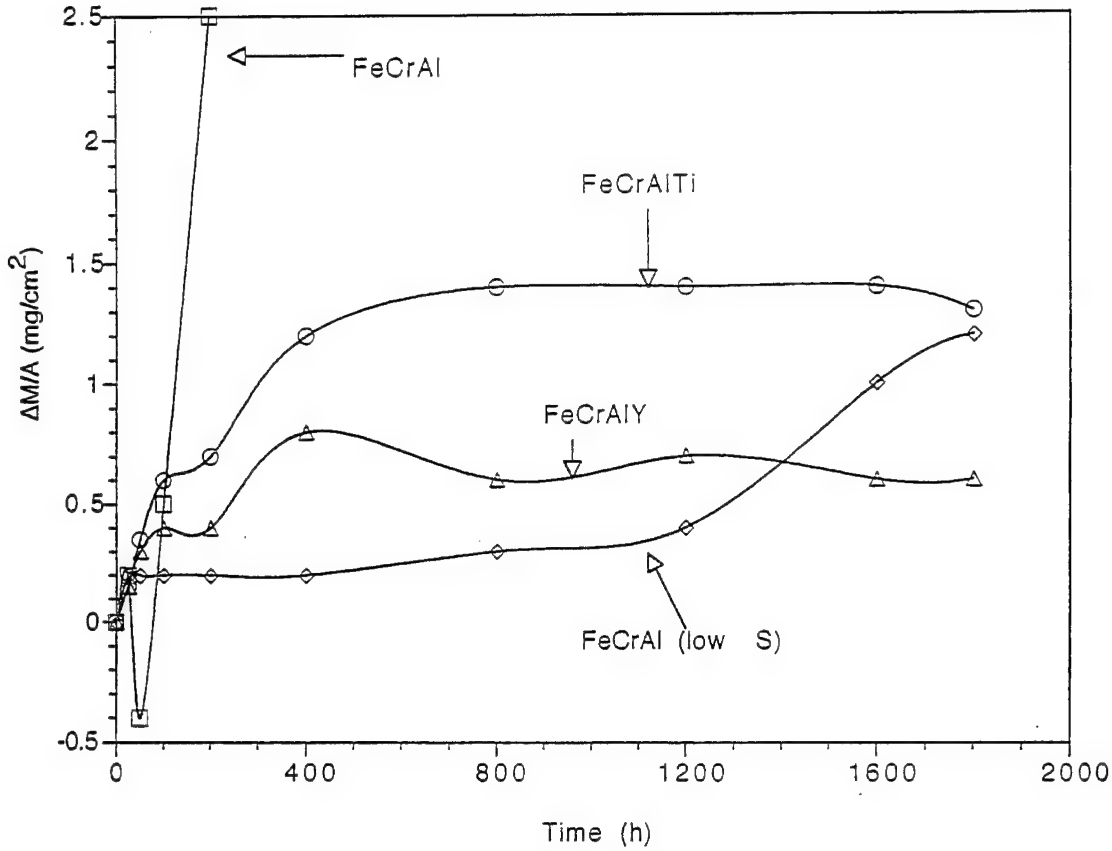

Figure 1. Mass change vs. time for doped and undoped FeCrAl alloys and hydrogen annealed FeCrAl alloys in cyclic oxidation in air at 1100°C.

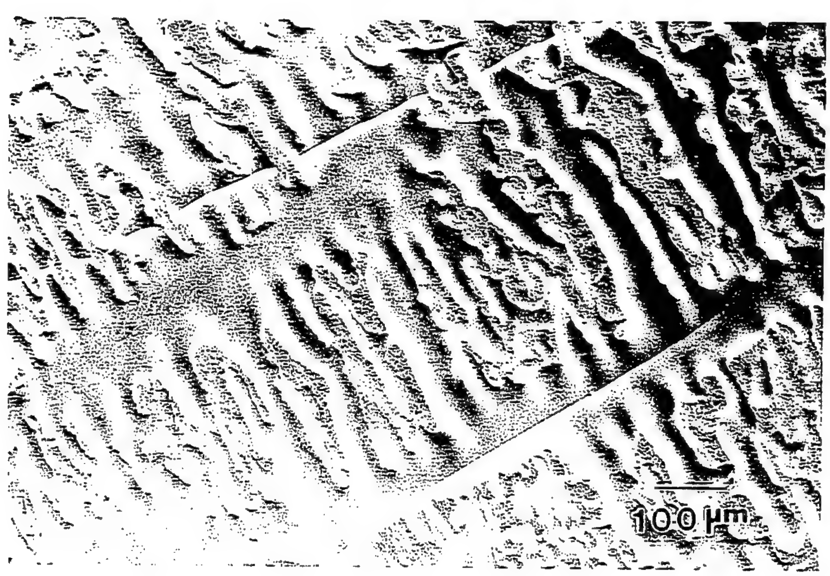

Figure 2. Alloy substrate after scale spallation for undoped FeCrAl oxidized isothermally for 100 h in air at 1150°C.

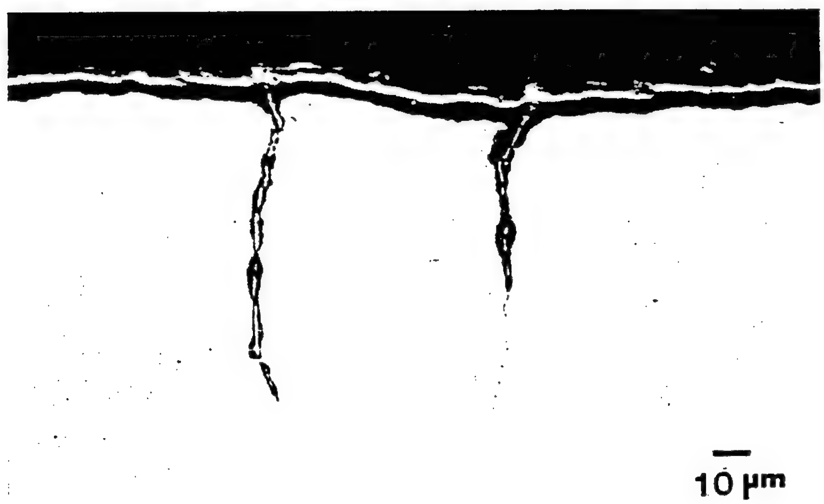

Figure 3. Cross-section of FeCrAl+Y after cyclic oxidation in air for 1700 h at 1100°C.

Figure 4. Cross-section of FeCrAl+Ti after cyclic oxidation in air for 1700 h at 1100°C.

a.

b.

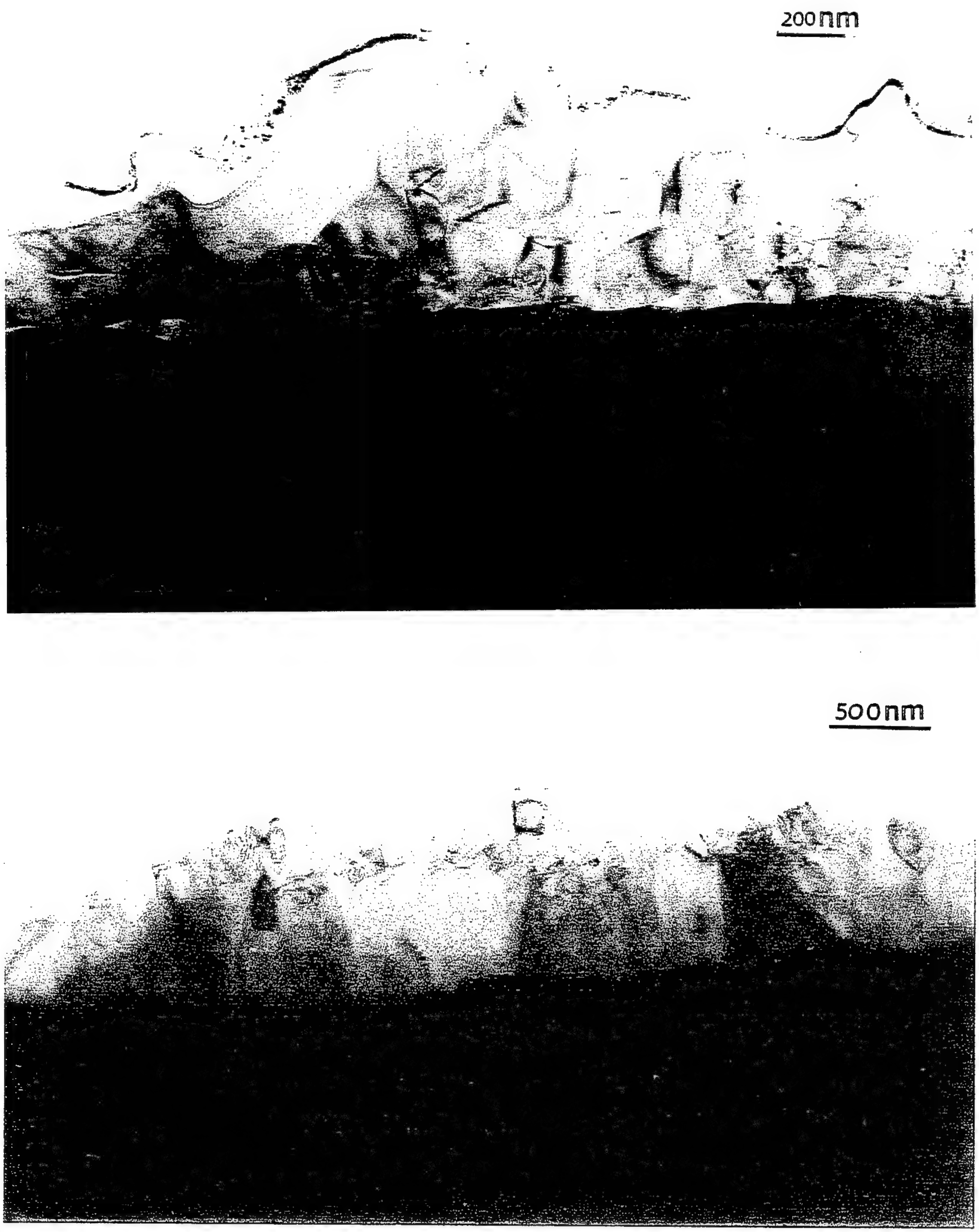

Figure 5. Cross-section TEM micrographs of the scale on FeCrAl+Ti oxidized for (a.) 1 h and (b.) 6 h at 1100°C.

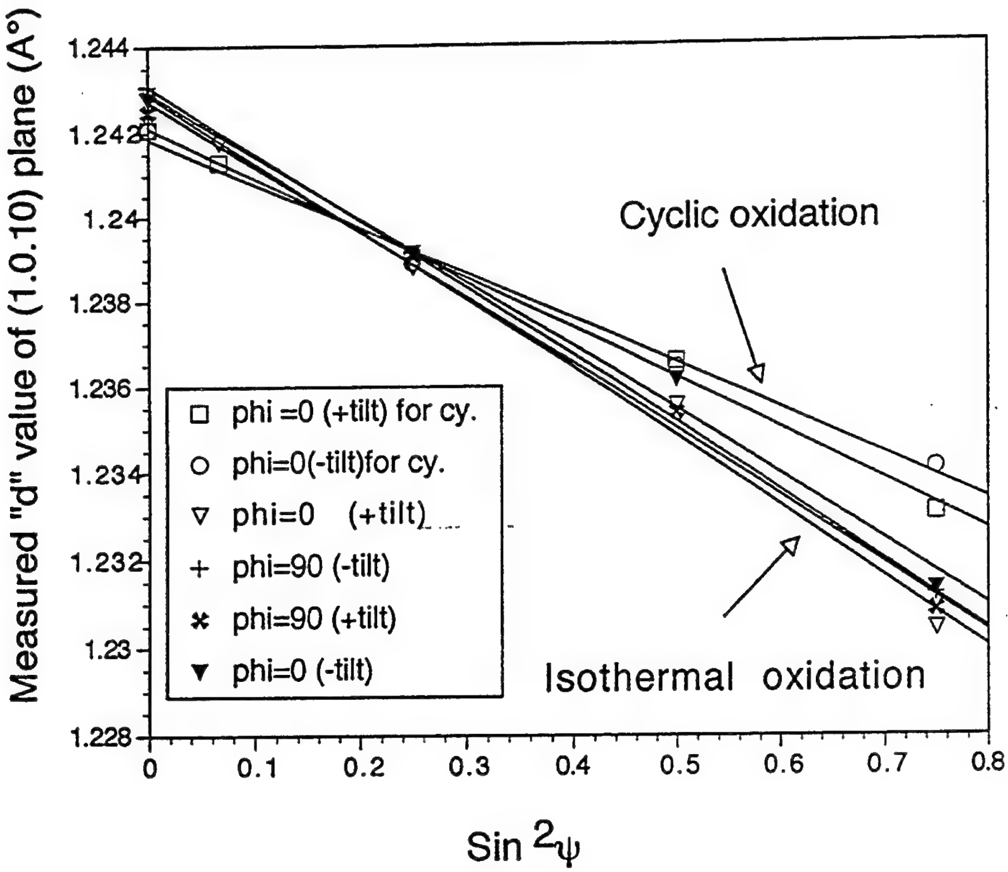

Figure 6. Plot of d-spacings for the (1,0,10) plane of α-alumina on FeCrAl+Ti oxidized isothermally for 72 h and and cyclically for 288 h at 1100°C.

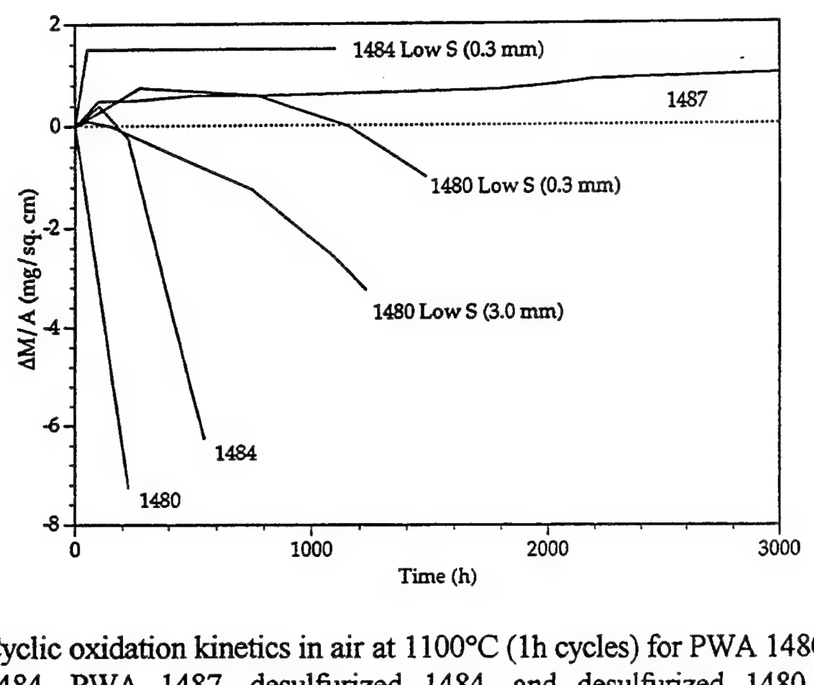

Figure 7. Cyclic oxidation kinetics in air at 1100°C (1h cycles) for PWA 1480, PWA 1484, PWA 1487, desulfurized 1484, and desulfurized 1480 of the indicated specimen thicknesses.

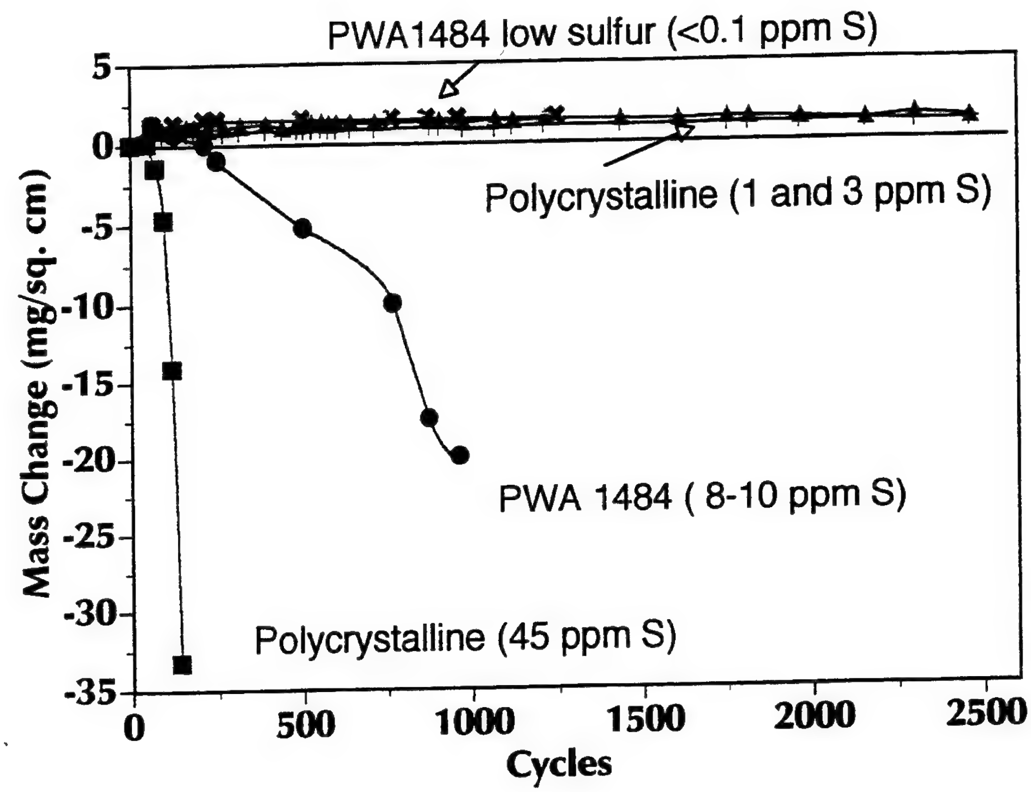

Figure 8. Cyclic oxidation kinetics at 1100°C in air for Ni-base superalloys containing various sulfur contents.

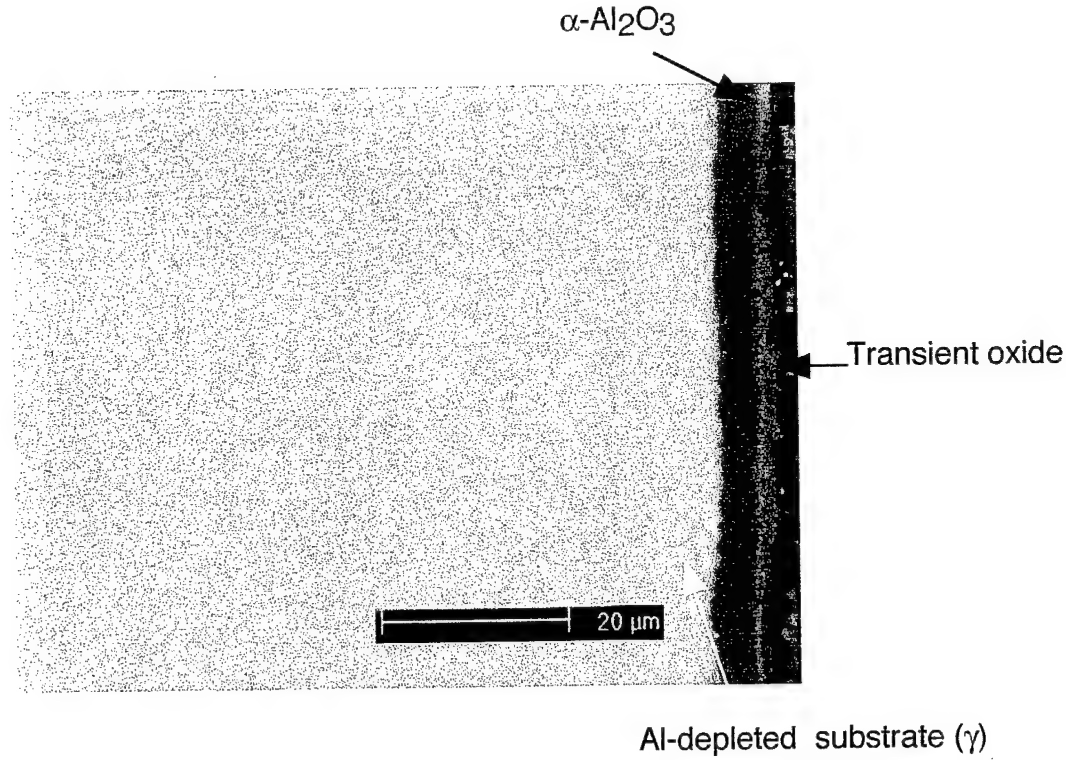

Figure 9. SEM cross-section micrograph of a polycrystalline alloy (1 ppm S) after cyclic oxidation for 2453 hours in air at 1100°C.

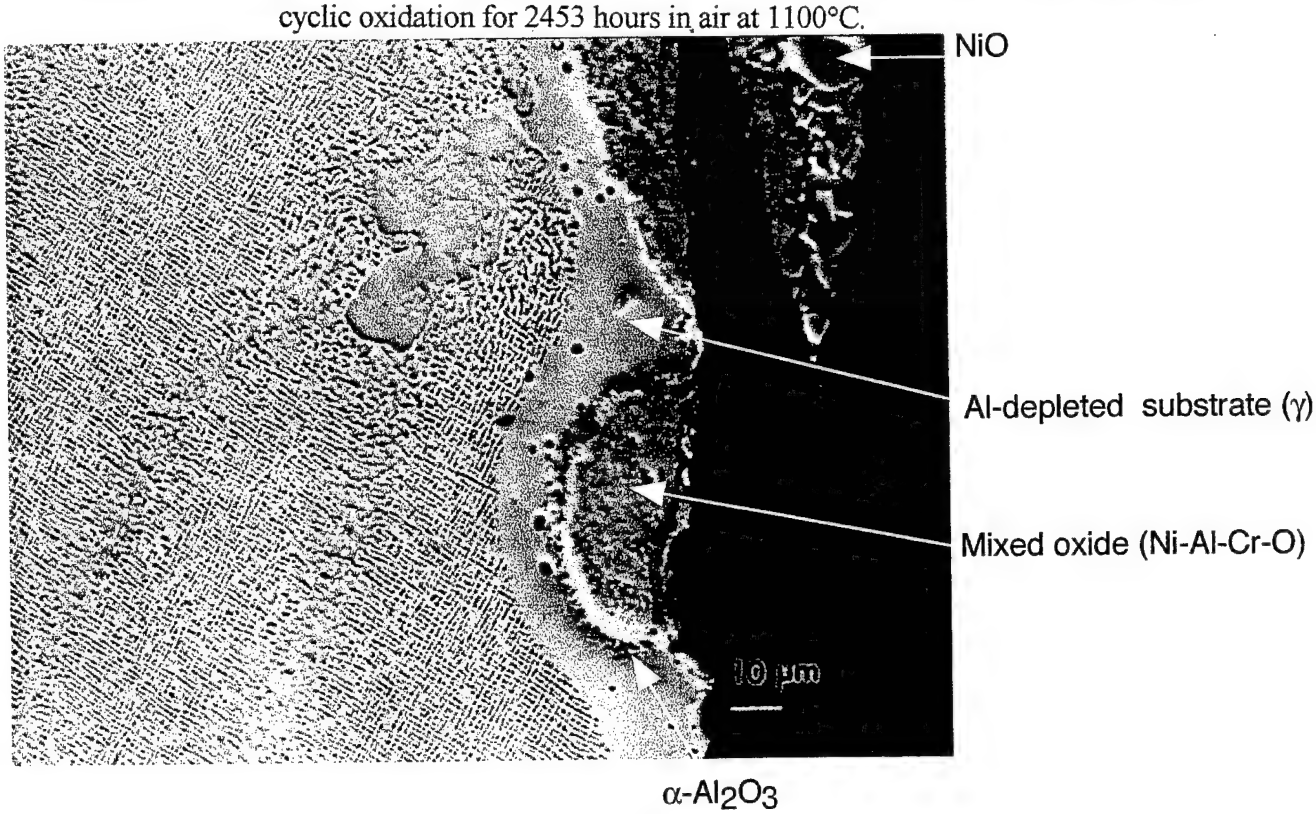

Figure 10. SEM cross-section micrograph of a polycrystalline alloy (45 ppm S) after cyclic oxidation for 117 hours in air at 1100°C.

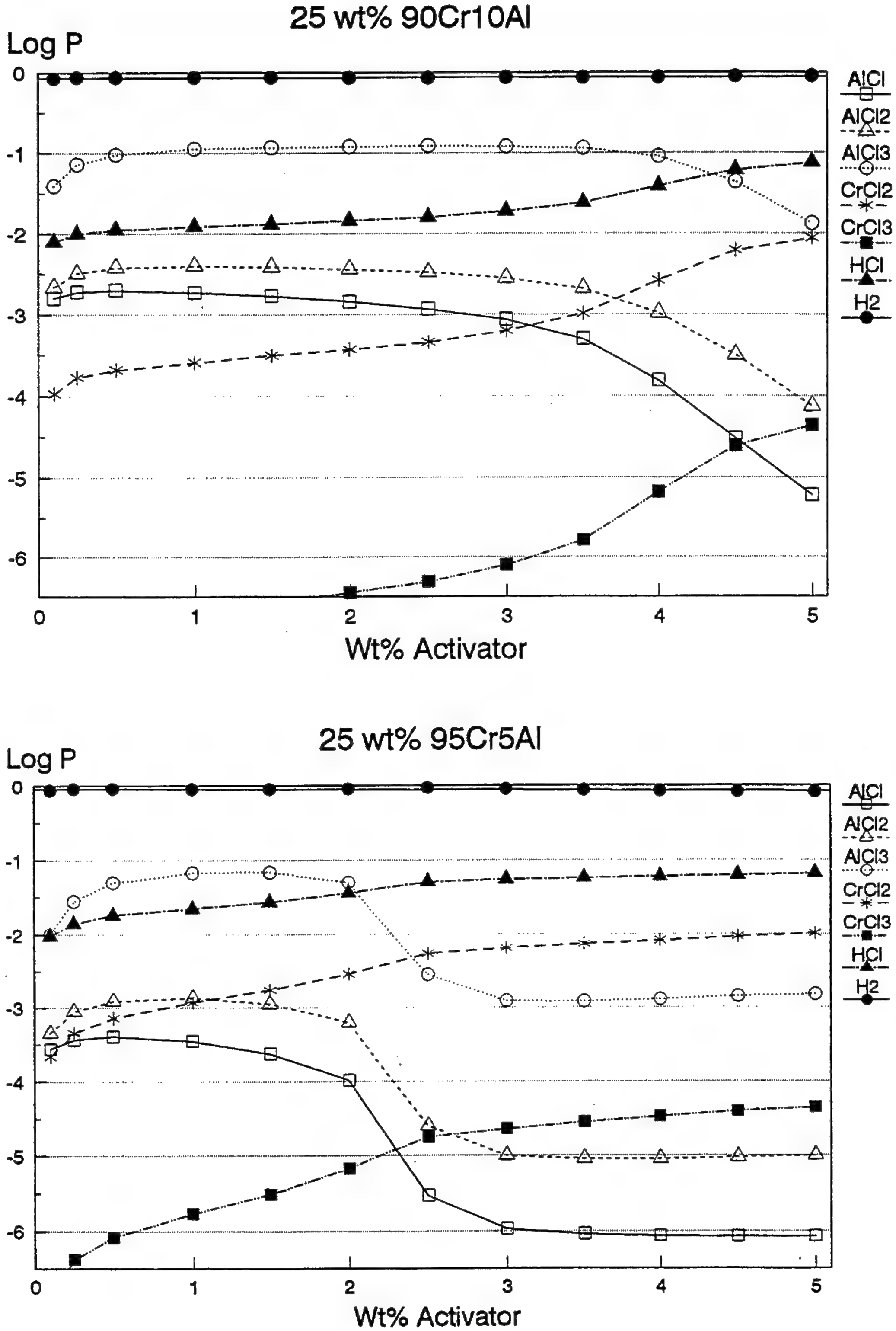

Figure 11. Equilibrium partial pressures at 1100°C in NH_4Cl-activated packs using Cr-Al masteralloys as the source.

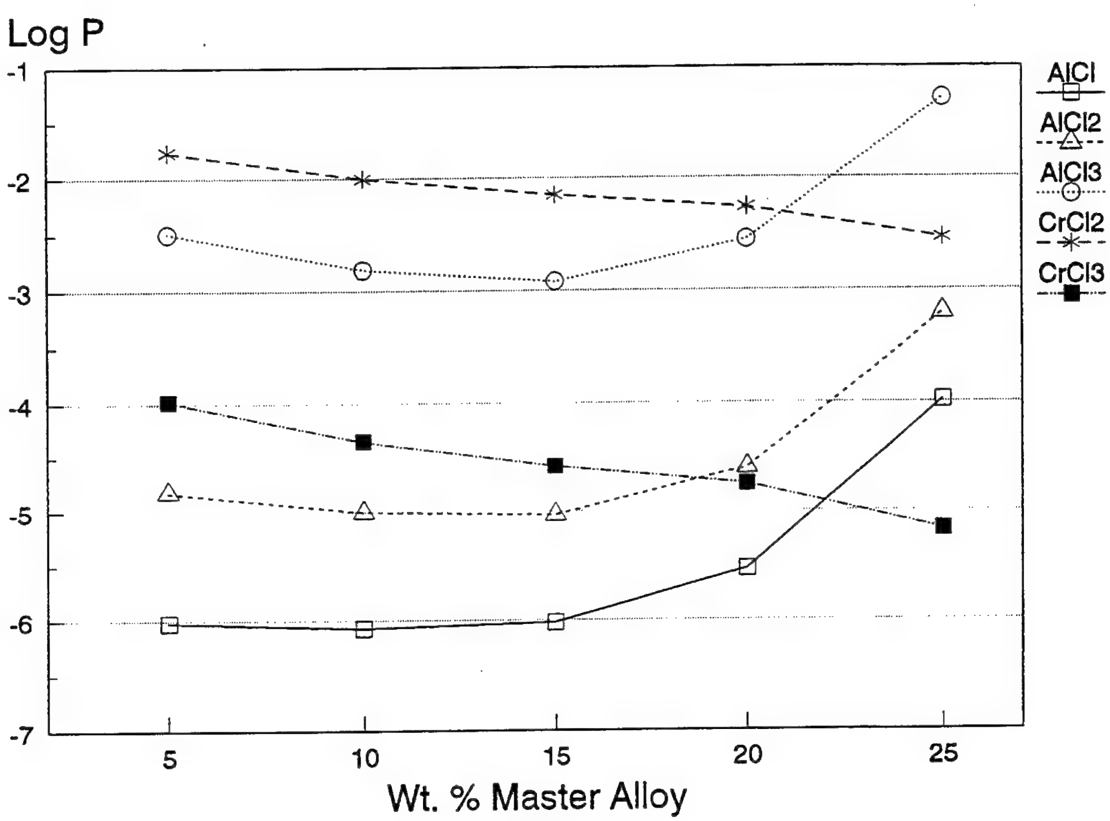

Figure 12. Partial pressures as a function of concentration of 95Cr-5Al masteralloy in pack activated with 2 wt% NH_4Cl at 1100°C.

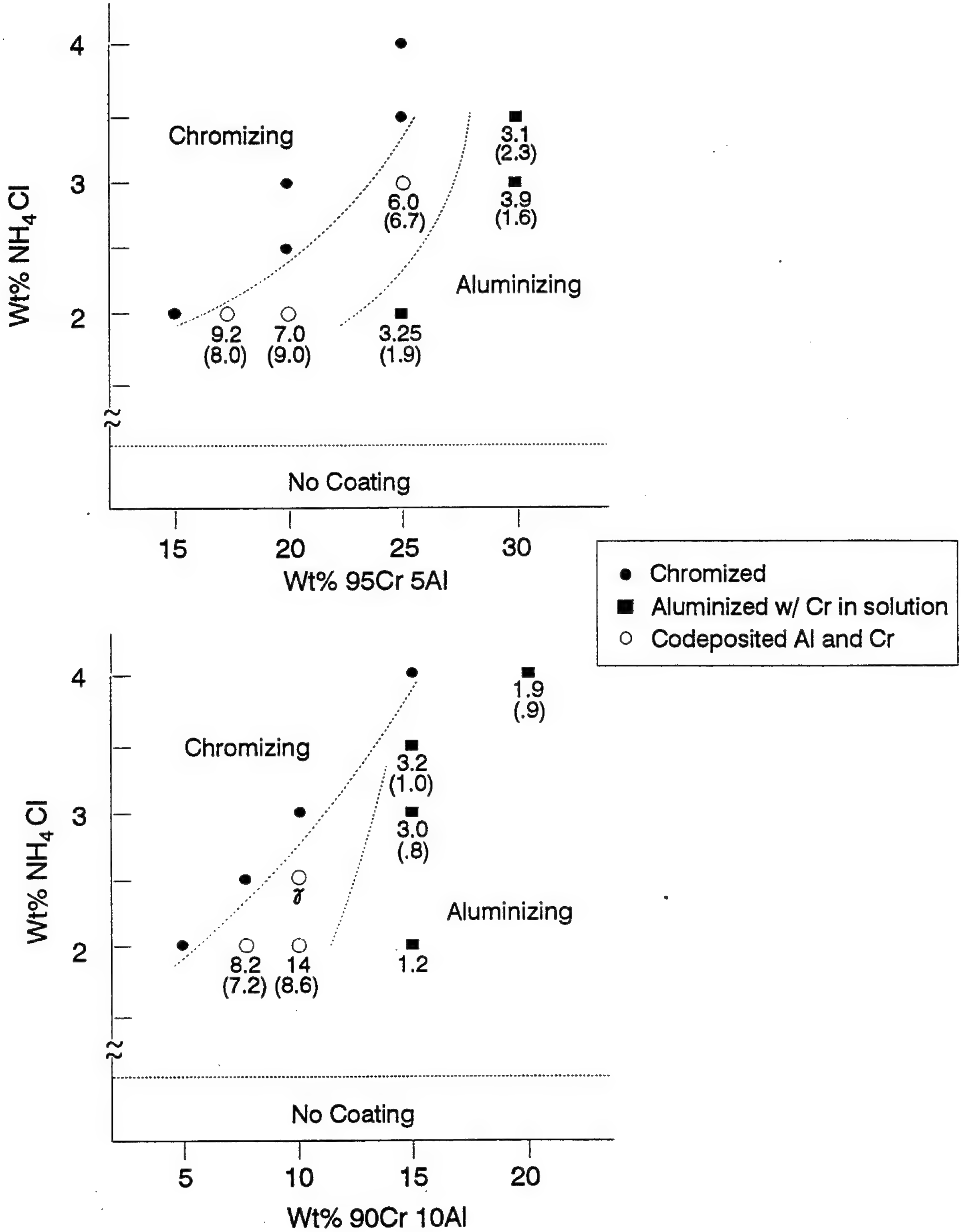

Figure 13. Maps for coatings deposited on Ni-270 using various amounts of NH_4Cl activator and Cr-Al masteralloys: (a) 95Cr-5Al, (b) 90Cr-10Al. Numbers on the map refer to near-surface chromium content.

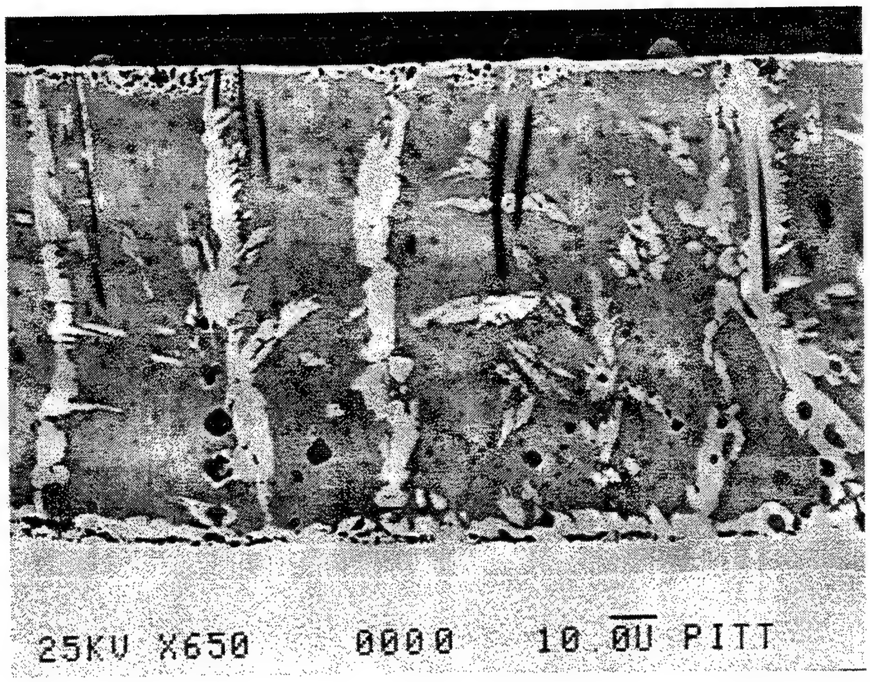

Figure 14. Coating developed on Ni-270 with a pack composition of 17.5wt% 95Cr-5Al masteralloy and 2 wt% NH_4Cl activator after 20 hours at 1100°C.

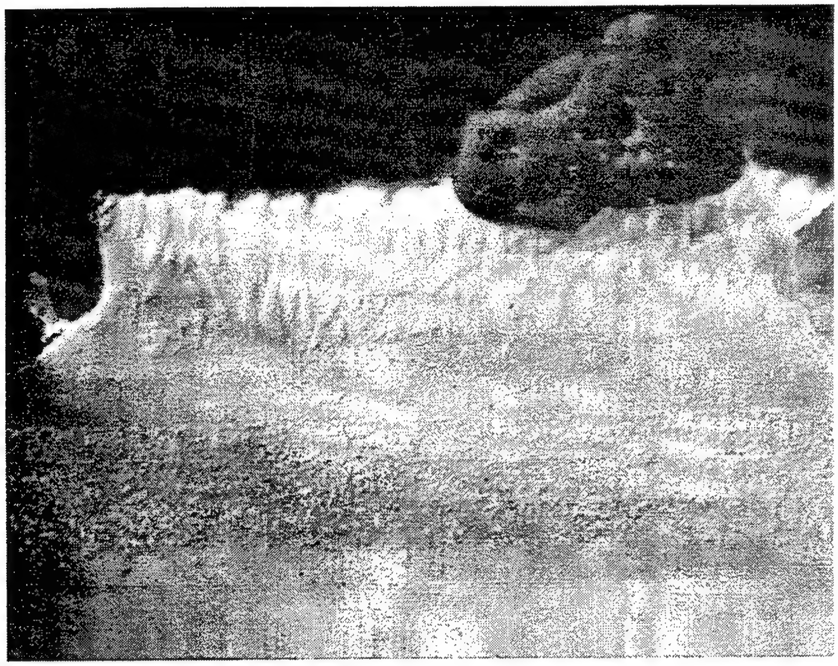

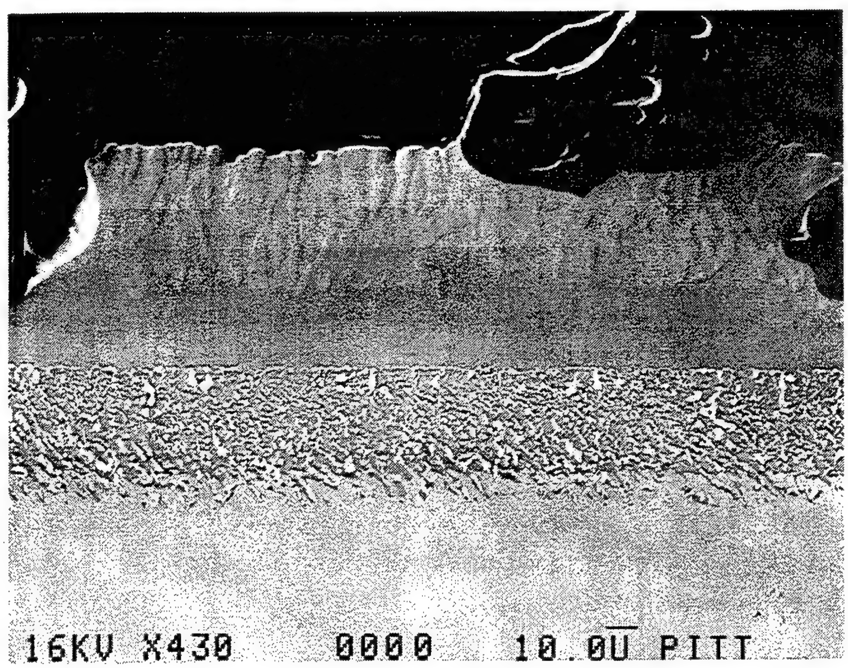

Figure 15. Coating developed on PWA 1484 using a pack composition of 17 wt% 95Cr-5Al masteralloy and 2 wt% NH_4Cl activator after 20 hours at 1100°C. At top is an optical micrograph and at bottom is an SEM(SEI) micrograph.

IV.A.2 The Removal of Sulfur from Liquid Metal to Concentrations Less Than One Part Per Million

Principal Investigator: Professor N. Birks
Materials Science and Engineering Dept.
University of Pittsburgh

Student: Mr. J. Patterson

IV.A.2.1 INTRODUCTION

Sulfur is present in most metals and alloys to some extent. It is regarded almost universally as having only deleterious effects on the properties of metals and substantial efforts are made to keep sulfur contents as low as practicable. The only exception is in the manufacture of "free cutting" steels when the presence of sulfur causes the machining swarf to form as chips rather than as a continuous ribbon.

It has always been metallurgical practice to keep the sulfur content as low as possible, consistent with cost and application. Consequently, sulfur contents of steels have fallen in specification from about 0.02 w/o to levels approaching 0.002 w/o for armor plate and line pipe steels[1]. The reduction of sulfur to these low levels of 20 ppm cannot be accomplished during normal steelmaking but requires separate, extra, processing in the form of "ladle metallurgy".

Low sulfur levels have always been desirable in steels but, in the case of superalloys, it was found that the adhesion of alumina scales to metallic substrates was greatly enhanced when the sulfur content of the alloy was reduced to 1 ppm and below[2].

Alloys, such as superalloys, that are designed for use at high temperatures rely on the formation of a passivating surface oxide for protection against surface oxidation. In most cases, the surface oxide formed is chromia or alumina and it offers effective protection so long as it remains adherent to the metal component surface. Under conditions of thermal cycling, the scale can lose adherence and spall. This removes the barrier layer and oxidation attack is, consequently, strongly accelerated. Thus, the discovery that metal scale adhesion is strongly enhanced when the sulfur content is reduced to below one part per million is significant. Unfortunately, the processing of bulk liquid superalloy to produce sulfur levels below 1 part per million has either not been developed or has not been reported in the open literature. The development of an effective process for this would be a significant commercial result.

Currently, laboratory techniques, based on removal of sulfur using dried hydrogen to convert it to hydrogen sulfide, are being used to demonstrate the beneficial effect of sulfur removal[3,4]. These techniques are neither rapid nor efficient but variations using a surface coating, have been patented with commercial application in mind[5].

The surface coating presumably prevents the formation of a compact alumina scale during the hydrogen treatment and therefore allows access of the hydrogen to the metal surface without hindrance. This will speed up the reaction but will not improve the efficiency of the process.

There is no doubt that the best time in superalloy production for the removal of sulfur is during processing of the liquid alloy. At this stage, the high temperature, the liquid state of the alloy and agitation of the processing promote rapid material transport and rapid reaction. These are ideal conditions under which to remove a contaminant down to very low concentrations.

In order to remove the sulfur in this way, a reaction is needed that will tie up the sulfur as a compound that is insoluble in the metal and that will result in a very low residual sulfur in solution. It is also important that the reaction should not compromise the alloy composition nor result in residual second phases that behave as inclusions.

Several suitable reactions are available, as follows

1. Reaction with lime, using carbon to maintain a low oxygen activity

$$CaO + \underline{S} + \underline{C} = CaS + CO_{(g)};\ \Delta G^{\circ} = 129183 - 68.76\ T\ J$$

Assuming that pure CaO is employed and, consequently, that pure CaS is produced, also neglecting any interactions in the liquid metal solution, the position of equilibrium for this reaction reads

$$\log K = \log \frac{a_{CaS} \cdot p_{CO}}{a_{CaO} \cdot h_c \cdot h_s} = \log \frac{p_{CO}}{h_c \cdot h_s} = 3$$

i.e. $\log h_s = \log p_{CO} - \log h_c + 6778/T - 3.61$

a_{CaS} and a_{CaO} are two activities of CaS and CaO. h_C and h_S are two henrian activites of C and S in the liquid metal. P_{CO} is the partical pressure of CO.

Using a modest vacuum of 10^{-6} atm and a carbon content of 0.1 wt%

$$\log h_s = -8.61 + 6778/T$$

Thus, at temperatures of 1600°C (1873K) and 1700°C (1973K) the lowest possible values attainable for sulfur content are 0.1 and 0.06 ppm respectively.

Thus, using pure CaO it is theoretically possible to obtain sulfur contents of the order of 10^{-2} ppm, depending on temperature and the level of the vacuum, which controls the carbon monoxide partial pressure.

2. Reaction with a rare earth oxide to form an oxysulfide such as

$$Y_2O_3 + \underline{S} + \underline{C} = Y_2O_2S + CO;\ \Delta G^{\circ} = 11065 - 165.01\ T\ J$$

The position of equilibrium for this reaction can be written as

$$\log \frac{a_{Y_2O_2S} \cdot p_{CO}}{a_{Y_2O_3} \cdot h_s \cdot h_c} = 8.63 - \frac{578.61}{T}$$

The reaction would be carried out using pure yttria and producing pure yttrium oxysulfide consequently.

$$\log h_s = \log p_{CO} - \log h_c - 8.63 + \frac{578.61}{T}$$

Assuming, as before, that $p_{CO} = 10^{-6}$ atm and $h_c = 0.1$ wt%.

$$\log h_s = 578.61/T - 13.33$$

At 1600°C (1873K) and 1700°C (1973K) the limiting sulfur contents would be 9.52×10^{-14} wt% and 9.19×10^{-14} wt% or 10^{-9} parts per million in each case, the effect of temperature being only slight.

The very high stability of the oxysulfide Y_2O_2S[6], coupled with the presence of carbon as reducing agent and being under vacuum, places the thermodynamic limit of sulfur activity at about 10^{-9} ppm. This is not attainable in practice but indicates that kinetics should be the only limiting factor.

In the above reactions elements such as Al, which are strong deoxidants, will act in the same way as carbon, but would result in the formation of a solid Al_2O_3 reaction product, dispersed in the melt.

The use of carbon as the deoxidizing medium in these reactions, coupled with a modest vacuum, means that the only deoxidation product is gaseous, CO. Thus, extra inclusions should not be produced to compromise the mechanical properties of the alloy.

IV.A.2.2 EXPERIMENTAL PROCEDURE

It is intended to melt nickel containing about 10-20 ppm sulfur and about 0.1% carbon in an oxide crucible. Vacuum induction melting will be used that will allow rapid heating, good temperature control and good mixing due to the electromagnetic stirring effect. The reaction will take place at the melt-crucible surface. Crucibles made of yttria will be used and samples will be taken as the melt proceeds.

Due to the difficulty in analyzing sulfur in metal at very low levels, the LECO technique will only be used above 40 ppm. Below this value the glow discharge mass spectrometer technique must be used. However, this technique is claimed to be accurate below 1 ppm of sulfur.

The melt will be sampled at melt out and at intervals during a run. The final sample will be taken as a core sample from the solidified ingot.

Sulfur removed from the liquid metal will form the oxysulfide on the crucible surface. It should be possible to detect these sites using the scanning electron microscope with energy dispersive spectrographic analysis.

Runs will be carried out in solid oxide crucibles for periods of 60 to 120 minutes.

IV.A.2.3 ACCOMPLISHMENTS AND SIGNIFICANCE

Several runs of an exploratory nature have already been made as follows.

Several melts were made using a 15 kg vacuum induction melting unit in which the metal charge is held in a refractory crucible under a vacuum that can be held as low as 10^{-4} tor. The standard crucible was made of zirconia. The experiment required the addition of CaO or Y_2O_3 as a reactant. It was also required that this should not be added as a powder in order to avoid the risk of formation of inclusions in the metal. Therefore the first melts were carried out using CaO and Y_2O_3 as a lining on the inner surface of the zirconia crucible that were in contact with the molten metal. It proved to be very difficult to obtain CaO or Y_2O_3 in forms that can be applied to the zirconia with sufficient adherence to withstand the heavy washing action induced by the induction heating. This circulation is needed if low sulfur levels are to be obtained, since it ensures that the sulfur in the metal is brought into contact with the reactive lining. If the lining does not maintain adherence with the zirconia crucible, the lining material floats to the surface and accumulates around the top of the crucible. This debris contains any sulfide that is formed and could be entrained when pouring samples. This will result in high sulfur analysis when the lining becomes part of the sample.

In the first melting experiments, 415 kg of pure nickel were held for 60 minutes at 1600°C. After the first run, the lime lining was found to have been completely removed from the zirconia crucible surface.

Two similar runs were made using a sprayed on Y_2O_3 lining on the zirconia crucible. In both cases the melt was held for 60 minutes and no change in sulfur was detected in the metal. In this case the melt had been made to contain 27 ppm sulfur and the sample taken after 60 minutes also had 27 ppm sulfur.

Since the Y_2O_3 coating was removed during the heat, it is possible that the lining was washed off by the liquid metal and remained in suspension as Y_2O_2S inclusions. A metallographic example of the sample did not reveal such inclusions.

It is clear that the technique of using spray coated zirconia crucibles is not successful. The coating that is applied does not adhere sufficiently strongly to the zirconia to survive the mechanical washing action that results from induction melting. Rather than engage in a lengthy process of developing adherent linings to zirconia crucibles, it was decided to carry out some melts in crucibles made from yttria. Such crucibles were found to be available from Howmet Corporation and the first one to be delivered was fired at 1500°C for two hours to present a

large surface area to the melt. Using yttria crucibles it is possible to ensure that the melt remains in contact with the active material. So long as such contact can be held, sulfur should eventually be removed because the thermodynamic driving force is very strong and, using lime crucibles, the technique has been shown to be capable of desulfurizing steel held under vacuum[7,8].

The first experimental run with the yttria crucible was made using a Ni-C-S alloy that was shown by LECO analysis to contain 48 ppm sulfur. During melting and on holding the molten metal in the crucible at 1600°C, substantial gas evolution was observed for the initial 20 minutes. The melt was continued for 60 minutes and was allowed to solidify in the crucible. This was done to avoid entraining any particles that accumulate around the lip of the crucible and which might be sulfur rich. The melt was found to have invaded the pores of the yttria crucible, it therefore apparently had no difficulty in wetting it. The metal casting was broken out and a sample taken from the center was analyzed using glow discharge mass spectrometry and was reported to contain 12 ppm sulfur.

This last experimental heat has apparently demonstrated that sulfur removal is taking place. It is unfortunate that the levels of sulfur are too low to be revealed using the SEM-EDS techniques which fail to reveal any sulfur in the system.

The next steps in this work will be to obtain hard fired crucibles of yttria (1680°C for 10 hours) to prevent metal invasion of the crucible.

IV.A.2.4 CONCLUSIONS

The technique that has been studied is shown to have substantial promise according to thermodynamic calculations.

The technique of melting in zirconia crucibles coated with an active lining was not found to be feasible due to poor adherence between the lining and the crucible.

Using a solid yttria crucible a strong indication was obtained that sulfur removal from the metal was occurring at 1600°C.

It remains to substantiate the above result and to establish the kinetics to isolate the rate determining step and, further, to establish a procedure for sulfur removal in practice.

IV.A.2.4 REFERENCES

1. E.T. Turkdogan; Fundamentals of Steelmaking, Institute of Metals, London, 1996.
2. J.G. Smeggil, A.W. Funkenbasch and N.S. Bernstein; Met. Trans., 17A, 923, (1986).
3. J.L. Smialek; Met. Trans. A, 18A, 164, (1987).
4. B.K. Tubbs and J.L. Smialek; "Effect of Sulfur Removal on Scale Adhesion to PWA 1480", p. 459 in Corrosion and Particle Erosion at High Temperatures, ed. V. Srinivasan and K. Vedula, TMMS, Warrendale, PA (1989).
5. W.P. Allen, N.S. Bornstein, S. Chin, M. DeCrescente, D.N. Duhl and, J.G. Smeggil; US Patent 5,346,563, Sept. 13 (1994).

6. D.A.R. Kay, W.G. Wilson and V. Jalan; Journal of Alloys and Compounds, 192, 11 (1993).
7. J.J. Reyes; M.S. Thesis, University of Pittsburgh (1983), "The Desulfurization of Steel by Lime under Vacuum".
8. T. Ototani, T. Dagawa, U Patent 4,729,787, March 8, 1988, Method of Producing an Fe Co Ni Alloy Having Low Contents of Sulfur, Oxygen and Nitrogen. The Removal of Sulfur from Liquid Metal.

IV.A.3 Improvement of Environmental Resistance of Titanium Matrix Composites

Principal Investigator: Professor F.S. Pettit
Materials Science and Engineering Dept.
University of Pittsburgh

Other Faculty Participants: Dr. G.H. Meier
Materials Science and Engineering Dept.
University of Pittsburgh

Students: Mr. R. Cerchiara

IV.A.3.1 INTRODUCTION

The alloy Ti-22Al-23Nb (atomic percent) is a possible matrix alloy for SiC reinforced composites. This alloy contains discontinuous α_2 (Ti_3Al)(37 vol%)[1], in a two phase mixture of orthorhombic (Ti_2AlNb) platelets (33 vol%) in a β_2 matrix (ordered Ti-Nb) (30 vol%). Such composites have projected use temperatures in excess of 600° to 750°C. If these use temperatures are to be realized, the oxidation of Ti-22Al-23Nb must be investigated and described. This section of this report is concerned with the oxidation of Ti-22Al-23Nb at temperatures between 500° and 900°C in oxygen, air and in water vapor. The results that are presented in the following have been presented in more detail in a previous publication[2].

IV.A.3.2 ACCOMPLISHMENTS AND SIGNIFICANCE

Experimental Procedures

The Ti-22Al-23Nb materials were obtained in monolithic, hot pressed foil ("neat") and composite form from P.R. Smith, Materials Directorate, Wright Laboratories, Dayton, Ohio. The Ti-22Al-21Nb-2Ta was obtained only in monolithic form. All of these materials possessed an $\alpha_2+\beta_2+O$ structure. The neat and composite panels possessed a residual β_2+O layer at the surfaces of as processes specimens.

Isothermal and cyclic oxidation experiments were performed on 1 cm^2 coupons. Isothermal experiments were performed at 500-900°C in a closed quartz reaction chamber where continuous weight change measurements were made using a Cahn microbalance. Cyclic oxidation experiments were performed at 525°C and 685°C where the coupon specimens were subjected to one hour cycles, 45 minutes at temperature and 15 minutes in the cold zone at room temperature.

Materials characterization of as-received and exposed specimens was performed using optical (OM), scanning electron (SEM) and transmission electron (TEM) microscopy, X-ray diffraction (XRD) and metallography electron diffraction (SAD), and Vickers microhardness profiles.

Starting Materials Characterization

Scanning micrographs of etched (Kroll's reagent) cross-sections of the monolithic Ti-22Al-23Nb and Ni-22Al-21Nb-2Ta, and the neat and composite Ti-22Al-23Nb based materials are presented in Figures 1-3. The monolithic alloys possessed a microstructure of primary α_2 grains surrounded by a β_2 + O phase mixture, Figure 1. The neat and composite materials possessed less coarse α_2 in the foil microstructure and a thin layer of β_2 + O at foil / foil and external interfaces, Figure 2. The two phase layer is formed during vacuum hot rolling of foil as Al is evaporated. The oxygen content of the orthorhombic material increased to 1670 ppm after processing to foil. Nitrogen and iron levels were 70 and 20 ppm, respectively. A gradient in microstructure is apparent in the case of the Ti-22Al-23Nb neat and composite panels. A decrease in the vol% of α_2 was observed as foil/foil and external interfaces were approached. Small precipitates within the α_2 are thought to be a form of O.

SCS - 6/Ti-22Al-23Nb panels were produced by Textron Specialty Materials. Fiber mats were prepared by "crossweaving" β-(Ti-48Nb) ribbon at ~ 1 mm intervals through rows of SCS - 6 fibers placed in an 0° orientation. Four of these mats were interspersed with five foils and hot pressed on a 35 vol% SCS-6 basis. Conservative consolidation parameters of 925°C/103 MPa./4hr were chosen to assure complete metal flow and foil - foil bonding. Mild steel bags were used and no binders were added during processing. The SCS - 6 fiber consisted of β - SiC deposited by chemical vapor deposition on a carbon precursor with a double pass carbon coating added to limit subsequent reaction with the alloy matrix[3], Figure 3.

Oxidation of Ti-22Al-23Nb in Dry Air and Oxygen

The oxidation kinetics for Ti-22Al-23Nb neat panels in dry air are presented in Figure 4. The oxidation kinetics conform to a parabolic rate law initially but transform to linear with time. At temperatures of 700°C and below linear kinetics were not observed after about 700 hours of oxidation. The oxidation kinetics in oxygen were similar to those for air but the parabolic rate constants were larger in oxygen. This difference was more evident at 900° than at 700°C and lower temperatures.

The microstructure of a typical specimen after oxidation is presented in Figure 5. XRD analyses of this scale showed that it was composed of TiO_2 and $AlNbO_4$. Platinum markers placed upon the surfaces of specimens prior to oxidation were located at the gas/oxide interface after oxidation, Figure 6. Beneath the oxide scale an "interstitial affected zone" (IAZ) was developed. This zone was evident due to microstructural features, Figure 7, and also by making hardness measurements of the zone in the alloy immediately beneath the oxide scale, Figure 8. For cases for which a transition in oxidation kinetics from parabolic to linear was observed, nodular oxide growths with cracks were observed at the gas-oxide surface, Figure 9.

The parabolic rate constants for oxidation of Ti-22Al-23Nb in air are compared to parabolic rate constants obtained with Ti-24Al-11Nb and Ti-22Al-21Nb-2Ta in Figure 10. There are small differences between these rate constants but all of them are substantially larger than parabolic rates for transport through alumina scales. In Figure 11 the parabolic rate constants for alloys containing titanium and aluminum as well as niobium are presented as a function of niobium content. In those alloys containing 10 atomic percent and less niobium, the oxidation rates are

controlled by transport through TiO_2. Both aluminum and niobium decrease the parabolic rate constants by altering the defect concentration through doping. Both titanium interstitials and oxygen vacancies provide transport through TiO_2. The relevant doping reactions are:

$$3Ti_i^{4+} + 2Al_2O_3 \rightarrow 4Al_i^{3+}\ 6O_0^X + 3Ti_{Ti}^X$$
$$3V_0^{2+} + Al_2O_3 \rightarrow 2Al_i^{3+} + 3O_O^X$$
$$Ti_i^{4+} + 2Nb_2O_5 \rightarrow 4Nb_{Ti}^{1+} + 10O_O^X + Ti_{Ti}^X$$
$$V_O^{2+} + Nb_2O_5 \rightarrow 2Nb_{Ti}^{1+} + 5O_O^X$$

where it can be seen that both Al_2O_3 and Nb_2O_5 cause these two defect concentrations to be decreased. In the case of Ti_3Al the oxide scale grows both inward via oxygen diffusion, and outward via diffusion of both titanium and aluminum interstitials, however above about 10% niobium, the oxide growth is virtually totally inward by oxygen diffusion via oxygen vacancies. Specimens of Ti-22Al-23Nb with a zone denuded of α_2 due to processing, oxidized more rapidly than specimens that did not contain this denuded layer. This effect is not large but it is reproducible.

As the niobium concentration exceeds 10%, the parabolic rate constants increase, Figure 11, and linear kinetics begin to appear after some period of parabolic oxidation. At the composition Ti-22Al-23Nb, $AlNbO_4$ is observed in the oxide scale. These increases are believed to be caused by the formation of Nb_2O_5 in the external scale. The niobium oxide appears predominantly as $AlNbO_4$ in the scale. It is proposed that the niobium oxide provides rapid transport paths which causes the parabolic rate constants to become larger. The formation of this oxide also causes cracking of the scale to occur with the appearance of the oxide nodules and linear oxidation kinetics. Schematic diagrams showing the changes in oxide growth modes as a function of niobium concentration are presented in Figure 12.

The IAZ develops beneath the oxide scale by the diffusion of oxygen through the β matrix phase as illustrated in Figure 13. A precipitate is formed in this zone as shown in Figure 7b and illustrated in Figure 13. Based upon XRD and TEM analyses this precipitate appears to be $(Ti,Nb)_XO$.

The smaller rates of oxidation in air versus oxygen are believed to be caused by (Ti,Nb)N that is developed at the oxide-alloy interfaces during oxidation in air. The mechanism by which the nitride affects the oxidation process is not understood. The distributions of TiO_2 and $AlNbO_4$ in the external scale are believed to affect the oxidation kinetics. The development of the nitride layers may alter the distribution of oxides in the external scale and consequently affect the magnitude of the parabolic rate constants. The linear rate constants did not exhibit any difference between air and oxygen.

Cyclic Oxidation Behavior and Water Vapor Effects

Cyclic oxidation tests were performed to compare cyclic and isothermal oxidation behavior. Experiments were also performed to determine the effects of water vapor on oxidation. Oxygen or air was passed through a deionized water bath held at various temperatures between 25°

and 75°C. A sealed quartz reaction chamber was used and the inlet was heated above the dew point temperature. Weight change versus time data for isothermal oxidation in wet (saturated at 25°C) and dry O_2 at 700°C are presented in Figure 14. Larger weight increases were evident for specimens oxidized in wet oxygen. This increase in weight change did not become larger as the oxygen was saturated with water at 75°C and, therefore, there was not a dependence on water vapor pressure.

Cyclic oxidation tests were performed between 25° and 525° or 685°C. Each one hour cycle consisted of 15 min at room temperature (25°C) and 45 min at 525° or 685°C. These tests were performed on Ti-2Al-23Nb as well as Ti-22Al-21Nb-2Ta and Ti-24Al-11Nb. The results obtained in dry air are presented in Figures 15 and 16. Some cracking and spalling of the oxide scales occurred. This condition caused the weight change versus time data to become constant after about 1000 hours at 525°C. Spalling of oxide also occurred at 685°C but the oxidation was more rapid and very substantial weight increases were observed for both Ti-22Al-23Nb and Ti-22Al-21Nb-2Ta after about 1000 hours of exposure. The presence of water vapor caused the cracking and spalling of oxide to occur sooner and to be more excessive, Figure 17. In Figure 18 the oxide scales formed on Ti-22Al-23Nb after about 6000 hours of cyclic oxidation at 685°C in wet and dry air are compared. The oxide scale is substantially thicker in wet air compared to dry air, however, the amount of oxidation in dry air at 685°C is still substantial.

The results that have been obtained by using water vapor indicate that water vapor has two adverse effects on the oxidation of Ti-21Al-23Nb. First, water vapor causes the isothermal oxidation rate to be increased. The reason for this increase is not certain but the most plausible explanation is that water vapor causes transport through voids and pores in the oxide scale to be increased. Such effects of water vapor have been documented for the oxidation of iron and cobalt[3].

Water vapor also causes the oxides formed on Ti-22Al-23Nb to crack and spall rather profusely. This effect causes substantial amounts of oxidation of both Ti-22Al-23Nb and Ti-22Al-21Nb-2Ta and neither of these alloys could be used for extended periods of time at 685°C without a coating to provide resistance against oxidation. Ti-24Al-11Nb is more resistant to oxidation but weight increases of 1 mg/cm^2 were observed at 685°C even in dry air after 6000 hours of oxidation.

The Effects of Al, Nb and Ta on Oxidation Behavior

The results presented previously show that there is not enough aluminum in Ti-22Al-23Nb to develop protective scales of Al_2O_3 on this alloy. The oxide scale that is formed is composed of TiO_2 and $AlNbO_4$. The aluminum does cause the growth rate of TiO_2 to be decreased compared to growth on pure titanium by causing the concentrations of titanium interstitials and oxygen vacancies to be decreased. Niobium at concentrations less than about 10% also causes the oxidation rate to be decreased by causing the concentrations of titanium interstitials and oxygen vacancies in TiO_2 to be decreased. It also appears that niobium causes the concentration of aluminum interstitials to be decreased. This could occur via the following reaction where the solubility of aluminum in TiO_2 is decreased.

$$2Al_i^{3+} + 3Nb_2O_5 \rightarrow 6Nb_{Ti}^{+1} + 12O_o^x + Al_2O_3$$

Such effects cause the scale growth modes to change from combined inward and outward to virtually completely inward growth, Figure 12. At niobium concentrations above 10%, Nb_2O_5 begins to form in the scale, it appears in combination with Al_2O_3, but it provides rapid transport paths through the scale with increased parabolic rate constants and transition from parabolic to linear kinetics after shorter exposure times.

In both isothermal and cyclic oxidation Ta caused a decrease in oxidation in the regions of parabolic oxidation, Figure 16, where Ti-22Al-21Nb-2Ta oxidized slower than Ti-22Al-23Nb. Tantalum did not have any effect on the linear oxidation kinetics. The reason for this effect of tantalum is not understood but it may be due to tantalum affecting the distribution of the rapid transport paths of niobium oxides in the external scale.

Oxidation of Composites

The oxidation kinetics of SiC reinforced Ti-22Al-23Nb are presented in Figure 19. The kinetics are similar to those of the neat panels, Figure 4, but some weight losses are evident at the lower oxidation temperatures due to oxidation of carbon that is present at the fiber-matrix interfaces. It is clear that such interfaces cannot be exposed to oxidizing environments.

Mechanical Testing of Unoxidized and Preoxidized Specimens

A few three point bend tests were performed on unoxidized and preoxidized monolithic specimens. These specimens were mechanically tested in laboratory air at 25°, 350° and 500°C. The bend tests were performed in a Mechanical Testing System (MTS) using a strain rate of $2\text{-}6 \times 10^{-3}$. At 25°C the ductility at fracture decreased as the preoxidation temperature was increased, Figure 20. The fracture toughness of the unaffected matrix began to dominate during deformation at 350°C and 500°C and the ductility was essentially constant and independent of the preoxidation condition. Chemical removal of the IAZ resulted in recovery of ductility of the preoxidized specimens tested at room temperature. These results show that the IAZ causes cracks to be initiated in specimens tested at room temperature and these cracks result in less ductility as the IAZ is increased in thickness. The IAZ has less effect on ductility as the test temperature is increased due to an increase in the fracture toughness of this alloy.

IV.A.3.3 SUMMARY

The oxidation kinetics of Ti-Al-Nb alloys have been found to be controlled by transport through TiO_2 at aluminum concentrations of 20-25 atomic percent and niobium concentrations up to 10%. The kinetics are parabolic and much larger than those for protective Al_2O_3 scales, but smaller than that for growth of TiO_2 on titanium. As the niobium concentration is increased beyond 10% the parabolic rate constants are increased and the kinetics change to linear after initial periods of parabolic oxidation. This is caused by the development of Nb_2O_5 in the scales which provides more rapid transport paths than through doped TiO_2 and which also causes cracking in the scales.

Cyclic Oxidation at 685°C has been shown to result in very substantial oxidation in dry air and Ti-22Al-23Nb cannot be used for extended periods of oxidation without a coating. Both isothermal and cyclic oxidation of Ti-22Al-23Nb is increased by the presence of water vapor in

air or oxygen. Oxidation in air is slightly less than that for oxidation in oxygen due to the formation of a nitride layer at the oxide scale-alloy interface. Tantalum in Ti-22Al-21Nb caused a slight decrease in the parabolic rate constants but had no effect on the linear kinetics.

The formation of the IAZ adversely affected room temperature ductility. The fracture toughness of the bulk alloy dominated at higher deformation temperatures and the fracture ductility was not degraded at 350° and 500°.

The oxidation of the composites is similar to the matrix phase but is further compromised by the rapid oxidation of carbon at exposed fiber-matrix interfaces.

IV.A.3.4 REFERENCES

1. Paul R. Smith and Jeffrey A. Graves, Tensile and Creep Properties of High Temperature Titanium Alloys in "Neat" Matrix Form, pp. 139-149, Orthorhombic Titanium Matrix Composites, Proceeding from Orthorhombic Titanium Matrix Composite Workshop held at the Westin Hotel, Cincinnati, OH, 26-28 July 1994, WL-TR-95-4068.
2. R.R. Cerchiara, G.H. Meier and F.S. Pettit, Mechanisms for Oxidation of Ti-22Al-23Nb SiC Reinforced Composites at Temperatures between 500° to 900°C in Oxygen, Air and Water Vapor, in Technical Report #WL-TR-97-4082, Orthorhombic Titanium Matrix Composites II Workshop Proceedings, December 10-12, 1996, Orlando, Florida.
3. G. Das, Met. Trans., 21A, 1572 (1990), A Study of the Reaction Zone in an SiC Fiber-Reinforced Titanium Alloy Composite.
4. A Rahmel and J. Tobolski, Corros. Sci., 5, 333, (1965).

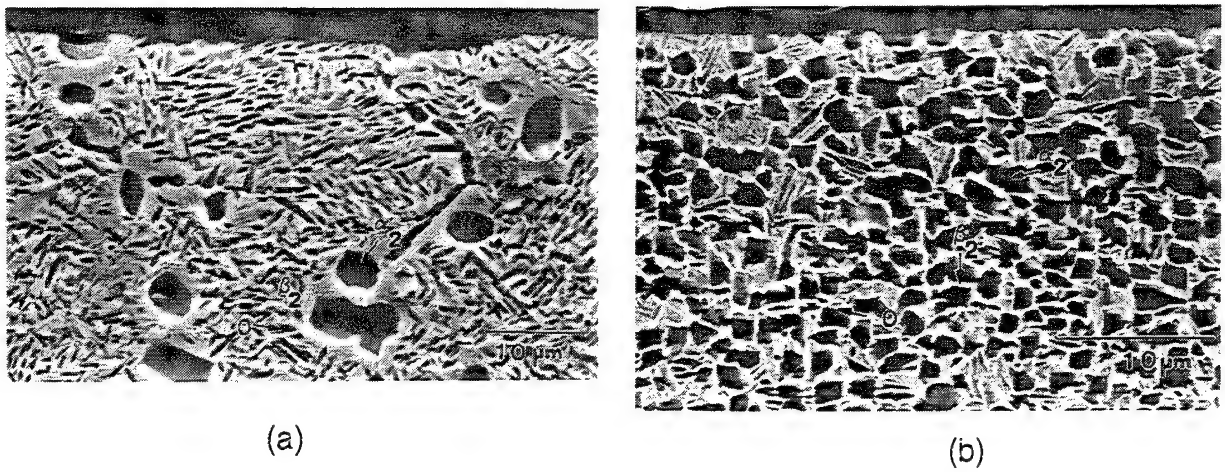

Figure 1 . Scanning micrographs showing the microstructures of Ti-22Al-23Nb, (a), and Ti-22Al-21Nb-2Ta, (b), in the as processed condition.

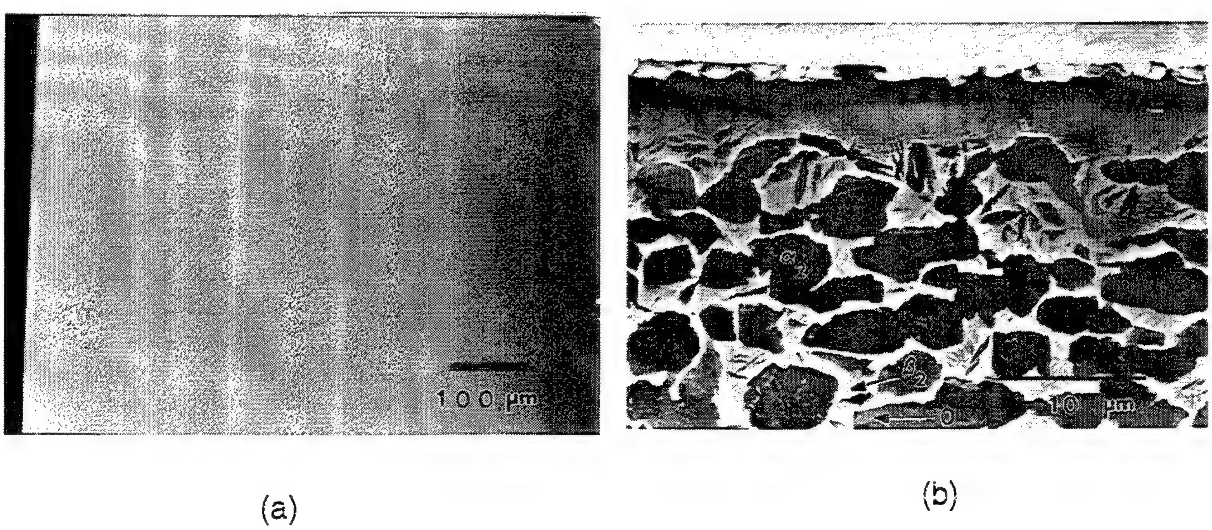

Figure 2. Micrographs showing the structure of Ti-22Al-23Nb neat panels in the as processed condition.

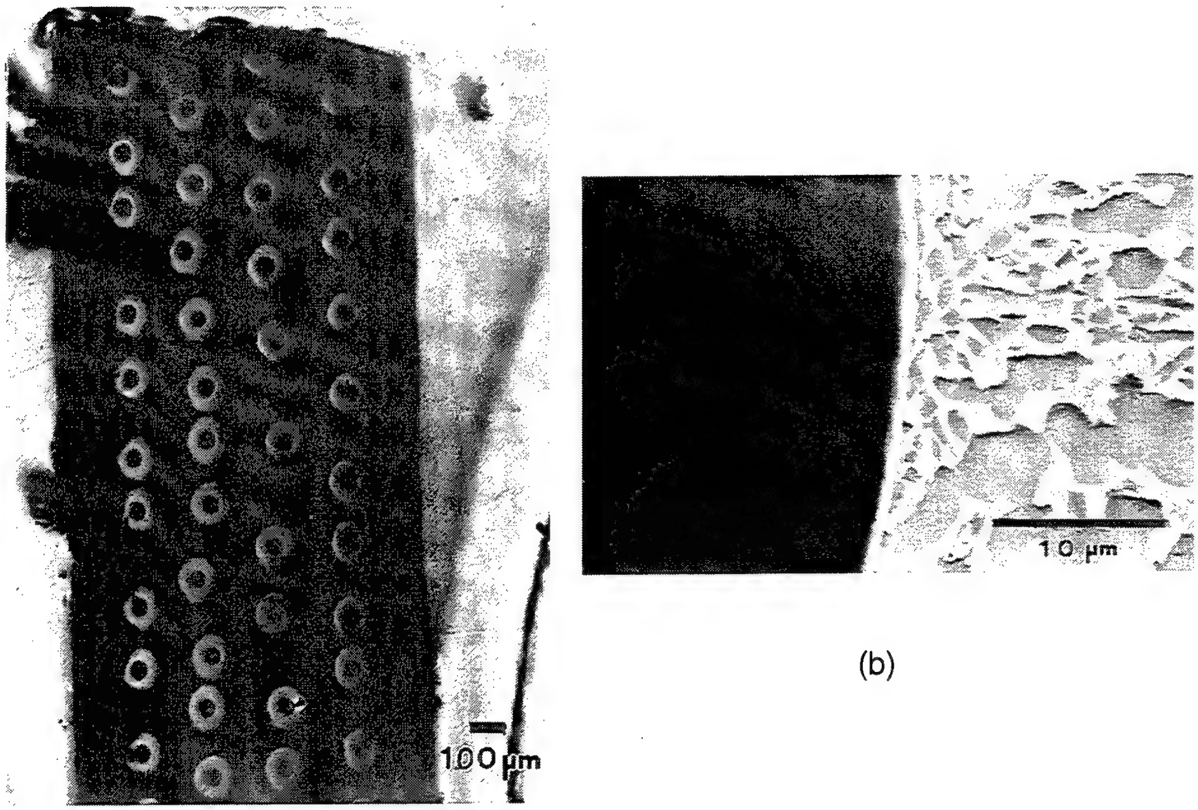

(a)

(b)

Figure 3. Photographs of a SCS-6 / Ti -22Al-23Nb composite in the as processed condition. A thin reaction zone is evident at the fiber-matrix interface.

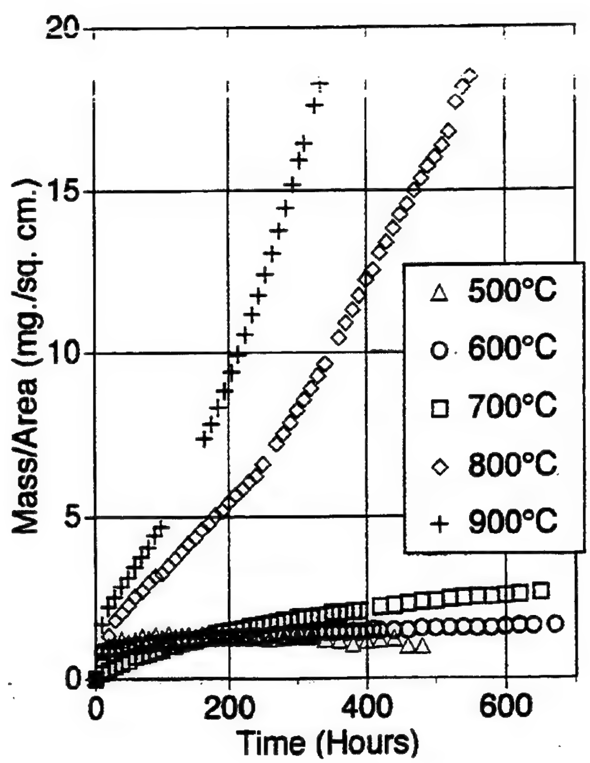

Figure 4. Weight change versus time measurements for oxidation of neat panels of Ti-22Al-23Nb at several different temperatures.

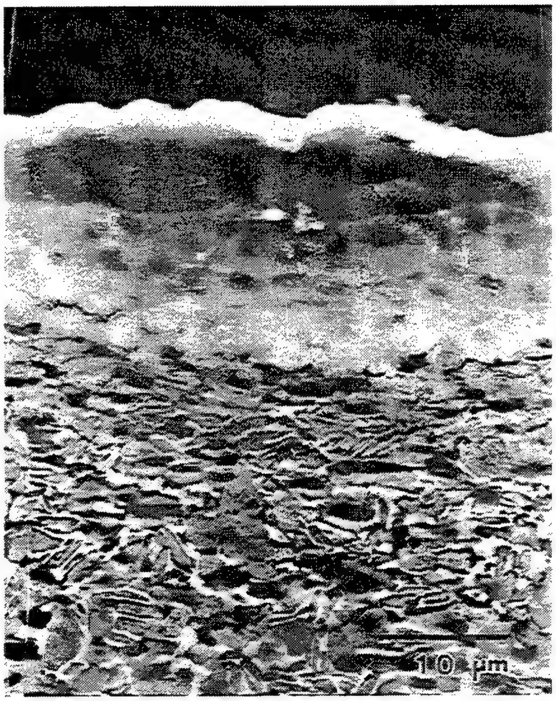

Figure 5. Scanning micrograph of neat panel of Ti-22Al-23Nb after 168 hrs at 800°C.

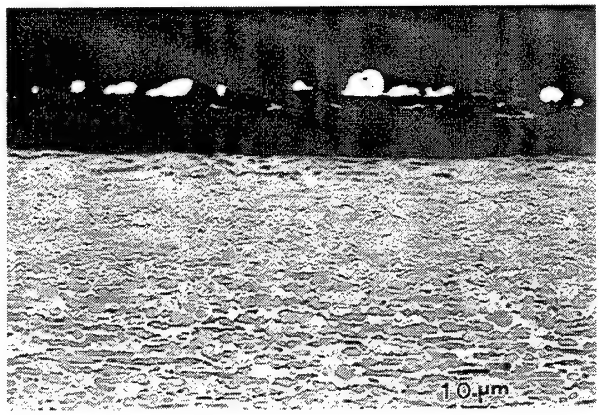

Figure 6. Scanning micrograph showing the position of platinum markers on Ti-22Al-23Nb.

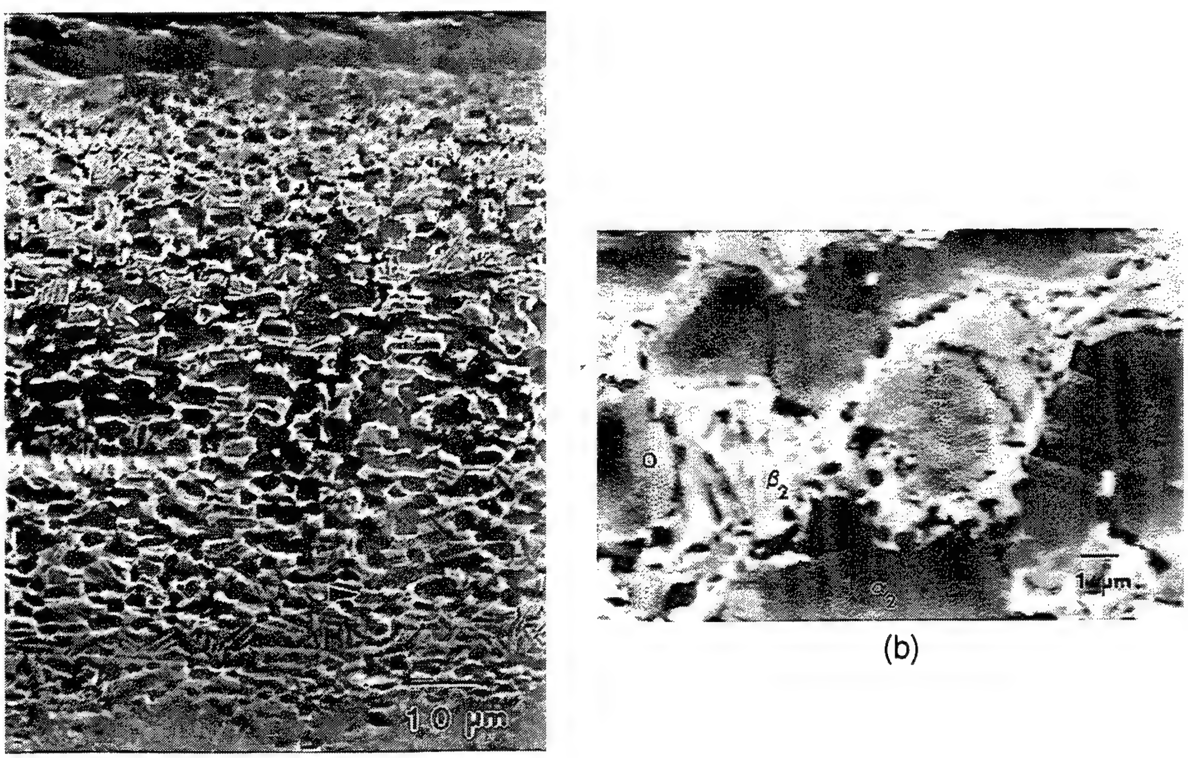

(b)

(a)

Figure 7. (a) Cross section of Ti-22Al-23Nb after 550 hrs at 800°C in air showing the interstitial affected zone. (b) Higher magnification of interstital zone showing O, α_2 and β_2 phases as well as what is believed to be an oxide phase.

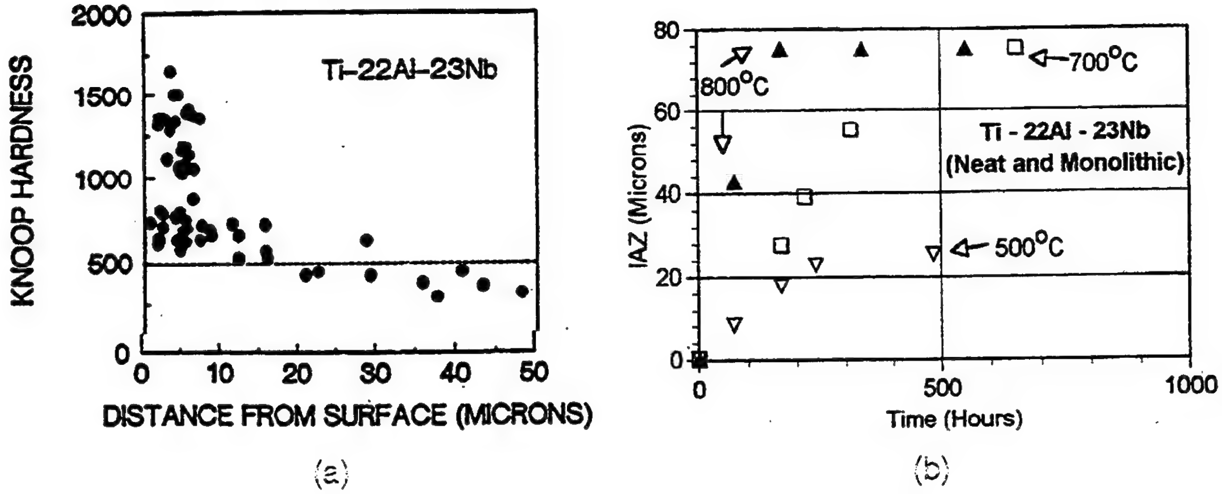

Figure 8. Hardness measurements were used to determine the thickness of the Interstitial Affected Zone (IAZ) (100 hrs. at 800°C), (a) and the thickness of the zone varied with time and temperature, (b).

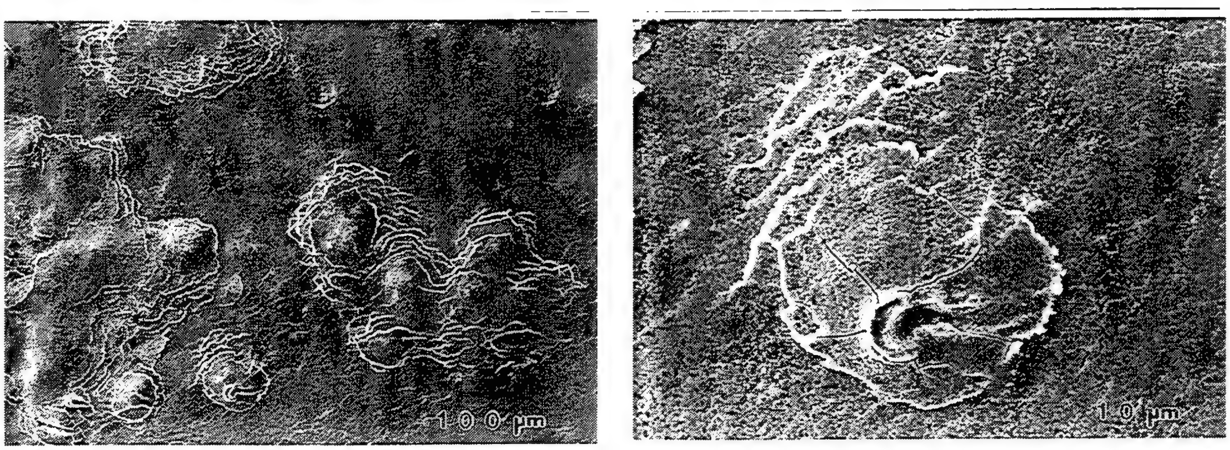

Figure 9. Scanning micrographs that show nodules with cracks that were observed as the oxidation kinetics changed from parabolic to linear (240 hrs at 800°C).

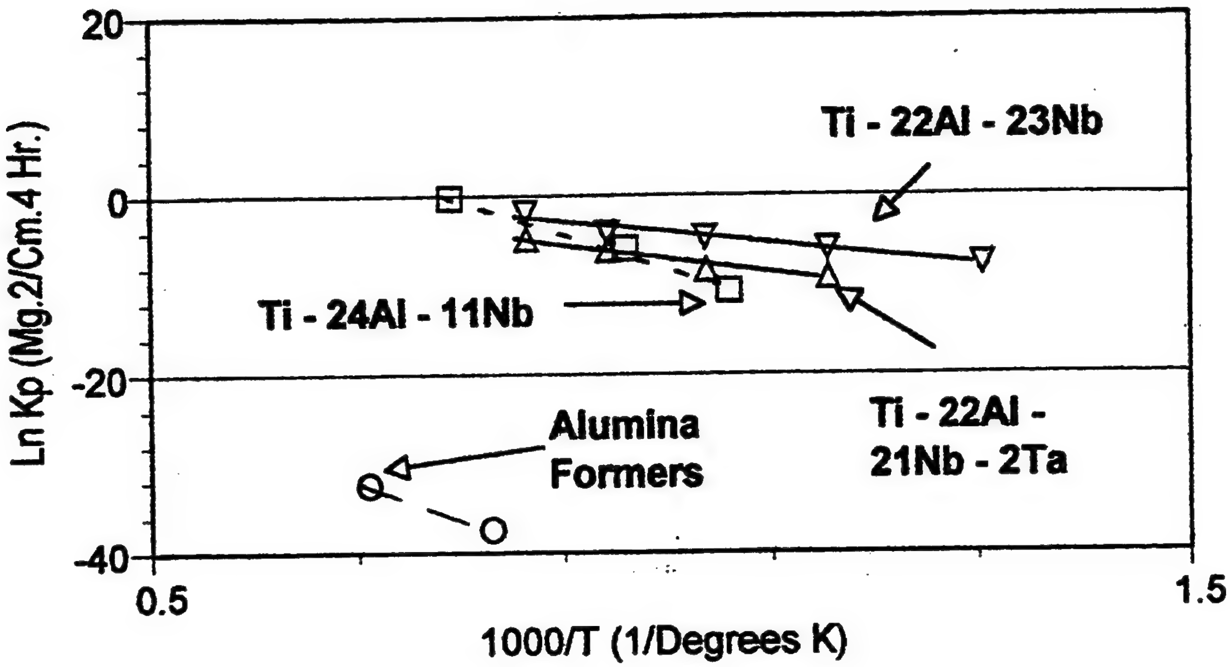

Figure 10. Comparison of the parabolic rate constants as a function of temperature for oxidation of Ti-22Al-23Nb, Ti-22Al-21Nb-2Ta, and Ti-24Al-11Nb. Some parabolic rate constants for growth of alumina scales on alloys are also included.

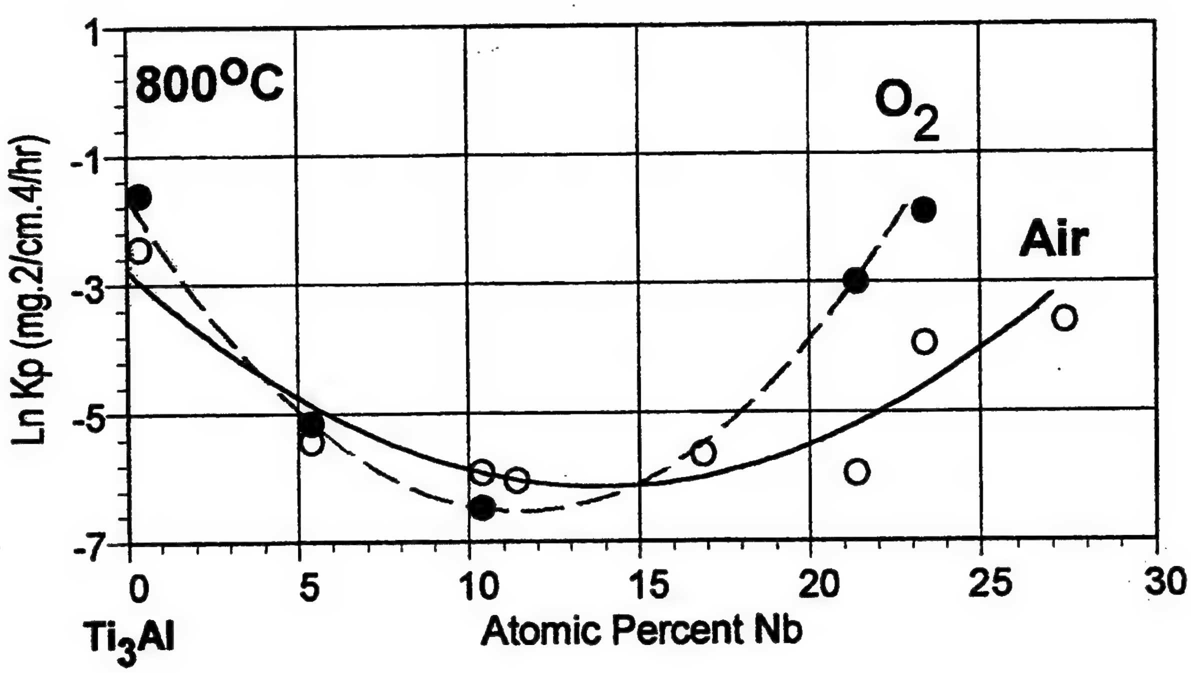

Figure 11. Parabolic rate constants for Ti-alloys containing about 25 atomic % Al as a function of Nb content.

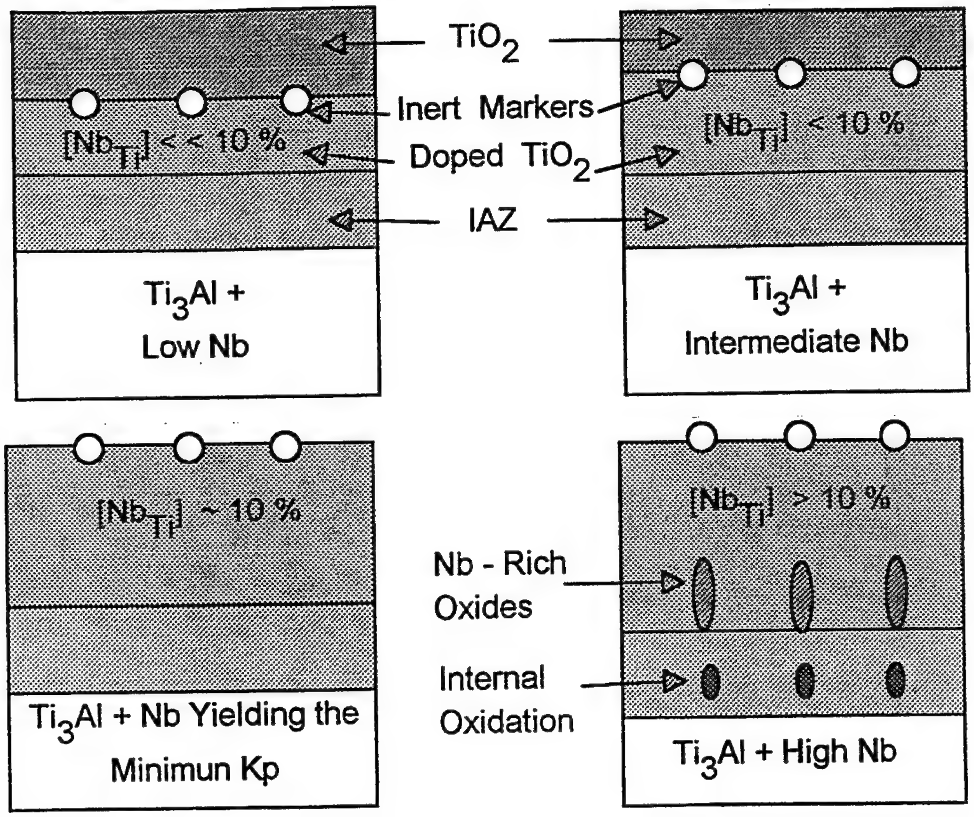

Figure 12. Schematics to show the changing modes of oxide scale growth as a function of Nb concentration.

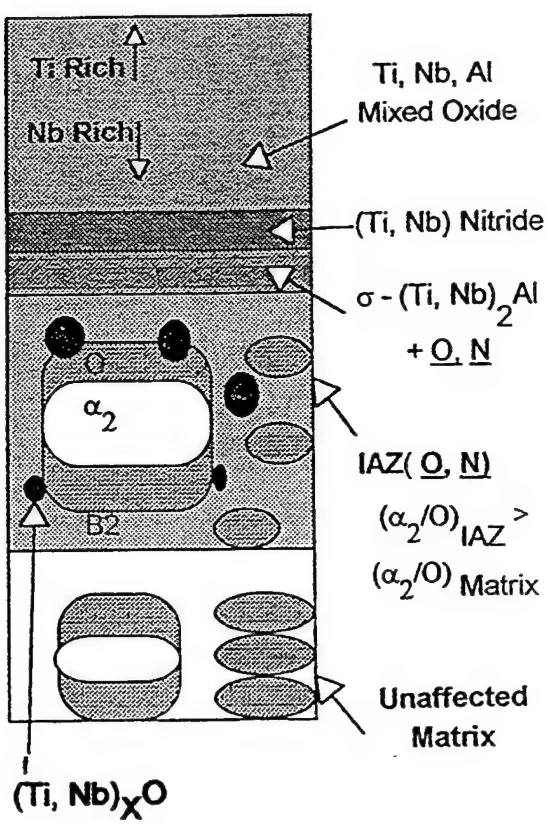

Figure 13. Schematic diagrams to illustrate the oxidation of Ti-22Al-23Nb along with the development of the IAZ.

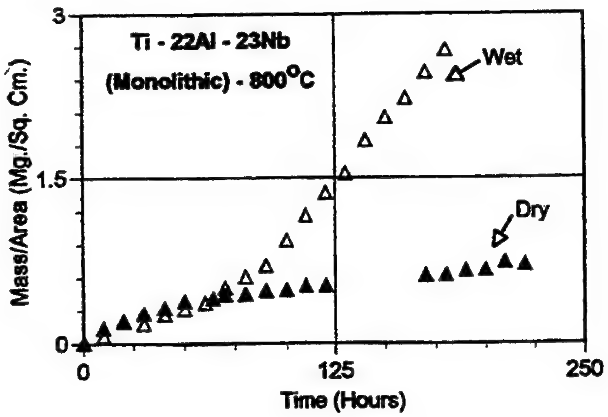

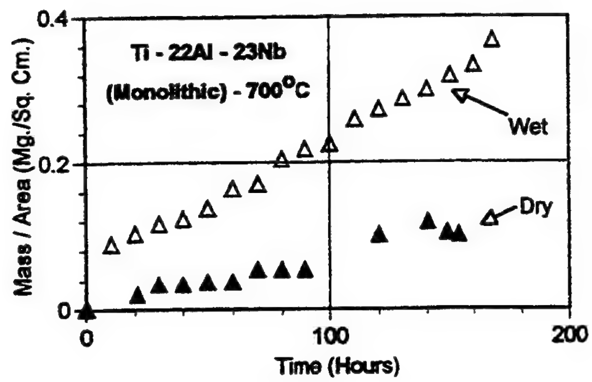

Figure 14. Weight change versus time data to compare the isothermal oxidation of Ti-22Al-23Nb in wet and dry air.

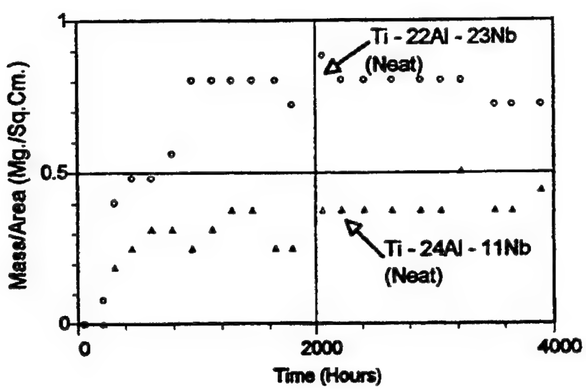

Figure 15. Weight change versus time measurements for the cyclic oxidation of Ti-22Al-23Nb and Ti-24Al-11Nb at 525°C in dry air.

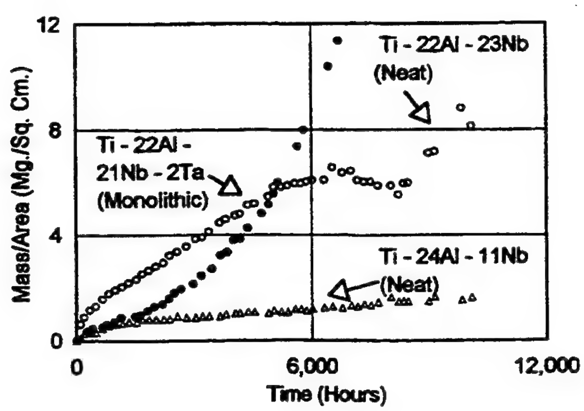

Figure 16. Weight change versus time data for the cyclic oxidation of Ti-22Al - 23Nb and Ti-24Al-11Nb in dry air at 685°C.

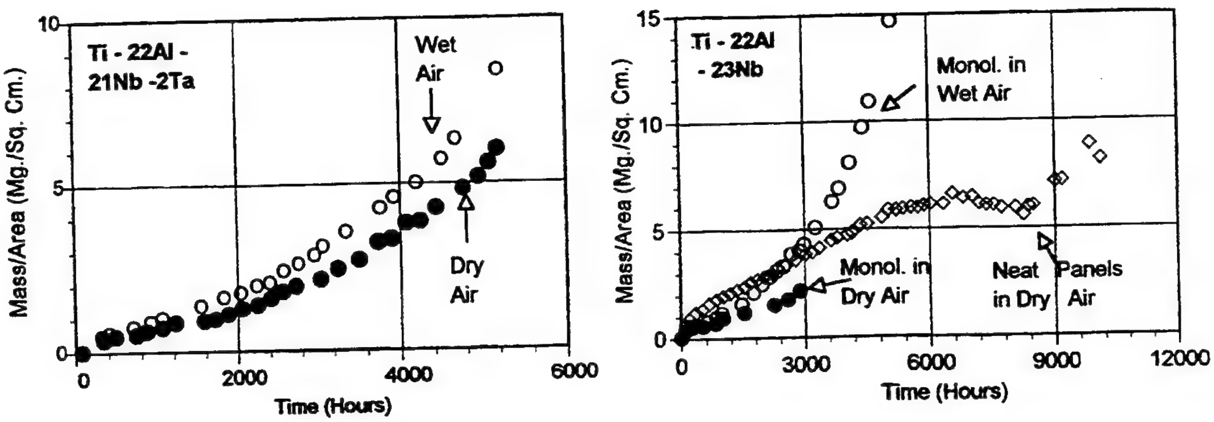

Figure 17. Comparison of cyclic oxidation data for Ti-22Al-23Nb and Ti-22Al-21Nb-2Ta at 685°C in wet and dry air.

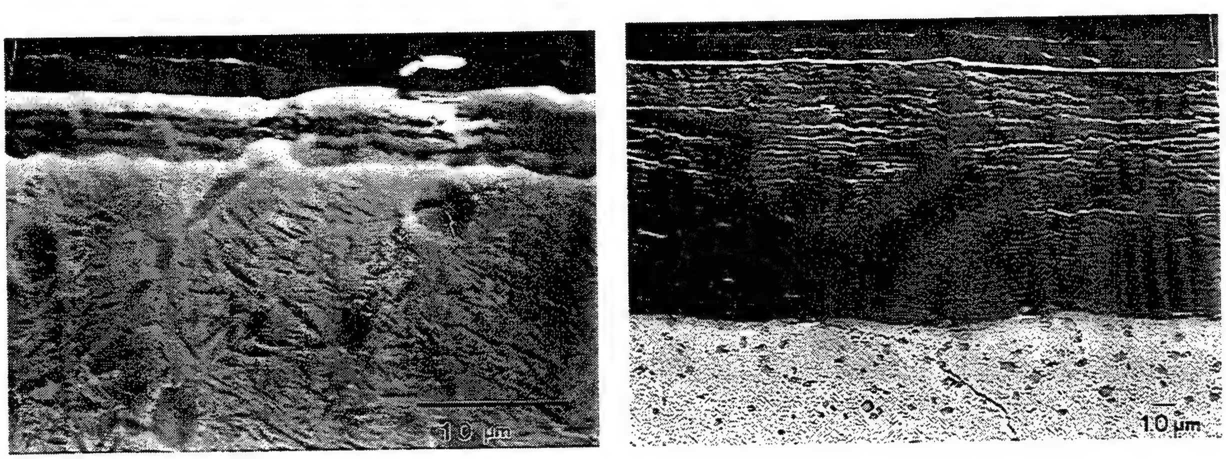

Figure 18. Comparison of the thickness of oxide scales formed upon Ti-22Al-23Nb after about 6000 hrs at of cyclic oxidation 685°C in dry (left) and wet (right) air.

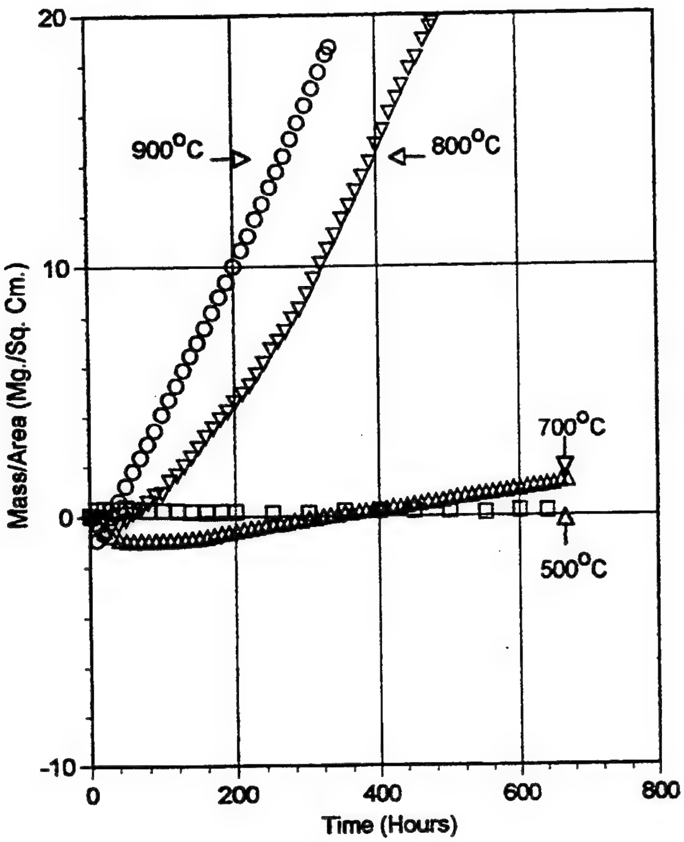

Figure 19. Weight change versus time data for the isothermal oxidation of SCS-6-Ti-22Al-23Nb in dry air.

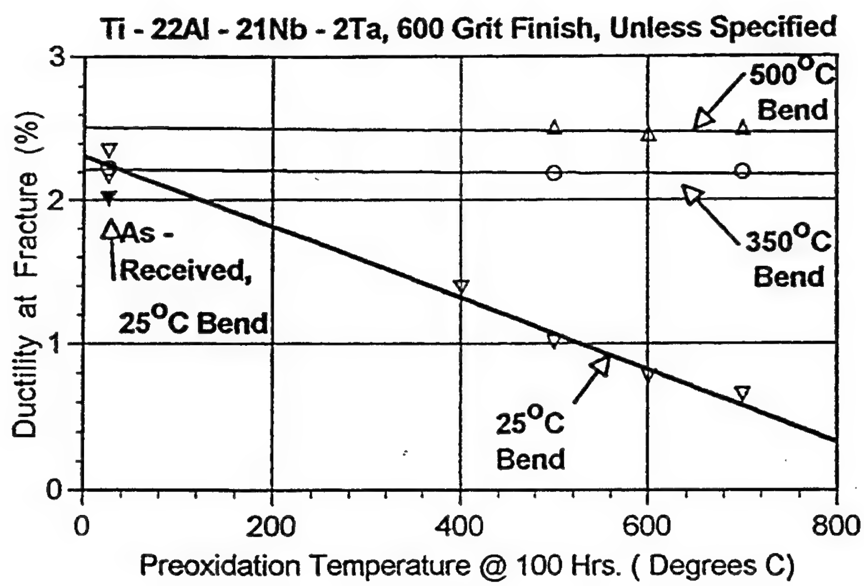

Figure 20. Ductilities at Fracture for Unoxidized and Preoxidized Ti-22Al-21Nb-2Ta

IV.A.4 Thermomechanical Processing of Titanium Aluminide Alloys

Principal Investigator:	A.J. DeArdo Materials Science and Engineering Dept. University of Pittsburgh
Other Faculty Participants:	Dr. C.I. Garcia Materials Science and Engineering Dept. University of Pittsburgh
	Dr. M. Hua Materials Science and Engineering Dept. University of Pittsburgh
Students:	R. Mutschler

IV.A.4.1 INTRODUCTION

Near-γ TiAl alloys have shown excellent potential for use in high temperature applications due to their very good strength and stiffness at elevated temperatures. However, the widespread application of these alloys have been limited due to their poor ductility and toughness, particularly at low temperatures. The metallurgical factors responsible for this behavior are not well understood. The large α grain size and the level of interstitial content, i.e. O_2, have been identified as two of the major factors responsible for the poor ductility and toughness. Near-γ TiAl alloys are intended for use at high temperatures, despite their intended application before this study no systematic studies had been conducted regarding the microstructural behavior of these alloys under isothermal conditions at elevated temperatures. Therefore, the central goals of the research conducted in this study are two-fold; (i) to gain an understanding of the microstructural stability of various microstructures (lamellar, duplex, and equiaxed) of near-γ alloys when subjected to long holding times at elevated temperatures, and (ii) to explore different thermomechanical processing paths to refine the microstructure, i.e. lamellar, duplex and/or equiaxed in these materials. The main focus is on refining the lamellar microstructure, which promises the best overall combination of properties provided the large grain size can be reduced.

IV.A.4.2 ACCOMPLISHMENTS AND SIGNIFICANCE

A master's degree was completed by R. Mutschler in December 1995, and this work was essentially comprised of isothermal heat treatments of TiAl alloys and the accompanying microstructural behavior[1]. The main conclusion drawn was that the lamellar microstructure is unstable at high temperatures and transforms over time to an equiaxed γ microstructure. A TTT diagram of this transformation is presented in Figure 1, where the alloy is air cooled from 1380C to a range of holding temperatures, from 1000°C to 1250°C, and held for times up to 72 hours. The lamellar to equiaxed transformation was seen to occur via two distinct mechanisms: the first, spheroidization of the α (or α_2) plates, was found to be driven by the reduction in overall surface area which accompanies spheroidization, this process also involved a change in aluminum concentration in the α and γ phases, see Figure 2. The second

mechanism involves growth of preferred orientation variants within the γ lamellae[2,3], wherein these oriented regions coarsen and grow, eventually forming equiaxed γ grains. This growth of selected orientation domains is the dominant mechanism in the microstructural transformation from lamellar to equiaxed grains. Further experiments indicated that the kinetics of this transformation can be accelerated by deforming the lamellar structure prior to transformation.

Another aspect of the microstructural transformations in near-γ TiAl alloys was also investigated. When these alloys are rapidly quenched from single phase α, γ is formed through a massive transformation. Prior to this study, only γ has been found in the massive microstructure[4,5]. However, fine laths of α_2 phase were found inside the massive microstructure of a Ti-49Al alloy[6], see Figure 3. The same orientation relationship which exists between α_2 and γ in the lamellar microstructure was found in the massively transformed microstructure, namely $\{111\}\gamma || \{0001\}\alpha_2$ and $<001>\gamma || <1120>\alpha_2$. It is interesting to note that in recent work by Hoydick[7], a similar orientation relationship is seen between the parent phase (which is HCP, similar to the α phase) and the product phase (which has $L1_0$ crystal structure, similar to the γ phase) of a massive transformation observed in a MnAl alloy.

The next phase of the research explored the refinement of lamellar microstructure through thermomechanical processing. For this purpose, an MTS hot deformation machine was modified to allow high temperature deformation under a protective atmosphere. A Kanthal alloy tube was welded to the upper die collar, which was made of IN-718 superalloy, and slid over the lower die collar. Flowing argon, which was gettered of oxygen using titanium sponge, was flooded into the system. A high temperature clamshell furnace was used to heat the specimen and deformation dies, which were contained within the protective tube. This experimental setup is illustrated in Figure 4. Prior to these experiments, the material was homogenized at 1380°C for four hours, and air cooled to produce a fully lamellar microstructure. This led to a lamellar grain size of 1600 μm, see Figure 5, which is the starting condition for all experiments involving deformation described below, with one exception, where the massive microstructure was used as the starting condition.

One set of experiments involved quenching specimens to produce a massive microstructure, and then heat treating the samples at high temperature and cooling to produce a fully lamellar microstructure. The purpose of this is to attempt to produce refined lamellar grains through heat treatments alone, without deformation. Samples of a Ti-47Al-2Cr-2Nb alloy were heated at 1380°C for 1 hour and water quenched, thus producing the massive microstructure, which contains a large amount of defects, such as dislocations, stacking faults, and antiphase boundaries[8]. The material was then heated to 1380°C or 1360°C for times of 5, 10, and 20 minutes. A plot of lamellar grain size vs. time at 1380 or 1360°C is presented in Figure 6. It is seen that the 1360°C reheating temperature produces a much finer lamellar grain size than the 1380°C reheating temperature. It is important to note that in the sample heated for 5 minutes at 1360°C, a fine grain size of just over 200 μm is reported. However, the transformation at 1360°C from massive γ to α is incomplete in this sample, and the size reported is of those lamellar grains which coexist with the untransformed massive γ. This partially transformed microstructure is revealed in Figure 7. From these experiments, it was seen that lamellar grain size could be reduced from 1600 μm to under 400 μm simply by reheating the massive γ microstructure.

The next set of experiments involved samples deformed 50% in compression at temperatures ranging from 1000°C to 1300°C , then heated at 1360°C for 10 minutes, and slow cooled to form the fully lamellar microstructure. The results are shown in Figure 8. In the 2Cr-2Nb containing alloy, the refinement is optimized with a deformation temperature of 1200°C, see Figure 9, where the resulting lamellar grain size is approximately 340 μm. The binary alloy appears to possess a coarser final microstructure, except for the sample deformed at 1100°C, in which the transformation to α at high temperature was incomplete. It should be noted that all deformations were performed at a strain rate of .001 per second.

Additional experiments were designed, the deformation temperature was selected based on the isothermal transformation diagram. It is believed that deformations above the nose of the "C" curve result in rapid recrystallization and growth of the equiaxed structure, hence leading to coarse lamellar grains after reheating. Deformation below the nose of the "C" curve, i.e. below 1150°C induces development of finer equiaxed grains, which leads to finer lamellar grains after reheating and cooling. One 2Cr-2Nb containing sample was first heated at 1380°C for one hour and water quenched, producing massive microstructure, and then deformed 50% at 1100°C, subsequently heated at 1360°C for 10 minutes, then slow cooled. The resulting lamellar grain size, which is given in Figure 10, was approximately 400 μm, so starting with a massive microstructure showed no significant benefit. The binary and 2Cr-2Nb alloys were both deformed 50%, heat treated at 1360°C for 10 minutes, then were deformed another 50% at 1100°C, and given the 10 minute heat treatment at 1360°C for 10 minutes to form the lamellar microstructure. As seen in Figure 10, the grain sizes of 290 μm and 264 μm, for the 2Cr-2Nb containing alloy and the binary alloy, showed an improved degree of refinement over the single hit experiments, although there were still some γ grains remaining in the microstructure, see Figure 11.

Another set of experiments focused on deforming 2Cr-2Nb containing samples at 1150°C, and holding at that temperature, in order to form a fine grained equiaxed γ microstructure. The fine γ grains would then provide a high number of nucleation sites for the α grains at high temperature, which would enable the production of fine lamellar grains. Figure 12a shows the microstructure of a sample compressed 50% and held for 60 minutes at 1150°C. Bands of fine γ grains are produced, with a grain size of about 15 μm. This sample is approximately 90% equiaxed γ. It has been reported[9] that in this temperature range, deformed near-γ TiAl alloys produce dynamically recrystallized γ grains as a softening mechanism. When this sample was heated to 1360°C for 10 minutes, a lamellar grain size of 280 μm was obtained, but the transformation was incomplete. When a similar sample was reheated at 1360°C for 20 minutes, the complete transformation yielded a lamellar grain size of 380 μm. The microstructures for these samples are shown in Figure 12 b and c. A sample that was compressed 50% at 1150°C, held at that temperature for 60 minutes, deformed an additional 50%, in an effort to create a fully equiaxed microstructure, then reheated at 1360°C for 10 minutes, transformed completely (Figure 12d) to a lamellar microstructure with a grain size of 474 μm. It is seen in these experiments that some progress has been made in refining the lamellar microstructure, but additional refinement can be achieved, by properly adjusting the processing parameters. If the reheating temperature is changed to just below the α transus, perhaps 1350°C, the small amount of remaining γ grains may help pin the α grains, leading to finer lamellar grains at low temperature.

IV.A.4.3 SUMMARY

- It was found that the lamellar microstructure is unstable at high temperature, and transforms over time to an equiaxed microstructure.

- Thermomechanical processing was able to reduce lamellar grain size from 1600 μm to under 400 μm, with further experiments most likely able to enhance the refinements.

- Lamellar refinement was also achieved by quenching to form massive microstructure, and then reheating.

IV.A.4.4 REFERENCES

1. R. Mutschler, M.S. Thesis, University of Pittsburgh, **1995**, unpublished.
2. C. R. Feng, D. J. Michel, C. R. Crowe, *Phil. Mag. Lett.*, **1990**, 61, 95.
3. H. Inui, M. H. Oh, A. Nakamura, M. Yamaguchi, *Phil Mag*, **1992**, A66, 539.
4. P. Wang, G. B. Viswanathan, V. K. Vasudevan, *Met. Trans. A*, **1992**, 23A, 690.
5. S. A. Jones, M. J. Kaufman, *Acta Metall. Mater.*, **1993**, 41, 387.
6. M. Hua, R. Mutschler, C. I. Garcia, A. J. DeArdo, *submitted to Scripta Met.*
7. D. Hoydick, PhD. Thesis, University of Pittsburgh, **1997**, unpublished.
8. W. J. Zhang, et. al., *Scripta Mat.*, **1996**, 35, 41.
9. M. H. Oh, et. al., *Acta Metall. Mater.*, **1991**, 40, 167.

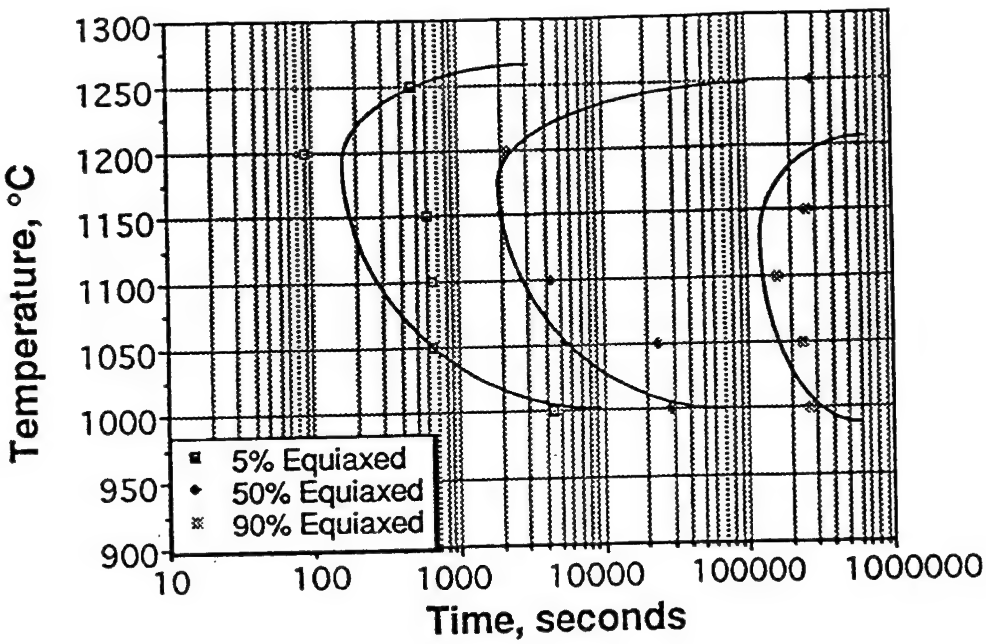

Figure 1. TTT diagram for Ti-48Al-2Mn-2Nb.

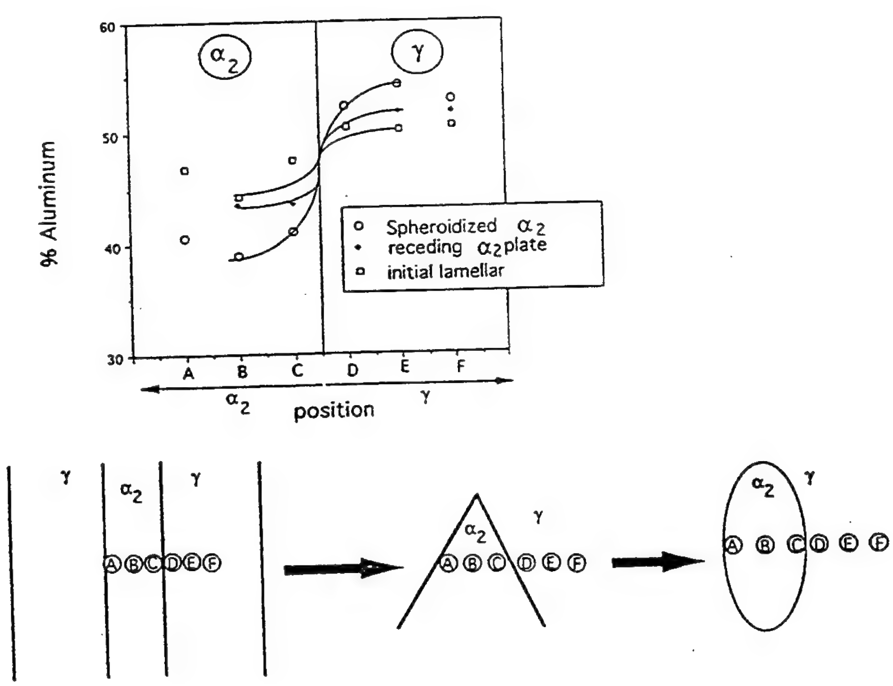

Figure 2. Change in aluminum concentration with position during spheroidization.

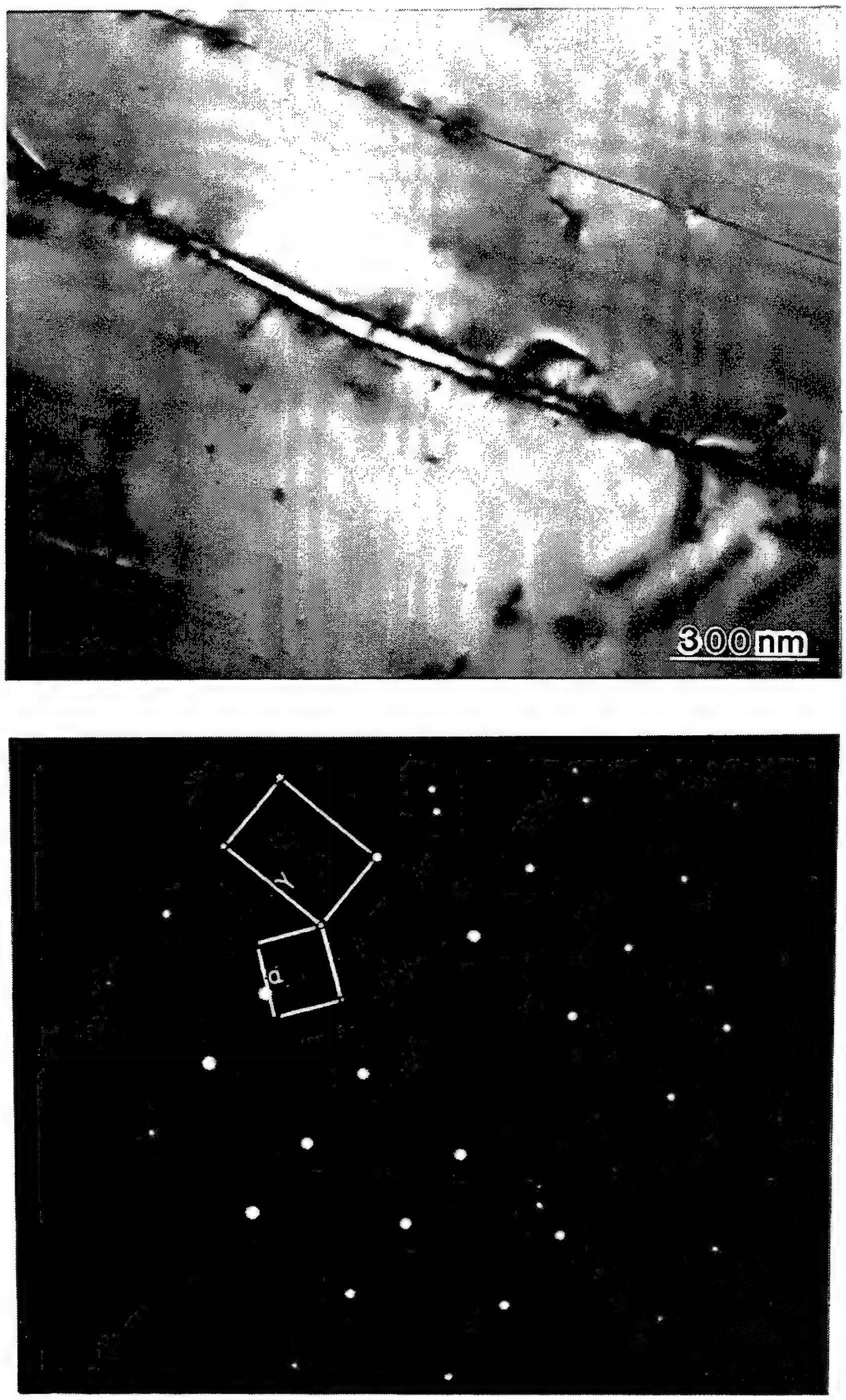

Figure 3. a) TEM micrograph of α_2 lath in a massive Ti-47Al sample, b) diffraction pattern from the area of the α_2 lath.

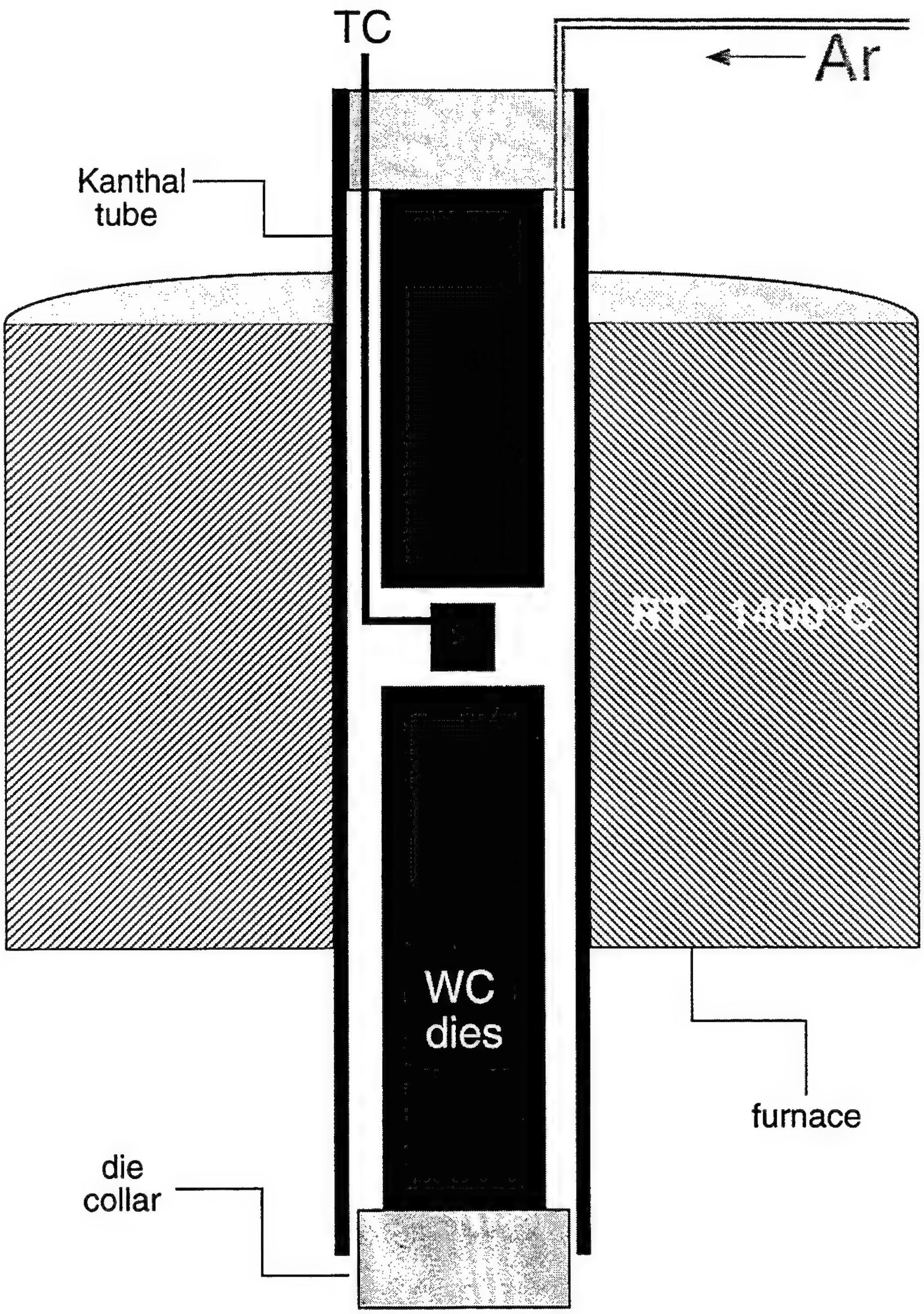

Figure 4. Schematic diagram of experimental setup for thermomechanical processing.

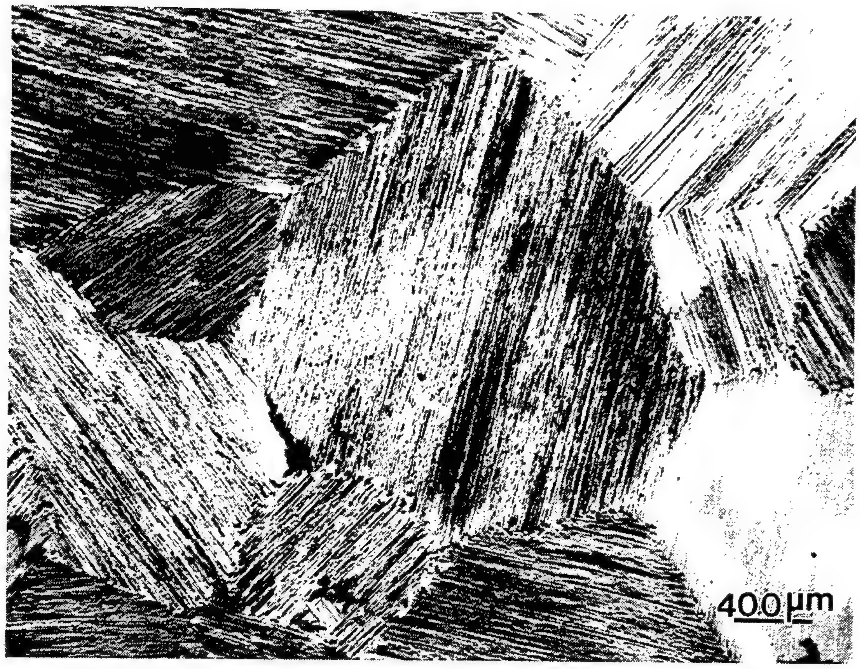

Figure 5. Micrograph of Ti-47Al-2Cr-2Nb, heated at 1380°C for four hours, and slow cooled to form a fully lamellar microstructure.

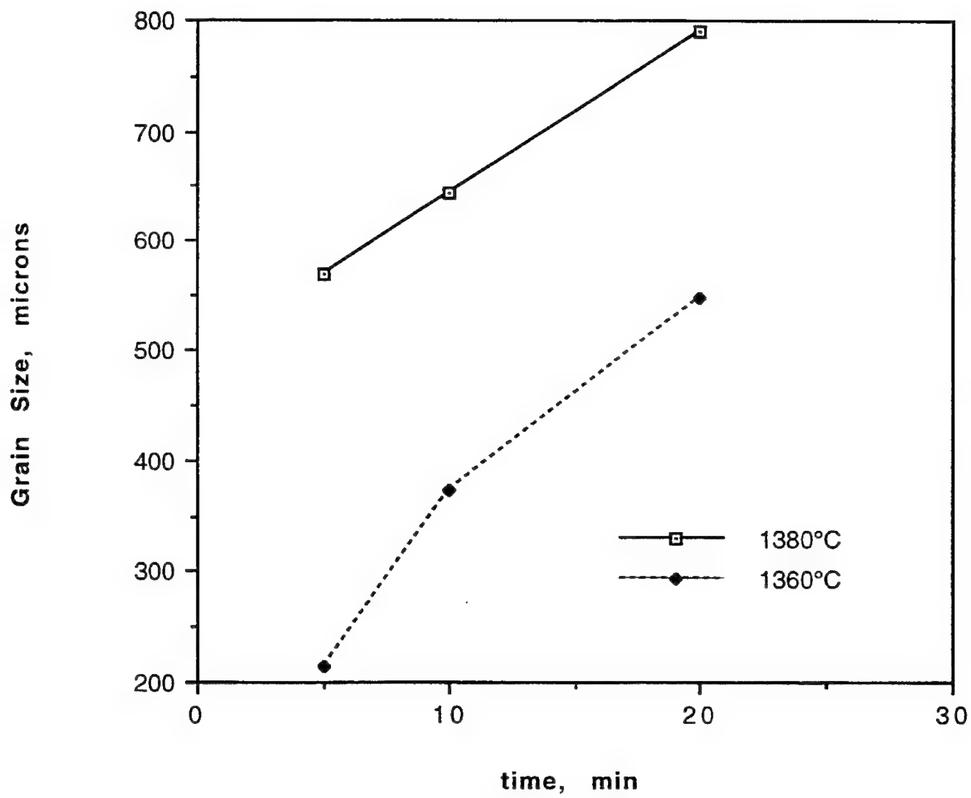

Figure 6. Lamellar grain size of Ti-47Al-2Cr-2Nb samples quenched to form massive microstructure, then heated at 1380°C or 1360°C for given times, and slow cooled to form lamellar.

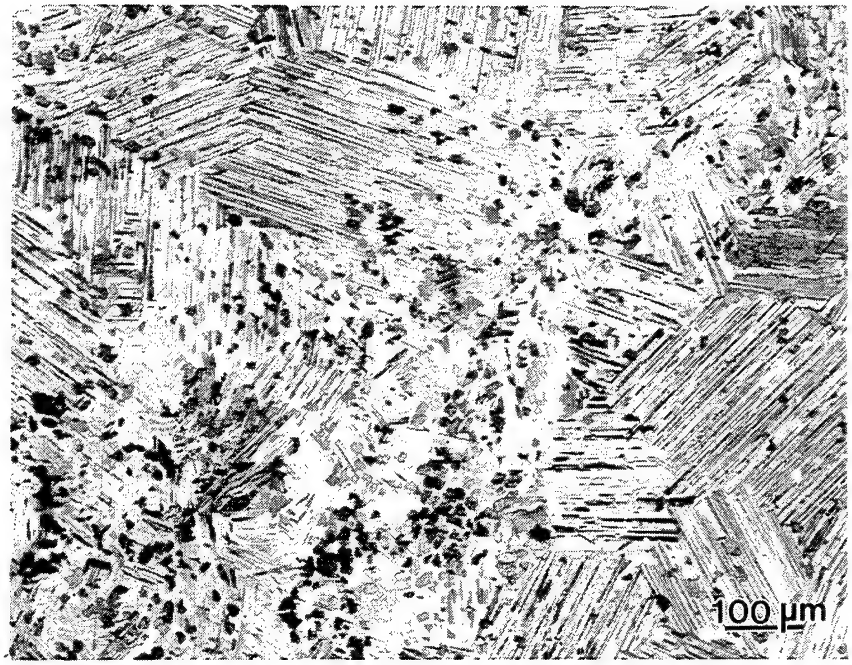

Figure 7. Micrograph of massive sample reheated at 1360°C for 5 minutes, and slow cooled.

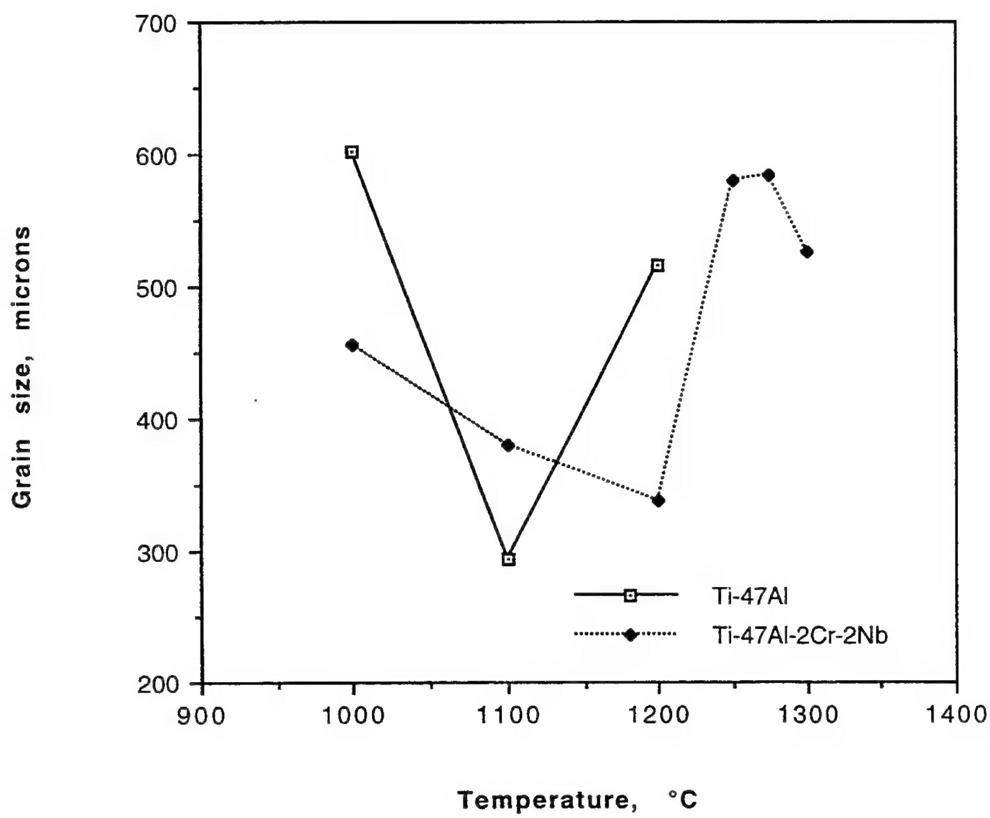

Figure 8. Lamellar grain size of samples deformed 50% at the given temperatures, and reheated at 1360°C for 10 minutes, and slow cooled.

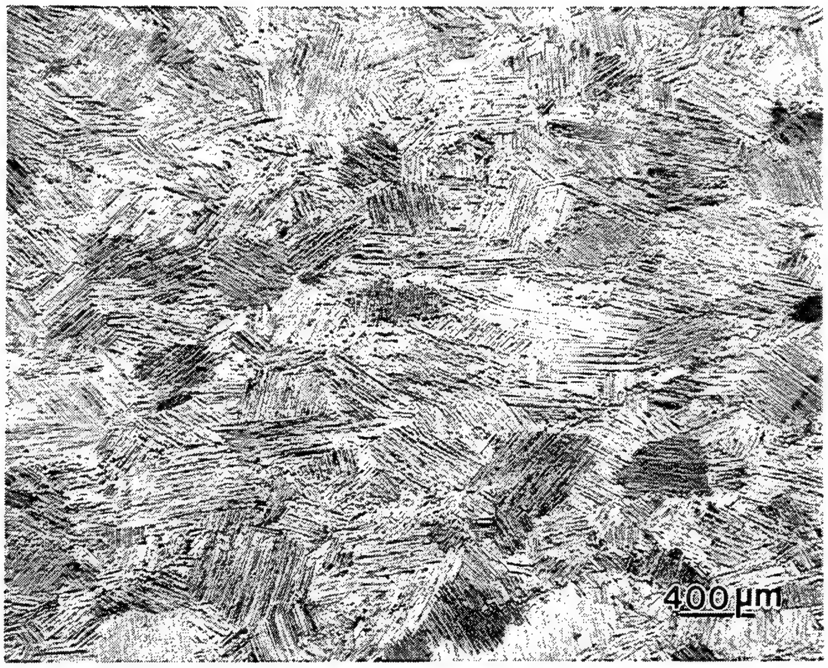

Figure 9. Micrograph of Ti-47Al-2Cr-2Nb sample deformed 50% at 1200°C, reheated at 1360°C for 10 minutes, and slow cooled.

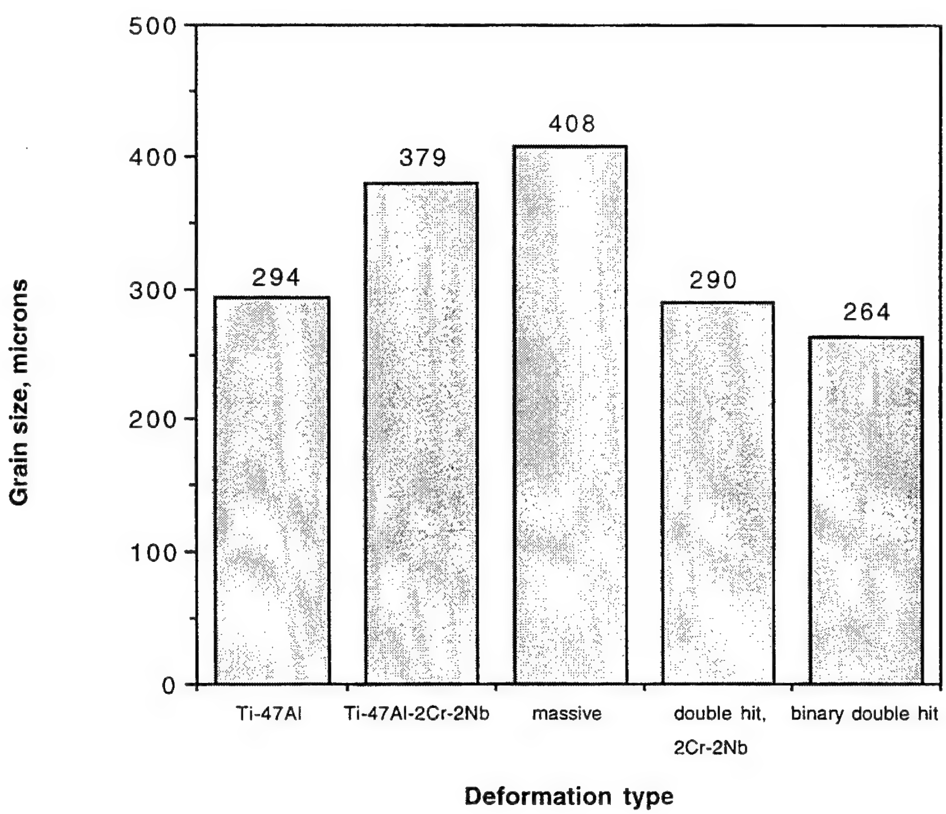

Figure 10. Lamellar grain size of samples deformed under various conditions at 1100°C, reheated at 1360°C for 10 minutes, and slow cooled.

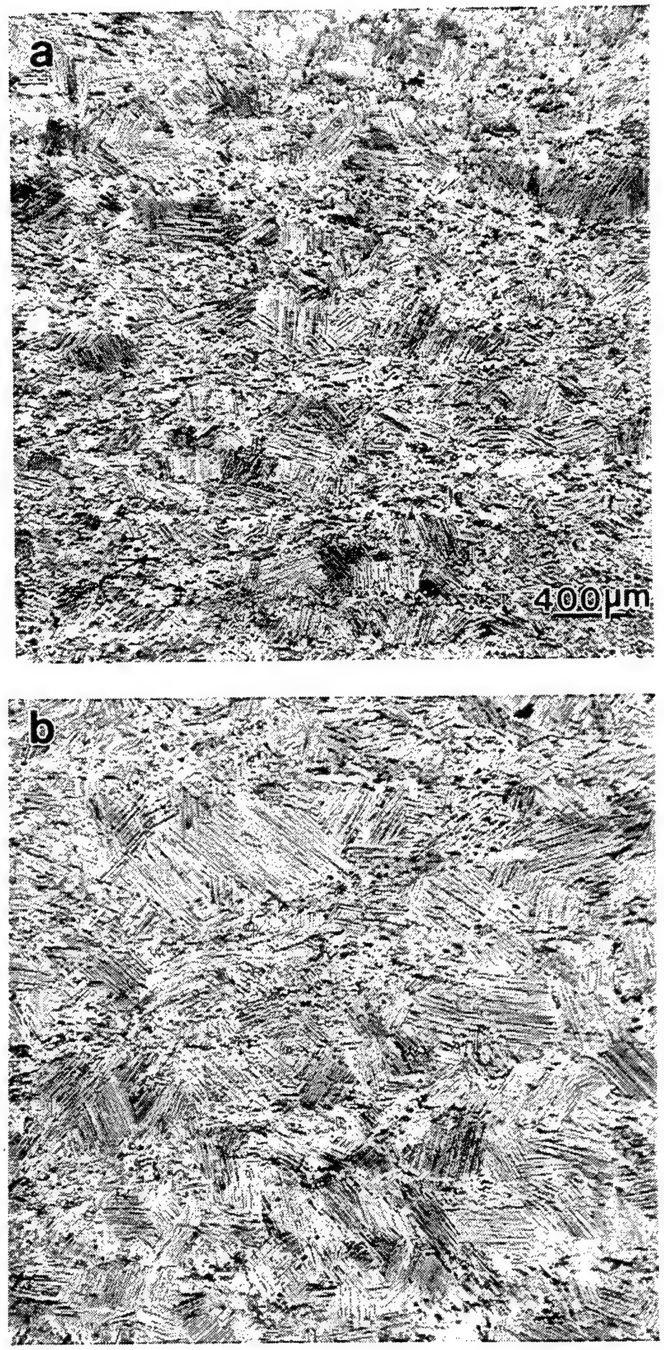

Figure 11. Micrographs of samples given two 50% deformation hits at 1100°C, with a reheat at 1360°C for 10 minutes following each hit: a)Ti-47Al-2Cr-2Nb, b)Ti-47Al.

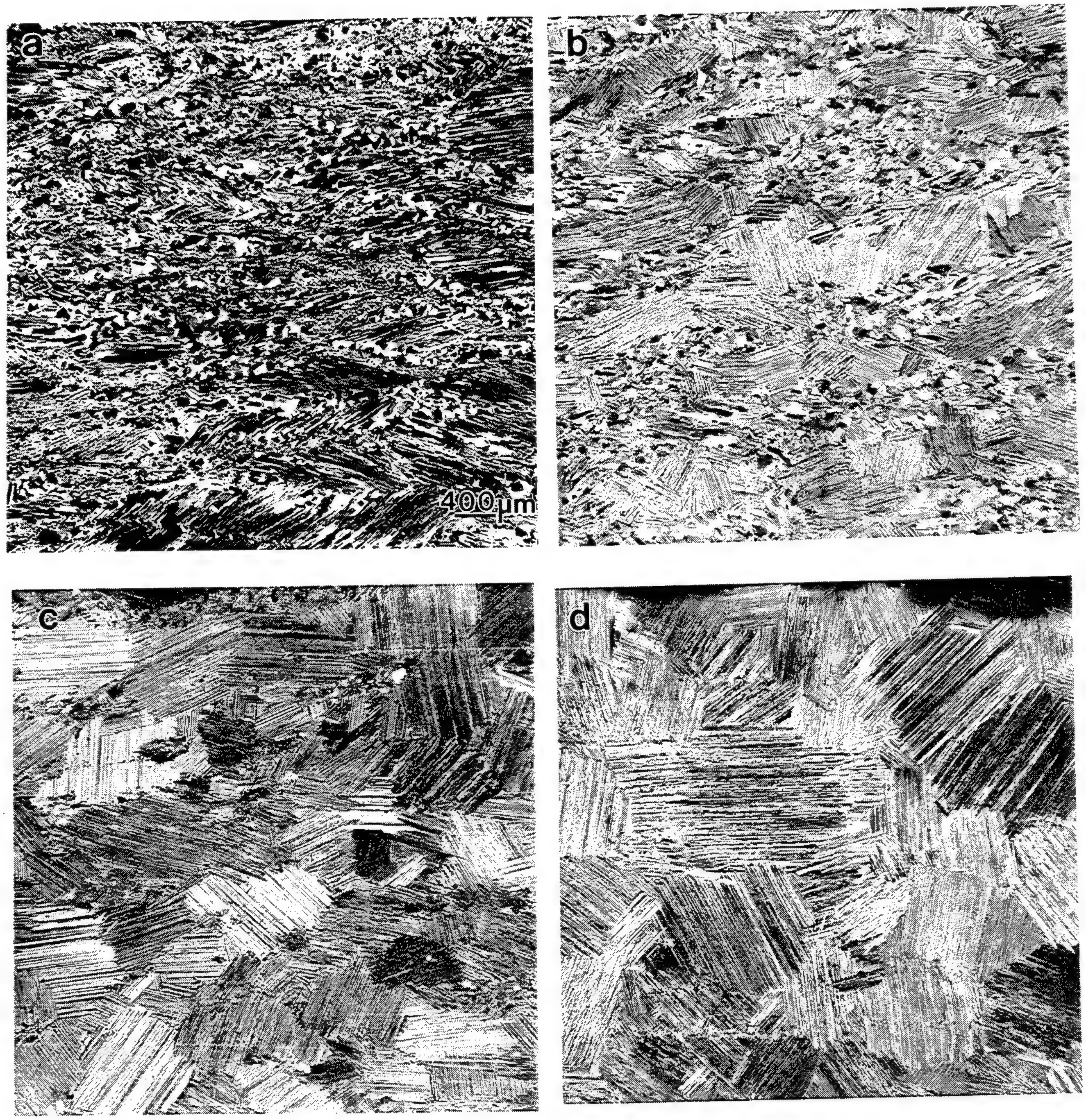

Figure 12 Micrographs of Ti-47Al-2Cr-2Nb samples deformed 50% at 1150°C and held for one hour, and a) no further processing, b) reheated at 1360°C for 10 minutes, c) reheated at 1360°C for 20 minutes, d) deformed an additional 50%, and reheated at 1360°C for 10 minutes.

IV.A.5 Oxidation of Intermetallics

Principal Investigator: Professor Gerald H. Meier
Materials Science and Engineering Department
University of Pittsburgh

Other Faculty Participants: Dr. N. Birks
Materials Science and Engineering Department
University of Pittsburgh

Dr. F. S. Pettit
Materials Science and Engineering Department
University of Pittsburgh

Dr. S. A. Asher
Department of Chemistry
University of Pittsburgh

Student: Ms. D. Berztiss

IV.A.5.1 INTRODUCTION

There is currently renewed interest in intermetallic compounds as potential high temperature structural materials. However, despite the fact that many contain significant amounts of Al or Si, most intermetallic compounds oxidize at rates which are prohibitively rapid. Analysis of this problem indicates that the only structurally-useful compounds which can form oxide films which will *possibly* be protective are TiAl, the aluminides of Ni (and Fe), and $MoSi_2$. Therefore, work in this project has been focussed on the oxidation behavior of TiAl, NiAl, and $MoSi_2$ and, in particular, their behavior in the temperature range 500 to 900°C.

The objectives of this project have been:

1. Understand the relations between environmental exposure and the development of oxidation morphology for γ-TiAl.
2. Understand the mechanisms of accelerated oxidation of NiAl and $MoSi_2$.

IV.A.5.2 ACCOMPLISHMENTS AND SIGNIFICANCE

Progress has been made in both areas. Considerable knowledge regarding the development of oxidation morphologies on TiAl has been gained and a fruitful collaboration in this area has been maintained with the Max-Planck Institut für Metallforschung in Stuttgart. Also, information from this project is being fed into a collaborative project with GE Aircraft Engines, sponsored by NAWC, on the effects of oxidizing environments on the mechanical properties of γ-TiAl. In the area of accelerated oxidation, a Ph.D thesis was completed in May, 1996. The following is a summary of the accomplishments in these two areas.

Oxidation of γ-TiAl

It has been known for 20 years that the oxidation of TiAl is highly sensitive to atmosphere composition and surface preparation. Choudhury et al., in a classic paper[1], studied the oxidation of TiAl (50 at% Al) in O_2 and air over the temperature range 800 - 1200°C. In O_2 cast TiAl which was abraded through 120 grit SiC formed alumina and exhibited k_p values $\approx 10^{-9}$ $g^2cm^{-4}hr^{-1}$ at 950°C but polished specimens formed TiO_2-rich scales and exhibited k_p values of about 10^{-5} to 10^{-6} $g^2cm^{-4}hr^{-1}$. Extruded TiAl formed alumina scales regardless of surface preparation. Choudhury et al. explained the effects of extrusion in terms of the absence of macroinhomogeneities which existed in the cast structure. The "surface finish effect", observed for the cast material was presumed to result from coarse grinding homogenizing the alloy at the surface. A Ti_3Al layer was reported to form between the oxide and the alloy for all the exposures. Oxidation behavior in air at 950°C was independent of specimen preparation or fabrication method with titania-forming kinetics (k_p about 10^{-5} - 10^{-6} $g^2cm^{-4}hr^{-1}$) observed in all cases. The scales were similar to those formed on polished specimens in O_2 at 950°C. Experiments to determine the species responsible for the difference between exposures in O_2 and air indicated that CO, CO_2 and H_2O impurities were not responsible nor was the difference in P_{O2}. It was, therefore, concluded that the increased rate of oxidation in air was a "nitrogen effect" although no N_2-containing phases were identified in the scale or substrate.

The "surface finish effect" for oxidation temperatures below 1000°C is illustrated in the mass gain vs. time plot in Figure 1 for Ti-50at%Al oxidized at 900°C. The ground (600 grit) surface results in very slow kinetics in O_2 as the result of continuous alumina formation as shown schematically in Figure 2a. The polished (1μm diamond) results in greatly accelerated kinetics as the result of the formation of a continuous layer of a mixed oxide, Figure 2b. Part of the beneficial effect of grinding may be in homogenizing the surface, as proposed originally by Choudhury et al[1]. Indeed, the distribution of the minor α_2 phase, generally present in TiAl, has been shown to influence the composition of the external scale[2,3]. However, an additional important effect is the recrystallization of the ground surface as illustrated in the transmission electron micrographs in Figure 1[3]. The deformed layer, produced by grinding, recrystallizes during the initial oxidation exposure to produce γ grains with a grain size on the order of 1 μm from a starting γ grain size on the order of 100 μm. No recrystallized layer forms on the polished surface. It has been suggested[3] that enhanced Al diffusion in the fine-grained layer promotes the formation of continuous alumina in the same manner as that reported by Giggins and Pettit[4] for the development of chromia films on Ni-Cr alloys.

The "nitrogen effect" prevents the formation of continuous alumina[5] so there is little effect of surface preparation on the oxidation rates of TiAl when the exposures are carried out in air, Figure 1. The morphologies developed in air are presented schematically in Figures 2c and d.

The micrographs in Figure 1 reveal an intermediate layer between the oxide and the γ phase. This zone is depleted in Al and was originally thought to be α_2[1]. However, an important observation was made by Dowling and Donlon in 1992[6] when they identified a cubic phase with a lattice parameter of 0.69 nm and a Ti/Al ratio of approximately 2/1. These observations were confirmed[5] and the cubic phase was found to have 432 point group symmetry[7]. Extensive TEM investigation of this phase using convergent beam electron diffraction (CBED)[8] showed it to

belong to one of two space groups, P432 or $P4_232$, and EDS analysis indicated an approximate composition of 57 at%Ti-33at%Al-10at%O[9]. Increased exposure times and/or higher oxidation temperatures result in the Al-depleted zone becoming two-phase as the result of nucleation of α_2 at the interface between the cubic phase and the parent γ[9]. This observation confirms earlier suggestions of a two-phase depletion layer based on WDS measurements[10], Auger electron spectroscopy[11], and x-ray diffraction[12]. The influence of the depleted zone on the oxidation behavior of γ alloys is not yet clear, however, it is crucial to the mechanical properties.

The oxidation behavior of TiAl can also be affected by alloying. Chromium is an alloying element of fundamental and practical significance. Small additions of Cr to γ ($\leq$ 5 at%) accelerate the growth of the mixed oxide by doping the TiO_2 to increase the concentration of oxide ion vacancies and/or titanium ion interstitials. However, at higher concentrations, the Cr promotes the formation of a continuous external layer of alumina. The mechanism is not completely clear since the alloys with 5 at% Cr or more contain a second phase (laves Phase) but one effect is that the "nitrogen effect" apparently does not operate in the presence of sufficient amounts of Cr even though nitrides form beneath the oxide during the early stages of scale formation.

Accelerated Oxidation of NiAl and $MoSi_2$

A number of intermetallic compounds, which form protective alumina or silica scales at high temperature, undergo accelerated degradation at intermediate temperatures. The observations actually involve several different, but related, phenomena which may be subdivided into "accelerated oxidation", "internal oxidation", "intergranular oxidation" and "disintegration". These may be defined as follows[13]:

Accelerated Oxidation - the alumina or silica is not continuous and significant amounts of the other component(s) of the intermetallic are present in the surface film. The overall oxidation rate is substantially faster than that for the growth of alumina or silica.

Internal Oxidation - precipitation of oxides rich in Al or Si within the intermetallic.

Intergranular Oxidation - special case of internal oxidation in which oxides form along grain boundaries within the intermetallic.

Pesting - disintegration (fracture) of the intermetallic into smaller particles at the oxidation temperature.

Grabke and co-workers[14] have shown that NiAl is susceptible in the temperature range 700 to 1000°C to intergranular oxidation at reduced oxygen partial pressures in the range 10^{-11} to 10^{-7} atm. and internal oxidation in the oxygen pressure range 10^{-2} to 10^{-22} atm. A particularly complex form of degradation occurs when exposures are carried out in evacuated silica ampoules containing buffer mixtures, such as Cu/Cu_2O. This attack, termed "pocks" consists of an outer zone of silicides and silicates (Si is the result of SiO vapor transport from the capsule walls) over an internal oxidation zone of alumina in virtually pure Ni. A substantial Al-depleted zone, which has transformed to Ni_3Al, is observed beneath the internal oxidation zone. The detailed mechanism for this process is not completely understood but is known to require conditions that

prevent the formation of a protective alumina layer (temperatures which favor formation of transition aluminas and possibly contaminants such as S) and a process which rapidly consumes Al (the internal oxidation). Work in this project has shown that pocks do not form when the buffer mixture is thoroughly dried prior to specimen exposure and pocks do not form on aluminide coatings on Ni-base superalloys. These observations are possibly all the result of conditions which favor the rapid establishment of α-alumina rather than transition aluminas.

Molybdenum disilicide is an intermetallic compound which has been extensively used for high temperature applications, particularly furnace heating elements. The oxides of Mo (MoO_2, MoO_3) are much less stable than SiO_2 so that silica should be the stable oxide for any but the most dilute Mo-Si alloys[15]. In fact, the nature of the external scale formed is a strong function of temperature. At temperatures above 600°C a protective film of SiO_2 develops on $MoSi_2$. However, in the temperature range 300 to 550°C a protective silica film does not form. This leads to the phenomenon of "accelerated oxidation"[15,16] which involves the formation of scales containing crystalline oxides of Mo and vitreous silica and rates which are orders of magnitude faster than those extrapolated from higher temperatures. Accelerated oxidation is a material property of $MoSi_2$, including single crystals. It has been proposed that the transition to protective silica formation is associated with the increase in volatility of the Mo-oxides as temperature increases[15,16]. This is shown schematically in Figure 3. At high temperatures the transient Mo-oxides evaporate and allow the silica regions to grow laterally into a continuous layer. At low temperatures the reduced volatility of the Mo oxides and slower growth of the silica prevent the development of a continuous silica layer. The rapid inward growth of MoO_3 results in continuous removal of the silica nuclei from the surface and produces an intermixed layer of MoO_3 and SiO_2.

If the $MoSi_2$ contains defects, such as microcracks or pores, the occurrence of accelerated oxidation within these defects can result in crack propagation and fragmentation of the $MoSi_2$. Fitzer[17] first described the phenomenon and named it "pest" in 1955. Since that time, many researchers have attempted to describe pesting of $MoSi_2$ and determine under what circumstances it occurs. Berkowitz-Mattuck et al.[18,19] studied zone-refined material of less than 75% theoretical density and found that pesting occurs in oxygen, but not nitrogen, carbon dioxide, carbon monoxide or argon, and that the rate of oxidation is very sensitive to the partial pressure of oxygen. Furthermore, as there is little or no lattice parameter change when $MoSi_2$ is equilibrated in oxygen, the solubility of oxygen in $MoSi_2$ is assumed to be very low. They concluded that, as a result of the high residual stresses introduced on cooling of the anisotropic material from the melt, a stress-enhanced oxidation could occur at the tips of Griffith flaws, eventually leading to brittle fracture. The disappearance of pesting at $T > 600$°C was explained as the result of plastic deformation of the matrix near the flaw accommodating the stresses. The cracks were found to be mostly transcrystalline. Westbrook and Wood[20] proposed that the catastrophic nature of the "pest" mechanism was the result of preferential intergranular diffusion of a gaseous element (most likely oxygen or nitrogen), coupled with a temperature dependent hardening reaction. Fitzer et al[17,21,22] and Schlichting[23] describe pesting of $MoSi_2$ as intercrystalline attack whereby each individual grain is enveloped by reaction product. They note that most oxidation occurs in pores or internally along pore canals, and failure occurs as the result of a wedging effect from oxide growth in the defect. Fitzer and Schlichting give no evidence that attack is intergranular and may only assume so, as pores tend to form predominantly along grain boundaries. This is inconsistent with Berkowitz-Mattuck et.al. who

found fracture from pesting to be predominantly transcrystalline. Recent work[15] has shown that while accelerated oxidation is generic to all forms of $MoSi_2$, grain boundaries alone do not result in pesting since dense HIPed $MoSi_2$ did not pest even though it was polycrystalline. Only cast material, which contained pre-existing microcracks, was observed to undergo pesting. It was concluded that pesting was the result of the occurrence of accelerated oxidation within the microcracks. There is a large change in volume going from Mo to MoO_3 ($\approx 340\%$), along with the volume change of forming SiO_2 from Si ($\approx 180\%$). These processes enhance the widening of the pre-existing cracks leading to pesting (i.e. turning to powder). These phenomena are illustrated schematically in Figure 3. This mechanism is supported by the observation of oxidation-induced growth of cracks formed in HIPed $MoSi_2$ by a microhardness indenter which ultimately resulted in pesting of a material which did not undergo pesting in simple oxidation exposures[24]. McKamey et.al.[25] have also concluded that pesting occurs as the result of oxidation in preexisting cracks and pores.

The accelerated oxidation of $MoSi_2$ at temperatures near 500°C involves an incubation stage, as indicated in Figure 4[26]. An extensive study of the development of the oxidation products using SEM, TEM, glancing angle XRD, laser Raman spectroscopy, and acoustic emission has indicated the following mechanism. The initially-formed oxide (incubation period) consists of nanocrystalline Mo_4O_{11} and amorphous silica and is rather protective, as shown schematically in Figure 5. This film breaks down as oxidation proceeds and the Mo_4O_{11} transforms to MoO_3. This transformation, which involves a volume increase, causes fracture of the scale and the oxidation rate becomes linear and the scale develops into that shown in Figure 3.

IV.A.5.3 SUMMARY

The oxidation mechanisms of γ-TiAl have been described in detail. The effects of surface preparation and nitrogen in the oxidizing atmosphere are now well understood. A collaborative effort with the Institut für Metallforschung, Stuttgart, Germany has identified the phases which form in the aluminum-depleted zone beneath the oxide which are expected to have a strong influence on the mechanical properties of γ-TiAl. The factors affecting accelerated oxidation of NiAl and $MoSi_2$ have been further clarified.

IV.A.5.4 REFERENCES

1. N. S. Choudhury, H. C. Graham, and J. W. Hinze, "Oxidation Behavior of Titanium Aluminides", in Properties of High Temperature Alloys, Z. A. Foroulis and F. S. Pettit eds., The Electrochem Soc., 1976, p. 668.
2. A. Gil, H. Hoven, E. Wallura, and W. J. Quadakkers: Corr. Sci., 34, 615 (1993).
3. J. M. Rakowski, F. Dettenwanger, E. Schumann, G. H. Meier, F. S. Pettit, and M. Rühle, "The Effect of Surface Preparation on the Oxidation Behavior of Gamma TiAl Base Intermetallic Alloys", submitted to Scripta Mater.
4. C. S. Giggins and F. S. Pettit, Trans. Met. Soc. AIME, 245, 2509 (1969).
5. J. M. Rakowski, F. S. Pettit, G. H. Meier, F. Dettenwanger, E. Schumann, and M. Rühle, Scripta Met. et Mater., 33, 997 (1995).
6. W. E. Dowling Jr. and W. T. Donlon: Scripta Met. et Mater., 27, 1663 (1992).
7. R. Field, J. Schaeffer, C. Austin, and T. Kelly: unpublished, GE Aircraft Engines, 1993.

8. Y. Cheng, F. Dettenwanger, J. Mayer, E. Schumann, and M. Rühle, Scripta Met. et Mater., 34, 707 (1996).
9. F. Dettenwanger, E. Schumann, J. Rakowski, G. H. Meier, and M. Rühle, submitted to Materials and Corrosion.
10. S. Becker, A. Rahmel, M. Schorr, and M. Schutze, Oxid. Metals, 38, 425 (1992).
11. R. W. Beye R. Gronsky: Acta Met. et Mater., 42, 1373 (1994).
12. N. Zheng, W. Fischer, H. Grübmeier, V. Shemet, and W. J. Quadakkers, Scripta Met. et Mater., 33, 47 (1995).
13. H. J. Grabke and G. H. Meier: Oxid. Metals, 44, 147 (1995).
14. M. W. Brumm, H. J. Grabke, and B. Wagemann: Corr. Sci., 36, 37(1994).
15. D. A. Berztiss, R. R. Cerchiara, E. A. Gulbransen, F. S. Pettit, and G. H. Meier, Mater. Sci. and Eng., A155, 165 (1992).
16. P.J. Meschter, Met. Trans., 23A, 1763 (1992).
17. E. Fitzer, Plansee Proc., 2nd Seminar, Reutte/Tyrol, Pergamon Press, 1956, p.56.
18. J. Berkowitz-Mattuck, P. E. Blackburn, and E. J. Felten: Trans. TMS-AIME, 233, 1093 (1965).
19. J. Berkowitz-Mattuck, M. Rossetti, and D.W.Lee, Met. Trans., 1, 479 (1970).
20. J.H. Westbrook and D.L. Wood, J. Nucl. Mater., 12, 208 (1964).
21. E. Fitzer and K. Reinmuth, "Die Reaktion hochschmelzender Silizide mit Stickstoff und Sauerstoff" High-Temperature Materials, 6th Plansee Seminar, Reutte Tirol, 24-28 June 1968, F. Benesovsky ed., Vienna, Springer Verlag, 1969, p. 767.
22. E. Fitzer and W. Remmele, "Possibilities and Limits of Metal Reinforced Refractory Silicides, Especially Molybdenum Disilicides", Fifth International Conference on Composite Materials, AIME, 1985, p. 515.
23. J. Schlichting, High Temperatures-High Pressures, 10, 241 (1978),.
24. D. R. Rishel, F. S. Pettit, and G. H. Meier: Univ. Of Pittsburgh ,Unpublished Research, 1992.
25. C. G. McKamey, P. F. Tortorelli, J. H. Devan, and C. A. Carmichael, J. Mater. Res., 7, 2747 (1992).
26. D. A. Berztiss, “Oxidation of Intermetallics: Molybdenum Disilicide, Titanium-Aluminum-Chromium Alloys, and Nickel Aluminide” Ph. D Thesis, University of Pittsburgh, 1996.

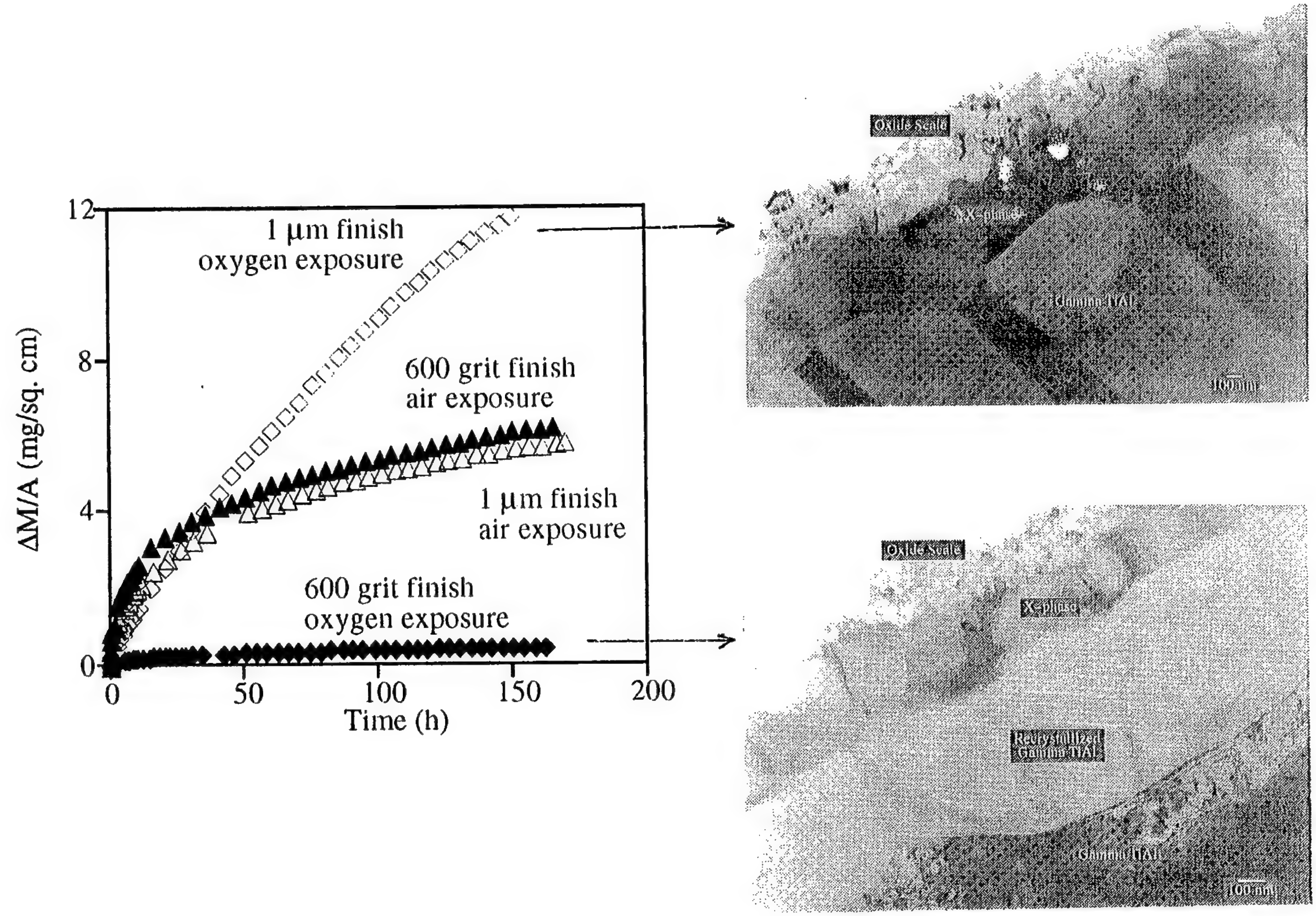

Figure 1. Oxidation rates for γ-TiAl at 900°C in air and oxygen with two surface finishes and cross-section TEM micrographs of specimens with two different surface finishes exposed in oxygen for 1 hour showing the recrystallized layer which forms on the ground specimen and the cubic "X-phase" which forms in the Al-depleted zone on both specimens.

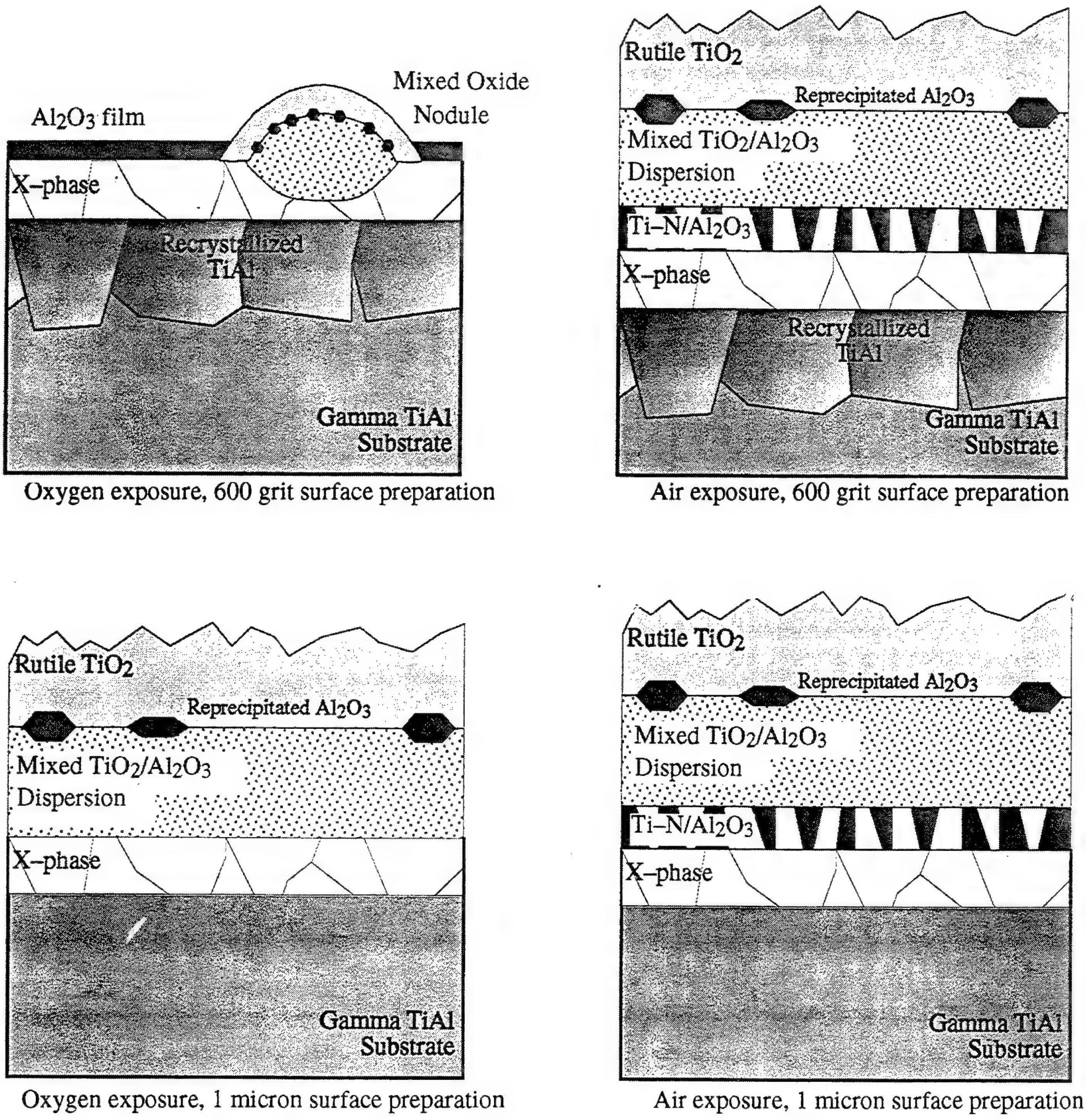

Oxygen exposure, 600 grit surface preparation

Air exposure, 600 grit surface preparation

Oxygen exposure, 1 micron surface preparation

Air exposure, 1 micron surface preparation

Figure 2. Schematic diagrams of the scales formed on γ–TiAl in the temperature range 800–900°C in air or oxygen and with two different surface finishes.

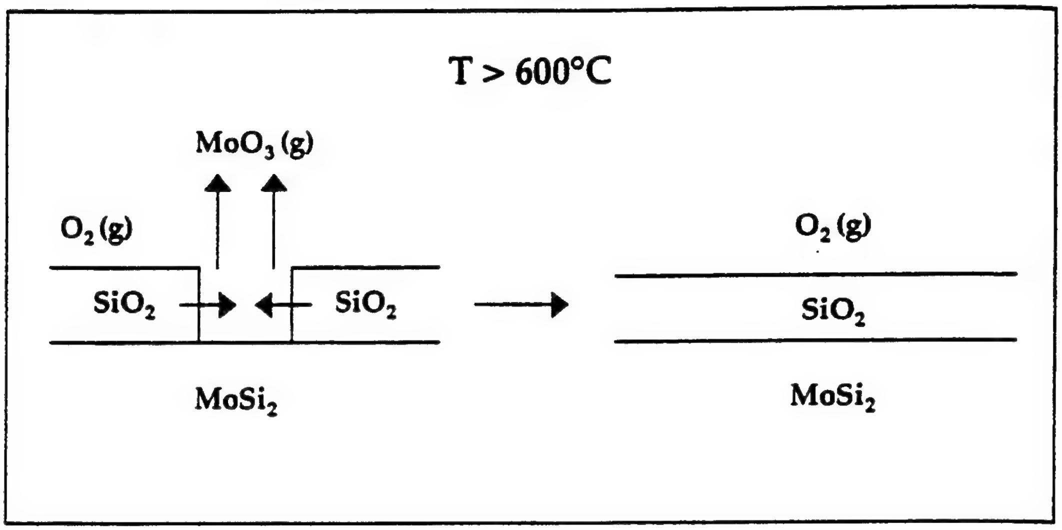

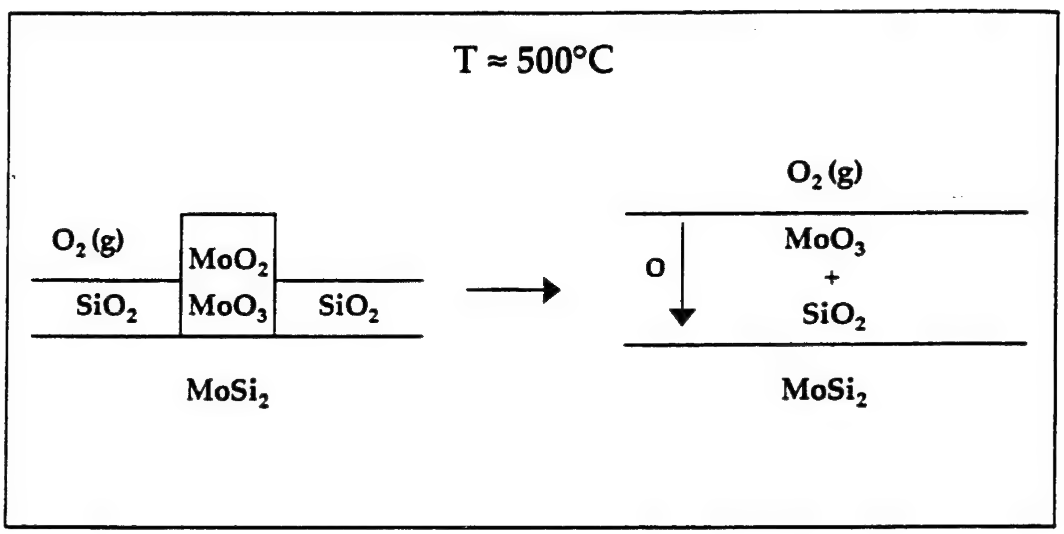

Figure 3. Schematic diagrams of the development of the oxidation morphology on $MoSi_2$ at temperatures of 600°C and higher (top) and the temperature range around 500°C (bottom).

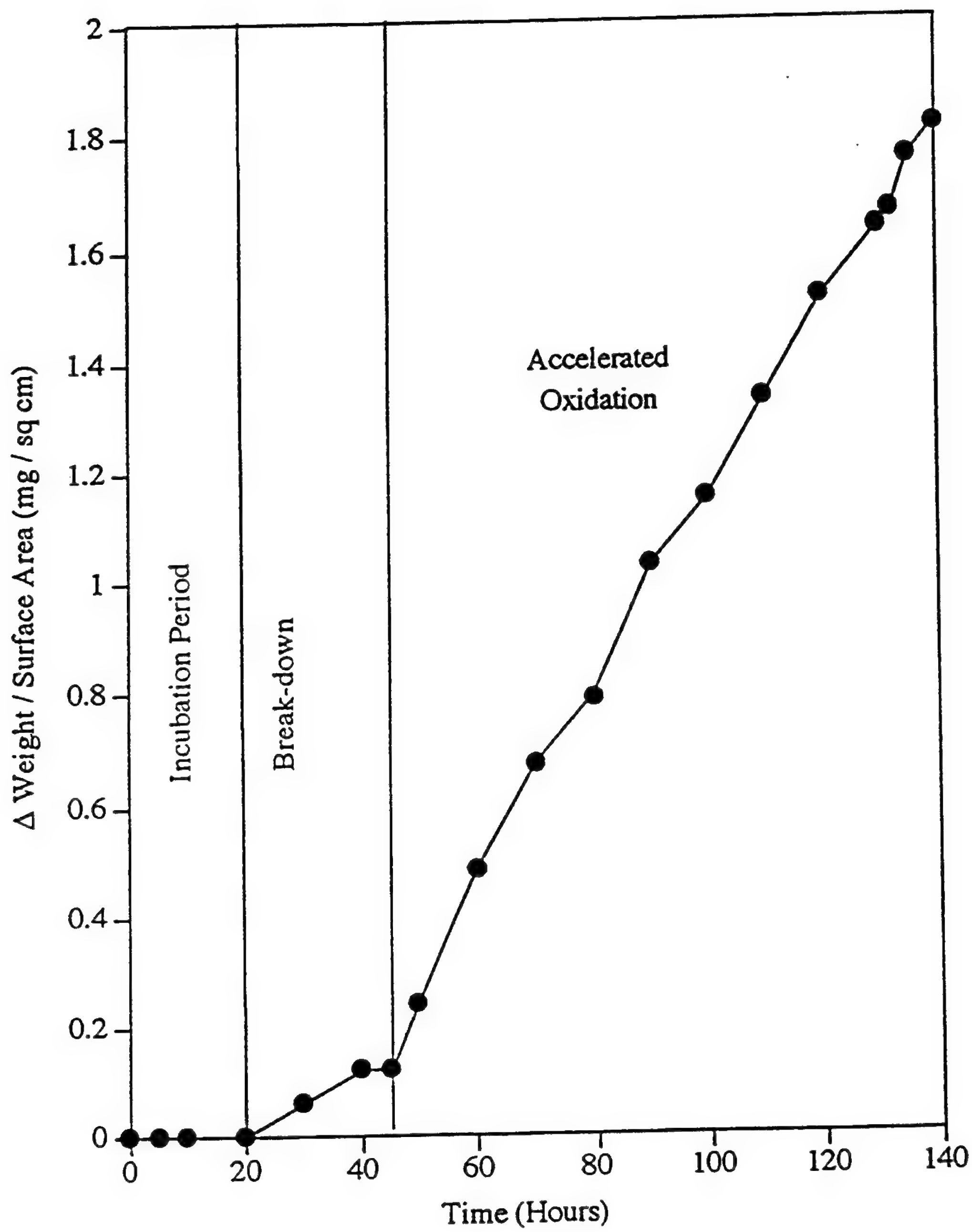

Figure 4. Mass change versus time for HIPed $MoSi_2$ oxidized in air at 500°C.

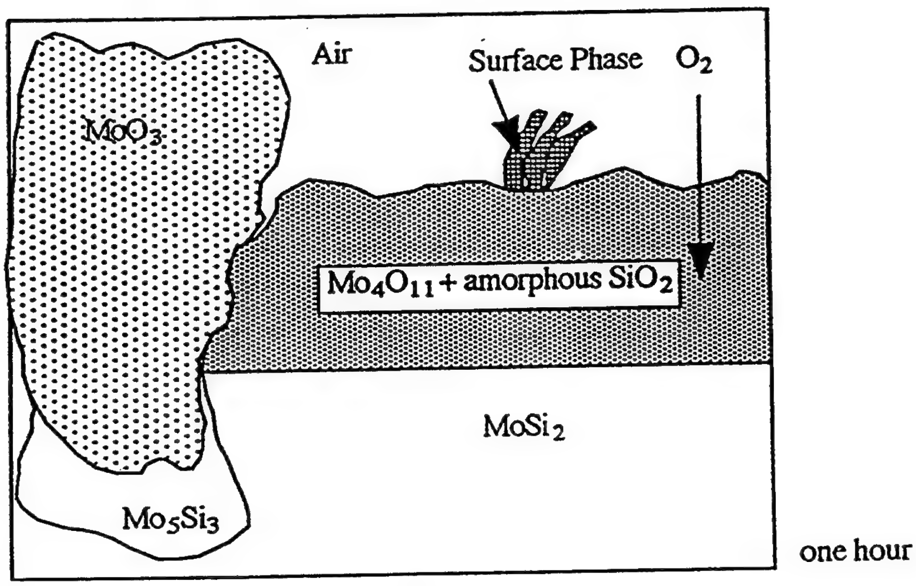

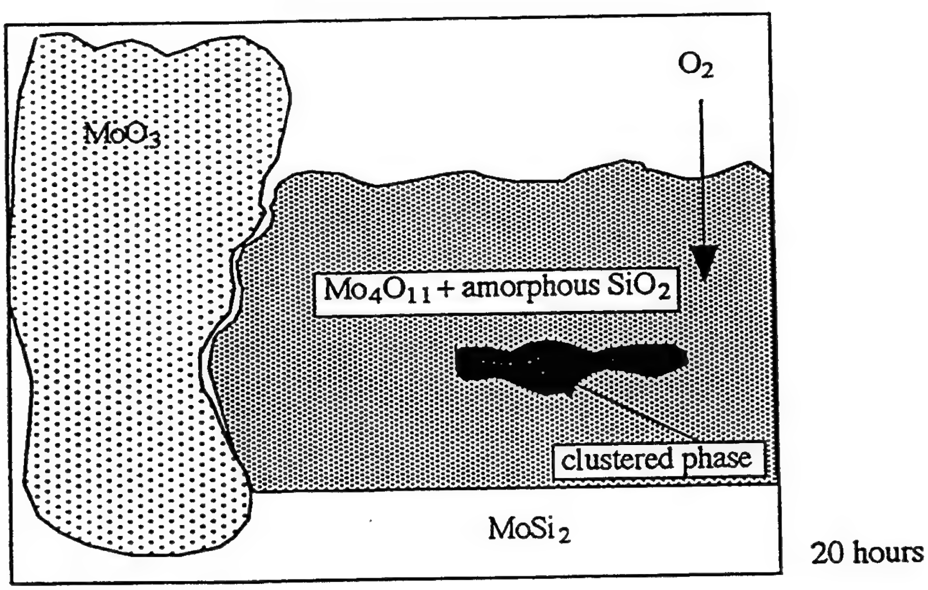

Figure 5. Schematic diagrams illustrating the oxidation behavior of HIPed $Mosi_2$ at 500°C during the incubation stage.

IV.A.6 Mechanisms of Degradation of Diamond Films

Principal Investigator:	Professor F.S. Pettit Materials Science and Engineering Dept. University of Pittsburgh
Other Faculty Participants:	Dr. S.A. Asher Chemistry Dept. University of Pittsburgh
	Dr. G.H. Meier Materials Science and Engineering Dept. University of Pittsburgh
Students:	Ms. J. Birch Mr. R.W. Bormett

IV.A.6.1 INTRODUCTION

This project has been concerned with the oxidation and wear of diamond films. Diamond films prepared by activated Chemical Vapor Deposition (CVD) were exposed to oxidizing conditions and also conditions causing wear induced by machining operations. Activation of the gases was achieved using the direct current arc plasma jet method or the hot filament method.

Oxidation of the diamond films was studied at temperatures between 500° and 700°C in oxygen pressures from one to 10^{-4} atmospheres. The oxidation kinetics were determined by performing weight change versus time measurements using an automatic microbalance. The diamond coated cutting tools were machined for different times on as cast Al-Si rod (Al-17.85 wt% Si - 5.12% Cu - 0.4% Fe). Some machining tests were done with gray cast iron rod. All specimens were characterized using optical metallography, scanning electron microscopy and UV Raman spectroscopy.

IV.A.6.2 ACCOMPLISHMENTS AND SIGNIFICANCE

Characterization of As Processed Diamond

Scanning micrographs of the free standing diamond films used in the oxidation investigations, which were fabricated by the DC arc plasma jet method, are presented in Figures 1 and 2. Crystal facets covered with growth steps are evident on the growth side of these films, Figure 1, whereas on the substrate side smaller grains are evident which often are separated by small voids that develop as adjacent grains impinge upon one another, Figure 2. Occasionally much large void areas were evident, Figure 2, which are believed to develop at sites on the substrate where nucleation of the diamond did not occur during the initial stages of diamond film deposition.

Surface features of the diamond films on cutting tools where deposition was achieved using the hot filament method are shown in Figure 3. Generally the grains were similar to those on diamond films fabricated by the DC arc plasma jet method but the growth steps were not as well defined on the former compared to the latter.

For diamond films prepared by both methods, UV Raman spectroscopy show the presence of diamond with a small amount of nondiamond species, Figure 4.

Oxidation of Diamond

The oxidation kinetics conformed to a linear rate law, Figure 5. The linear rate constants obeyed an Arrhenius relationship for fixed oxygen pressures, Figure 6, with activation energies that depended upon oxygen pressure as shown in Table 1. The linear rate constants at constant temperature were a function of oxygen pressure as shown in Figure 7. At 700°C the linear rate constants exhibited an oxygen pressure dependence of $P_{O_2}^{0.5}$. This exponent was determined to be about 0.6 and 0.8 at 600°C and 500°C, respectively.

The oxidation attack of diamond was preferential. This was especially evident for small rates of attack, for example low oxygen pressures or low temperatures. Typical features are presented in Figures 8,9 and 10. The crystal facets on the growth side of the diamond films exhibited attack at edges and at the interstices between facets, Figure 8. The preferential attack on the substrate side occurred at preexisting defects, Figure 9. For cases where the rate of attack was high the attack became more uniform, however, the oxidized surface was still highly irregular, Figure 10.

The results from UV Raman spectroscopy showed that the nondiamond intensity decreased during oxidation at temperatures up to about 800°C. This suggests that the preferential attack may be caused by oxidation of the nondiamond species in the films. Above 900°C the nondiamond component increased substantially during oxidation but it was not large at 1000°C as at 950, Figure 11. These results suggest that diamond begins to transform to carbon above 900°C which in turn is oxidized. At 1000°C the rate of oxidation is faster than the transformation rate so the amount of nondiamond decreases.

The pressure dependence of the linear rate constants and the activation energies that have been obtained indicate that the rate determining step for oxidation of diamond between 500° and 700°C is the adsorption and dissociation of oxygen. Some transformation of diamond to carbon begins to occur at 900°C and above. At such temperatures the rate of oxidation determines whether diamond or carbon is oxidized. For high oxidation rates that exceed the transformation rate, diamond is oxidized.

Wear of Diamond Films

As diamond coated cutting tool inserts were used to machine the as-cast Al-Si rod, wear scars developed on the insert, Figure 12. The morphological features within the wear scar, Figure 13, indicated that wear was occurring via a fracturing process since similar features were evident in fractured diamond films, Figure 14. The morphological features that developed in

wear scars upon machining cast iron differed markedly from those for machining the aluminum-silicon alloy, Figure 15. The diamond facets were no longer evident and a smeared texture remained, Figure 15.

UV Raman spectroscopy of the as processed, diamond-coated inserts showed the presence of diamond with a small amount of nondiamond. No changes in the relative amounts of diamond and non-diamond was observed after machining either the nonferrous or ferrous materials. Furthermore, there was no evidence of oxidation in either case.

The features that developed during machining of the nonferrous material showed that wear of the diamond coating occurred by fracturing of the diamond. In contrast the wear of diamond during machining of the cast iron appears to occur via a chemical reaction between the diamond and the iron. To examine this reaction, a piece of diamond was sandwiched between two pieces of iron and exposed at 800°C in an argon hydrogen gas mixture for four hours. The crystal facets on the diamond film disintegrated when in contact with the iron and the iron was enriched in carbon. This chemical reaction must involve carbon diffusion into the iron and, also Fe_3C formation since Fe_3C is thermodynamically stable for carbon in contact with iron at 800°C. The disintegration of the diamond is still not understood but this process shows that diamond cannot be used to machine ferrous materials.

IV.A.6.3 SUMMARY

Diamond films have been investigated during oxidation and during machining. The oxidation process involves linear kinetics with the rates of oxidation in the temperature range 500° - 700°C being controlled by adsportion and dissociation of oxygen on diamond. At temperatures of 900°C diamond begins to transform to graphite and graphite can be involved in the oxidation but at high oxidation rates the oxidation process has been found to proceed faster than the transformation.

The wear of diamond coatings during machining of non-ferrous metals has been shown to occur via the fracturing of diamond facets on the diamond coating. Diamond has been shown to react with ferrous materials and hence degrades via chemical wear upon machining ferrous materials.

IV.A.6.4 REFERENCES

1. J.T. Yates and F.S. Pettit, First Annual Report, Cross-Disciplinary Materials Research Program, University of Pittsburgh, AFOSR F49620-950-1-0167, September 1995.
2. R.M. Lizewski, "Characterization of Diamond Film Oxidation", Master of Science Thesis, Materials Science and Engineering Department, University of Pittsburgh, Pittsburgh, PA 15261, (1994).
3. C.E. Johnson, M.A. Hasting and W.A. Weimer, J. Mater. Res., 5, 2320 (1990).
4. Q. Sun and M. Alam, J. Electrochem. Soc., 139, 933 (1992).
5. W. Zhu, X.H. Wang, A.R. Badzian and R. Missier, New Diamond Science and Technology, pp. 821-825, 1991 MRS Int. Conf. Proc., (1991).

TABLE 1

The Activation Energies of CVD Diamond for Different Pressure of Oxygen

Oxygen Pressure (atm)	Activation Energy (kJ/mol) & kcal/mol)	
10-4 (argon)	-293.88	-70.22
.05	-245.6	-58.69
.10	-230.9	-55.18
.20	-223.85	-53.48
.70	-227.07	-54.26
1.0	-207.99	-49.7

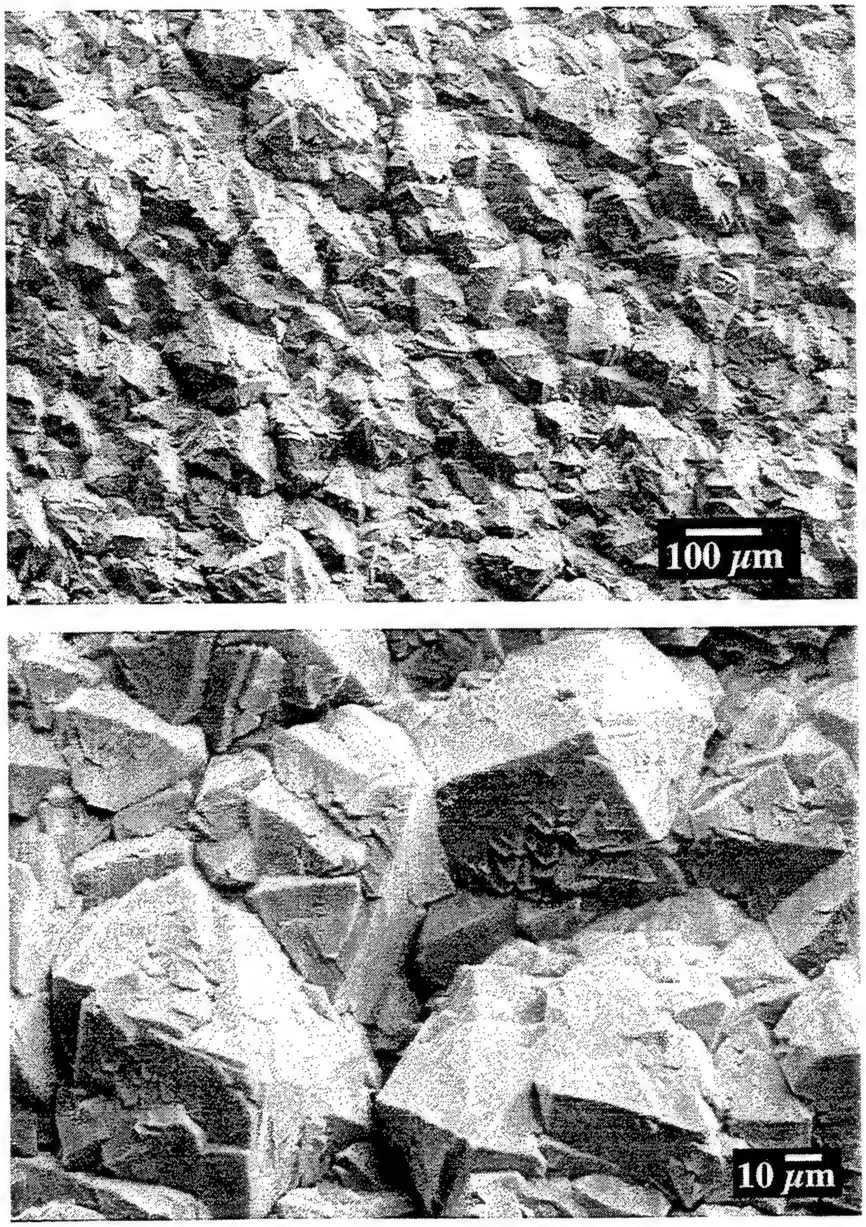

Figure 1. SEM micrographs showing the surface morphology for the growth side of a film formed by the DC arc plasma jet method. Crystal facets are covered with many surface imperfections.

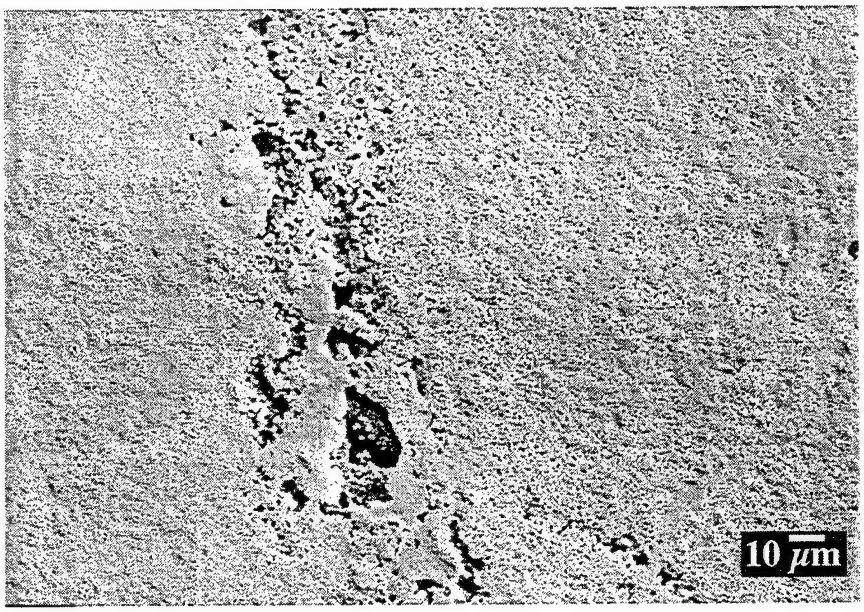

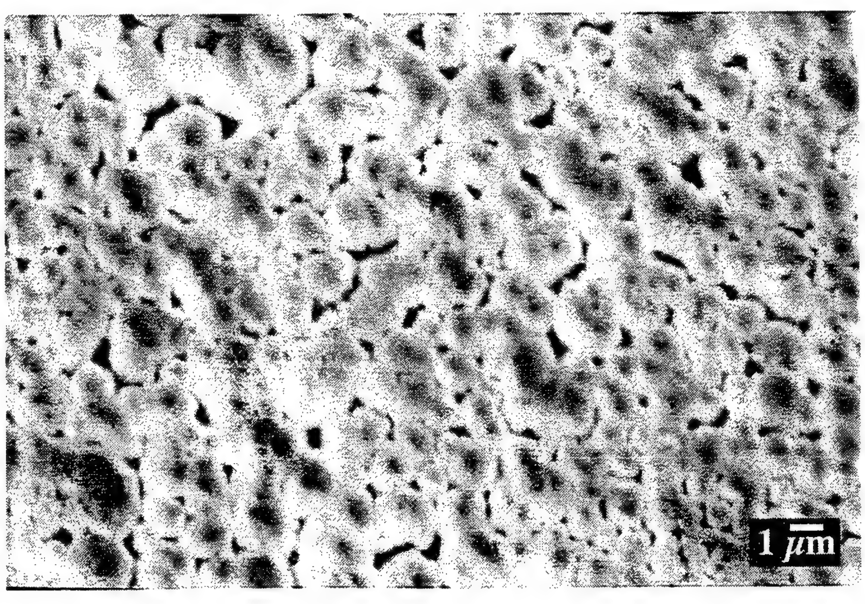

Figure 2. SEM micrographs showing the surface morphology for the substrate side of a film formed by the DC arc plasma jet method. Many surface imperfections such as voids and cracks are present. Quite large voids were occasionally evident (upper photograph) where nucleation of diamond did not occur during the initial formation of the diamond film.

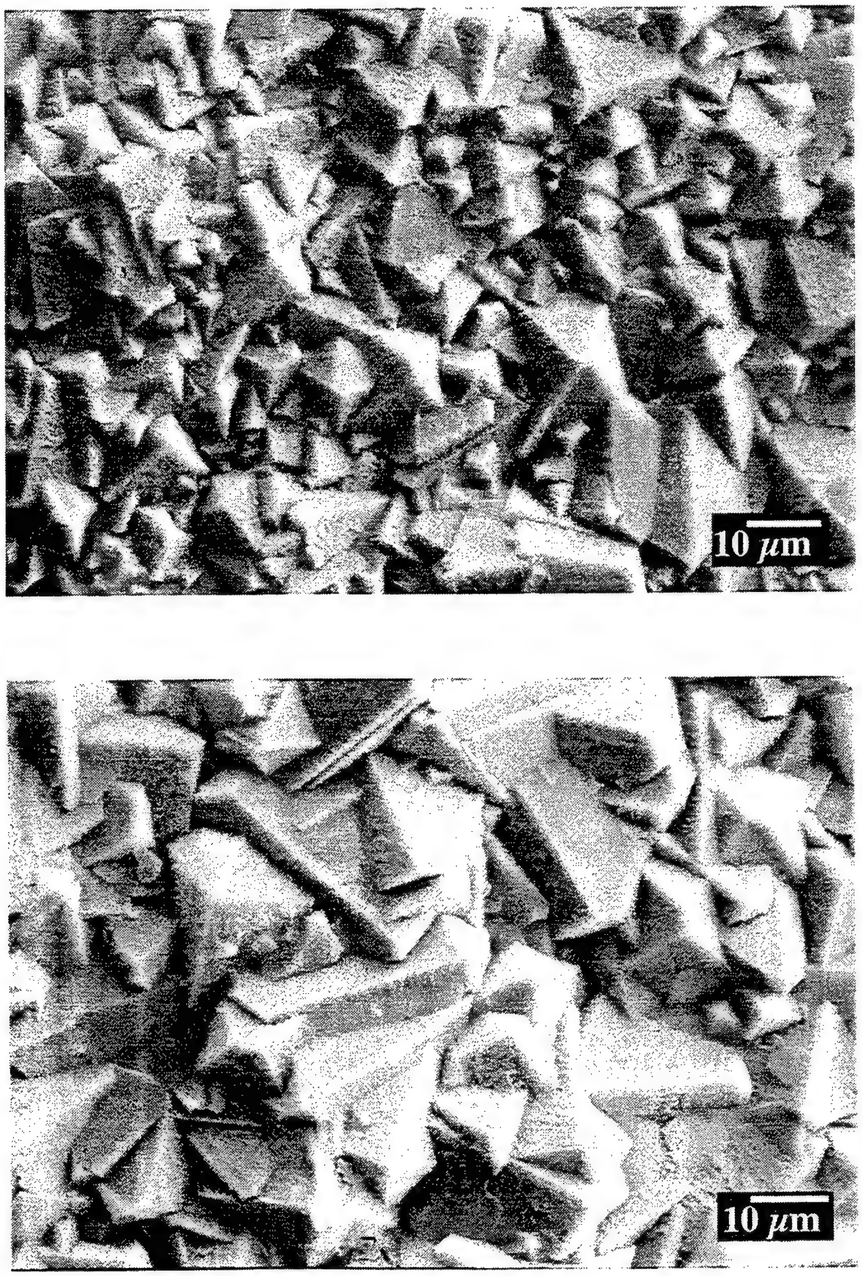

Figure 3. SEM micrographs of representative areas on turning tool insert formed by the hot filament method. Grains range in size from ca. 10 to 30 μm

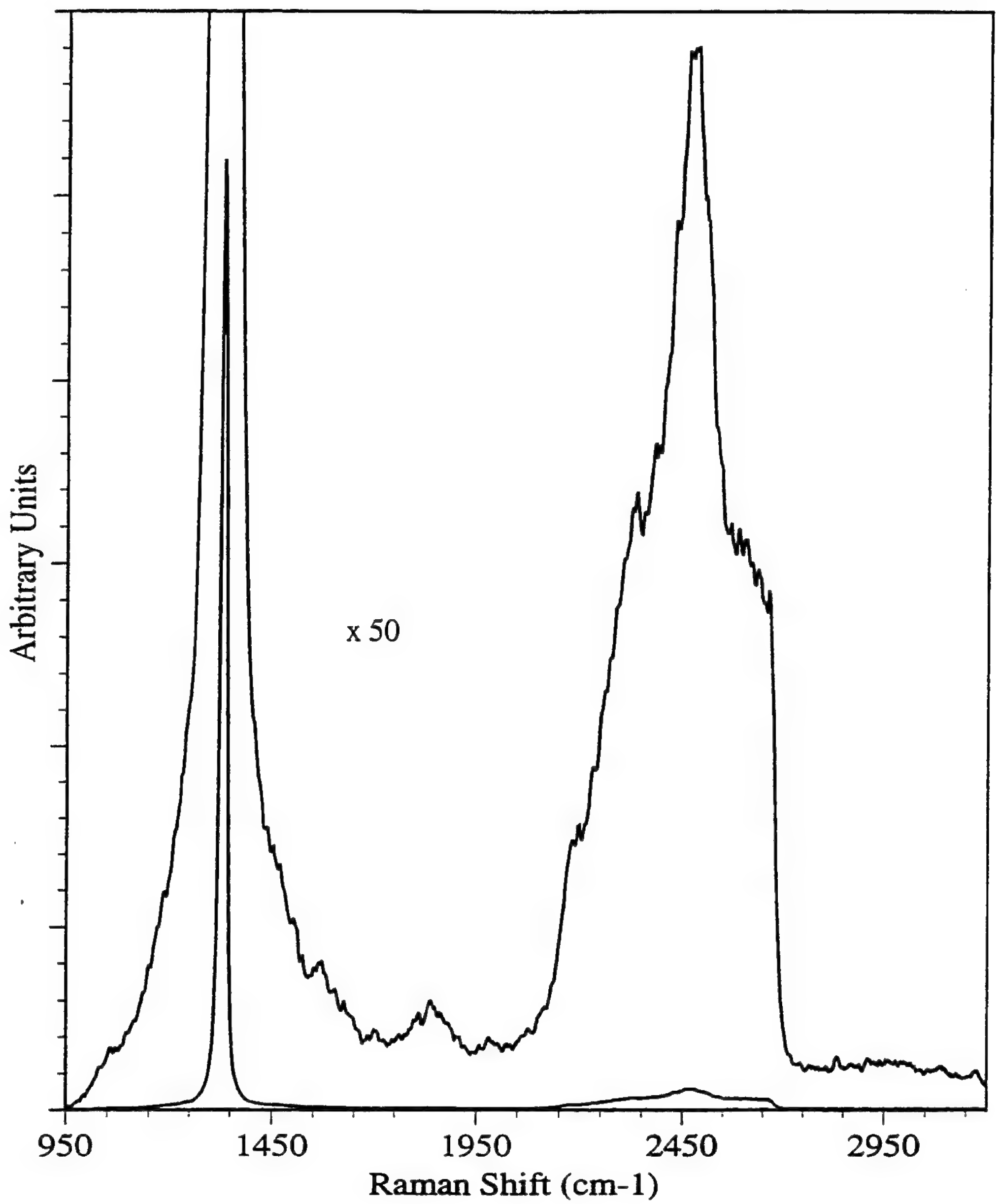

Figure 4. Typical UV Raman spectra of the free-standing CVD diamond film fabricated by the DC arc plasma jet method. A diamond band at 1332 cm^{-1}, a nondiamond carbon band at ca. 1580 cm^{-1}, a second order band at ca. 2450 cm^{-1}, and a nondiamond carbon band at ca. 3000 cm^{-1} are evident. The excitation wavelength was 228.9 nm.

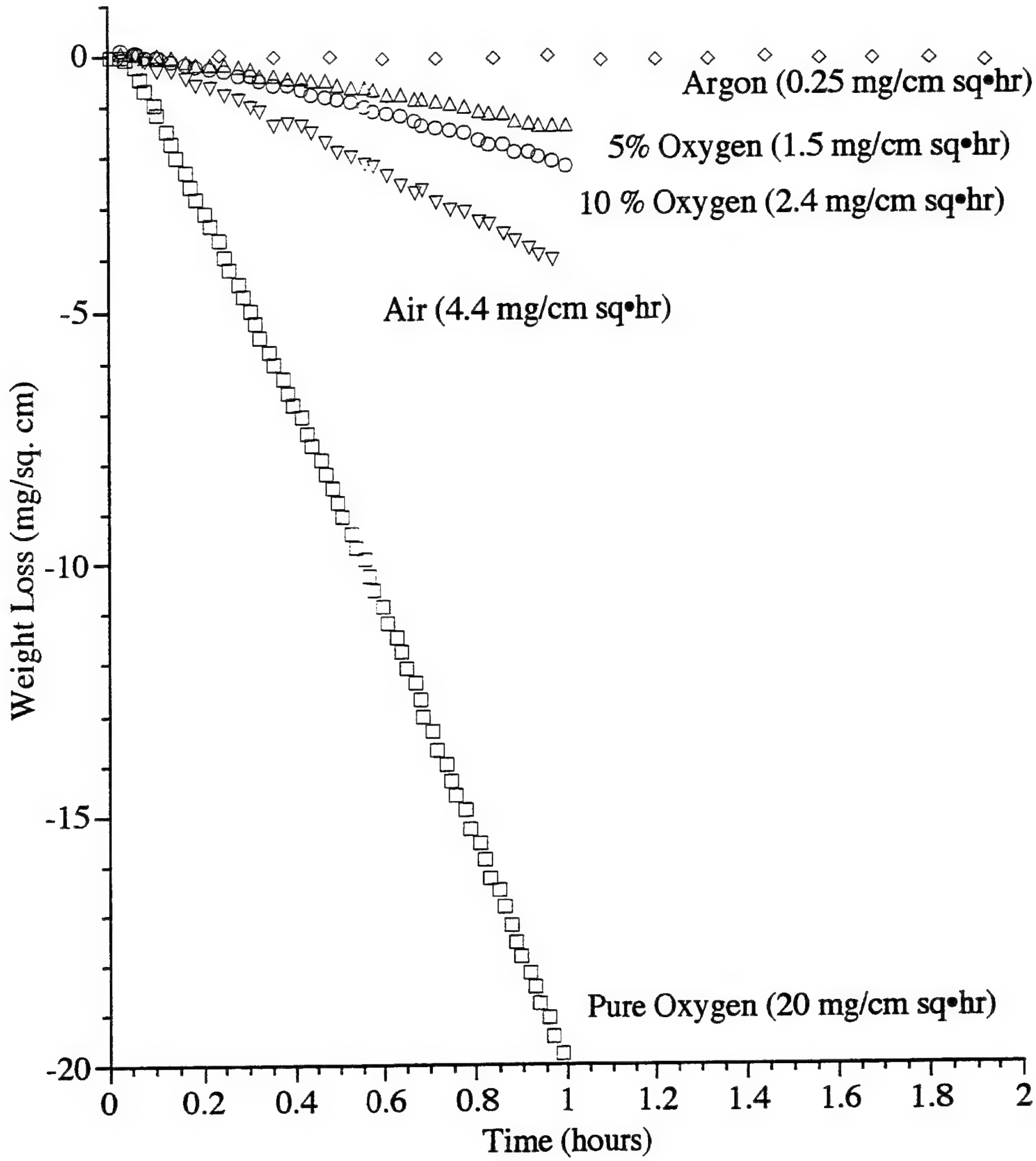

Figure 5. Relative weight loss versus time measurements of diamond oxidized at 700°C as a function of the partial pressure of oxygen.

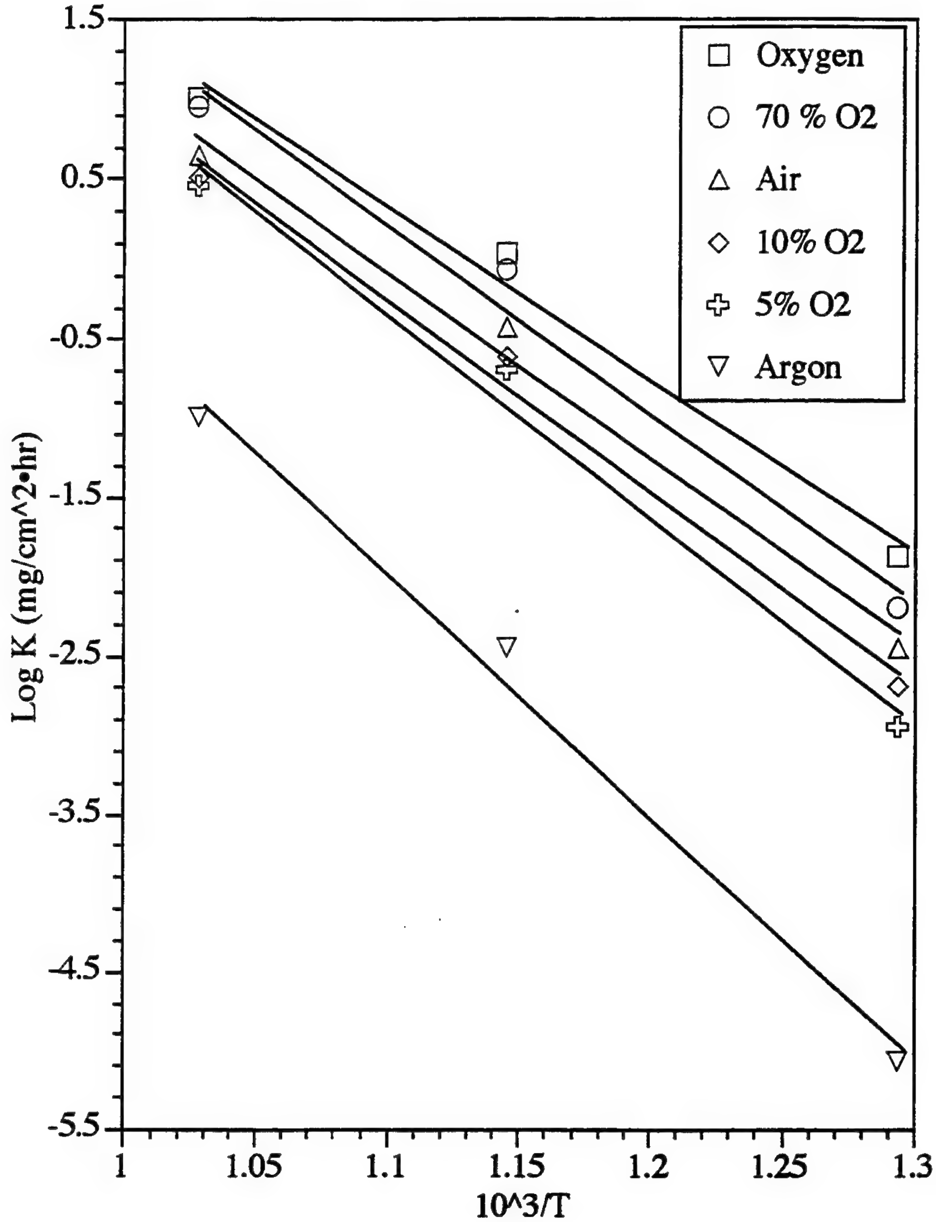

Figure 6. Arrhenius plot showing the temperature and pressure dependence of the linear rate constants obtained from the oxidation of DC arc plasma jet fabricated CVD diamond films.

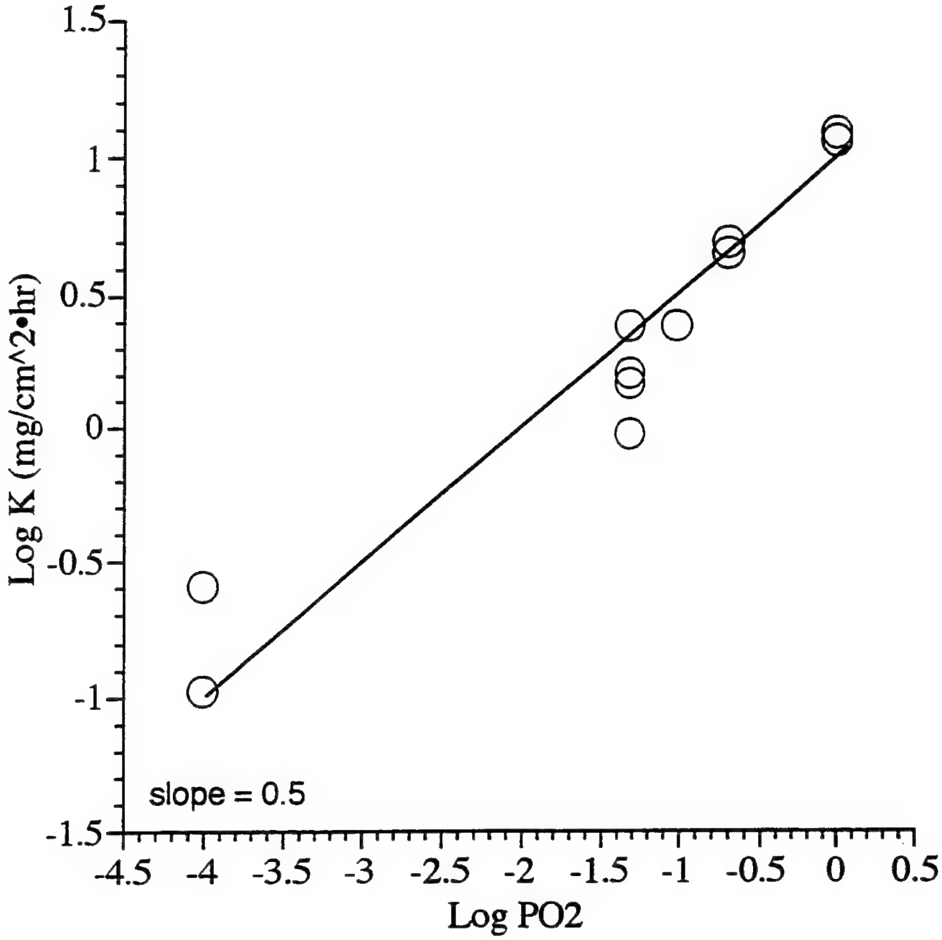

Figure 7. Plot of the log of the rate constant versus the log of the partial pressure of oxygen at 700°C. The slope was found to be approximately 0.5.

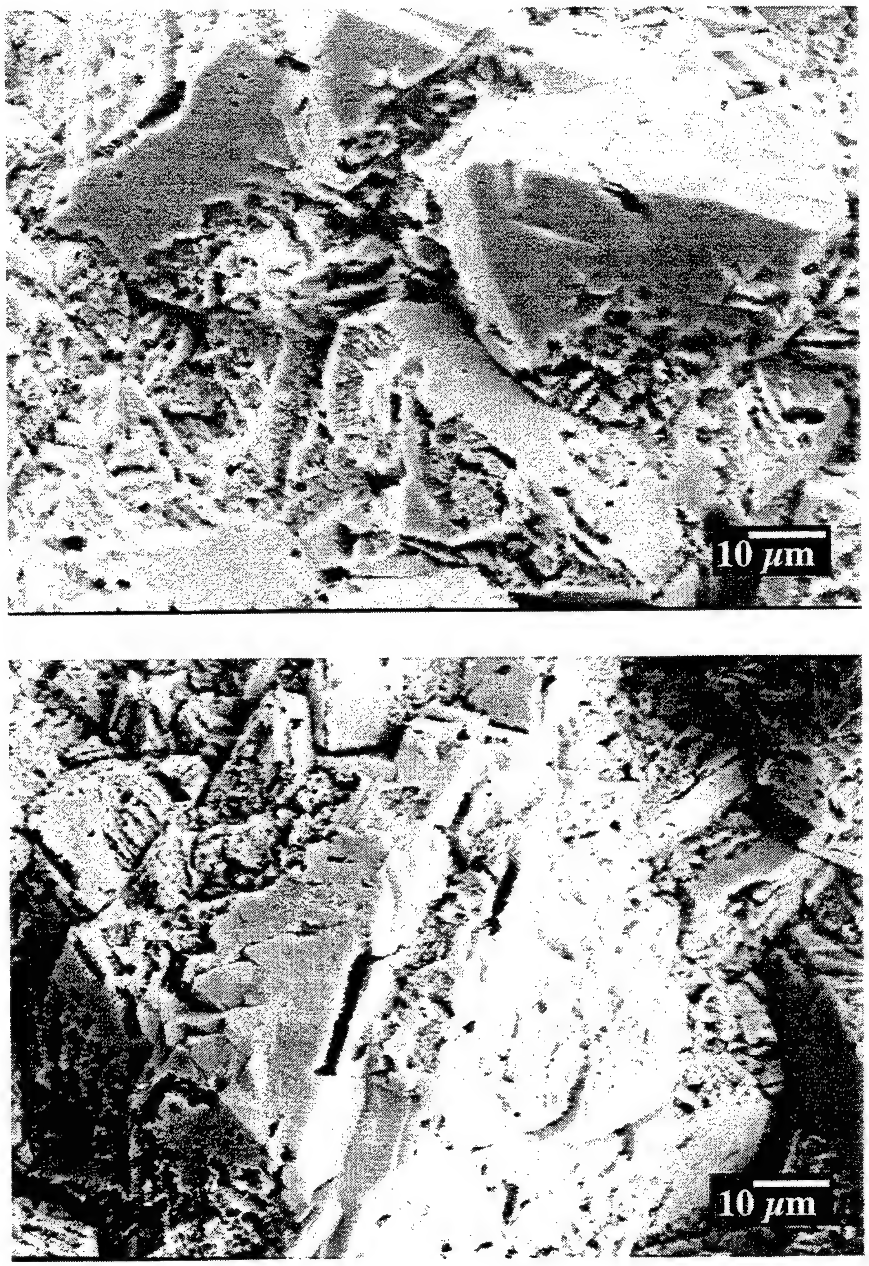

Figure 8. SEM micrographs of the growth side of a free-standing diamond film after 24 hours of oxidation in argon at 700°C ($Po_2 \sim 10^{-4}$ atm) showing preferential attack at the edges of facets and the interstices between facets.

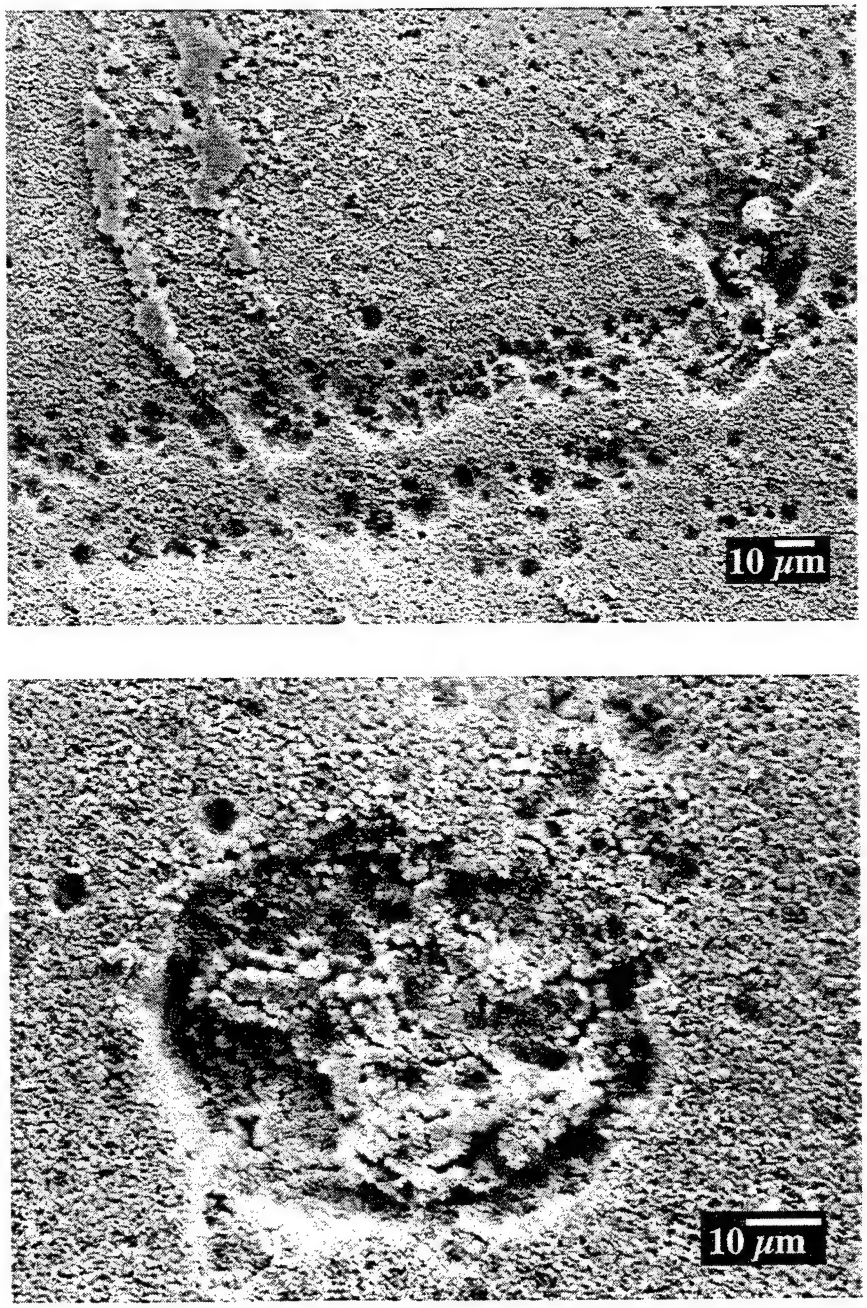

Figure 9. SEM micrograph showing the effect of oxidation on the substrate side of a diamond film oxidized for 24 hours at 700° in argon ($Po_2 \sim 10^{-4}$ atm). Oxidation at preexisting defects results in larger void areas.

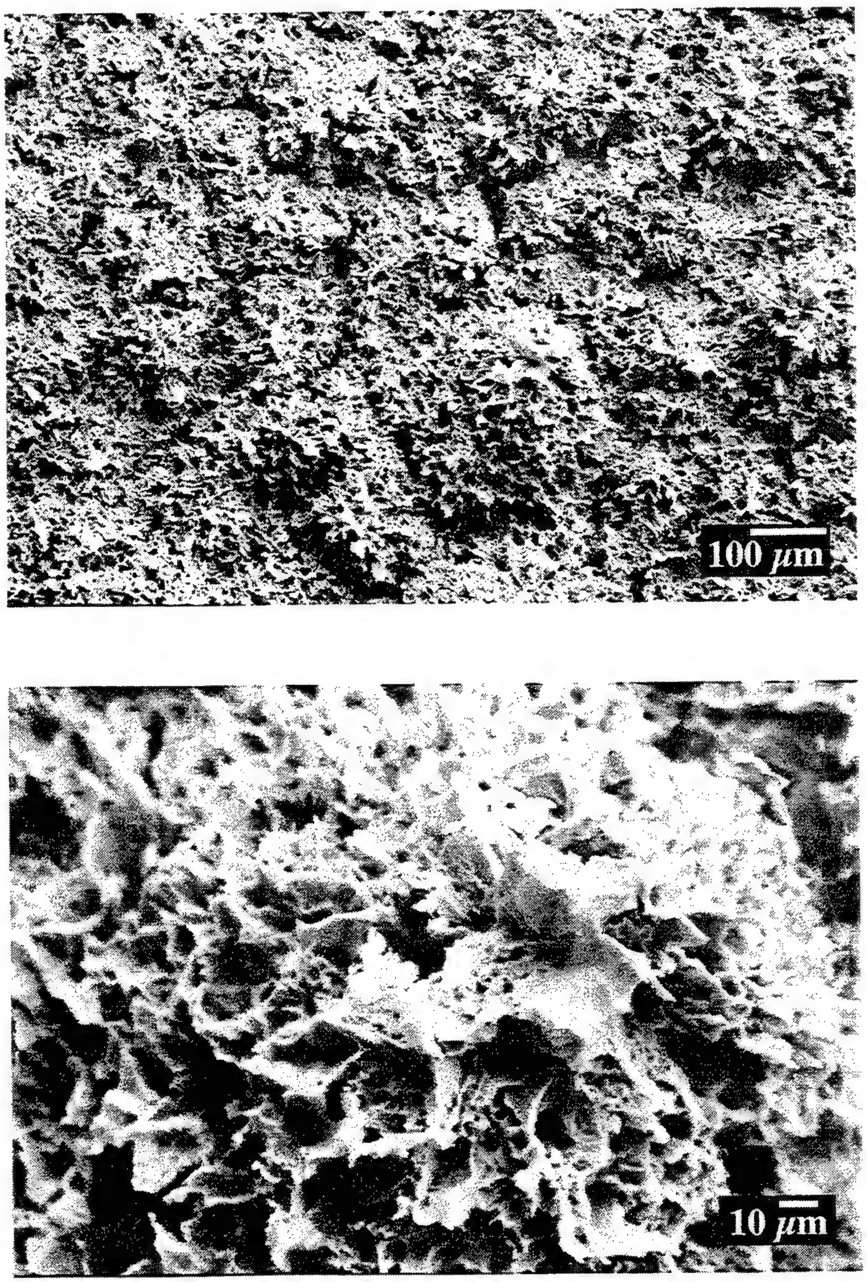

Figure 10. SEM micrographs showing features that develop during oxidation of diamond for 1 hr at 700°C in oxygen.

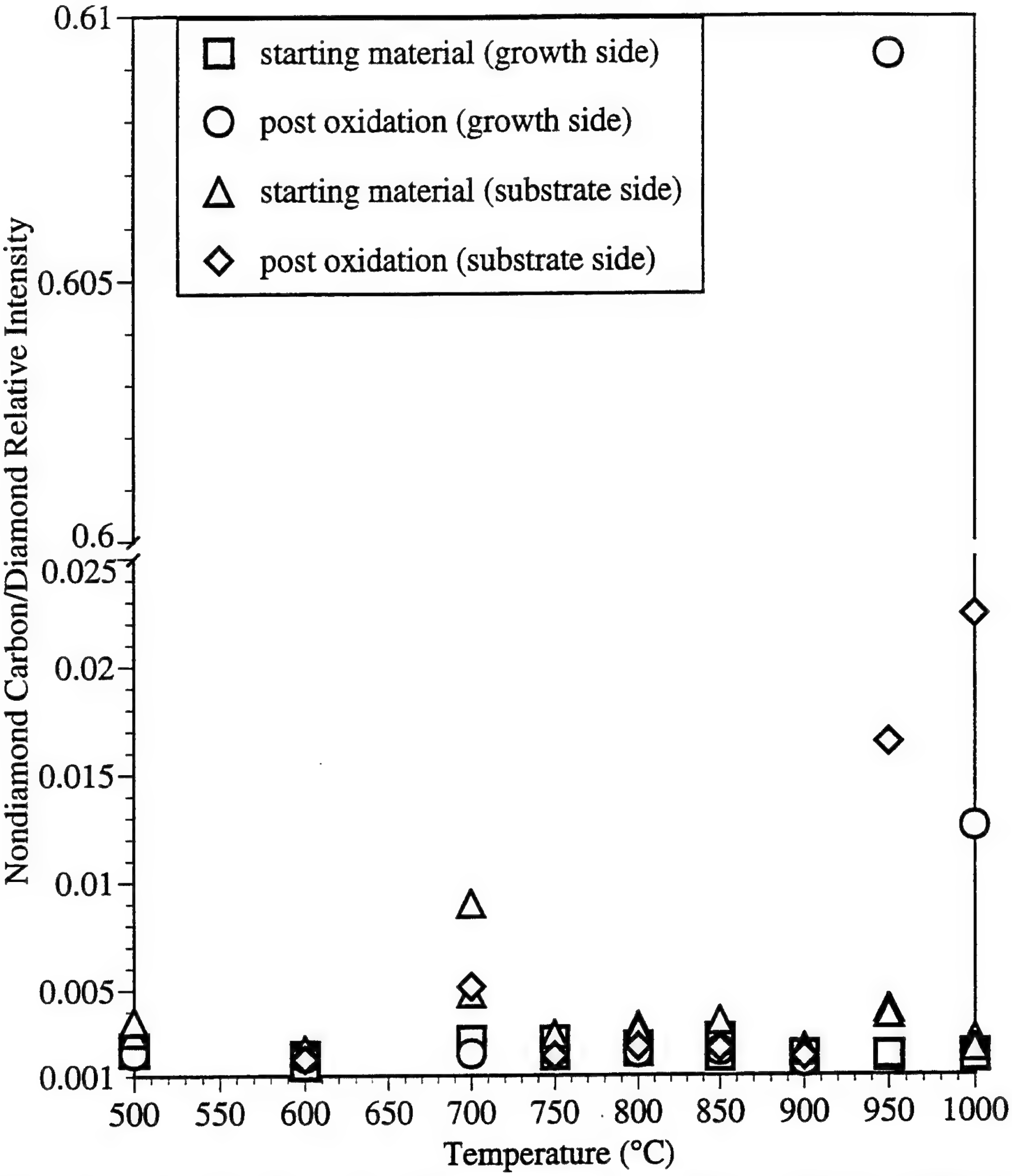

Figure 11. Plot of nondiamond carbon/diamond relative instensities as a function of exposure temperature, above 900° it is believed that diamond begins to transform to carbon.

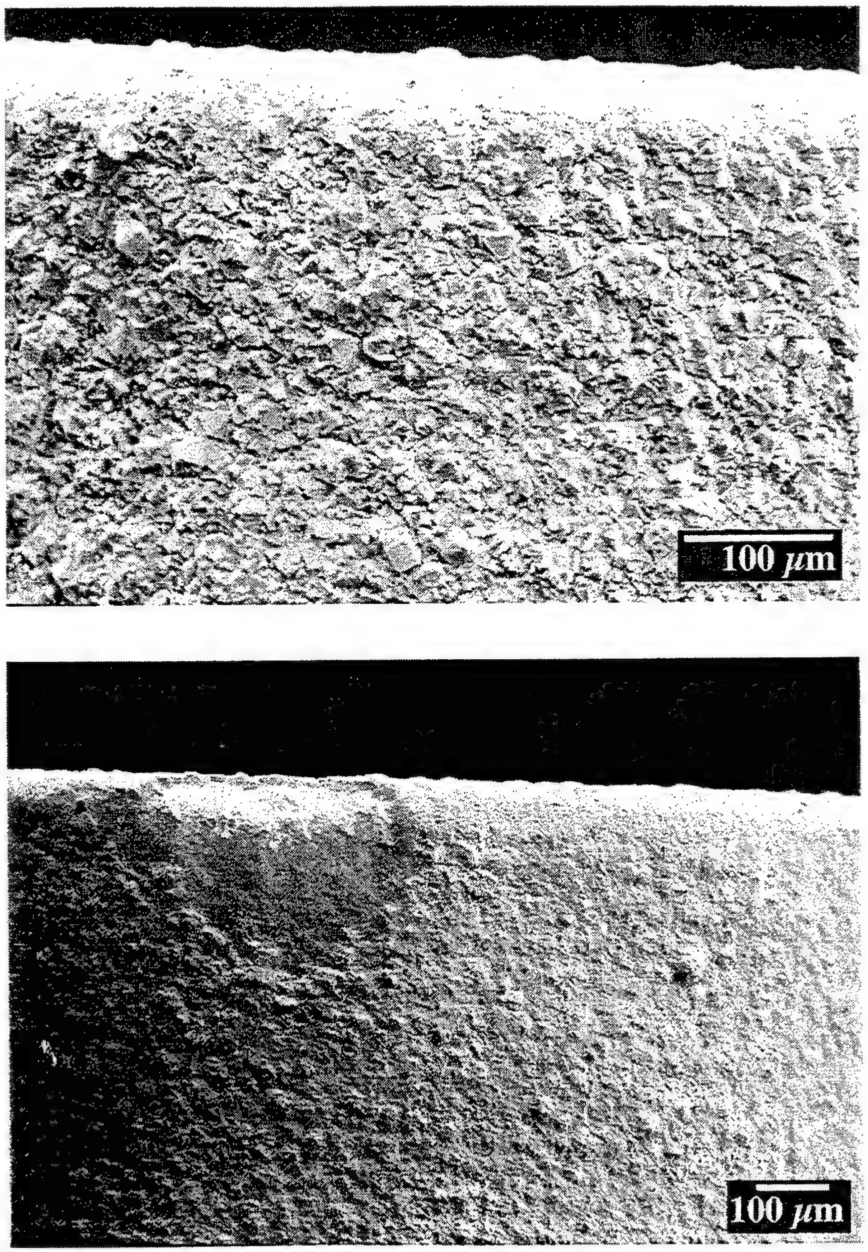

Figure 12. SEM micrographs of tool insert a) 30 seconds of machining and b) 60 seconds of machining an Al-Si alloy, a wear scar develops.

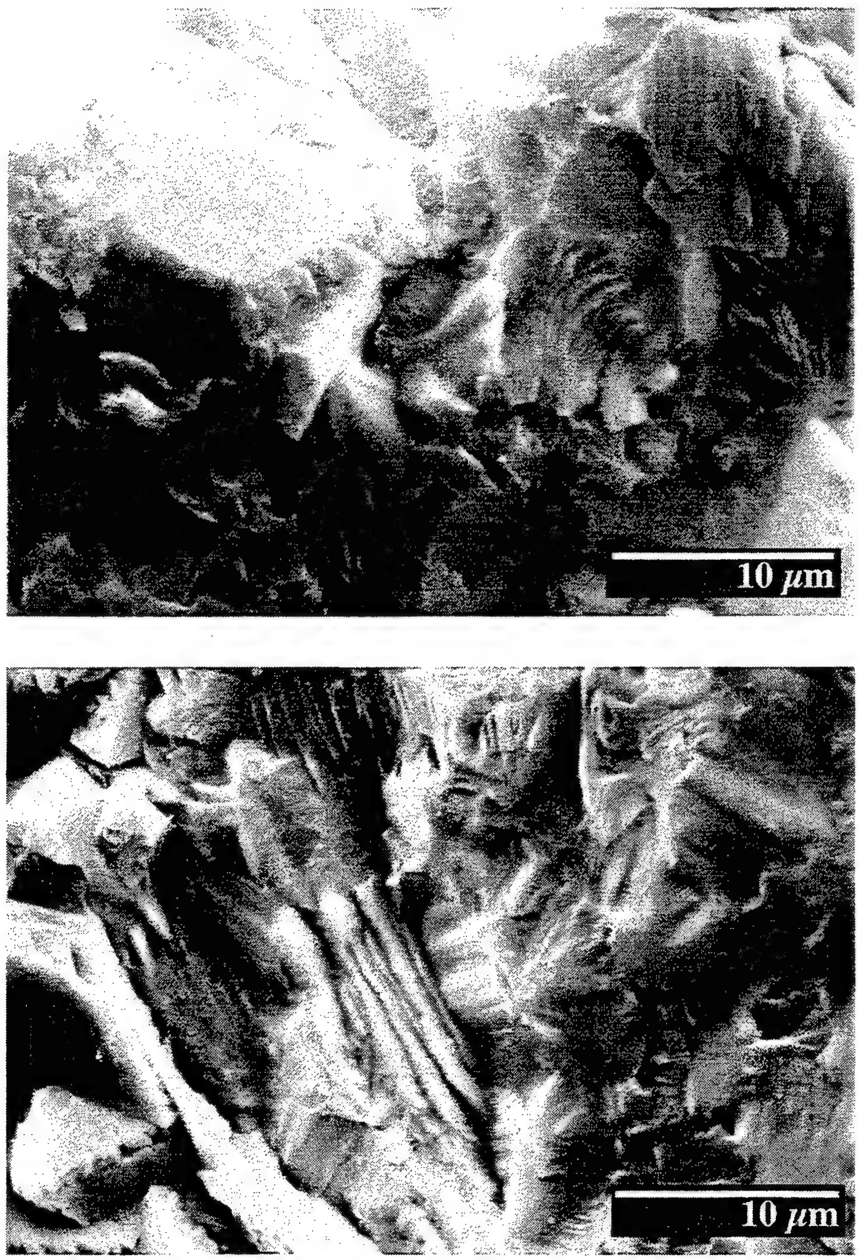

Figure 13. SEM micrographs of the fractured microstructure of the CVD diamond coated turning tool resulting from the machining process of the Al-Si alloy.

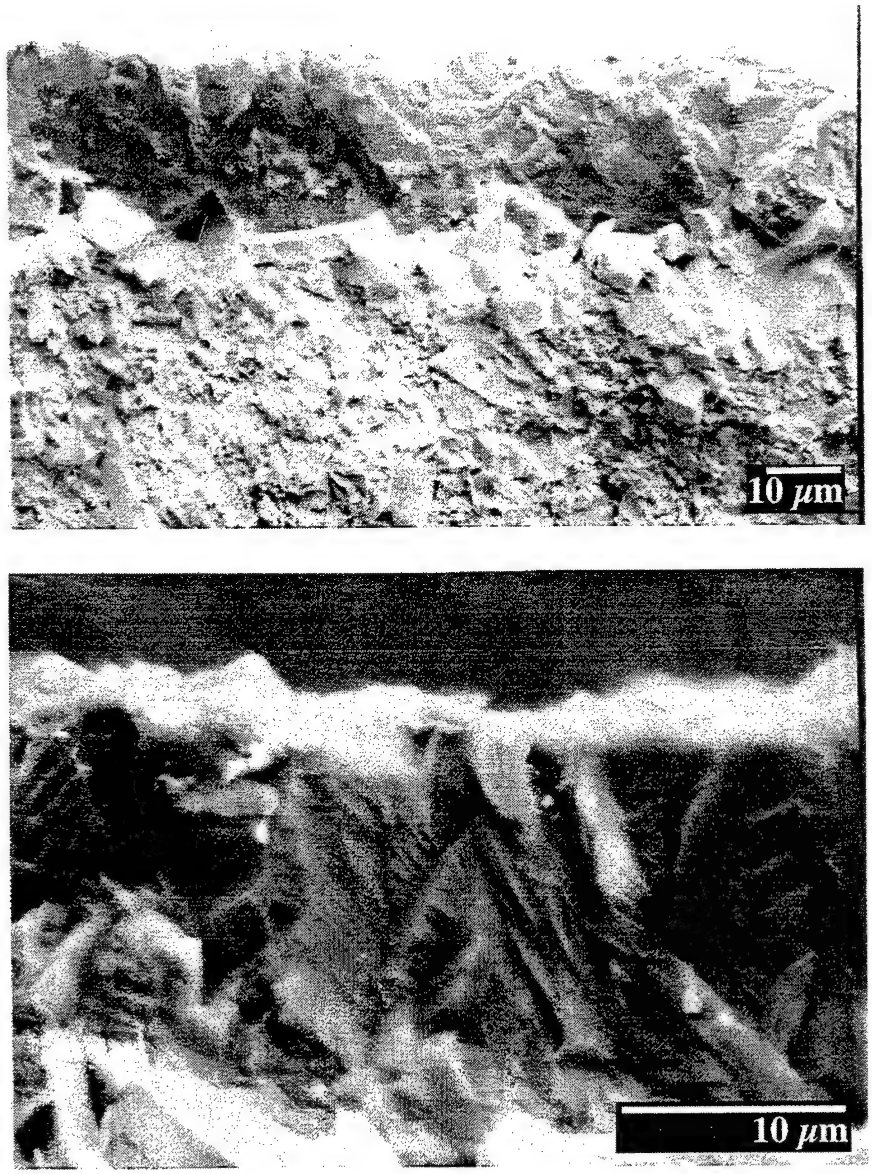

Figure 14. SEM micrographs showing the morphology of a fractured diamond coating on a tool insert in cross section.

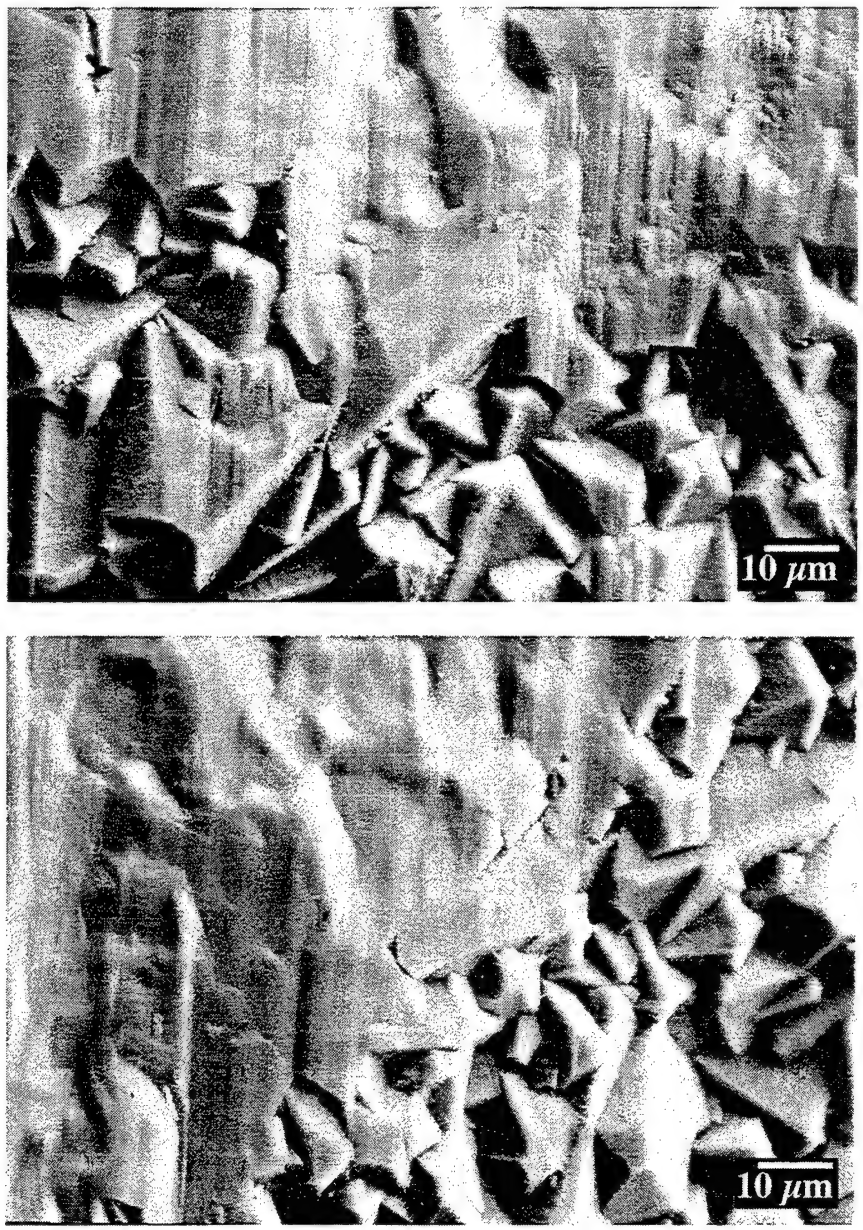

Figure 15. SEM micrographs illustrating typical surface morphologies in the wear regions of a tool insert used to machine cast iron.

IV.A.7 UV Resonance Raman Spectroscopy for In-Situ Diagnostics of Growing Diamond Films

Principal Investigator:	Professor Sanford A. Asher Department of Chemistry University of Pittsburgh
Other Faculty Participants:	Dr. Fred S. Pettit Materials Science and Engineering University of Pittsburgh
	Dr. Robert E. Witkowski Consultant, Department of Chemistry University of Pittsburgh
Students:	Mr. R. Bormett Mr. J. Worthington

IV.A.7.1. INTRODUCTION

The objective of our work is to construct a novel UV Raman spectrometer on a CVD diamond deposition chamber and to demonstrate its ability to monitor diamond growth in real time. We are developing this technology in collaboration with the Diamond Technology Group at the Westinghouse Science and Technology Center (WSTC). We have formalized this collaborative effort with WSTC through a Joint Research Agreement that permits the University of Pittsburgh staff to work on site at the Science and Technology Center.

Visible Raman spectroscopy has been an essential tool for the characterization and identification of chemical vapor deposited (CVD) diamond and diamond like films. However, the signal-to-noise ratio of the visible Raman data is often degraded by strong fluorescence of highly defective diamond. We have recently shown that CW UV lasers operating between 228-250 nm, near and within the diamond bandgap, allow the measurement of Raman spectra without interference from fluorescence and photoluminescence, and that resonance Raman enhancement increases the information content of the Raman data. For example, we have measured for the first time the third-order phonon bands of diamond which are particularly sensitive to the diamond crystallite size. We have also demonstrated the ability of UV Raman to measure the C-H stretching bands of nondiamond carbon and to determine the atomic percentage of hydrogen in CVD diamond films.

The ability to measure fluorescence free spectra and measure the C-H stretching bands makes UV Raman spectroscopy the method of choice for monitoring and characterizing both high- and low-quality CVD diamond and diamond like films. This approach appears ideal for use as an *in-situ* monitor of growing diamond films and for monitoring the gas phase precursors[1].

Professor Asher's laboratory at the University of Pittsburgh has pioneered the development of UV Raman spectroscopy for the study of aromatic molecules[2]. Over the last ten years they

demonstrated and characterized the selective enhancement of symmetric vibrations of polycyclic aromatic hydrocarbons (PAH)[3-6]. Their previous PAH studies clearly demonstrate the utility of UV resonance Raman spectroscopy for studying and characterizing different sized aromatic fused rings[3]. For example, the excitation profiles of PAH such as pyrene and coronene which contain 4 and 6 fused benzenoid rings are very narrow and the Raman bands are characteristic of the specific compounds[6]. These fused aromatic ring structures are analogous to some of the smaller graphitic carbon inclusions in diamond films. In fact, the PAH have Raman bands similar to those observed for non-diamond carbon inclusions; the carbon atomic motions in the PAH are similar to those in graphite.

The UV Raman studies of diamond and CVD diamond films at the University of Pittsburgh were the first to utilize CW excitation within the diamond band gap at 228.9 nm and have recently been extended further into the bandgap to 206 nm. The lack of fluorescence in the 228.9 and 244 UV Raman spectra of diamond and CVD diamond films allowed us to monitor: 1) the intensity and position of the third-order phonon bands of diamond (Fig. 1), 2) the evolution of the nondiamond carbon species from graphite-like to amorphous carbon-like (Fig. 2) and 3) the carbon-hydrogen (C-H) stretching vibrations of the nondiamond components of the CVD film (Figs. 3 and 4). The third-order phonon band is sensitive to the size of the diamond crystallite; it decreases in intensity and shifts to lower frequency as the diamond crystallite size decreases. We showed that the relative intensity of the C-H stretching bands at ~ 2930 cm^{-1} to the diamond first-order phonon band at 1332 cm^{-1} is proportional to the atomic fraction of covalently bound hydrogen in the CVD diamond films. UV Raman diamond measurements have significantly greater information content than do visible Raman measurements[1].

We wish to note that there is significant interest in developing *in situ* monitors of diamond film growth. Rosman et al[7] recently described the use of a visible wavelength pulsed laser source for *in-situ* measurements. The short laser pulsewidth (nsec) allowed them to gate the detection to reject the blackbody radiation. Our CW UV approach is superior because we will have higher S/N ratios and we avoid photochemical, thermal degradation and nonlinear phenomena which result from high laser excitation pulse powers.

IV.A.7.2 ACCOMPLISHMENTS AND SIGNIFICANCE

Through a formal, joint contract agreement, the University of Pittsburgh and Westinghouse Science and Technology Center, are developing new UV Raman based *in-situ* spectroscopic monitoring techniques to permit on-line control of growing CVD films with a wide range of tailored material characteristics: grain size, optical transparency, thermal conductivity, electrical conductivity, hardness and fracture toughness[8-10]. We have completed the UV Raman spectrometer construction, on an emission port of the ASTeX 1.5 kW microwave plasma reactor (Fig. 5) and have begun measuring diamond Raman *in-situ* during growth. Figures 6 and 7 show the first in-situ UV Raman spectrum of diamond, obtained after initial nucleation and after 10 hrs diamond growth. The high UV Raman cross sections and the weak plasma emission permit these high S/N studies, even with this unoptimized UV Raman spectrometer.

These measurements are only possible with UV Raman excitation because of its freedom from fluorescence interference, because of its resonance enhancement and because of its spectral

immunity from the broad band black body plasma emission that occurs from the heated substrate and plasma. We will also continue our investigation of the diamond structural dependence of the third order phonon band of diamond and will develop correlations between diamond crystallite size and the third order phonon band position and intensity.

Additionally, we are investigating the 206 nm excited Raman and photoluminescence spectrum of CVD diamond. Preliminary UV Raman measurements which excite well within the diamond bandgap with 206 nm light shows strong scattering of the Raman first, second and third order phonon bands. In addition, narrow photoluminescence bands are expected which occur just below the diamond bandgap. These 206 nm excited room temperature photoluminescence emission bands appear to be those observed in cryogenic temperature cathode luminescence[8]. The bandgap emission of diamond is expected to depend upon the presence of defects such as vacancies, inclusions, grain boundaries, etc. Our initial measurements show that the intensity and the position of these photoluminescence bands shift between CVD diamond films grown under different conditions.

We will continue our investigation of the Raman and emission intensities, positions and linewidths as a function of diamond crystallite size and as a function of defect levels which depend upon growth conditions.

IV.A.7.3 SUMMARY

Our most significant accomplishments over this grant period include:

- We have demonstrated that we can measure *in-situ* UV Raman spectra of growing diamond films by building a new CW UV Raman spectrometer onto an ASTeX 1.5 kW CVD diamond reactor. The strong temperature dependence of the diamond Raman frequencies allow us to sensitively monitor the temperature at the growing diamond surface.

- We recently demonstrated that resonance Raman excitation within or close to the diamond bandgap dramatically improves spectral signal-to-noise ratios. For example, the lack of fluorescence in the 228.9 and 244 UV Raman spectra of CVD diamond films allow us to monitor: 1) the intensity and position of the third-order phonon bands of diamond; 2) the evolution of the nondiamond carbon species from graphite-like to amorphous carbon-like; and 3) the carbon-hydrogen (C-H) stretching vibrations of the nondiamond components of the CVD film. The third-order phonon band is sensitive to the size of the diamond crystallite; it decreases in intensity and shifts to lower frequency as the diamond crystallite size decreases. We showed that the relative intensity of the C-H stretching bands at $\sim$2930 cm^{-1} to the diamond first-order phonon band at 1332 cm^{-1} is proportional to the atomic fraction of covalently bound hydrogen in the CVD diamond films. UV Raman diamond measurements have significantly greater information content that do visible Raman measurements.

- We have excited diamond photoluminescence bands with excitation at 206 nm within the diamond bandgap. These photoluminescence bands are identical to those observed with cathodoluminescence studies in vacuum at low temperature. These photoluminescence bands

are sensitive to diamond defect structures; these emission spectra offer a powerful new approach for studying growing CVD diamond films.

IV.A.7.4 REFERENCES

1. R.W. Bormett, S.A. Asher, R.E. Witkowski, W.D. Partlow, R. Lizewski, and F.S. Pettit, *J. Appl. Phys.* 77 (11), 5916 (1995).
2. S.A. Asher, *Ann. Rev. Phys. Chem.*, 39, 537-588 (1988); S.A. Asher, Anal. Chem. 65,59A; 201A (1993).
3. S.A. Asher, R.W. Bormett, X.G. Chen, D.H. Lemmon, N. Cho., P. Peterson, M. Arrigoni, L. Spinelli, and Cannon, *J. Appl. Spectroscopy*, 47, 628 (1993).
4. S.A. Asher, *Anal. Chem.* 56, 720-724 (1984); S.A. Asher, *Anal. Chem.* 56, 2258 (1984).
5. R. Rumelfanger, S.A. Asher, and M.B. Perry, *Appl. Spectroscopy* 42, 267 (1988).
6. C.M. Jones, and S.A. Asher, *J. Chem. Phys.*, 89, 2649 (1988).
7. N. Rosman, L. Abello, J.P. Chabert, G. Verven, and G. Lucazeau, *J. Appl. Phys.*, 78 (1), 519 (1995).
8. W.D. Partlow, J. Ruan, R.E. Witkowski, W.J. Choyke, and D.S. Knight, *J. Appl. Phys.* 67 (1), 7019 (1990).
9. W.D. Partlow, R.E. Witkowski, and J.P. McHugh, in *Applications of Diamond Films and Related Materials*, Ed. by Y. Tzeng, M. Yoshikawa, and A. Feldman, Elsevier Science Publishers, B.V., 163-168 (1991).
10. R.E. Witkowski, and W.D. Partlow, *Industrial Heating*, 50-52, March (1991).

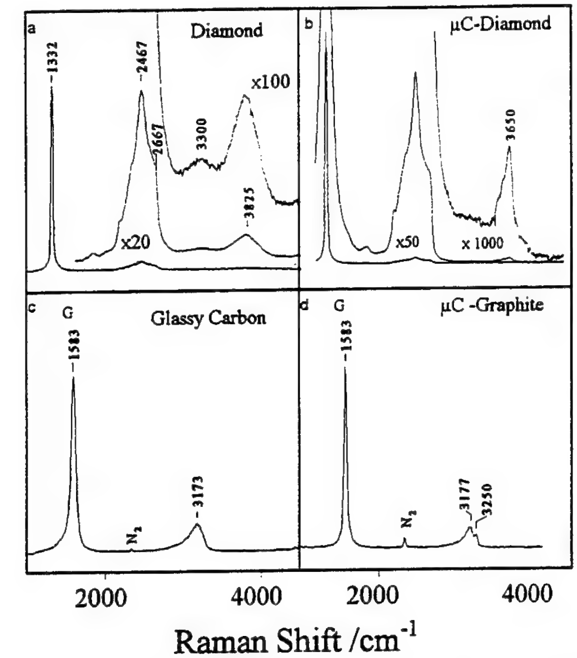

Figure 1. 228.9 nm excited Raman spectra of a) gem quality diamond, b) microcyrstalline diamond c) GC 20 glassy carbon, d) micro-crystalline graphite (< 1 um). The spectra were obtained with 2-5 mW of laser power focused to ca. 25 μm spot size with total integration times of 1 to 3 minutes and a spectral resolution of ca. 25 cm^{-1}.

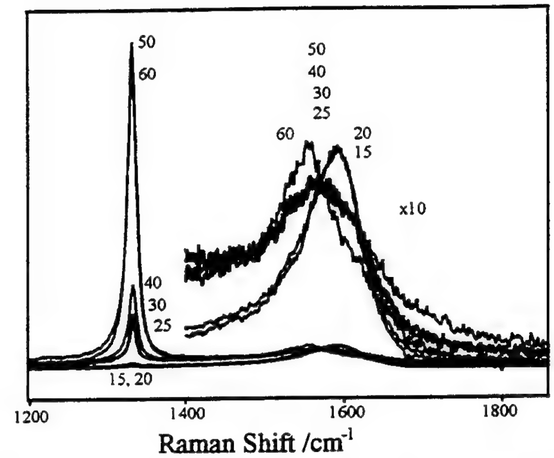

Figure 2. 244 nm excited Raman spectra of microwave grown CVD diamond films grown with 15, 20, 25, 30, 40, 50 and 60 sccm oxygen flow rates measured with ca. 50 mW focused to ca. 25 μm spot size with total integration times of 100 s the spectral resolution is 4 cm^{-1}. The data have been normalized to the Raman intensity at 1570 cm^{-1}.

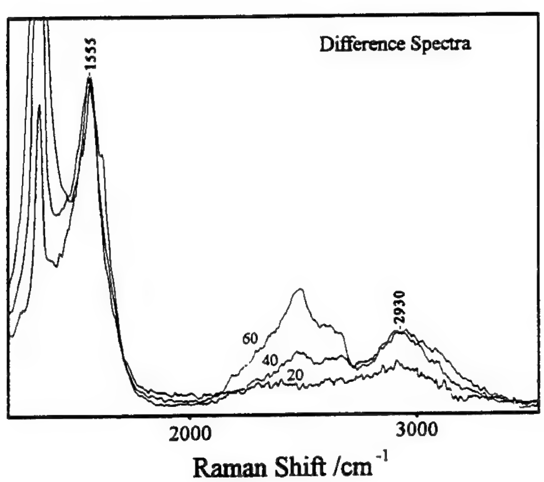

Figure 3. 228.9 nm Raman difference spectra of microwave grown CVD diamond films grown at 20, 40, and 60 sccm oxygen flow rates minus that of the 15 sccm oxygen grown film.

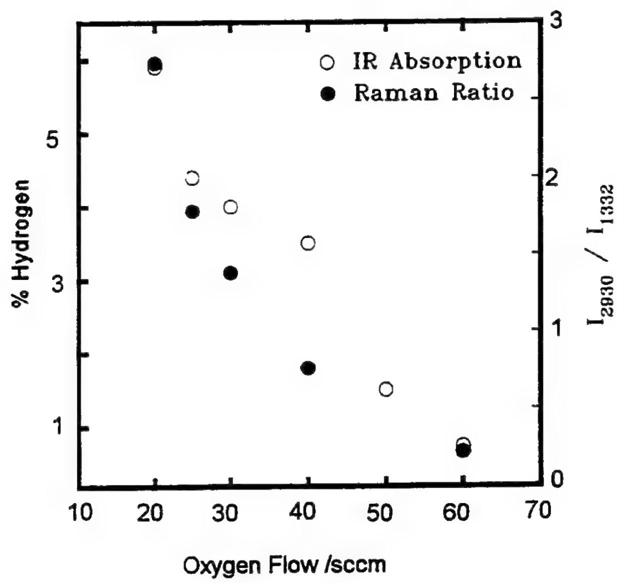

Figure 4. Comparison of the oxygen flow rate dependent atomic percentage of hydrogen for the microwave grown CVD diamond films determined by IR absorption (open circles) with the ratio of the Raman C—H stretching band area to the first order diamond phonon band area for 228.9 nm excitation (filled circles)

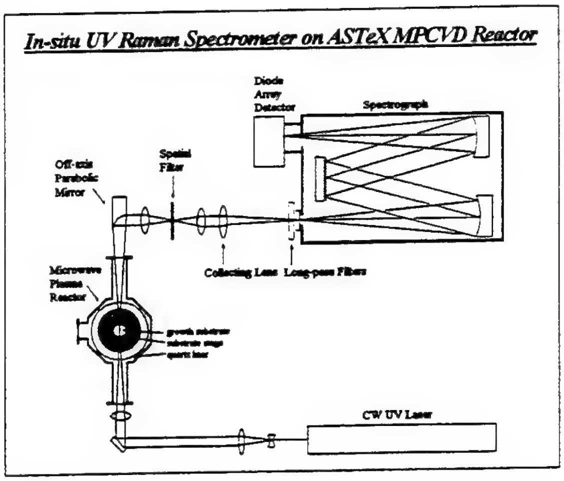

Figure 5 Schematic diagram of the CW UV Raman spectrometer system.

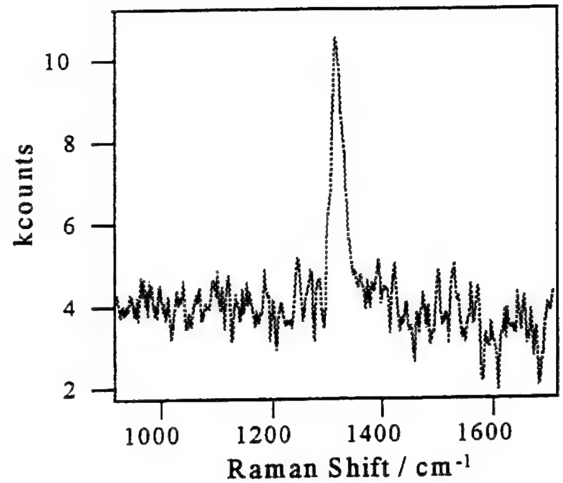

Figure 6 CVD diamond first-order phonon band after initial nucleation.

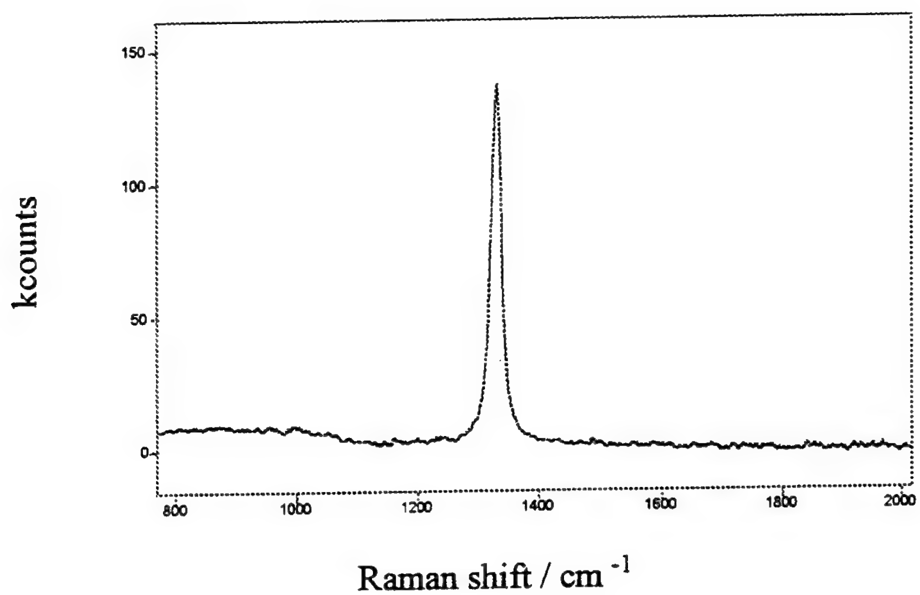

Figure 7 CVD diamond first-order phonon band after 10 hr. growth time

IV.A.8 Shear Processing of Binary Polymeric Blends

Principal Investigator: Professor J. Thomas Lindt
Materials Science and Engineering Dept.
University of Pittsburgh

Other Faculty Participants: Dr. Stanislav A. Patlazhan
Materials Science and Engineering Dept.
University of Pittsburgh

IV.A.8.1 INTRODUCTION

The commercial development and manufacturing of high performance polymer blends and alloys as is usually carried out in single- and twin-screw extruders at elevated temperatures and high rates of deformation. It has been shown[1] that structuring of blends occurs under conditions dominated by shearing stress, during which the following sequence of events evolves (Fig.1):

1. The granules of the ingredients undergo simultaneous melting and shear deformation to form stacked lamellas varying in thickness between, say, 1 - 50 μm.

2. The lamellar structures disintegrate into threads and elongated drops by capillary instabilities.

3. The terminal morphology is formed by simultaneous coalescence and breakup of the liquid bodies present in the system.

The objective is to find a theoretical interpretation of the mechanism of the surface forces driven instabilities involved in (2) and (3) in the environment of simple shear flow. The specific goals are theoretical predictions of the kinetics of development of transient and final blend morphologies as a function of the physico-chemical properties of the system and the externally imposed flow.

Our analysis concerning the formation and spacial development of the lamellas was reported previously.

IV.A.8.2 ACCOMPLISHMENTS AND SIGNIFICANCE

The problem of stability of layered systems undergoing shear flow involves the determination of the eigenvalues of hydrodynamic equations. Yih[2] developed the long-wave perturbation theory applied to the Orr-Sommerfeld equations, formulated for a plane Couette flow comprised of *i* layers of Newtonian medium. The amplitudes of the small periodic disturbances of wavelength, λ, in the stream functions were represented by expansions in wavenumber, $\alpha = 2\pi/\lambda$, $\phi i(y) = \phi_{io}(y) + \alpha\phi_{i1}(y) + O(\alpha^2)$. Consequently, the dispersion relation for the complex wave velocity of the disturbances was obtained in the form of $c = c_o + i\alpha c_1 + O(\alpha^2)$. His approach[3] suggests that the plane Couette and Poiseuille stratified flows

of two liquids are unstable if $(n^2 - m)(1 - m) > O$; m is the viscosity ratio and n the thickness ratio of layers 1 and 2.

Yih's solution[2] has been used in stability analysis of shear flows in a variety of stratified liquid systems, including non-Newtonian fluids[4-6]. Yih's stability criteria stipulate, however, that shear flows are destabilized by long-wave disturbances even if the depths of the layers are equal, in contradiction to measurements on plane Poiseuille flow[8]. These and other discrepancies prompted us to take a fresh look into the basic problem of long-wave linear stability of the two-fluid Couette flow in a shallow channel ($\alpha n^3 < \triangleleft$) which ultimately has led to the new exact long-wave asymptotic solution reported here.

The most significant differences between our findings and Yih's[2] are:

- first: the dispersion relation for the complex wave velocity of disturbances is adequately described by a wavenumber expansion in the fractional, 1/3-order, as opposed to the (truncated) integer-power series of Yih.

- second: the unstable mode, associated with positive disturbance growth rates, is described by the inequality,

$$(m - n^2)(1 - r^{1/3} m^{1/3}) > O$$

where r is the density ratio of the liquids constituting the layer. At equal liquid densities, $r = 1$, this inequality suggests the opposite compared to Yih's stability regime[2,3].

Our work suggests that, under the conditions of plane Couette flow of two superposed fluids, the flow is stable with respect to the long-wave interfacial disturbances, at $n = 1$. This is indirectly supported by experimental observations on Poiseuille flow in a rectangular channel[8], that show a stable interface between fluid layers of equal depths and nearly equal densities.

Figures 2(a) and 2(b) show the dependence of the growth rate of the disturbances of a wavelength λ on the viscosity ratio at different thickness and density ratios. The product of the growth rate, c_1, and the Reynolds number, R, decreases with increasing viscosity ratio. In the limit, as $m \rightarrow \infty$, the stable behavior for a single-liquid Couette flow[8] is recovered. The density ratio can drastically influence the stability mode. Figures 2(a) and 2(b) show that c_1 is positive (unstable mode) at $r = 1$ and negative (stable mode) at $r = 0.01$ in a wide range of m and n. The generalized stability diagram, defined in the m-n^2 - domain (Fig.3), shows that the unstable modes of the two-fluid plane Couette flow are defined by $r^{-1} > m > n^2$ and $n^2 > m > r^{-1}$. Note that this diagram, drawn for $r=1$ and $m=1$ as an example, predicts the stable regimes directly opposite to those deduced by Yih[3].

Our finding that, in the limit of the shallow channel approximation, $\alpha n^3 << 1$, the dependence of the imaginary part of the complex wave velocity depends on the fractional power of the wavenumber is consistent with the earlier results for plane Couette flow of two superposed fluids with thickness ratios restricted by $\alpha n^3 >> 1$[3,6]. Significant differences exist, however, between these two limiting cases. In case of $\alpha n^3 << 1$ the real wave velocity c_o does not depend on the wave number nor on the density ratio while $C_o \propto (\alpha r)^{1/3}$ at $\alpha n^3 >> 1$. In

addition, in the limit of αn^3 the unstable flow mode takes place when the viscosity ratio $m > 1$, regardless of the density ratio r. Under the condition of $\alpha n^3 << 1$, the mode of interfacial stability depends on the relationship between m, r and n and the growth rate c_1 tends to decrease with increasing thickness of the upper layer (see Fig. 4).

As far as the physical interpretation of the interface evolution goes, we conclude, that under the assumptions of shallow channel flow, the vorticity waves are in phase with each other at the interface between the fluids, shifted however relative to the displacement wave. The vorticity waves propagate ahead of the displacement wave in the unstable mode but trailing it in the stable mode (Fig. 5 and 6). In the neutral mode, $m=n^2$ or/and $m=r^{-1}$, the waves of vorticities and displacements are symmetrical relative to the interface between the fluids, in phase for $m > 1$ and out of phase for $m < 1$.

The vorticity waves along with the displacements of the interface are shown for the unstable mode in Fig. 5(a) and Fig. 5(b) for $m < 1$ and $m > 1$, resp. The flow domain is divided into cells, across which the vorticity changes its direction. The fluid elements rotate clockwise in the cells with negative vorticity disturbances, and counterclockwise in the cells with positive vorticity.

In the stable flow mode, the retardation of the vorticity waves gives rise to rotation of the liquid elements in the direction which minimizes the vertical velocity, producing damping at the interface (Fig. 6 (a) and 6 (b)).

The final stages of the morphology development in immiscible liquid-liquid dispersions under shear flow are controlled by the simultaneous breakup and coalescence of drops. We have analyzed these phenomena in the environment of simple shear flow of two Newtonian liquids of small viscosity ratio between the dispersed and continuous phase as under these conditions the theory of breakup of single drops is relatively well developed[9-12].

The demarcation between the stable and unstable states for a drop is given by the critical capillary number, Ca_{crit}, the value of which depends on the type of flow and is a function of the viscosity ratio[13-15]. If the shear rate or drop size are large enough to make the capillary number exceed the critical value, $Ca > Ca_{crit}$, the elongated drops become unstable and eventually burst. If the capillary number approaches its critical value, $Ca \sim Ca_{crit}$, a single drop will break up into two daughter drops of approximately equal size. At $Ca >> Ca_{crit}$ the breakup produces a set of small drops for which radii are proportional to the cross-section of the stretched drop[16].

In concentrated systems, all drops interact with their neighbors that constitute the disordered environment of the dispersion. The local fluctuations in their relative positions are associated with the fluctuations in the local stress fields and thus exhibit random deviations from the undisturbed macroscopic flow. As a result, both elongational and compressive components arise in the local stress tensor. These fluctuations in stress alter the stability of the system by affecting the breakup time spectrum, relative to the reference (average) state for single drops, thus broadening the boundary regime that separates the stable and unstable states. Experimental evidence[17] suggests that within the conditions of these experiments the behavior of drops in dispersions is in qualitative agreement with that observed with single drops.

The key processes in the development of dispersion morphology, coalescence and breakup are stochastic processes, random in time. The competition between them, under the conditions of simple shear flow, was studied in a number of papers while the attention was focused on the evolution of the total number of drops and estimation of the average domain size, as opposed to a drop size distribution function[18-23].

To represent more realistically the structure development in a dispersed system, we have introduced a continuous drop size distribution function into the analysis. Such functions, generalized from the Smoluchowski equation, are based on the formulation of continuity of mass transfer in the dispersed phase to describe the temporal changes in the drop size distribution due to the breakup and coalescence that control the rates of appearance (birth) and disappearance (death) of drops. Our population balance equations, written in terms of the number drop density $n(\kappa_i,t)$ for each drop size at an arbitrary instant, t, represent the conservation of the drop volume during the breakup and coalescence processes determine the drop size distribution from the two opposing rates of drop birth, $B(\kappa_i,t)$, and death, $D(\kappa_i, t)$, once the specifics of the drop breakup and coalescence under simple shear flow are added.

The present numerical solution of the population balances evaluates the morphology development as a function of: (i) the initial drop size distribution in the dispersion and (ii) the viscosity ratio, assuming bursts into droplet pairs.

The subsequent evolution of the drop distribution function from the initially homogeneous dispersion is shown in Fig. 7 for two values of viscosity ratio, $\lambda = 10^{-3}$ and $\lambda = 2 \cdot 10^{-3}$ at times of 0, 20 and 100 s, all at constant shear rate, $\gamma = 1\ s^{-1}$, viscosity of the continuous phase, $\eta_c = 1300$ Pa.s, interfacial tension, $\sigma = 0.004$ N/m, and volume fraction of the dispersed phase, $\varphi=0.2$. During shearing single maxima in the distribution functions tend to form while the number fraction of the large drops continuously decreases. The numerical analysis shows that under the simple shear flow conditions for drops of Ca > 1 this evolution pattern arises while the breakup rate is much higher than the rate of coalescence.

The breadth of the distributions at any given moment depends on the value of the viscosity ratio: the higher the λ, the narrower the distribution of drop sizes. This behavior is due to the larger breakup frequency at higher viscosity ratios.

One of the notable features of the distribution functions predicted to develop in simple shear flow is the existence of a precipitous drop in the number fraction of drops in the vicinity of the critical relative volume, corresponding to the critical capillary number, separating the stable and unstable states of the drops. The number of small drops increases at $Ca < Ca_{crit}$ while it decreases at $Ca > Ca_{crit}$ due to stepwise breakup. In principle, the sharp change in the distribution function may be mitigated by coalescence. The solution of the population balance equations is not particularly sensitive, however, to coalescence under these conditions.

The inclusion of a nonuniform initial distribution of drop sizes reveals some new morphological features, not explored previously. If initially a certain number of drops exceed the critical relative volume, a bimodal distribution eventually appears as a result (Fig. 8). The time over which the bimodal distribution can exist will increase with a decreasing viscosity ratio as the breakup is relatively slow. A bimodal distribution has been detected by light scattering[24].

Figure 9 shows the predicted behavior of the average drop size as a function of the volume concentration of the dispersed phase, calculated for the stepwise mechanism of breakup at two different viscosity ratios at time t = 150 s. It is seen that at simple shear flow, the average radius increases approximately in a linear manner with concentration, in good agreement with experimental data at low viscosity ratios[18]. The dependence of the average drop size on concentration is more pronounced at lower viscosity ratios.

IV.A.8.3 SUMMARY

Our most significant accomplishments:

1. We have obtained a new exact solution to the eigenvalue problem of instability of two sheets of immiscible Newtonian liquids undergoing simple shear flow. We have concluded that the well established linear perturbation theory[2], leading *by definition* to an integer power polynomial in wavenumber for the complex wave velocity is incorrect; our exact solution shows that the complex velocity is proportional to the fractional power of 1/3.

   The unstable states, predicted by this new approach, are in agreement with the experimental data, unlike the previous theory[2]. This new concept is further supported by the newly introduced physical arguments based on the vorticity distributions associated with the traveling interfacial waves.

2. We have integrated the previous fragmented knowledge on coalescence and breakup of liquid bodies into a novel framework of differential population balances, allowing the temporal evolution of the distribution of minor phase in the matrix to be better understood. New is the adaptation of the population balances to simple shear flow from its traditional version for turbulent flows.

   Both findings directly relate to the sequence of events observed in mechanical blending of high performance polymeric blends. They provide a rational basis for the design of blends' morphology from first principles, so far missing in the engineering methodology in this important technological area.

IV.A.8.4 REFERENCES

1. Lindt J.T. and Ghosh A.K., Polym. Engrng. Sci., **32**, 1802 (1992).
2. Yih C.S., J.Fluid Mech. **27**, 337 (1967).
3. Yiantsios G. and Higgins B.G., Phys.Fluids A **1**, 1484 (1989).
4. Khan A.A. and Han C.D., Trans. Soc. Rheol. **21**, 101 (1977).
5. Anturtkar N.R, Papanastasios T.C. and Wilkes J.O., AIChE Journal **36**, 710 (1990)
6. Su Y.-Y.and Khomami B., J.Rheol. **36**, 357 (1992).
7. Hooper A.P., Phys.Fluids **28**, 1613 (1985).
8. Kao T.M. and Park C., J.Fluid.Mech. **52**, 401 (1972).
9. Tomotika, S., Proc.Roy.Soc. (London), **A150**, 322-337 (1935).
10. Mikami, T., Cox, R.G. and Mason, S.G.,Int. J. Multiphase Flow, **2**, 113-138 (1975).
11. Hinch, E.J. and Acrivos, A., . Fluid Mech. **98**, 305-328 (1980).
12. Khakhar, D.V. and Ottino, J.M., Int. J. Multiphase Flow, **13**, 71-86 (1987).

13. Grace, H.P., “Dispersion phenomena in high viscosity immiscible fluid systems and application of static mixers as dispersion devices in such systems,” Eng. Found. Res. Conf.Mixing, 3rd, Andover, N.H. (1971) , republished in Chem. Engng. Commun. **14**, 225-277 (1982).
14. Torza S., Cox, R.G. and Mason, S.G., J. Coll. Interface Sci., **38**, 395-411 (1972).
15. Bentley, B.J. and Leal, L.G., J. Fluid Mech. **167**, 241-283 (1986).
16. Tjahjadi, M. and Ottino, J.M., J. Fluid Mech. **232**, 191-219 (1991).
17. Schubert, H. and Armbruster, H., Chem.-Ing.-Tech., **61**, 701-711 (1989).
18. Tokita, N. "Analysis of Morphology Formation in Elastomer Blends", Rubb. Chem. Technol., **50**, 292 (1977).
19. Elmendorp, J.J. and Van der Vegt A.K., Polym. Engng.Sci., **26**, 1332 (1986).
20. Fortelny, I. and Kovar, J., Eur. Polym. J., **25**, 317 (1989).
21. Huneault, M.A., Shi, Z.H. and Utracki, L.A., Polym. Engng. Sci., **35**, 115 (1995).
22. Janssen, J.M.H. and Meijer H.E.H., Polym. Engng. Sci., **35**, 1766 (1995).
23. Lynggae-Jorgensen J., personal communication, 1990
24. Sullivan, D.M. and Lindsey, E.E., Ind. and Engng. Chem. Fund., **1**, 87-93 (1962).

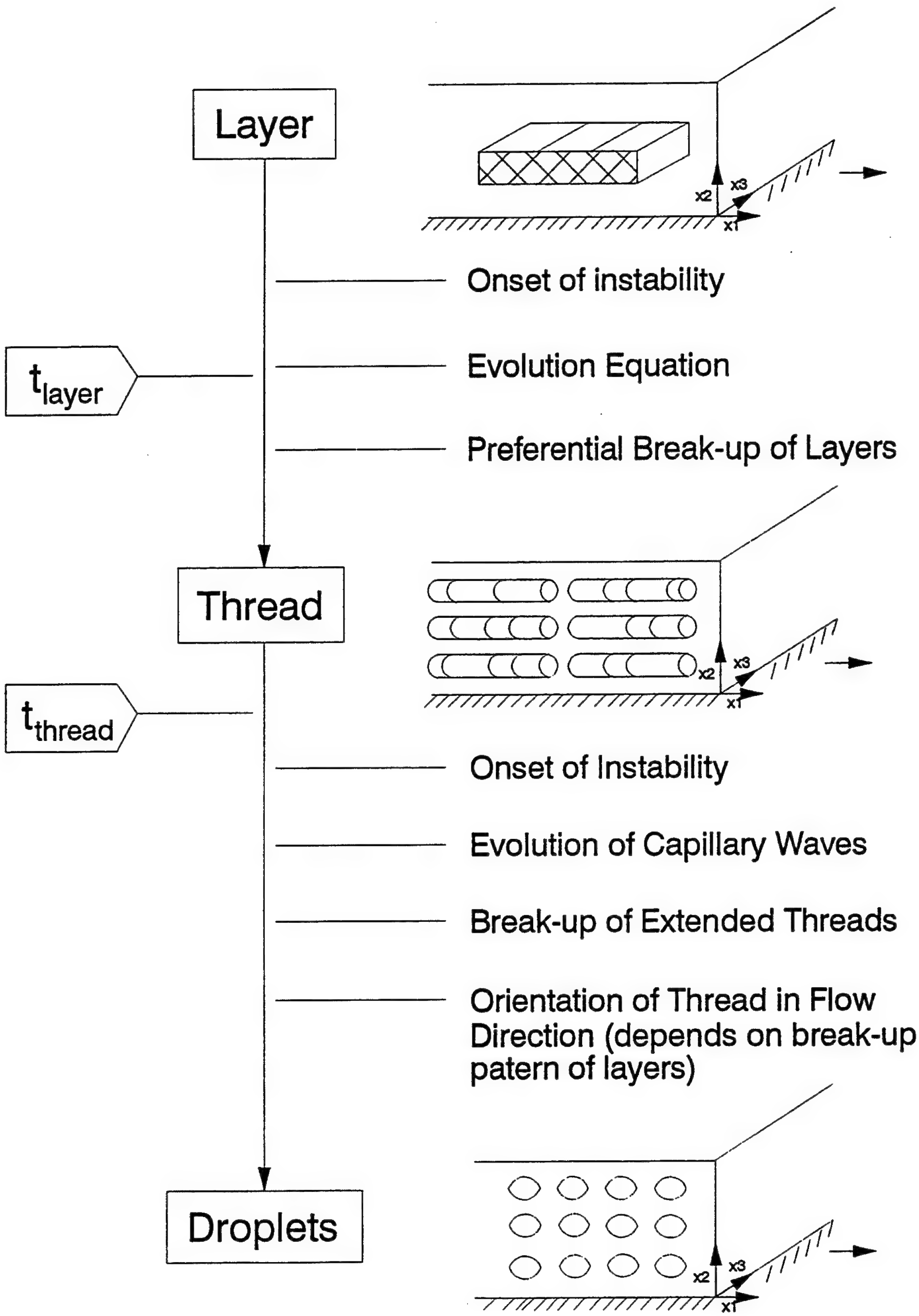

Figure 1. Schematic showing the blend morphology development sequence

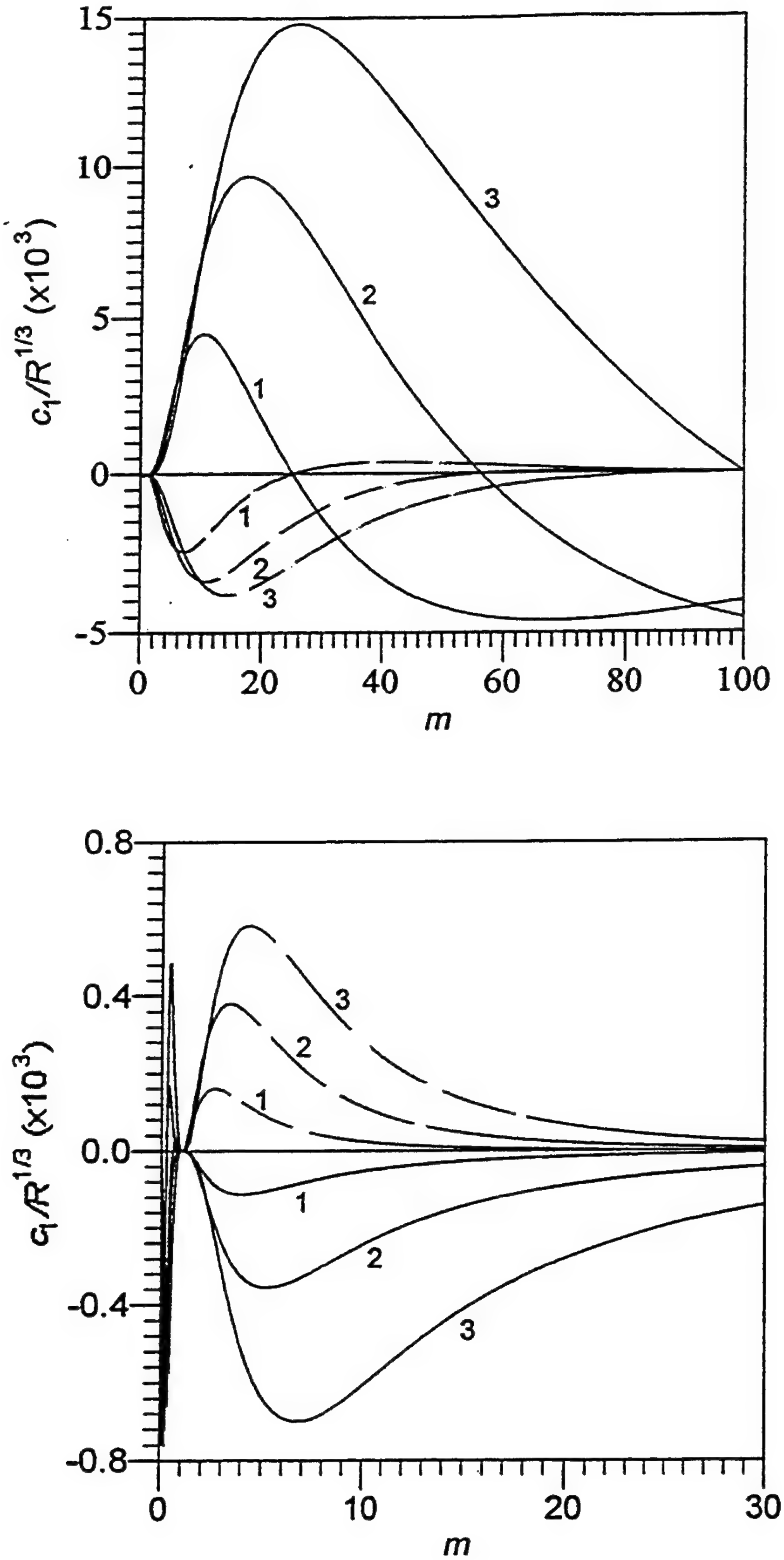

Fig. 2. Dependence of growth rate $c_1 / R^{1/3}$ on viscosity ratio m for $r = 1$ (solid curves) and $r = 0.001$ (dashed curves): (a) 1. $n = 0.5$, 2. $n = 0.75$, 3. $n = 1.0$; (b) 1. $n = 5.0$, 2. $n = 7.5$, 3. $n = 10.0$.

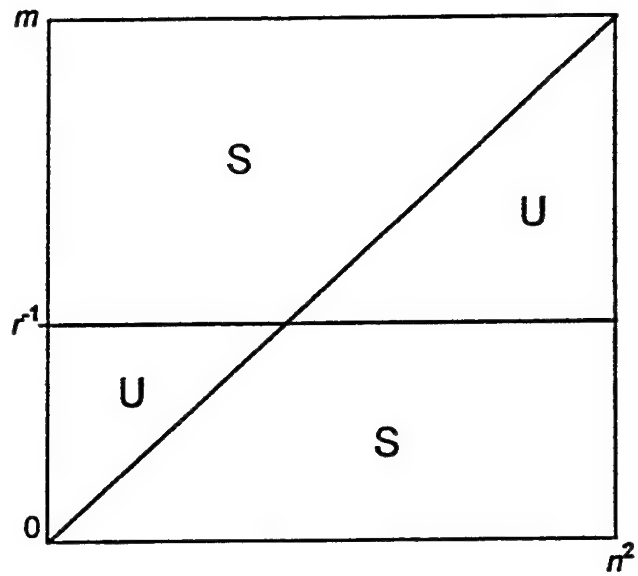

Fig. 3. Stability diagram in the plan of viscosity ratio m and thickness ratio n. Lines correspond to neutral stability. Stable regions are denoted by S and unstable regions by U.

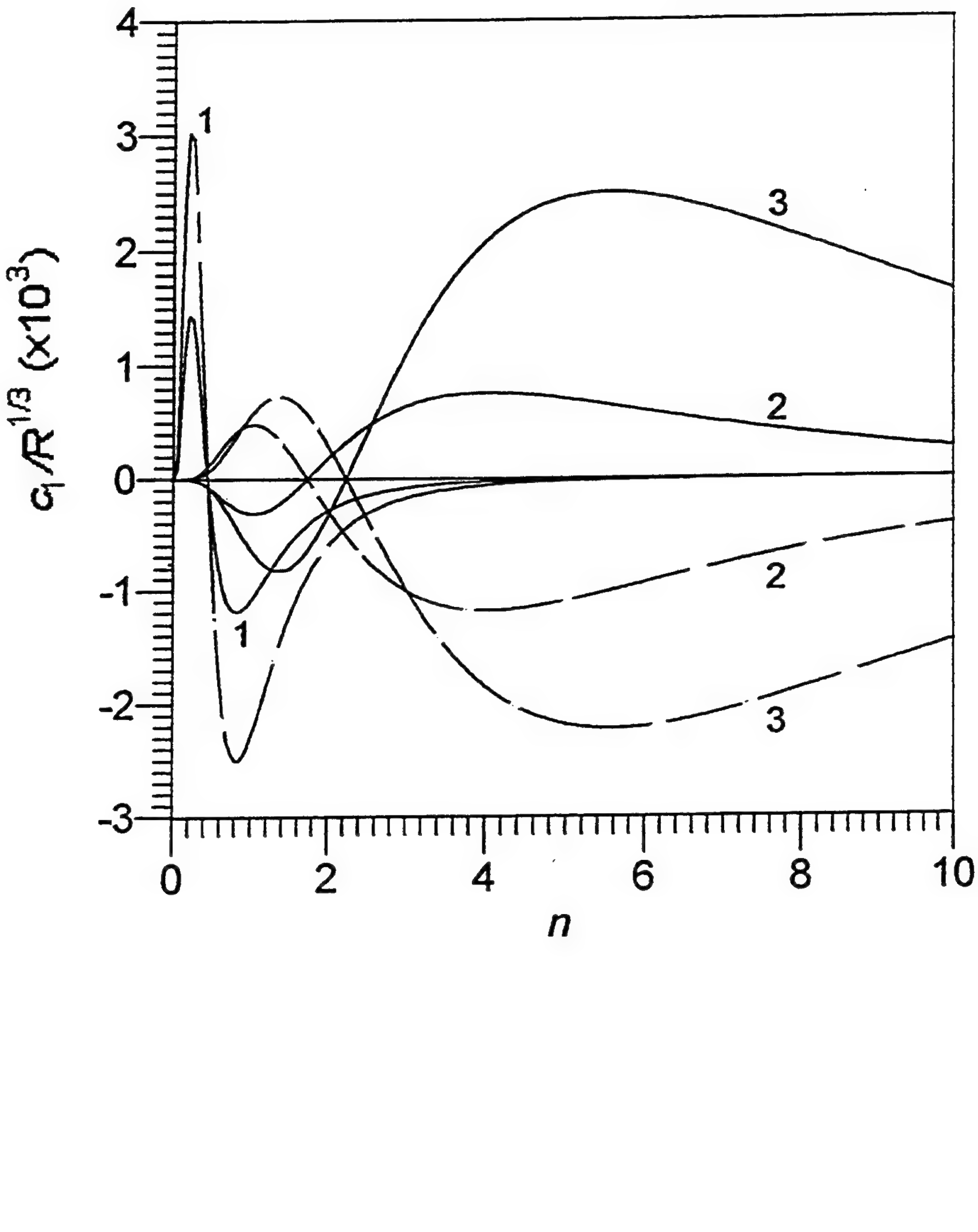

Fig. 4. Dependence of growth rate $c_1 / R^{1/3}$ on thickness ratio n for $r = 1$ (solid curves) and $r = 0.001$ (dashed curves): 1. $m = 0.2$, 2. $m = 3.0$, 3. $m = 5.0$.

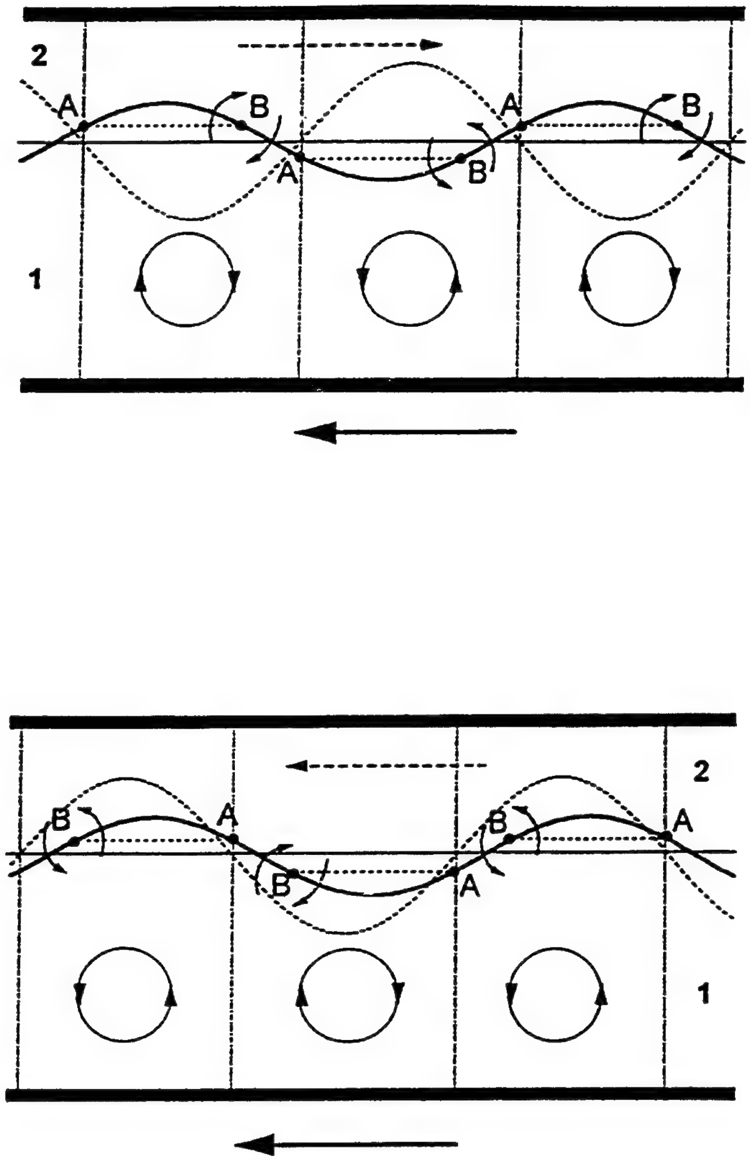

Fig. 5. Arrangement of displacement (thick solid curves) and vorticity (dashed curves) waves at the interface between superposed fluids in the unstable mode: (a) $m < 1$ and (b) $m > 1$. Circle arrows denote directions of fluid rotation. Dashed arrows denote direction of wave propagation relative to interface.

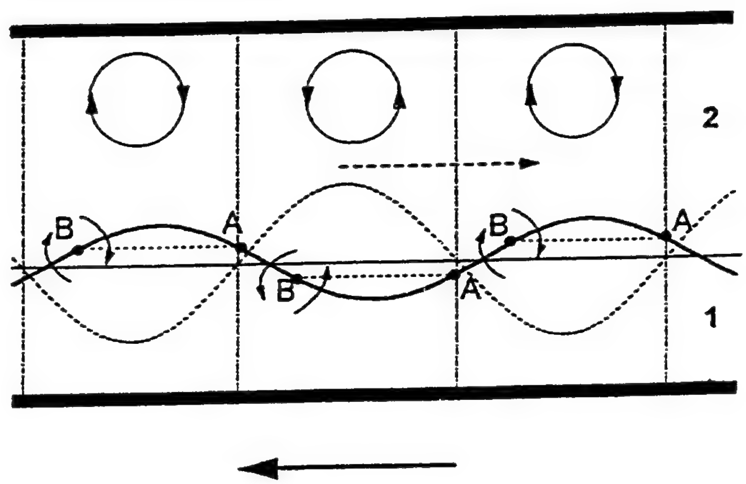

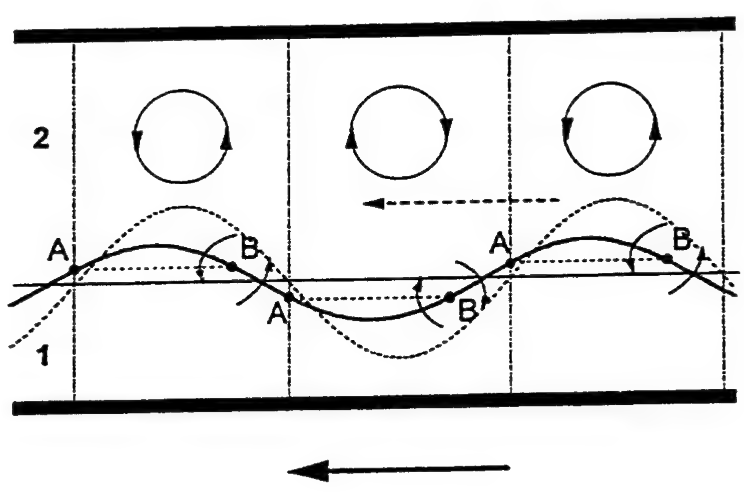

Fig. 6. Arrangement of displacement (thick solid curves) and vorticity (dashed curves) waves at the interface between superposed fluids in the stable mode: (a) $m < 1$ and (b) $m > 1$.

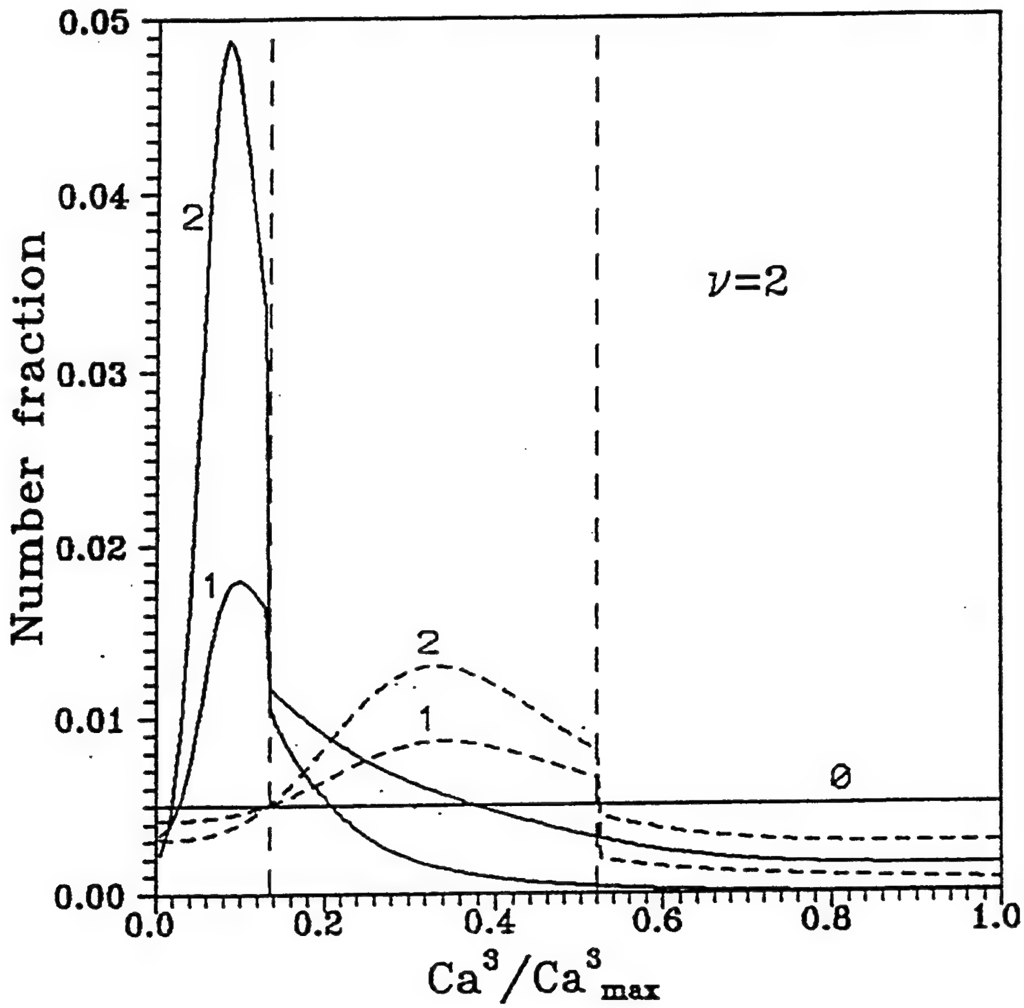

Fig.7. Evolution of the size distribution functions from a uniform distribution for the stepwise mechanism of breakup, ν =2 : 1. t = 20 s, 2. t = 100 s. Solid lines correspond to $\lambda = 2\cdot10^{-3}$, dashed lines to $\lambda = 10^{-3}$

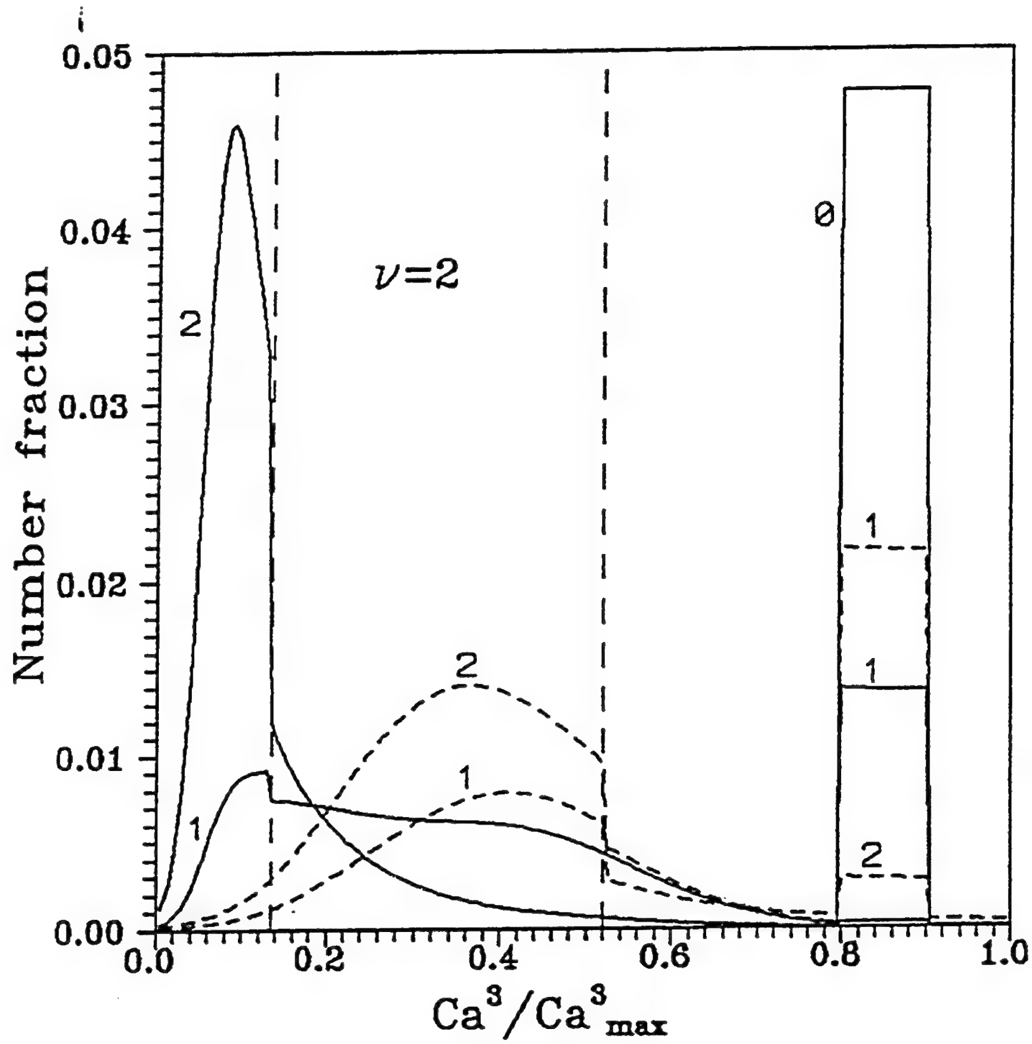

Fig.8. Evolution of the size distribution functions from nonuniform distribution for the stepwise mechanism of breakup, ν =2: 1. t = 20 s, 2. t = 100 s. Solid lines correspond to $\lambda = 2 \cdot 10^{-3}$, dashed lines to $\lambda = 10^{-3}$.

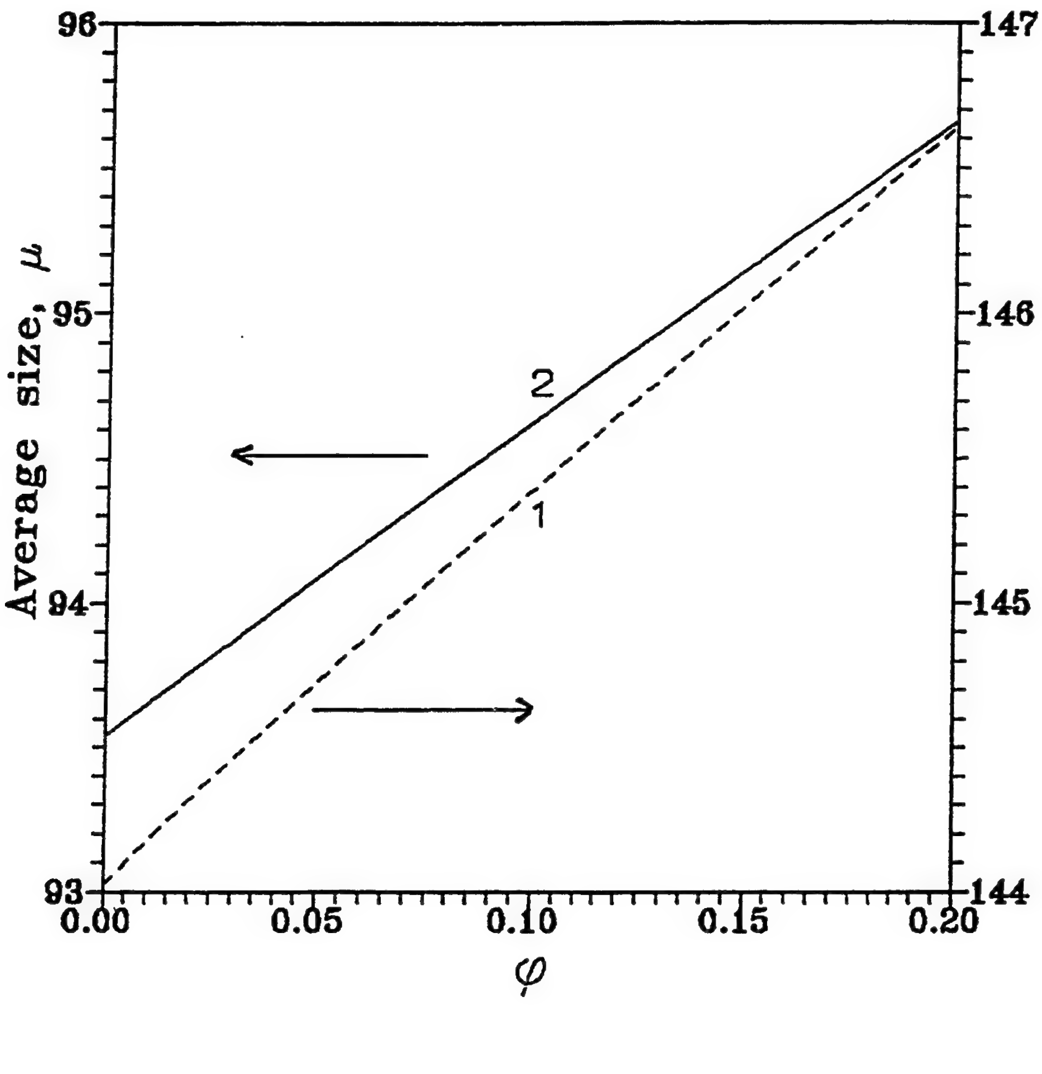

Figure 9. The dependence of the average drop size on the volume concentration of the dispersed phase for the stepwise mechanism of breakup at t = 150 s: 1. $\lambda = 10^{-3}$, 2. $\lambda = 2 \cdot 10^{-3}$.

IV.A.9 Theoretical Modeling to Improve Adhesion and Strengthening of Polymer Blends.

Principal Investigator: Professor A.C. Balazs
Materials Science and Engineering Dept.
University of Pittsburgh

Other Faculty Participants: Dr. E. Zhulina
Visiting Research Professor

Student: Dr. N. Gross
Materials Science and Engineering Dept.
University of Pittsburgh

IV.A.9.1 INTRODUCTION

The aim of our previous research was: 1) to determine the effect of molecular architecture on the effectiveness of copolymer compatibilizers and 2) to design polymer films that provide a protective coating on solid substrates. Copolymers additives, or "compatibilizers", enhance the structural integrity of polymer blends by localizing at the interface between the immiscible polymers, lowering the interfacial tension and "gluing" the phases together. Our studies allowed us to isolate the copolymer architectures that yield the optimal interfacial behavior. Our second goal involved pinpointing the factors that control the conformation of chains adsorbed or tethered on a surface. Through these studies, we established guidelines for creating self-healing coatings, as well as patterned films for opto-electronic applications. Below, we summarize the findings from this research.

IV.A.9.2 ACCOMPLISHMENTS AND SIGNIFICANCE

To accomplish the first aim, we used theoretical models and computer simulations to determine the optimal copolymer architecture for reducing the interfacial tension, γ, between immiscible homopolymers A and B[1]. We first compared the interfacial behavior of the different linear chains, namely random, diblock and alternating copolymers. We then contrasted the properties of these linear chains to the interfacial behavior of star and comb copolymers. At fixed molecular weight, the diblock copolymers are the most efficient at reducing γ. However, when we compared random and comb copolymers with diblocks at different molecular weights, we observed that the longer random or comb copolymers are more efficient than short diblocks. Since the random and comb copolymers are substantially less expensive to synthesize than the diblocks, the results can have a significant technological and economic impact. Overall, these studies allow us to predict the reduction in interfacial tension produced by a wide variety of copolymers and thereby, permit a rational design of cost-effective and efficient compatibilizers.

Our research also involved designing protective polymer coatings. One method of providing a protective coating is to chemically tether polymer chains onto the surface. When chains are tethered or grafted onto a surface, the system is referred to as a polymer "brush". Actual surfaces may contain imperfections, such as holes, pits and pores. In order to establish guidelines for coating these more realistic surfaces, we determined the behavior of chains that are: 1) grafted onto a planar stripe of finite width, and 2) tethered around a circular pore[2].

When these brushes are immersed in a poor solvent, the chains associate into a variety of complexes that can effectively cover the pores and "repair" the surface. By calculating the free energy of these complexes, we determined how their size scales with chain length, solvent quality, grafting density and the dimensions of the substrate. We also constructed a "phase diagram" for the possible morphologies that can occur in these systems. We used Monte Carlo simulations to visualize the structure of the associated complexes and test our predictions from the analytical theory. The results reveal how to design "self-healing" coatings. The findings also reveal how tethered chains can be used to regulate the flow of molecules through the substrate and thereby control the permeability of the system.

Polymer brushes can also be tailored to form thin films that contain well-defined structures or patterns. These patterned films are particularly useful in a variety of opto-electronic devices. A current technological goal is to gain control over the size and features of such polymer films. By taking advantage of the molecular weight, chemical composition and the phase behavior of the grafted chains, one can design coatings that contain lateral patterns with the desired dimensions. Recently, we determined the patterns that form when Y shaped AB copolymers are grafted onto a flat surface[3]. One "arm" of the Y is an A homopolymer, the other arm is an incompatible B chain and the short "stem" tethers the entire copolymer to the surface. We used scaling theories to investigate the behavior of the brush formed from these chains in the melt regime and in the presence of a solvent. In particular, we determined how solvent quality, grafting density, and chain length affect the structure of the grafted layer. We then calculated a phase diagram that delineates the regions where the different structures appear. The diagram reveals that variations in the solvent quality give rise to a rich variety of lateral structures. Specifically, in poor solvents and in the case where the Flory-Huggins interaction parameter between the A and B chains, χ_{AB} is approximately zero, the chains form "pinned micelles" similar to those formed by homopolymers (see Figure 1). Introducing an effective A-B repulsion (by setting $\chi_{AB} > 0$), however, causes significant structural changes. The micelles split into two separate micelles, each composed of pure A or B. Within the grafted layer, the chains rearrange so that A blocks associate with neighboring A's and the B blocks aggregate with neighboring B's. In effect, the layer now self-assembles into a checkerboard pattern. The results of this study provide guidelines for fabricating patterned or highly ordered thin films.

Novel morphologies are also observed when AB diblocks are tethered to a surface[4,5]. Here, we set $\chi_{AB} = 0$ and assume the surrounding solution to be poor solvent for both components. The blocks, however, have different affinities toward the solvent. For example, we consider the host fluid to be a poorer solvent for B than for A. Furthermore, the chains are tethered to the surface through this B block. In this case, the block copolymers associate into "onion" structures, where the less soluble components (the B's) form the inner core and the more soluble components (the A's) form the outer layer. The chains adopt this conformation since it minimizes the surface tensions within the system. Grafting such diblocks uniformly on the surface (and exposing the layer to a poor solvent) will yield an ordered array of onions on the substrate. The size and separation between the onions can be altered by varying the molecular weight of the A and B blocks.

An effective means of binding two surfaces is to coat each with a polymer layer and bring the coated surfaces into contact. The polymers form bridges that extend from one surface to the other and thus, provide the necessary adhesion. We recently used a self-consistent field (SCF)

theory and scaling arguments to determine the behavior of homopolymers that bridge two parallel surfaces[6]. Here, one end of each chain is tethered to surface 1 and the other end is tethered to surface 2. We determined the behavior of these chains when the system was immersed in a poor solvent. For a finite range of surface separations, the polymers form pinned micelles that are preferentially located on one surface. While the tethering segments (at surface 2) are relatively stretched, this conformation is energetically favorable because the polymers on the surface avoid contact with the solvent. As the surface separation is increased further, the cost of stretching the chains increases and finally exceeds the gain in energy associated with having the micelles adsorbed on the wall. At this point, there is a discontinuous "jump" of the micelles to the center of the gap. This "jumping" is a discontinuous transition and in the limit of long chains constitutes a first-order phase transition. The transit ion also leads to a discontinuous change in the size of the pinned micelles.

The aim of our future research is to develop guidelines for controlling the microstructure of a polymer mixture and consequently, the overall strength of the composite. To this end, we will determine quantitative relationships among: the architecture of the compatibilizers, the reduction in interfacial tension brought about by this additive, the size and shape of the domains that are formed, and the overall mechanical properties of the blend. We will also determine how shear and other flows affect the domain size and morphology.

IV.A.9.3 SUMMARY

In summary, we compared the behavior of various AB copolymers at the interface between two immiscible homopolymers, A and B. Our findings indicate that these theoretical methods can be used to predict the efficiency of a large class of compatibilizers and therefore, can provide guidelines for fabricating high-strength polymer blends.

Through our studies on brushes, we determined the scaling behavior for the micelles and other structures that form when chains are tethered to finite regions on a substrate and are surrounded by a poor solvent. The studies are particularly relevant in the case where the substrate is a porous membrane or film. Our results reveal the conditions under which the grafted chains can cover a pore or expose an opening. Thus, the findings provide guidelines for tailoring the permeability of the system.

If the tethered chains form regular, distinct patterns on the substrate, the surfaces can be utilized to create novel opto-electronic devices, or efficient micro "reaction vessels". We isolated conditions that drive polymers to form patterned films on solid surfaces and determined how varying the molecular structure or chemical environment affects the formation, size and shape of the patterns within the film. Through these studies, we established guidelines for tailoring the structure of the copolymer and the substrate to yield the desired interfacial characteristics. The results facilitate the development of films for: optical modulators, anti-fouling membranes, selective filtration systems, and sensors.

In the final study, we isolated a novel phase transition for polymers restricted between two surfaces and immersed in a poor solvent. The properties of these tethered polymers change dramatically as a function of the separation between the surfaces. The abrupt changes should be experimentally accessible, for example, by the chemical forces apparatus. The changes in

polymer density with surface separation will also lead to changes in the index of refraction or viscosity of the fluid. Thus, the system can be used to modulate the propagation of light in the medium or control the diffusion rate of particles through slits and channels. Though some hysteresis may be inevitable in actual systems, one can cycle back and forth between these states. Due to this distinctive change in morphology, the entire assembly could be used as a force sensor, altering the nature of a signal that passes through the layer when the confining surfaces change their separation.

IV.A.9.4 REFERENCES

1. Lyatskaya, Y., Gersappe, D., Gross, N. and Balazs, A. C., "Designing Compatibilizers to Reduce Interfacial Tension in Polymer Blends", J. Phys. Chem., 100 (1996) 1449.
2. Gross, N., Zhulina, E. and Balazs, A. C., "The Behavior of Grafted Polymers in Restricted Geometries Under Poor Solvent Conditions", J. Chem. Phys., 104 (1996) 727.
3. Zhulina, E. and Balazs, A. C., "Designing Patterned Surfaces By Grafting Y-Shaped Copolymers", Macromolecules 29 (1996) 2667.
4. Zhulina, E., Singh, C.and Balazs, A. C., "Forming Patterned Films with Tethered Diblock Copolymers", Macromolecules, in press.
5. Zhulina, E., Singh, C.and Balazs, A. C., "Tethered Diblock Copolymers in Selective Solvents", submitted, Macromolecules.
6. Singh, C., Zhulina, E. Gersappe, D, Pickett, G.and Balazs, A. C., "A "Jumping Micelle" Phase Transition", submitted, Macromolecules.

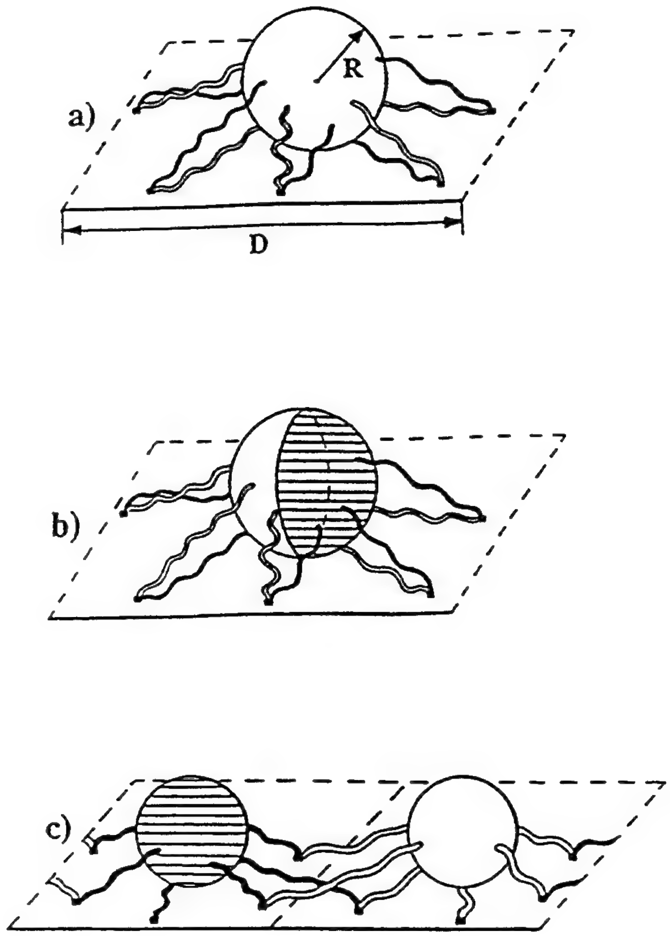

Figure 1. Schematic drawings of pinned micelles formed by Y-shaped block copolymers. In **(a)**, χ_{AB} is zero and the blocks are homogeneously distributed within the micelle. In **(b)**, $\chi_{AB} > 0$ and the blocks are weekly incompatible. In this case, the A and B blocks extend away from each other and we have "internally segregated micelles". Here, the blank hemisphere represents the A region, while the hashed area represents the B domain. In **(c)**, χ_{AB} is sufficiently large that the blocks are highly incompatible. The original micelle phase-separates into two smaller micelles and we refer to this structure as a "split micelle". E. Zhulina and A. C. Balazs, Macro 29 (1996) 2667.

IV.A.10 Measurement of Residual Stresses in Films

Principal Investigator:	Professor J.R. Blachère Materials Science and Engineering University of Pittsburgh
Other Faculty Participants:	Professor G.H. Meier Materials Science and Engineering University of Pittsburgh
Student:	Mr. C. Sarioglu

IV.A.10.1 INTRODUCTION

Residual stresses play a major role in most applications of materials, ceramics, polymers, metals and particularly composites. These stresses develop during processing and finishing of components and may dramatically affect their life. This is the case, for instance, of stresses induced in welds of metals and ceramics[1]. Residual stresses promote corrosion and fatigue. The "traditional" effects of residual stresses are extensively documented in the literature[2-3]. Residual stresses can also dramatically decrease or increase the mechanical properties of ceramics in bulk or as films (coatings). In advanced materials this is particularly obvious as protective films will deteriorate in service due to residual stresses or may be enhanced with the appropriate stress level and distribution[4]. Optoelectronic industries depend on thin film technologies. Much evidence suggests that residual stresses are invariably present in the films and that they have a critical influence on the mechanical, electrical and optical properties and the reliability of optoelectronic devices[5].

The measurement of residual stresses in materials is critical in applications of materials which are at the heart of Materials Engineering. Of many methods of measurement of residual stresses, X-ray diffraction (XRD) is non destructive, most versatile and universally used[6,7]. However it requires high precision and experience. The objectives of this project were to develop at the University of Pittsburgh expertise in the measurement of stresses by X-ray diffraction. This research emphasizes the measurement of residual stresses in films and their substrates, e.g. in scales formed by oxidation of superalloys and sputtered films. A new method was developed to measure in-situ the growth stresses of oxides with hexagonal structures. It is having a major impact on the understanding high temperature oxidation of superalloys.

IV.A.10.2 BACKGROUND

The regions of a sample accessible for stress measurement by XRD are controlled by the X-ray penetration and will not exceed tens of micrometers. It can be reduced by thin film diffraction to tens of nanometers.

In the materials and the X-ray literature a distinction is made between macrostresses and microstresses[8]. Macrostresses are assumed to vary over macroscopic distances, i.e. distances much greater than the grain size. They are balanced across interfaces such as that between a film

and its substrate. They are typically thermal stresses. Microstresses are residual stresses which change magnitude and/or sign over lengths of the order of the grain size. These stresses are associated with processes such as film growth, phase transformations, precipitation, etc. Usually, microstresses cannot be measured "individually" by XRD since they are often intrinsic to the layer and balanced within the layer. However they may contribute an average "pseudomacrostress" to the residual stress measured by XRD.

The stress normal to the free surface of a film is usually assumed to be zero. Neglecting shear stresses, the resulting biaxial stress can be expressed quite simply for an isotropic elastic medium[8,9] or more generally, as described by Noyan and Cohen[10]. In any case the quantities measured are strains which can be measured by XRD as a change in lattice spacing with inclination with respect to the surface of the sample. This strain is usually expressed[10], referring to Figure 1, as:

$$(\epsilon_3)_{\phi\psi} = \frac{d_{\phi\psi} - d_o}{d_o} \tag{1}$$

in which d_o is the lattice spacing of the selected (hkl) planes parallel to the surface and $d_{\phi\Psi}$ is the lattice spacing of these (hkl) planes normal to OB. With the coordinates of Figure 1 it can be shown that this strain is expected to be proportional to $\sin^2 \Psi$. For a biaxial stress in the irradiated layer, the previous equation can be expressed as[10]:

$$\frac{d_{\phi\psi} - d_o}{d_o} = \frac{1+\nu}{E} \sigma_\phi \sin^2 \psi - \frac{\nu}{E} (\sigma_1 + \sigma_2) \tag{2}$$

If the $\sin^2 \Psi$ curve is linear, as is expected from an isotropic surface layer which is polycrystalline and not textured, the stress in any direction ϕ can be calculated from E, ν, and d_o. It is measured as the slope of the $\sin^2 \Psi$ vs d line. This is the well known $\sin^2 \Psi$ method. Often the lattice constant at $\Psi=0$ is substituted for the unstrained value, with little error since it is in the denominator of the expression for the strain.

There may be a number of complications which result in non linear plots such as the presence of shear stresses, which results in splitting of the plots generated by positive and negative tilts. In other cases the $\sin^2 \Psi$ plots have oscillations. For textured materials, the X-ray elastic constants must be used, they can be calculated approximately or determined experimentally[10]. Another possible complication is the existence of stress gradients normal to the surface of the sample which result in bending of the $\sin^2 \Psi$ plot.

IV.A.10.3 ACCOMPLISHMENTS AND SIGNIFICANCE

The dual arm and parallel beam collimator accessories for the XRD powder machines have been purchased and installed early in this program. They are a key to the use of the powder machine for this research while maintaining reasonable availability for other research in the Department and the University.

Capabilities have been developed in four XRD stress measurement methods. These methods are the classical tilt and rocking techniques, which are equivalent and are based on the

determination of the $\sin^2 \Psi$ curves. In the third method, the tilting method has been extended to thinner films by the use of fixed low incidence techniques. An XRD machine with an open eulerian cradle provides the tilting of the specimen in symmetrical diffraction ("classical" method) or asymmetric diffraction with fixed low incidence. The rocking technique is performed on the powder machine. The powder machine and the dual arm are also used with a hot stage.

The design of the powder machine and the hot stage make it desirable that the specimen be nearly horizontal during the high temperature experiments. For this purpose a new fixed (low) incidence XRD technique, the fixed incidence multiplane method (FIM), using more than one set of (hkl) planes has been developed. Usually for residual stress measurements, one {hkl} plane is tilted (or rocked) in order to measure the strain at various angles to the surface. With fixed incidence and a fixed specimen, diffraction occurs for different sets of {hkl} planes with different inclinations with respect to the surface thus providing the equivalent of the tilting or rocking in the other methods.

For the $\sin^2 \Psi$ interpretation of the results of this new method, of fixed incidence on a fixed specimen, the strains obtained for different planes are plotted on one line. This is simple for films having cubic structures assuming that they are elastically isotropic. However most cubic structures are not elastically isotropic and many films of technological interest such as the alumina and chromia scales, of concern here, are hexagonal and not isotropic. However this is resolved by the selection of {hk0} planes for the stress measurements since $(1+\nu)/E = 1/2S_2(hkl)$ and $S_2(hk0) = 2s_{11} - s_{12} - s_{13}$ for hexagonal crystals according to the Reuss model[11].

The preferred method at room temperature is the tilting method. It has been found that when planes such as the (1,0,10) plane of alumina are used the anisotropy can be corrected using the well established single crystal elastic constants of alpha alumina in the Reuss average[12]. The Reuss average was selected because it was found to be a better approximation for thin layers[13]. The alumina scales have very weak preferred orientations (textures), although they have columnar structures, and it has not been found necessary to correct for the texture of the scales. An example of data measured on FeCrAl oxidized for 72 hours is given in Figure 2[12]. The reproducibility of the data is demonstrated for two orientations of ϕ, 0 and 90°, on the surface of the scale. For both orientations, the points of Figure 2 associated with corresponding positive and negative values of Ψ are superposed. The magnitude of the compressive stress in the scale parallel to the surface is $^{-}$4400 MPa.

The four methods have been tested at room temperature and shown to give equivalent results. They have already been used for the measurement of residual stresses in chromia and alumina scales. The room temperature data are well behaved i.e. the $\sin^2 \Psi$ plots are good straight lines with no splitting or oscillation. These results have been presented and accepted for publication[12,14]. Results for alumina scales on FeCrAl alloys are in close agreement for the calculated residual stresses with data obtained in Stuttgart by laser fluorescence[14]. The implications of these results for the materials science and technology of superalloys has been discussed in Section IV.A.1 written by G.H. Meier. D.R. Clarke[16]reported very large stress gradients in alumina scales on FeCrAl obtained by laser fluorescence measurements. The Stuttgart group reports smaller gradients. The sensitivity of the XRD method to stress gradients was considered. It appears that agreement is being reached that stress gradients are fairly small, if any, in the scales under study.

Significant results have been obtained in measurements of residual stresses in oxide scales at room temperature. The ultimate objective of this research was to measure the stresses in the FeCrAl scales at high temperatures, particularly at oxidation temperatures of the order 1100°C, since the thermal stresses are generated on cooling and thus the growth stresses can be measured directly. This is of great interest for the understanding of oxidation. The growth stresses usually obtained indirectly give contradictory results. Measurements in the hot stage were presented in Cambridge in September[17].

In-situ measurements of growth stresses have been performed on FeCrAl with and without additions of Ti and Y. The measurements are made by the fixed incidence multiplane technique developed in this project at temperatures of 1000° or 1100°C. Results are shown for the in-situ oxidation of the FeCrAlY (Fig. 3). The growth stresses measured are compressive and large (-1400 MPa at 1100 C). This number is in agreement with the growth stresses calculated from the measured residual stresses and the thermal stresses calculated from the thermal expansions of the substrate and oxide[16]. For undoped FeCrAl the growth stresses are a little smaller but still sizable. The high temperature measurements are usually made using 3 sets of (hkl) planes. However, in recent studies of the evolution of growth stress as a function of time only two sets of planes are used to minimize the time it takes to get the data. In all cases the $\sin^2 \Psi$ method is still used, thus, not requiring additional assumptions about d_o.

A close review of the sources of uncertainty in the measurements has been performed with emphasis on the mutiplane technique. As a result some procedural improvements have been made. In-situ stress measurements can be reproduced within ±200MPa. A new calibration method is under study.

These measurements of growth stresses have made a significant contribution to the field of oxidation of metals as recognized recently at the "Miniworkshop on Stresses in Oxide Films/Scales" organized by DOE in February 1997[18]. Participation was on invitation only of major contributors to the field. J.R.Blachère made the presentation on the measurement of stresses by XRD. One conclusion of the workshop was that growth stresses were significant in magnitude as established in great part by this work.

While the goals of this project have been met amply, this research is continuing with a study of the evolution of stress in the alumina scales in-situ as function of time and as the temperature is lowered. It is too early to make definitive statements about the results except that the mutiplane method optimized for these measurements is generating reliable results.

While the oxide scales under study have weak textures, the sputtered cobalt alloy films under investigation for the next generation of hard drive magnetic media are so heavily textured that the XRD peaks can be followed only over tilts of 10 to 20 degrees. As a result, the tilt method is impractical. The experimental problem is compounded by the thickness of the films of the order of 20-40nm. The strains generated in these films has been compared by measurements of the change in lattice parameter of the alloys. This was performed by the low incidence parallel beam diffraction method with incidences of the order of 0.4 degrees. The results have been correlated with magnetic data[19]. No particular difficulty is encountered in the measurement of stresses in the underlayer which is thicker. Measurements have been performed recently in FeTaN films for magnetic heads. There are no particular difficulties since the films are thick

(about 0.5 μm) and not very textured so that the tilting technique can be used. A new approach based on the multiplane method is under consideration for the very thin Co alloys for magnetic media. However a difficulty remains with the correction for the very strong texture of the film. This is under study.

IV.A.10.4 SUMMARY

Outstanding capabilities have been developed for the measurement of residual and growth stresses in materials by XRD. Expertise has grown rapidly over the past two years and significant contributions are being made to the field of oxidation. Our laboratory is beginning to be recognized as a major contributor in the field of stress measurement in films and scales.

IV.A.10.5 REFERENCES

1. P.J. Yvon et al, Effects of the Metal Workpiece Properties on the Residual Stresses in Silicon Nitride-Metal Brazed Joints" Submitted to Mat. Sci. and Eng. 12/1994.
2. V. Hauk et al, Residual Stresses: Measurement Calculation, Evaluation, DGM 1991.
3. E. Macherauch and U. Wolfstieg, "Recent German Activities in the Field of X-ray Stress Analysis" Mat. Sci. Eng. 30 (1977) 1-13.
4. B.L. Ballard and P.K.Predecki, "Stress-Depth Profiles in Magnetosputtered Mo Films Using Grazing Incidence X-ray Diffraction (GIXD)", Adv. X-ray Anal. 37,189-196 (1994).
5. K. Inoda et al, Stress-induced Grain Boundary Fractures in Al-Si Interconnects", J. Vac. Sci. Technl. B., 5 (2): 518 (1989).
6. B.D. Cullity, Elements of X-ray Diffraction, 2nd ed.,Addison-Wesley, 1978.
7. B.D. Cullity, "Some Problems in X-ray Stress Measurements" Advances in X-ray Analysis, 20, 259-271, 1976.
8. I.C. Noyan, "Defining Residual stresses in Thin Film Structures", Advances in X-ray Analysis, 35A, 461-473, 1991.
9. De Buyser, P. Van Houtte, E.Aernoudt " X-ray Measurement of Residual Stresses in Thin Layers" in Ref.1 27-32.
10. I.C. Noyan and J.B. Cohen, Residual Stress, Springer-Verlag, 1987.
11. P. Van Houtte and L. De Buyser,"The Influence of Crystallographic Texture on Diffraction Measurements of Residual Stress", Acta Metall. Mater. 41 [2] 323-336, 1993.
12. C. Sarioglu, J.R. Blachère, F.S. Pettit, G.H. Meier, J.L. Smialek, and C. Monnicke, "The Effects of Reactive Element Additions, Sulfur Removal, and Specimen Thickness on The Oxidation Behavior of Alumina-Forming Ni and Fe-base Alloys", 4th International Symposium on High Temperature Corrosion and Protection of Materials, Les Embiez, France, May 1996, Proceedings in press in Materials Science Forum.
13. W. Serruys et al, "Calculation of X-Ray Elastic Constants in Isotropic and Textured Materials", Int. Conf. on Residual Stress, ICRS2, Nancy, France, Nov.1988.
14. C. Sarioglu, C. Stinner, J.R. Blachère, N. Birks, F.S. Pettit, G.H. Meier and J.L. Smialek, "The Control of Sulfur Content in Ni-base Single Crystal Superalloys and its Effects on Cyclic Oxidation Resistance". International Symposium on Superalloys Conference Proceedings, 1996 (in press).
15. Specimens measured at the Max Planck Institute in Stuttgart were measured at the University of Pittsburgh in order to compare the two methods on the same samples.

16. D.M. Lipskin and D.R. Clarke, "Measurement of the Stress in Oxide Scales Formed by Oxidation of Alumina-Forming Alloys", Oxidation of Metals 45, 3/4, 267-280,1993.
17. C. Sarioglu, J.R. Blachère, F.S. Pettit and G.H. Meier, "Room Temperature and In-Situ High Temperature Strain or Stress Measurement by XRD Technique", "Microscopy of Oxidation 3", in press.
18. P.F. Tortorelli, "Miniworkshop on Stresses in Oxide Films/Scales", Orlando Feb.1997.
19. B. Zhang, W.R. Bennett, C. Gao, G.C. Ranch and J.R. Blachère, "CoCrTa/CoCrPtTa Double-Layer Films for Magnetic Recording", Intermag '96 in

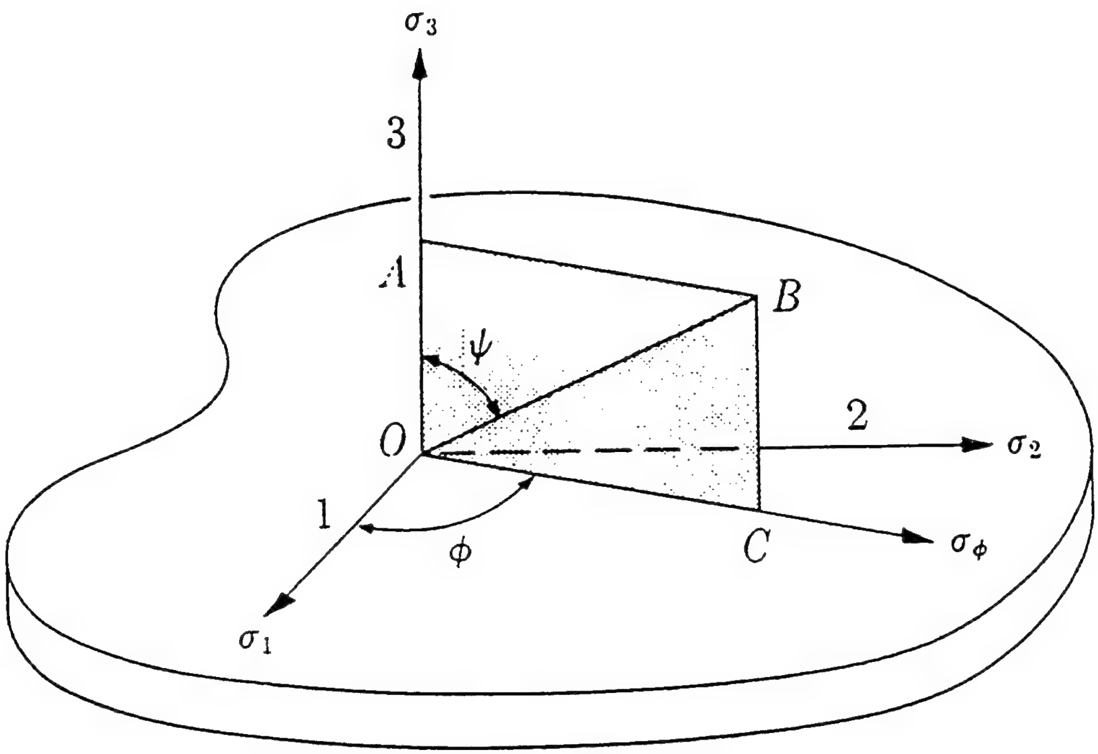

Figure 1. Stresses at the surface of a stressed body (σ_3=0). The stress to be measured is σ_ϕ (after ref. 2).

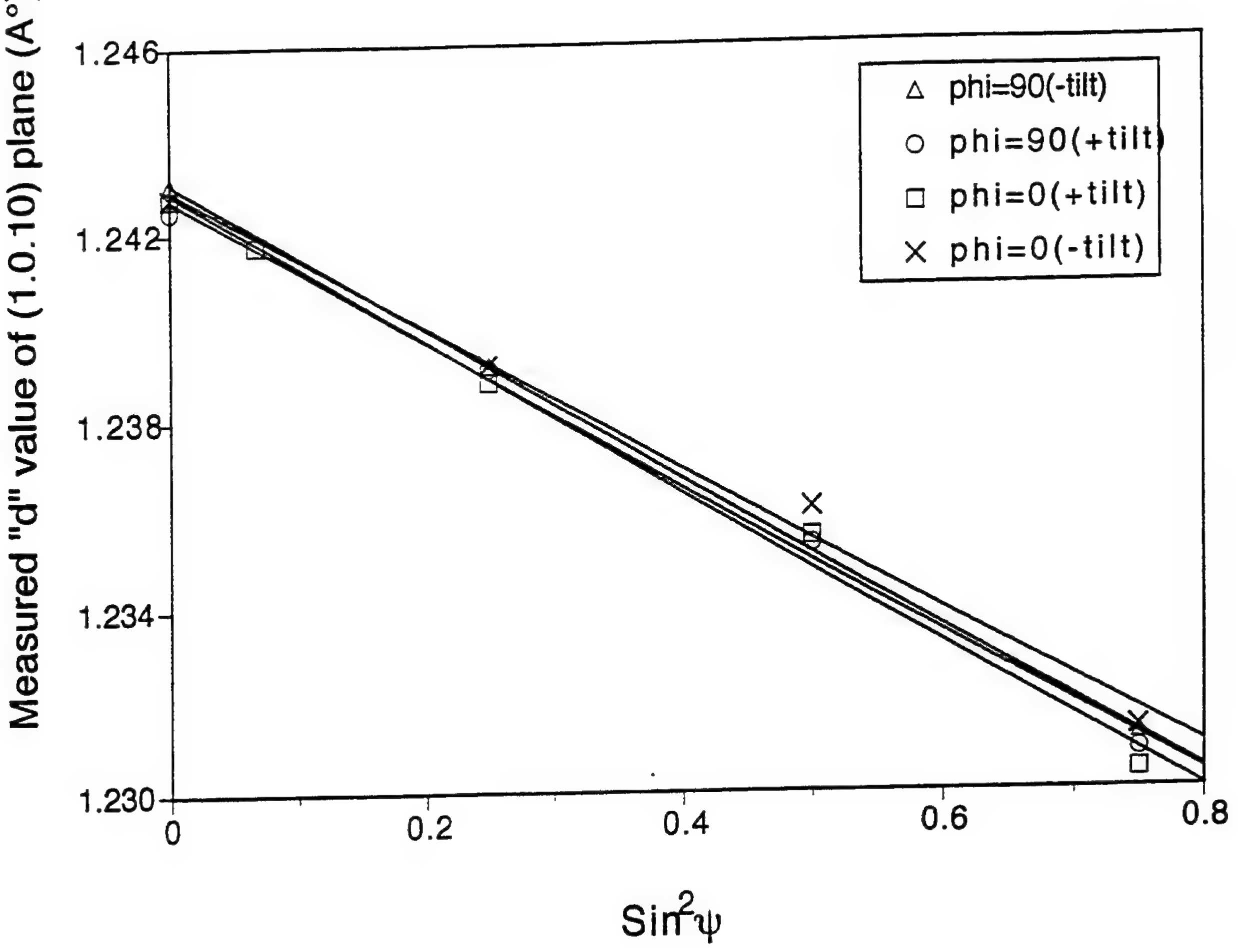

Figure 2 Sin^2 Ψ plot of d-spacings measured for the (1,0,10) plane of α-alumina scale on FeCrAl with Ti additive oxidized for 72 hours at 1100°C.

Figure 3. Residual (growth) stresses in alumina scale formed on FeCrAlY at 1100 °C in air for 375 minutes

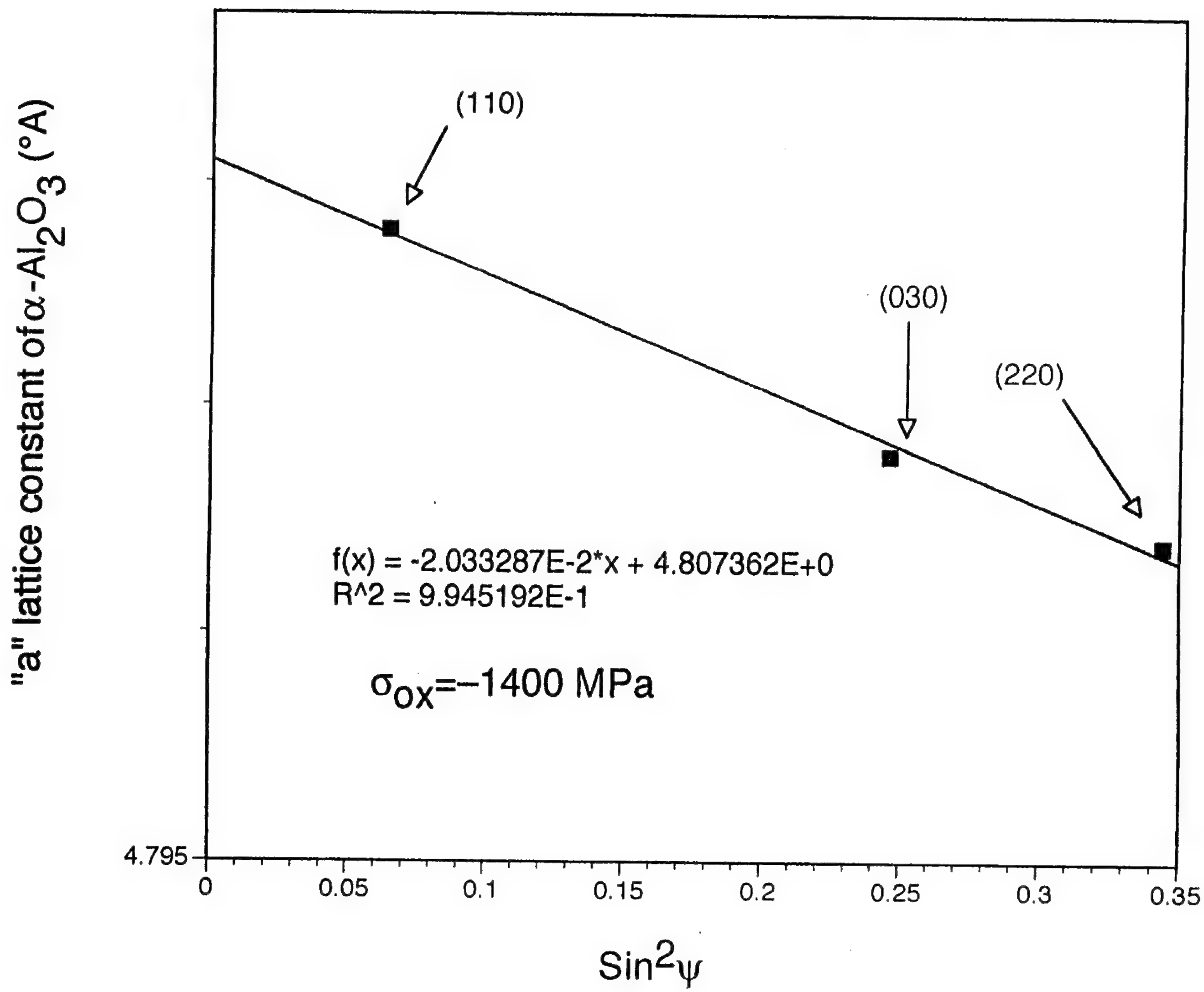

IV.A.11 A Study of the Effect of Two-Phase Flow on the Solidification of Alloys and Composites

Principal Investigator: Professor R. A. Stoehr
Materials Science and Engineering Department
University of Pittsburgh

Students: Mr. C. Loyprasert
Mr. U. Akdas

IV.A.11.1 INTRODUCTION

Segregation on both the microscale and macroscale commonly occurs during the casting and solidification of metals, and it usually results in reduced performance of the product. Segregation results from relative motion of the liquid and solid phases during solidification. Such relative motion may be due to differences in density, surface tension, rejection of solute from the growing solid phase, or the feeding of shrinkage.

Modeling, both computer and physical modeling, of metal casting has reached a high level of maturity in the areas of heat transfer, fluid flow, and solidification kinetics. Computer modeling is the basis for widely used CAD systems for castings. Older CAD systems simply predicted solidification times and whether a casting could be produced free of voids and cracks. Now the objective is to predict segregation, microstructure, and properties of the casting. This is turning the attention of the modeling community to two phase and multiple phase flow. Such flow is responsible for macrosegregation in all types of castings; ingots, continuous castings, and foundry castings. Understanding it is also extremely important if we are to improve some of the newer materials processes, including metal matrix composite casting (e.g., Duralcan, an aluminum alloy/silicon carbide cast composite), rheocasting, slush casting, and metal powder injection molding.

The objective of the current research is to determine the effect of forced fluid flow during the solidification of multiphase materials and to contribute to the development of modeling systems that can predict the development of segregation in metal castings and in cast composites.

IV.A.11.2 ACCOMPLISHMENTS AND SIGNIFICANCE

This research is being conducted to evaluate the effect of two phase flow during solidification on the development of segregation in cast materials. Experiments have been performed using Duralcan[1] - a cast composite material containing 20% SiC particles in a matrix of Aluminum Alloy F3S (9.0%Si-0.5%Mg) - as a model system. This work was performed as the M.S. thesis of Umar Akdas[1]. Similar experiments are being performed on Aluminum Alloy A356 (Al-7.5%Si-0.3%Mg) without reinforcing particles, but these tests have not been completed at the time of this report.

[1]Duralcan is a trademark of the Aluminum Company of Canada. Appreciation is expressed to them for supplying the material used in these experiments free of charge to the University of Pittsburgh.

The effect of fluid flow during solidification was evaluated using several different mold configurations with concentric rotating probes. Diagrams of the experimental apparatus and of the mold/probe sets are shown in Figures 1(a) through 1(c). The molds and probes have been machined from steel, and they are coated with colloidal graphite before casting each specimen to simulate the practice commonly used in the production of permanent mold castings.

By conducting the basic experiments in the cylinder and cone molds with the concentric rotating probes it is possible to control the relative influence of gravity and centrifugal forces and to observe the effect of particle pushing by the advancing solid interface. Rotational speeds were varied from 0 to 360 RPM. Specimens were also produced without inserting the probe, that is, as normal open top castings.

Segregation of the SiC particles was observed on both the microscale and macroscale. Microscale segregation consisted of exclusion of the SiC particles from the primary alpha-aluminum dendrites as shown in Figures 2 and 3. This segregation occurred in specimens made both with and without rotation of the probe. The effect is consistent with the theory and previous observations of previous investigators.

Macroscale segregation was more specifically influenced by rotational speed of the probe At lower speeds, gravity dominated and at higher speeds, the rotational effects became more important. The least macrosegregation of the SiC particles was observed at the intermediate rotational speed of 100 RPM. Macrosegregation of the SiC particles can be seen in the micrographs in Figures 2 and 3 taken from the specimens prepared at 20 RPM and 200 RPM respectively. Quantitative metallography performed with an Olympus PMG-3 light microscope interfaced with a Leco 2001 image analysis system was used to determine the area percentages of SiC particles and of distinct silicon grains. These values were recorded as a function of position in the specimens. In Figures 4 and 5, these values are plotted on three dimensional graphs wherein the horizontal axes are the relative radial position (R/R_0) and the relative vertical position (Z/Z_0). The area percentage of SiC or Si is the vertical axis. These show that in the specimen prepared at 20 RPM the higher density SiC particles are segregated toward the bottom (low values of Z/Z_0) while the lower density silicon grains segregate toward the top (Z/Z_0 near unity) of the specimen. At 200 RPM this vertical segregation is shown to be less severe. At 200 RPM the region near the outer periphery (R/R_0 near unity) and top (Z/Z_0 near unity) has a very high concentration of silicon grains but is denuded of SiC particles. These segregation patterns could be expected from the difference in density of the SiC (ρ = 3.25 g/cm^3), the aluminum alloy matrix (ρ = 2.65 g/cm^3), and the silicon (ρ = 2.4 g/cm^3).

A large number of blocky silicon grains were observed in the region at the outer edge of the rotating probe (R/R_0 and Z/Z_0 near unity). This is shown more clearly in the scanning electron micrographs found in Figure 6. The silicon grains were nearly the same size (approximately 25μm) as the SiC particles. Figure 6 (a) shows silicon grains apparently forming on the SiC particles, while 6 (b) taken from the region between the rotating probe and the wall of the mold shows large detached silicon grains and almost no SiC. The composition of the matrix alloy (9.0% Si) is considerably hypoeutectic, the binary eutectic composition being 11.6% Si. If this alloy is cast without the SiC particles, the silicon phase usually precipitates as thin platelets in the interdendritic regions unless the alloy is modified by the addition of strontium or sodium shortly before casting. Modification alters the interfacial energies and results in

globular silicon. As the primary aluminum rich solid phase forms, the remaining silicon rich liquid would rise to the outer edge of the rotating disk probe. Since it is known that considerable supersaturation is required before the silicon phase will precipitate in the unmodified alloy, this region may reach a hypereutectic composition before solidification begins. Then the silicon phase could precipitate in the blocky form observed in these micrographs

IV.A.11.3 SUMMARY

Experimental data has been collected on the influence of fluid flow on the development of segregation in multiphase metal castings. This data shows that forced flows can result in changed segregation patterns, especially when the phases have considerable differences in density as is true in the aluminum alloy/silicon carbide cast composite material (Duralcan). The experiments with the rotating probe showed that segregation was minimized at intermediate forced convection (100 RPM in these experiments), leading to the conclusion that there will be an optimum mold filling speed for these materials. It also shows that the resulting morphology of the solidifying phases may be altered by the interaction of the reinforcing particles and the flow of the liquid metal.

Next this research must correlate this data with the computer models of fluid flow in castings, so that systems can be developed that will predict when and where segregation might occur in castings. Then systems can be developed that will allow the control of flow during the production of castings so that unwanted segregation can be avoided.

IV.A.11.4 REFERENCES

1. Akdas, Umar Needat, *The Effect of Fluid Flow on Segregation of Aluminum-Silicon Carbide Particle Composites,* M.S. Thesis, University of Pittsburgh, 1997.

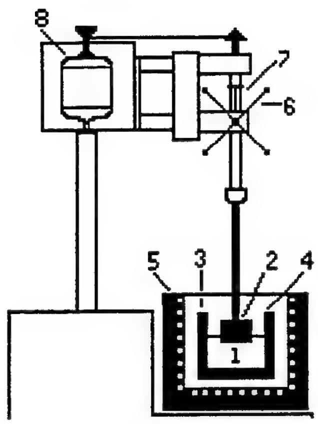

1. Melt
2. Rotating Probe
3. Mold
4. Resistance Furnace
5. Chuck
6. Vertical Position Control
7. Vertical Position Caliper
8. Variable Speed Motor

(a) General schematic drawing of furnace and press

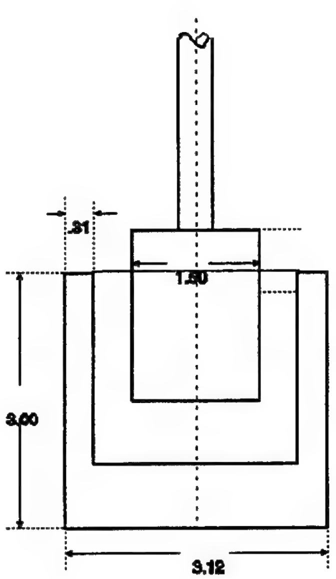

(b) Concentric cylindrical mold and rotating probe. (Dimensions are inches)

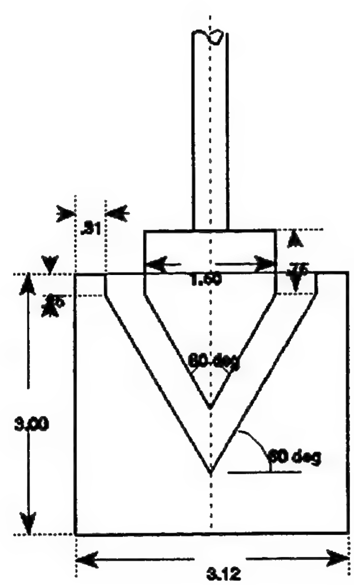

(c) Drawing of cone shaped mold with concentric rotating probe.

Figure 1. Experimental setup for controlled fluid flow during the solidification of multiphase alloys and composites.

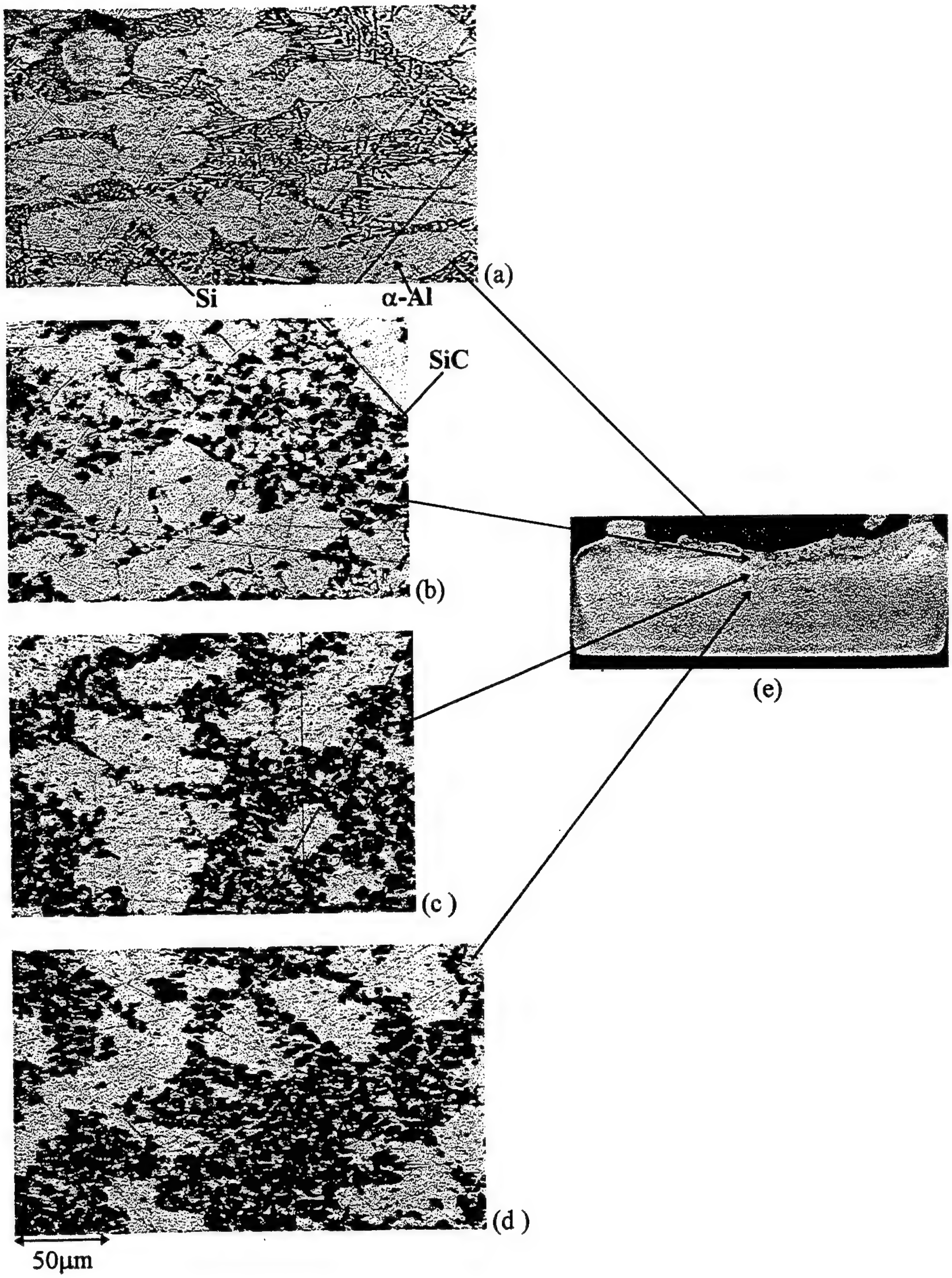

Figure 2. Micrographs from the aluminum alloy/silicon carbide composite material cast in the cylindrical mold with the concentric probe rotating at 20 RPM.

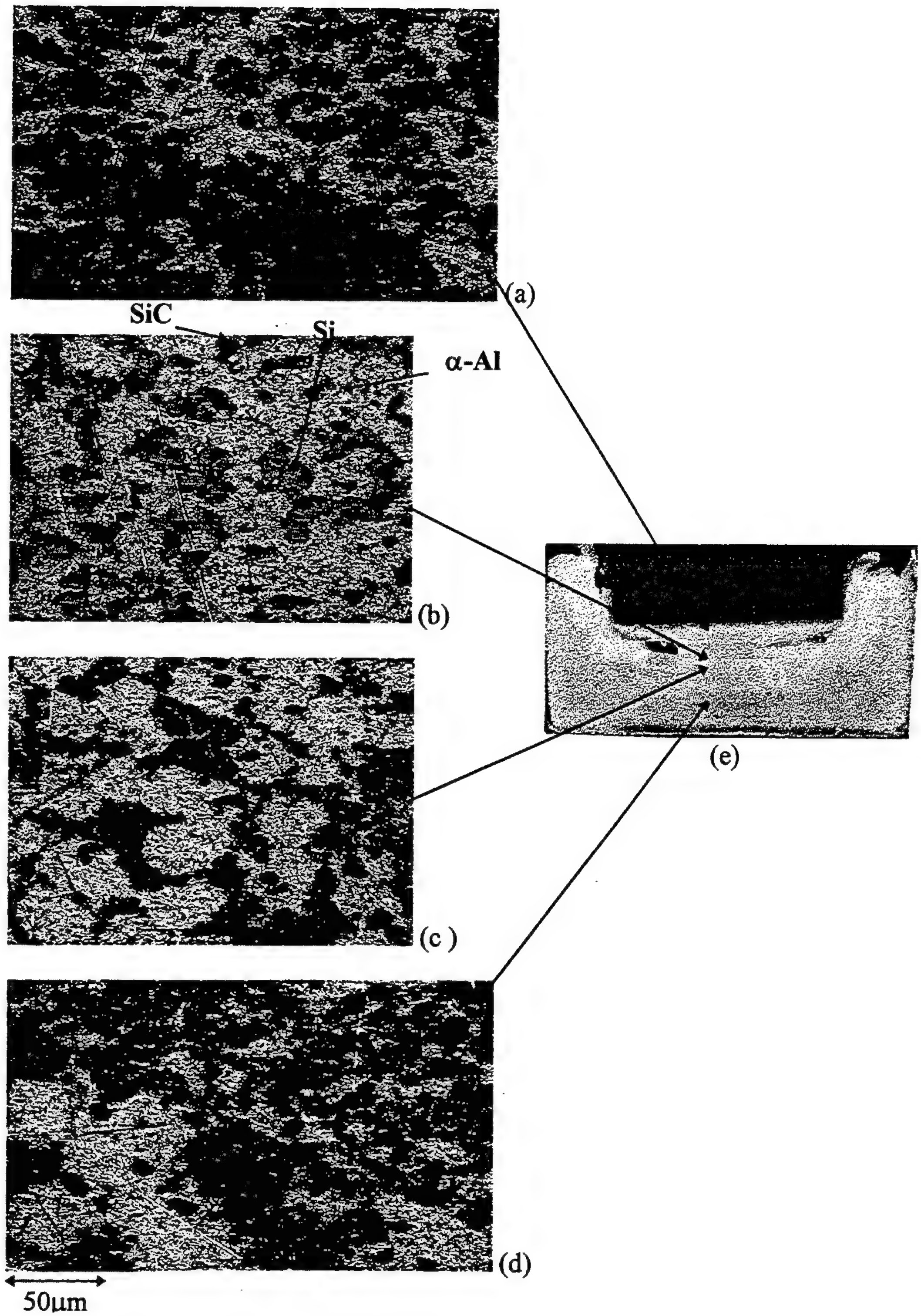

Figure 3. Micrographs from the aluminum alloy/silicon carbide composite material cast in the cylindrical mold with the concentric probe rotating at 200 RPM.

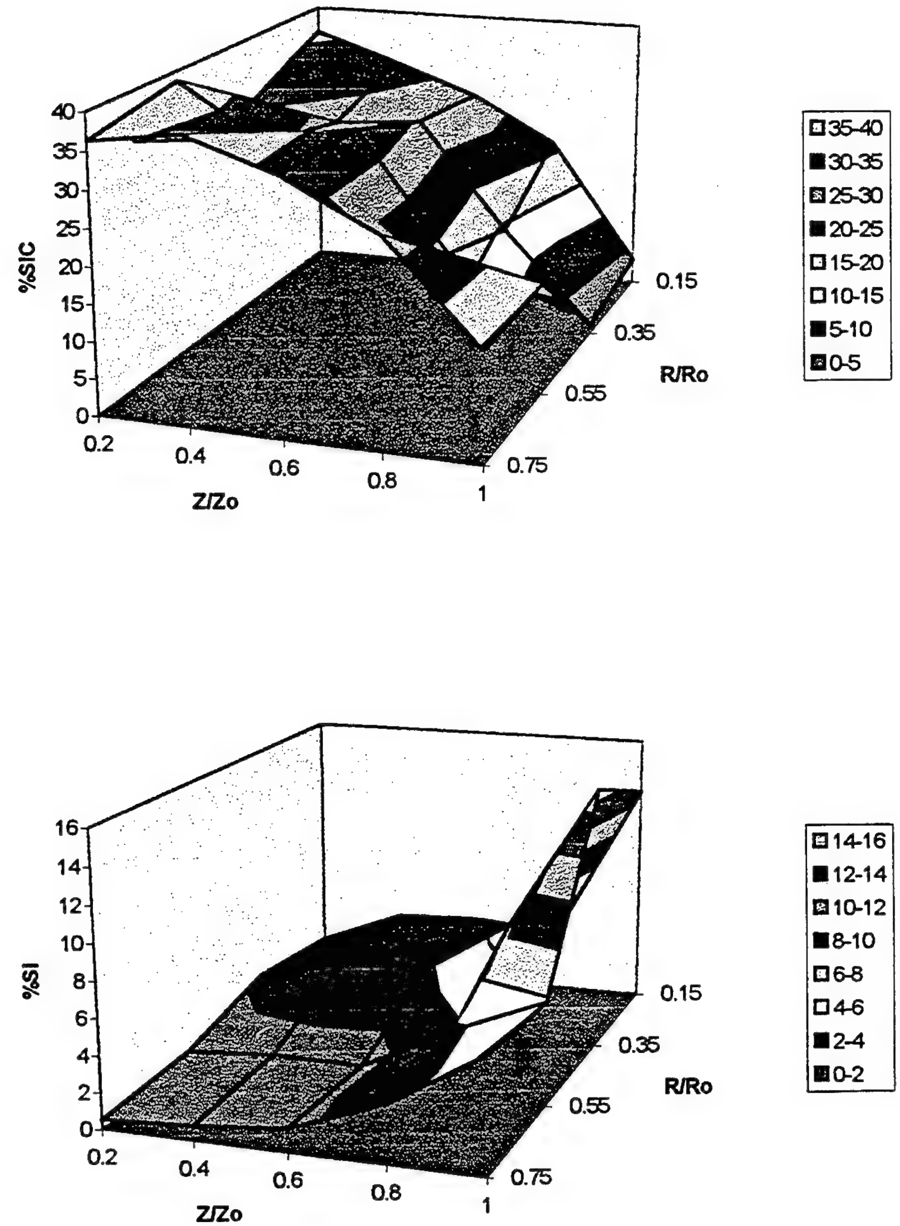

Figure 4. Maps of the distribution of SiC particles and Si grains in the specimen made at 20 RPM. Z/Z_0 is relative vertical position with 1.0 at the top. R/R_0 is relative radial position with 1.0 at the periphery of the specimen.

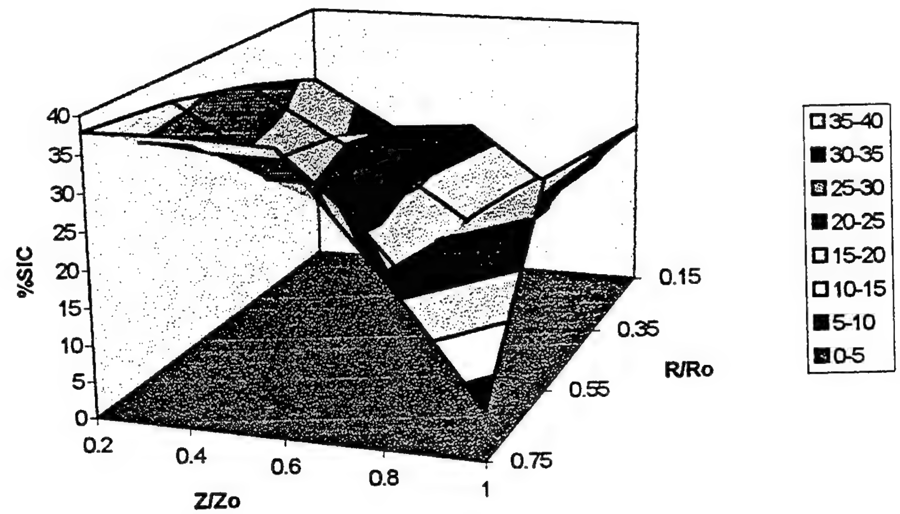

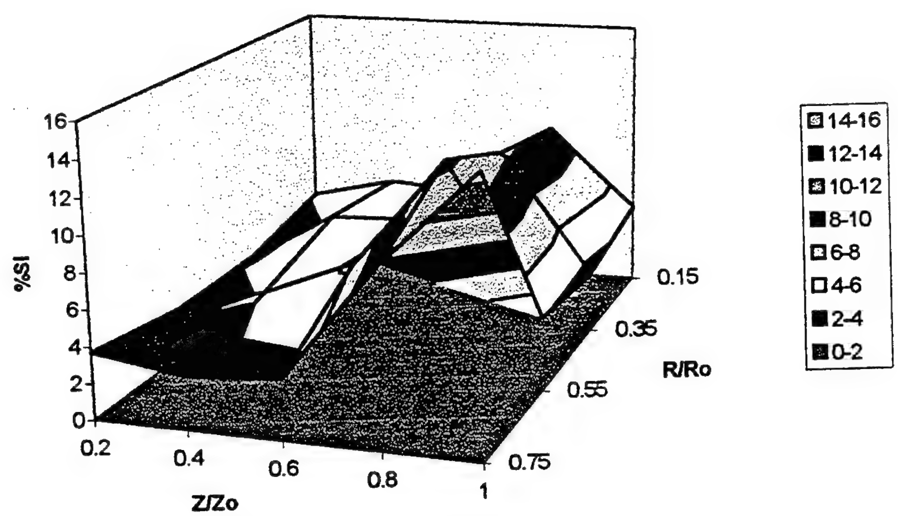

Figure 5. Maps of the distribution of SiC particles and Si grains in the specimen made at 200 RPM. Z/Z_0 is relative vertical position with 1.0 at the top. R/R_0 is relative radial position with 1.0 at the periphery of the specimen.

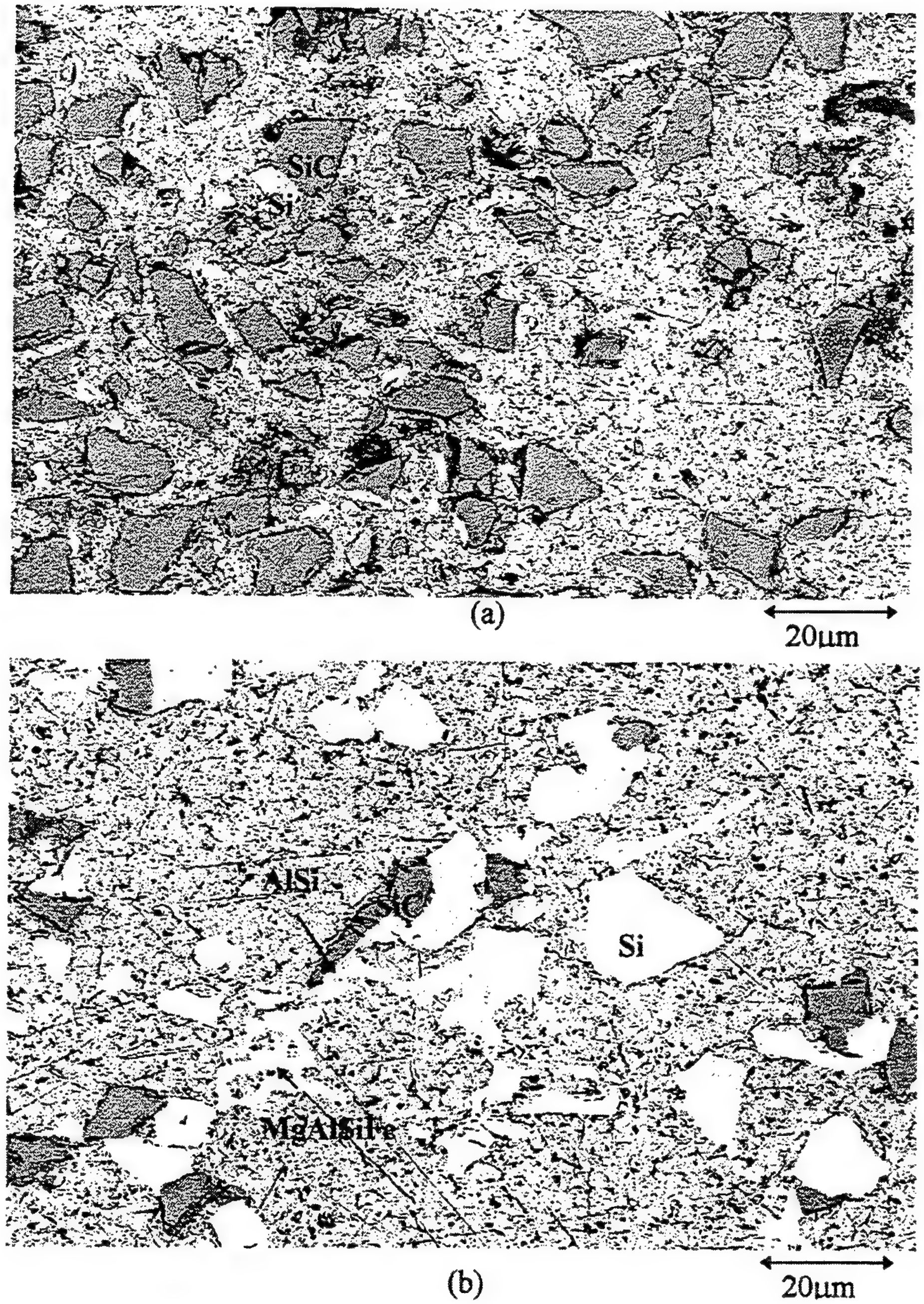

Figure 6. SEM micrographs made by back-scattered electrons in the atomic number contrast mode showing the formation of the Si phase on SiC particles in (a) and large blocky Si grains in a region depleted of SiC in (b).

IV.A.12 Generation of Microcellular Biodegradable Polymers in Supercritical Carbon Dioxide

Principle Investigator: Professor E.J. Beckman
Chemical Engineering Department
University of Pittsburgh

Students: Ms. D. Sparacio

IV.A.12.1 INTRODUCTION

There are several biomedical applications that require the use of microcellular polymeric materials with well defined porosity, such as guided tissue regeneration and cell transplantation. In the area of guided tissue regeneration, porous implants are used as size selective membranes to promote the growth of a specific tissue in a healing site[1-5]. The membrane allows nutrients to pass through, while excluding the diffusion of undesirable tissue cells into the site. Ideally, the implant should be inherently biocompatible, have well-defined cell sizes, be resorbable with appropriate biodegradation rates, and be manageable in a surgical setting. Lactide-glycolide copolymers are synthetic aliphatic polyesters that are biocompatible and bioresorbable. The copolymer ratio can be adjusted to obtain various rates of bioabsorption.

One method for generating porous membranes is a solvent-casting particulate-leaching process[6]. This technique involves adding sodium chloride particles to a polymer solution, evaporating the solvent, leaching the salt out with water, and drying the polymer. Microcellular materials are widely produced via phase separation in a homogeneous solution, followed by removal of the solvent[7]. Inducement of the phase separation can be temperature, molecular weight, or pressure driven. In the pressure induced technique, the polymer is swollen in the presence of a supercritical fluid , followed by a pressure quench by which the pores are generated and the gas is removed in a single step. Goel and Beckman showed that poly(methylmethacrylate) foams processed in supercritical carbon dioxide had cell sizes in the range of 0.4 to 20 μm and bulk densities in the range of 0.4 to 0.9 g/cm3[8].

In our investigation, we generated microcellular aliphatic polyester processed in supercritical carbon dioxide. The effect of pressure and temperature on cell size and bulk density were studied.

IV.A.12.2 ACCOMPLISHMENTS AND SIGNIFICANCE

Pellets of 85:15 lactide-glycolide copolymer (Medisorb Technologies, Tg=45°C) were first formed into disks via a vacuum mold. The disks were 11 mm in diameter, 2.5 mm thick and weighed 0.30 grams.

The disks were foamed in a stainless steel high pressure cell equipped with a pressure transducer, thermocouple, and heating jacket. The temperature of the cell was controlled to within $\pm$ 1° C by a PARR Model 4842 PID temperature controller. A Haskel air driven gas booster was used to pressurize the carbon dioxide. In a typical experiment, the disk was placed into a Pyrex liner and placed into the high pressure cell. The cell was flushed three times with

carbon dioxide and then pressurized and heated to the desired saturation pressure and temperature. Experiments were run from 1 hour to 24 hours depending on the parameter studied. Once the experiment was completed, the pressure was quenched within 30 seconds via venting of the carbon dioxide. The bulk densities of the foamed samples were determined via simple liquid displacement measurements.

Scanning electron micrographs were taken of each sample at 5 kVolts and magnifications ranging from 100x to 500x. The samples were prepared for SEM by freezing in liquid nitrogen, fracturing the surface, mounting the fracture on stubs with carbon paint, and sputter coating with a 100 to 150 C layer of gold. The SEM images were used for the determination of average cell size and size distribution. A LECO model 2001 image analyzer system was used to generate a binary image from which the mean cell size for each cell is calculated from eight feret (or diameter) measurements. Once the computer calculated the cell sizes, a histogram was generated to determine the mean cell size and standard deviation for the sample.

Figure 1 is a scanning electron micrograph of foamed PLA-PGA showing the typical structure of the cells generated via the pressure quench method. The cells have an open structure. During processing, it was found that the polymer was so plasticized by the CO_2 that the polymer takes on the shape of the container upon foaming.

Average cell sizes as low as 11 μm have been produced. The effect of CO_2 pressure on cell size is shown by the preliminary data in Figure 2. Initially, the cell size decreases with increasing pressure up to approximately 4000 psi. The same pressure effect was shown by Goel and Beckman for PMMA foamed in supercritical CO_2 using the pressure-quench method[8,9]. As pressure increases, the critical nucleus size decreases and the nucleation rate increases, resulting in a larger number of smaller cells. The critical nucleus size and nucleation rate are functions of the physical properties of the polymer-gas mixture, which strongly depend on the composition of the mixture[10]. Therefore, the cell size is very dependent on the amount of CO_2 sorbed.

Interestingly, Figure 2 shows that at higher pressures, the cell size begins to increase with increasing pressure. This behavior suggests that, for a given temperature, there may be a pressure at which a minimum cell size is produced. There may be factors which become significant only at higher pressures which limit the amount of CO_2 sorbed. At higher pressures, free volume in the polymer decreases with hydrostatic compression. Also, the viscosity may be increasing with increasing pressure, resulting in a decrease in nucleation rate. It seems that the effect is even more drastic as temperature decreases. Since free volume decreases and viscosity increases with decreasing temperature, one would expect a more significant effect.

Figure 3 shows results for the effect of temperature on average cell size. It appears that cell size decreases with decreasing temperature to approximately 40°C. However, experiments performed at 35°C show a sharp increase in cell size. Perhaps as we approach the critical temperature of CO_2 (T_c=31°C) limited nucleation occurs.

In addition to the cell size data discussed above, the foam bulk densities were also measured. Bulk densities range from 0.17 to 0.31 g/cm^3 depending on the process conditions.

IV.A.12.3 SUMMARY

In this study, a pressure induced phase separation method was utilized to generate microcellular biodegradable polymers (Lactide-glycolide copolymers) in supercritical carbon dioxide. Cell sizes ranged from 11 to 70 μm and bulk density from 0.17 to 0.31 g/cm3. The effects of pressure and temperature on cell size were investigated. Data suggest that a minimum occurs in cell size as a function of pressure.

IV.A.12.4 REFERENCES

1. N.M. Blumenthal, *J Periodontol,* **59**, 830 (1988).
2. C. Dahlin, L. Sennerby, et. al., *Int J Oral Maxillofac Implant,* **4**, 19 (1989).
3. A. Linde, P. Alberius, et. al., *J Periodontol,* **64**, 1116 (1993).
4. T. Scantlebury, *J Periodontol,* **64**, 1129 (1993).
5. J. Gotlow, *J Periodontol,* **64**, 1157 (1993).
6. A. Mikos, G. Sarackinos, et. al., *Biomaterials*, **14**, No. 5 (1993).
7. A. Bottino, G. Camera-Roda, et. al., *J Membr Sci*, **57**, 1 (1991).
8. S.K. Goel and E.J. Beckman, *Polym Eng Sci*, **34**, 1137 (1994).
9. S.K. Goel and E.J. Beckman, *Polym. Eng. Sci.*, **34**, 1148 (1994).
10. A.V. Yazdi and E. J. Beckman, "Bubble Nucleation in Polymer Mixtures," in *Polymer Devolatilization*, Marcel Dekker, New York (1996).

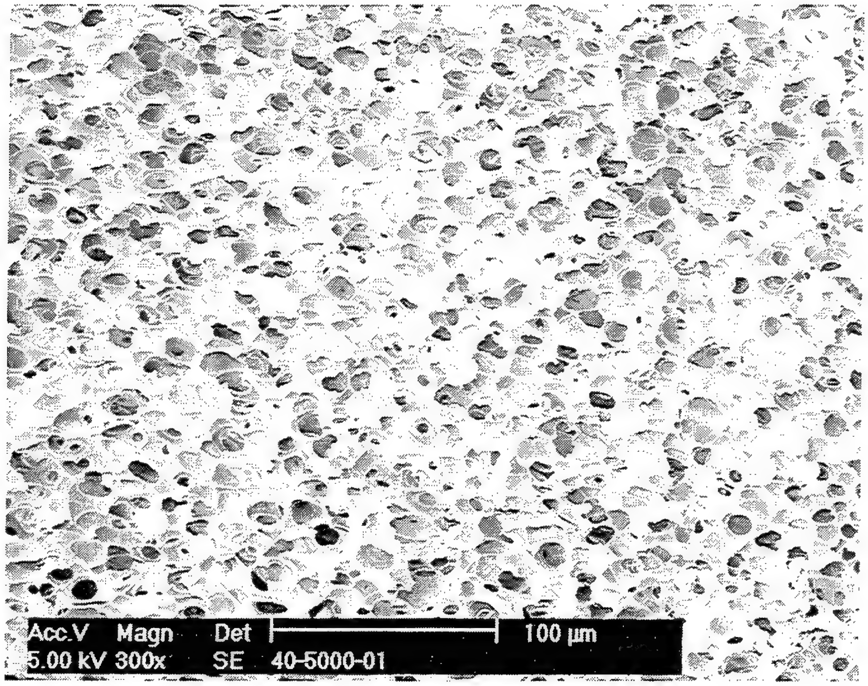

Figure 1: Typical microcellular structure of PLA-PGA foam generated via CO2 pressure quench (T=40°C, P= 5000psi).

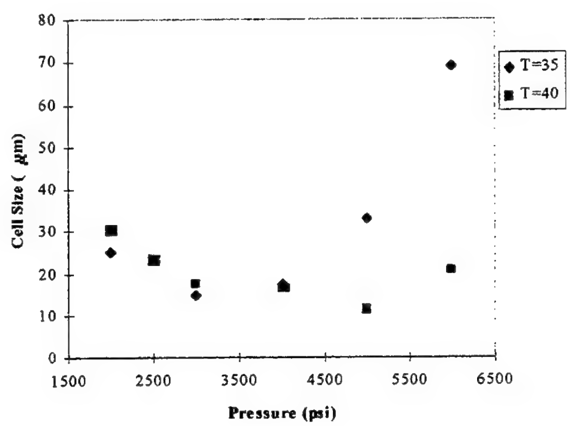

Figure 2: Average cell size as a function of pressure

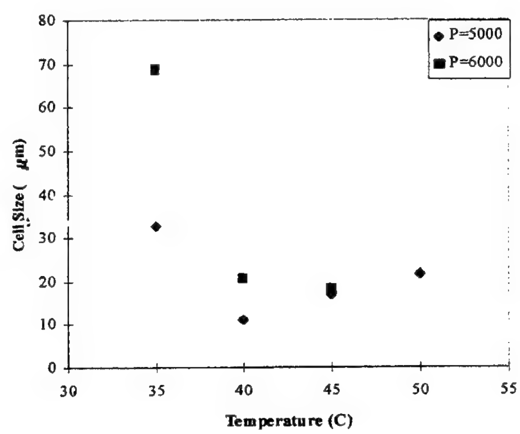

Figure 3: Average cell size as a function of temperature

IV.B OPTOELECTRONICS

IV.B.1 New MQW Structures for Switching Devices

Principal Investigator:	Professor D.W. Langer Department of Electrical Engineering University of Pittsburgh
Other Faculty Participants:	Dr. J. Falk Department of Electrical Engineering University of Pittsburgh
Students:	Mr. D.-S. Min Mr. F. Yousuf

IV.B.1.1 INTRODUCTION

High speed switches and modulators are important devices for modern communication and computer systems. An ideal switch (or modulator) operates in subnanosecond or picosecond times and requires minimal optical or electrical input to accomplish its function. Fabrication of the device should be amenable to planar integration techniques so that many functions could be executed on a single chip. III-V compound semiconductor technology is the most promising basis for such an Opto-Electronic Integrated Circuit (OEIC) development[1]. New device concepts have to be generated which - while maintaining high figures of merit - allow such integration.

The specific objectives of this task are the design and fabrication of AlGaAs/GaAs Multiple Quantum Wells (MQWs) materials which are to be optimized for two novel devices using these materials. The devices switch (on/off) or modulate transmitted optical signals by exploiting the superior electro-optical coefficient of MQWs. In particular: The materials to be designed and fabricated are for use in:

a) A Mach-Zehnder interferometer made from rib-etched waveguides. The wave-guide will use MQWs in the guiding layer. For a given length, this device will be up to five times more sensitive as an electric field detector than a similar $LiNbO_3$ interferometer.

b) A high speed modulator that normally operates as a total internal reflector. The modulator consists of a metal, multiple quantum well, dielectric structure. Applying a voltage to the multiple quantum well changes its reflective index. The change in refractive index produces a strong coupling to a plasmon at the surface of the metal. Excitation of the plasmon destroys the total internal reflection.

IV.B.1.2 ACCOMPLISHMENTS AND SIGNIFICANCE

a) The electro-optic coefficients of the multiple quantum well structure were recomputed for application in above devices. The coefficients depend on the thickness of the GaAs quantum

wells, the thickness of the AlGaAs barriers, the Al-to-Ga ratio of the barriers, the wavelength and temperature of operation, and the applied voltage (linear or non-linear) region[2]. Our evaluations and designs are based on published theoretical and experimental data which we had to extrapolate and generalize - according to our judgment and experience.

b) In the design of the Mach-Zehnder interferometer, using MQW rib-type waveguides, we succeeded in shortening the device length considerably. The plan to use impurity induced diffusion of the MQW structure in the Y-sections was abandoned and a new scheme was pursued. The latter also allows widening of the y-branch, i.e. shortening of the interferometer dimensions, and has the advantage of being easier to fabricate. As shown in Figure 1, it is based on a decrease of the index in the Y- region caused by a decrease in the heights of the rib. Without changing the insertion loss, the Y-angle can be increased from 2 to 8 degrees (Figure 2) which accomplishes a significant reduction of the length of the interferometer. These results were reported at the SPIE Conference and are accepted for publication in the Journal "Fiber and Integrated Optics"[3].

c) We have designed and analyzed composite, two-dielectric, one metal, modulator materials. We have begun growth and evaluation of these materials. These composites use the excitation of surface plasmons[4] as the basis for a high-speed reflection modulator[4-9]. The plasmon excitation will be turned on and off by the applied voltage which will change the refractive index of a multiple quantum well layer of GaAs/AlGaAs in contact with a metal (silver or gold)[10].

The theory of plasmon modulators has been formulated in a manner amenable to numerical calculations. The results of this theory have been programmed using a widely used software package (MATHCAD). These numerical calculations allow us to determine the variation of modulator reflectivity as a function of incident angle and as a function of an applied dc electric field. The MQW material is used because of its large change of refractive index with applied dc electric field. When a plasmon is excited at the metal/dielectric interface the reflectivity from the composite structure decreases from near unity. Examples of our numerical calculations are shown in Figure 3. The reflectivity of the modulator with and without an applied voltage is shown.

The growth of composite structures has begun. Thin layers of gold have been evaporated on GaAs. A prism coupler[11] has been used to launch a traveling wave into the GaAs and to excite a plasmon at the metal/dielectric (air) interface. The reflectivity of the composite Material changed dramatically as the angle of incidence was varied about the plasma excitation angle. A more complicated material has been designed and built. This structure is a multi-mode GaAs waveguide with metal conductors surrounding the GaAs. This structure should allow detuning the plasmon resonance by application of an electric field to the structure. All current experiments emphasize the excitation of plasmons, and the tuning of the plasmon resonance with an electric field. Current experiments use, because of their ready availability, undoped GaAs wafers. Future experiments will use multiple-quantum-well material.

IV.B.1.3 SUMMARY

- The design of MQW systems with defined optical properties (index of refraction and electric field dependence of the index) has been refined.

- A new concept was developed which allows us to shorten the length of the interferometer which incorporates two Y-branches without an increase of losses.

- The analytical theory of plasmon modulators which include a multiple-quantum-well dielectric layer is complete. The numerical analysis based on this theory can be used to predict the conditions necessary to excite a plasmon in the structure and to predict the reflectivity of the composite material as a function of applied electric field, wavelength and angle of incidence.

- Measurements of metal/GaAs composites have begun. Excitation of a plasmon has been observed. A structure that should show electric field tuning of the plasmon resonance has been built.

IV.B.1.4 REFERENCES

1. M. Deagenais, R. Leheny, H. Temkin, P. Bhattacharya, J. Lightwave Technol., **8**, 846 (1990).
2. Dietrich Langer and Yoshinobu Maeda, Jpn.J.Appl. Phys., **34**, Suppl.34-1, 173 (1995).
3. D.-S. Min, D. W. Langer, D. K. Pant and R. D. Coalson, SPIE Proceedings: **3006**, 459-467 (1997).
4 E. Kretschmann, Z. Physik, **241**, 313-324 (1971).
5. H. Raethner, Surface Plasmons, Springer-Verlag, (1988).
6. A. Otto, Zeitschrift für Physik, **216**, 398-410 (1968).
7. O. Solgaaard, F. Ho. J. I. Thackara and D. M. Bloom, Appl. Phys. Lett., **61**, 2500-2 (1992).
8. C. Jung, S. Yee and K. Kuhn, J. Lightwave Technol., **12**, 1802-1806 (1994).
9. C. Jung, S. Yee and K. Kuhn, Appl. Optics, **34**, 946-949, (1995).
10. H. Rahman, D. W. Langer, J. Falk and S. H. Park, Int. J. Optoelectronics, **8**, 259-266 (1993).
11. J. Singh, Optoelectronics, McGraw Hill (1996) pp. 122-4.

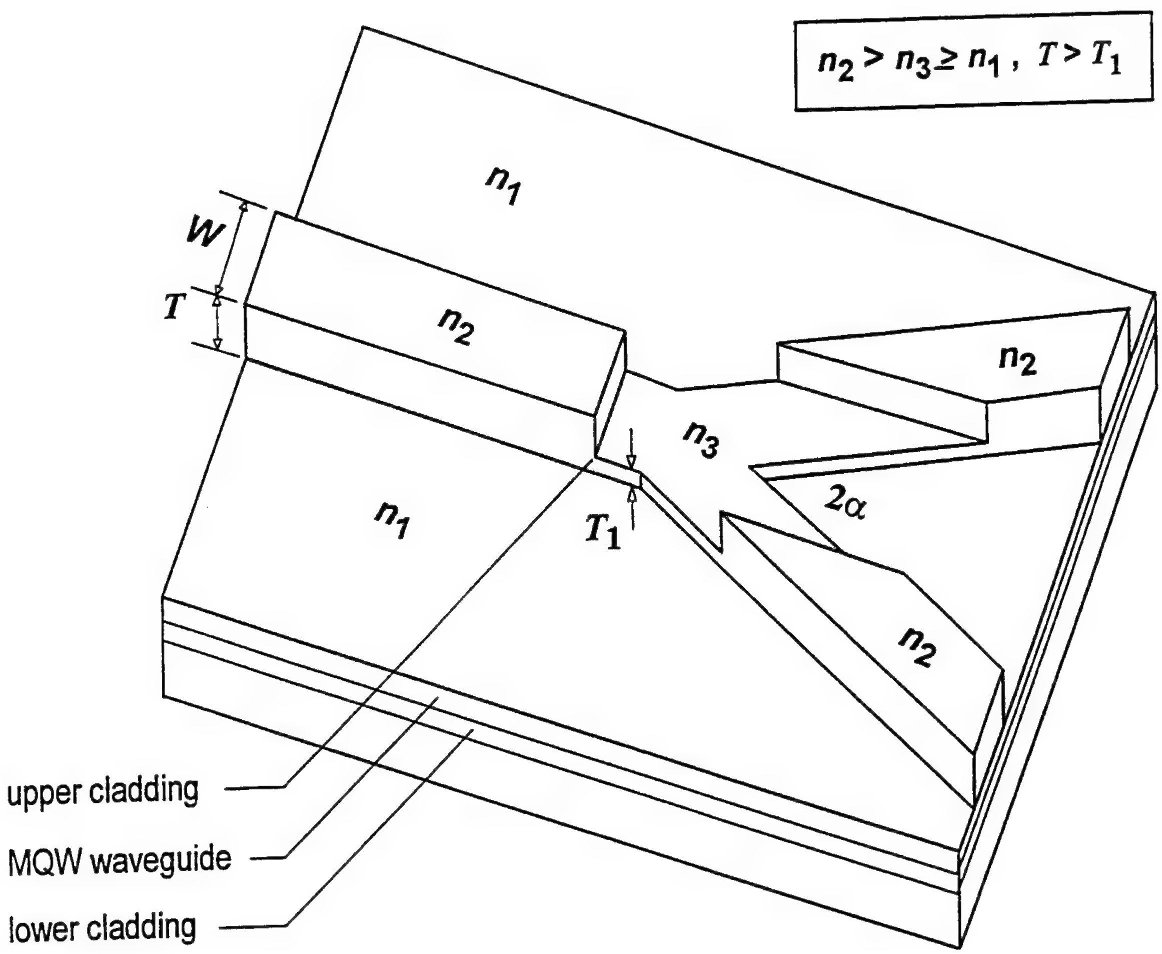

Figure 1: New waveguide Y-branch structure which, by reduction of rib-heights, has a lower index in the guide region. It reduces loss at wider branching angles and therefore a significant shrinking of the device size.

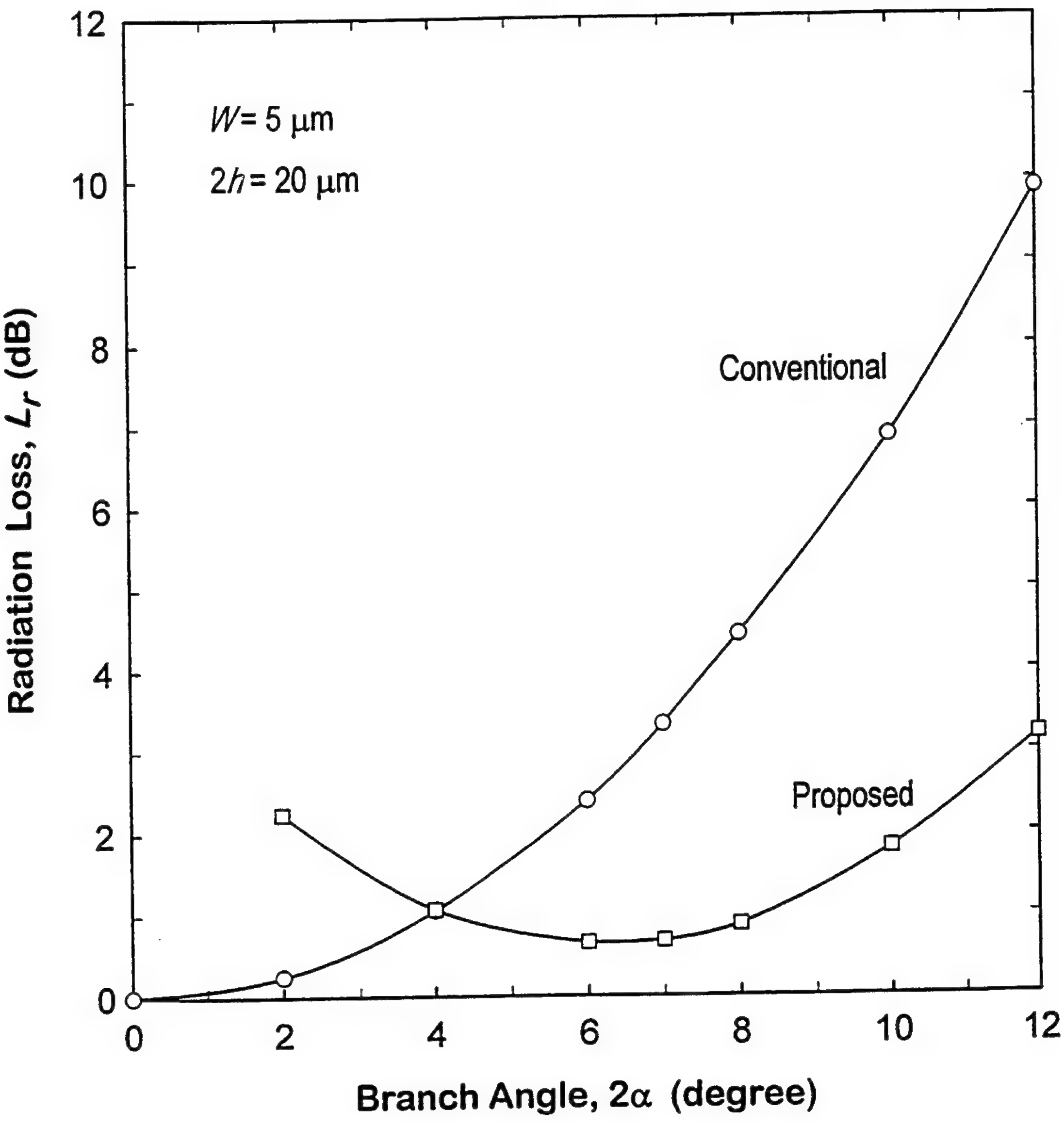

Figure 2: Radiation loss versus y-branching angle for a conventional rib-type Y-branch and our newly developed, reduced-height Y-branch. A branch angle of 8 degree is achievable with a loss of less than 1 Db.

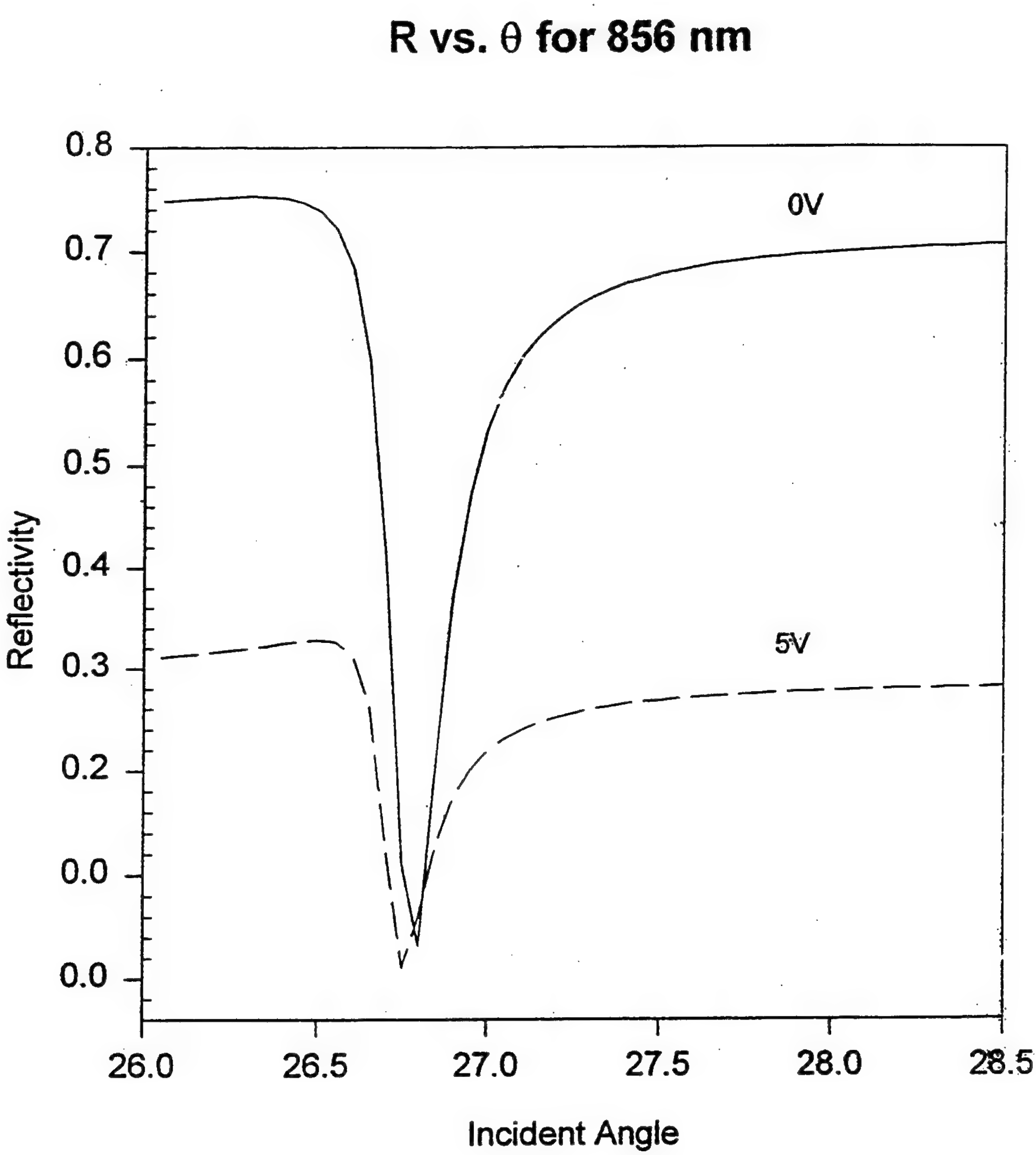

Figure 3: Theoretical reflectivity of a multiple-quantum-well, silver, air, plasmon modulator. The silver layer is 50 nm thick.

IV.B.2 Novel Laser Eye Protection and Optical Switching Devices Fabricated From Polymerized Crystalline Colloidal Arrays

Principal Investigator: Professor Sanford A. Asher
Chemistry Department
University of Pittsburgh

Students: Mr. J.M. Weissman
Mr. G. Pan
Mr. L. Liu

IV.B.2.1 INTRODUCTION

We have concentrated our research on the development of new optical devices based on colloidal crystalline arrays (CCA) of submicron sized colloids. These arrays are formed by self-assembly of highly charged monodisperse polymer spheres. Our research focuses on developing synthetic methodologies to create and tailor the spheres for various applications and on using these colloids to prepare so called "smart" materials which respond in a specific manner to external stimuli.

IV.B.2.2 ACCOMPLISHMENTS

We developed methods to polymerize crystalline colloidal arrays (CCA, Figure 1) within hydrogels polymerized from a variety of acrylamide monomers. We are exploiting this powerful CCA self assembly process as a synthetic motif to prepare highly order mesoscale periodic structures for use in chemical separation processes, separation membranes, novel optical device fabrication and for thin 2-D display devices and for novel optical sensors. The fabrication process involves the self assembly of a crystalline colloidal array[1,2] within a mainly aqueous medium which contains polymerizable monomers and crosslinking agents[3]. We use UV photoinitiation to polymerize the array into an acrylamide hydrogel. The final hydrogel film has the colloidal array (generally body centered cubic, BCC) semirigidly locked in position (Figure 2). The film is sufficiently stable to allow further chemical modifications to create novel, processible mesoscopic periodic arrays for novel applications.

BCC Array of Absorbers

We have synthesized a hydrogel containing a BCC array of low refractive index ($n=1.39$) highly fluorinated colloidal particles containing absorbing dyes[4]. We have refractive index matched these particles such that the real part of the refractive index is homogeneous throughout, but where a BCC array periodicity exists in the imaginary part of the refractive index. Our theoretical modeling predicts that this array should be highly optically nonlinear to incident pulsed lasers at wavelengths absorbed by the dye[1,4]. The colloidal particles should heat, and the real part of the refractive index of the BCC array of particles will diverge from that of the medium; the array will "pop up" to Bragg diffract light. This system will act as an optical limiter and optical switch. We recently experimentally observed this switching (Figures 3, 4), and intend to further refine this system[1,2].

High Efficiency Bragg Diffracting Arrays

We recently discovered that the diffraction efficiency of BCC and FCC CCA dramatically increase (more than 10-fold) for light incident normal to the (110) BCC or the (111) FCC planes, for light at half the wavelength diffracted in first order by these planes[5]. We discovered that this anomalous efficiency increase is due to the orientation of numerous planes which fortuitously diffract light at half the wavelength (Figure 5)[5].

BCC Array of Smart Size Switchable Spheres

We have utilized poly N-isopropylacryl-amide (PNIPAM), which is known to undergo a phase transition from a shrunken, hydrophobic phase at ca. 31°C, to a swollen, hydrated phase at room temperature, to prepare switchable smart materials[3,6]. For example, we developed a synthesis using PNIPAM to create monodisperse, highly charged, microgel colloidal particles. We formed CCA from these spheres, and found that the shrunken sphere CCA diffracts much more efficiently than does the swollen sphere CCA, due to the larger refractive index mismatch between the shrunken spheres and the aqueous medium (Figure 6). Thus, the CCA light transmission and diffraction can be controlled by temperature. We should be able to use this system as an optical limiter if we add absorbing dye; laser heating of the dyed system will cause the spheres to shrink; the diffraction efficiency will increase and the incident laser light will not transmit.

BCC Array in a Smart Switchable Lattice

We have polymerized a BCC array of polystyrene colloids in a hydrogel composed of PNIPAM (Figure 7). As the temperature is increased the PNIPAM matrix contracts and the BCC lattice shrinks[6]. This decreases the diffracted wavelength (Figure 7). We have demonstrated that we can shift the diffraction from the far red into the near UV. This material acts as a tunable reflector if the temperature changes homogeneously[6]. If only small regions are heated, an image is created which reflects light of a color defined by the temperature. We recently demonstrated this effect by adding a dye to the PNIPAM CCA, and by heating it with a low power Ar+ laser beam. This device has both light switching capability and possibility for use as a reflective thin film display device.

Rapid Response Gels

We developed approaches to add linear polymers to the PNIPAM gels to increase the response rate for shrinking and swelling[7].

IV.B.2.3 REFERENCES

1. S.A. Asher, S.Y. Chang, A. Tse, L. Liu, G. Pan, Z. Wu, and P. Li, "Optically Nonlinear Crystalline Colloidal Self Assembled Submicron Periodic Structures for Optical Limiters," Mat. Res. Soc. Symp. Proc. Vol. 374, Materials Research Society (1995).
2. S.A. Asher and G. Pan, "Crystalline Colloidal Array Optical Switching Devices," Proceedings of NATO Advanced Research Workshop on Nanoparticles in Solids and Solutions, in press (1996).

3. H.B. Sunkara, J.M. Weisman, B.G. Penn, D.O. Frazier, and S.A. Asher, "Design of Intelligent Mesoscale Periodic Array Structures Utilizing Smart Hydrogel" Polymer Preprints 37, 453 (1996).
4. A. Tse, Z. Wu, S.A. Asher, "Synthesis of Dyed Monodisperse Poly (methyl methacrylate) Colloids for the Preparation of Submicron Periodic Light-Absorbing Arrays," Macromolecules 28, 6533-6538 (1996).
5. L. Liu, P. Li, and S.A. Asher, "Fortuitously Superimposed Lattice Plane Secondary Diffraction in Crystalline Colloidal Arrays", Phys. Rev. Let., submitted (1996).
6. J.M. Weissman, H.B. Sunkara, A.S. Tse, and S.A. Asher, "Thermally Switchable Periodicities and Diffraction from Novel Mesocopically Ordered Materials," Science 274, 959 (1996).
7. J.H. Holtz and S.A. Asher, "Highly Responsive Hydrogels and Polymerized Crystalline Colloidal Arrays", Macromolecules, submitted (1996).

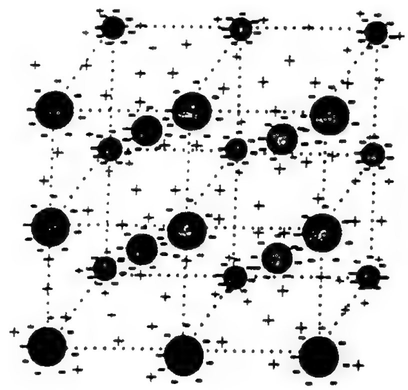

Figure 1: A body centered cubic crystalline colloidal array (CCA). The organic or inorganic colloidal particles self assemble into a cubic array. The negative charges are functional groups covalently bound to the surfaces of the colloids, while the positive counterions freely diffuse in the suspending medium.

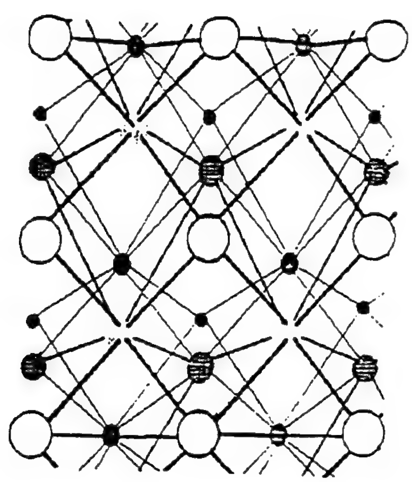

Figure 2: The polymerized crystalline colloidal array (PCCA) has the BCC CCA spatially locked in a hydrogel matrix.

Figure 3: Transmission spectrum of 138 nm dyed poly (hepta-fluorobutyl methacrylate) crystalline colloidal array solidified in a polyacrylamide hydrogel matrix. The ca. 650 nm peak results from the PCCA diffraction and the broad 520 nm peak results from dye absorption. We refractive index match the colloid to the medium and measure the predicted nonlinear optical diffraction phenomenon.

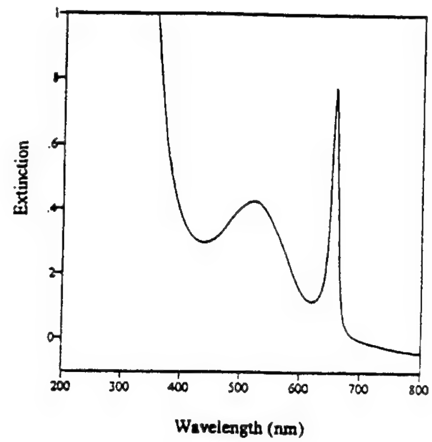

Figure 4: These nonlinear phenomena are measured by monitoring the pump beam energy dependence of the Bragg diffraction intensity. The relative value of Bragg diffraction intensities (Ron/Roff) were monitored at various pump beam energies. Measurements are taken with the refractive index of the medium (n_m) either slightly larger or smaller than that of the particles (n_p). For $n_m = 1.4045 > n_p$, pump beam heating is expected to decrease n_p further, and the diffracted intensity should increase. For $n_m = 1.361 < n_p$, the pump heating will again cause n_p to decrease. The resulting decrease in the refractive index mismatch causes the Bragg diffraction intensity to decrease.

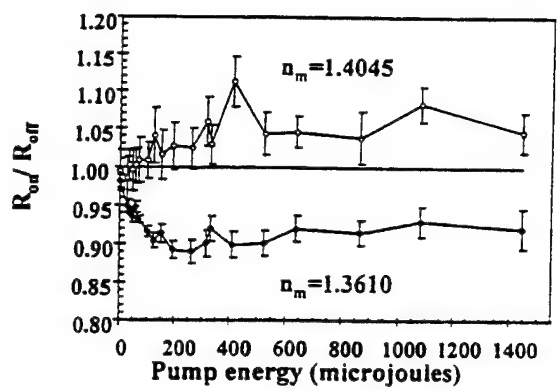

Figure 5: Primary and secondary diffraction of a 6.1 μm thick CCA. a. Primary diffraction at λ from the BCC (11) plane in first order. b. Intense secondary diffraction at $\lambda/2$ due to superposition of diffraction from numerous lattice planes.

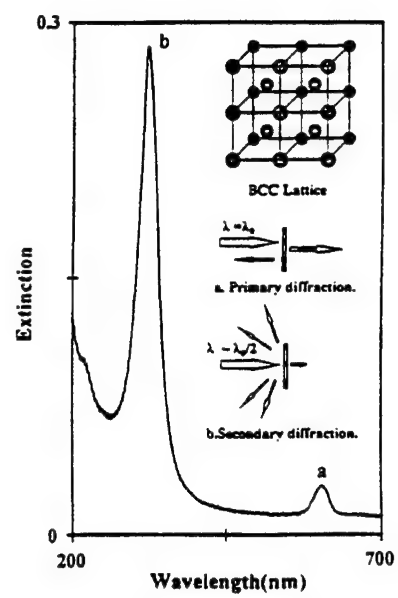

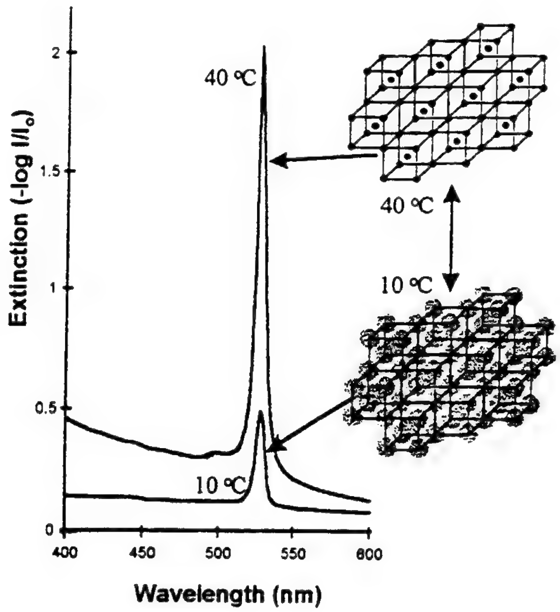

Figure 6: Diffraction from CCA of PNIPAM particles at 10°C and 40°C. The 40°C diffraction increases because of the increased particle refractive index upon "shrinkage".

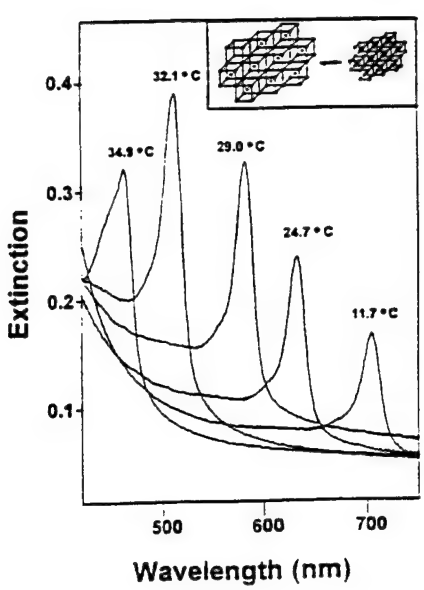

Figure 7: Temperature tuning of the diffracted wavelength from a PCCA of polystyrene spheres embedded within a PNIPAM hydrogel across the entire visible spectrum. As the gel matrix responds to temperature changes, the spheres are forced to move along with the gel, changing the lattice constant, and thus the diffracted wavelength.

IV.B.3 Synthesis of New Optically Nonlinear Materials from Metallo-Organic Compounds and Polymers

Principal Investigator:	Professor N.J. Cooper Chemistry Department University of Pittsburgh
Other Faculty Participants:	Dr. M. Hopkins Chemistry Department University of Pittsburgh
Students:	Ms. T. Utz Ms. J. Oh Ms. H. Brison Mr. R. DaRe

IV.B.3.1 INTRODUCTION

The objective of this project is to develop a new generation of molecular NLO materials based on hybrid organic/inorganic compounds in which large molecular hyperpolarizabilities are consequent on the coordination of transition metal centers to highly polarizable conjugated ligands. We are particularly interested in systems which exploit the unique properties of transition metal centers by means of strategies such as the use of metals in negative oxidation states as donor ligands (these should be both more powerful and more polarizable donors than conventional organic donors), and the use as donor or acceptor sites of ligands which can switch between two bonding modes with different electronic impacts on the metal center.

IV.B.3.2 ACCOMPLISHMENTS AND SIGNIFICANCE

It is well understood that transition metal complexes of NO have available to them a unique degree of electronic flexibility arising because a simple bending motion effectively oxidizes the metal center by two electrons:[1]

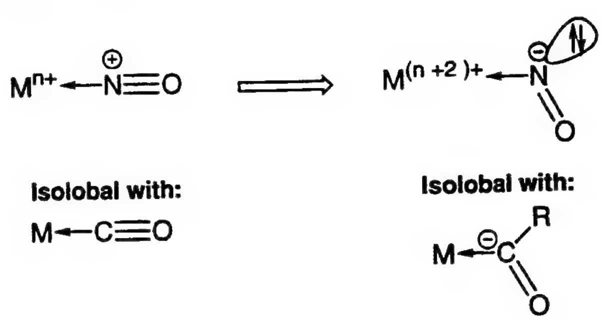

We have been attempting to apply this flexibility to the design of molecular NLO materials and have sought to prepare complexes containing both linear nitrosyl ligands as acceptor groups and conjugated para-amino phenyl ligands as donors. This lead us to synthesize and then

nitrosate the novel para-amino phenyl complex of W(0) shown below, but much to our surprise this did not lead to replacement of a carbonyl ligand by NO and instead resulted in insertion of NO into the W–aryl bond to give a structurally characterized nitroso arene complex:

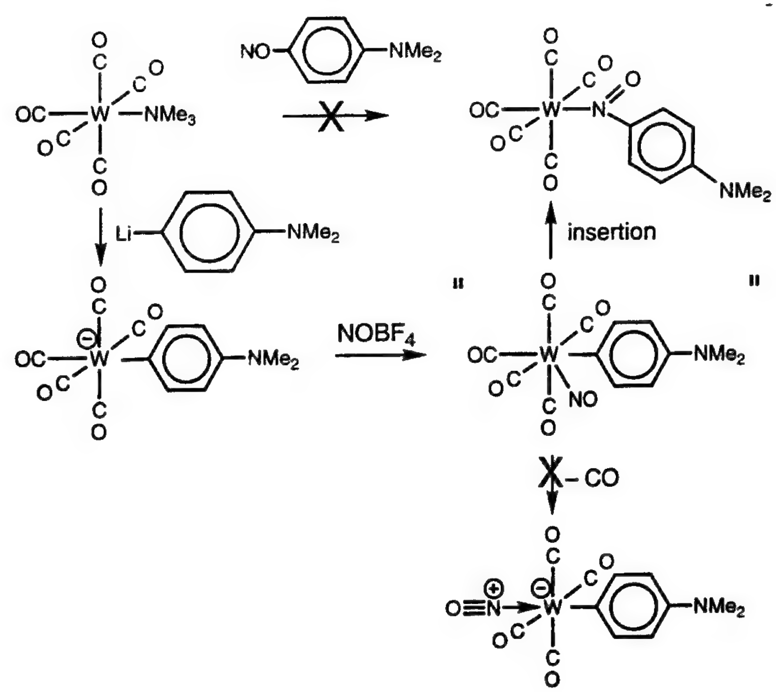

This fascinating reaction probably involves an intermediate nitrosyl complex which undergoes a rapid nitroso/aryl insertion reaction. This unusual reaction provides a powerful new route to nitroso arene complexes; nitroso*alkane* complexes are typically prepared by displacement of a labile donor ligand from the coordination sphere of a metal by the free nitroso alkane ligand,[2] but nitroso arenes are not strong enough bases to displace even weak donor ligands, and the W(0) complex in the Scheme can only be prepared by the nitrosation pathway.

The arylnitroso ligand has dramatic effects on the electronic spectrum of the "$[W(CO)_5]$" fragment, and adds a strong (ϵ = 16,000 L mol^{-1} cm^{-1}) MLCT absorption band at 600 nm. This suggests that the complex has all of the components required for a large second order molecular NLO coefficient, and since the complex also exhibits unusually well resolved vibrational structure in its electronic spectrum we anticipate developing an exceptionally precise understanding of the electronic structure of the molecule.

IV.B.3.3 SUMMARY

We have developed a convenient new route to W(0) nitroso arene complexes by nitrosation of arylate complexes. This results in an unprecedented insertion of NO into a W–aryl bond, to give a nitroso arene complex which can not be prepared by conventional approaches. The electronic structure of this unique complex is under investigation.

IV.B.3.4 REFERENCES

1. (a) Richter-Addo, George; Legzdins, Peter Chem. Rev. 1988, 88, 991. (b) Mingos, D. Michael P.; Sherman, Darren, J. Adv. Inorg. Chem. 1989, 34, 293.
2. Pilato, Robert S.; McGettigan, Colleen; Geoffroy, Gregory L; Rheingold, Arnold L.; Geib, Steven J. Organometallics 1990, 9, 312.

IV.B.4 A New Method for the Growth of Single Crystal Epitaxial Films of SiC and a Critical Evaluation of the SiC Single Crystal Surface Conditions Required for the Production of High Quality Oxide Layers

Principal Investigator: John T. Yates, Jr.
Surface Science Center
Chemistry Department
University of Pittsburgh

Other Faculty Participants: W.J. Choyke
Department of Physics and Astronomy
University of Pittsburgh

Student: Mr. J. Xu

IV.B.4.1 INTRODUCTION

Silicon carbide (SiC), as a wide bandgap material, will be the semiconductor of choice for a variety of applications in the high temperature, high current density, high frequency and high radiation dose regimes. This material is also an excellent template for gallium nitride (GaN) film epitaxial growth. The objective of our research on this project was to use a novel chemical activation method to grow SiC films. In addition, a novel method for activating the growth of SiO_2 films in highly localized regions at low temperatures has been devised.

IV.B.4.2 ACCOMPLISHMENTS

Three research papers have been written and submitted for publication. These papers deal with three topics related to the objectives of this project.

A. Amorphous SiC film Formation using Electron Bombardment to Stimulate the Surface Decomposition of Methylsilane

A central finding of the work is that low energy electrons may be used to enhance the growth rate of semiconductor films under chemical vapor deposition conditions. Electrons activate the breaking of chemical bonds in the precursor molecule and provide, in some cases, unlimited film thicknesses in the growth process.

For SiC deposition, we chose the molecule $CH_3SiH_3$12 as the precursor. This molecule, possessing the correct stoichiometry to form SiC, has just become available recently as a high purity compound for semiconductor applications. We found, by working on a Si(100) surface, that the use of 100 eV electrons in conjunction with exposure to a broad thermal molecular beam of CH_3SiH_3, led to the deposition of very thick films of amorphous $SiO_{.5}CO_{.5}H$ films. These films grow to increasing thickness as the deposition process continues, and there seems to be no limit to the thickness achievable. By heating the film to 1200 K, copious hydrogen evolution occurs, and an amorphous SiC film is produced. The amorphous SiC film exhibits a plasmon

loss energy at 22 eV, which is characteristic of SiC. Heating to 1300 K does not result in SiC film crystallization.

B. Role of the -SiH_3 Functional Group in Silane Adsorption and Dissociation on Si(100)

In the course of the studies discussed above, we discovered the critical role of the -SiH_3 functional group in CH_3SiH_3 in forming a covalent chemisorption bond to silicon and other semiconductor surfaces. It is this bonding which anchors the molecule to sites on the growing film surface, holding the molecule in place for subsequent activation by electron impact. The silane group is postulated to form this bond by means of rehybridization into an electronic structure which involves pentacoordinate silicon, and bonding to the silicon surface occurs initially without Si-H bond scission.

C. Use of Electron Impact Activation of Adsorbed O_2 Molecules on Si(100) to Induce Oxidation

The formation of a localized oxidized layer on Si(100) has been achieved using O_2 as an adsorbed molecular precursor. Electron impact (100 eV) results in O_2 activation and dissociation, producing a localized silicon dioxide structure. Thus, one can write an oxide layer on a silicon surface using an electron beam. The quality of the SiO_2, as judged from its XPS spectrum, is very high, and the thickness of the oxide layer can be made greater than that achievable by lengthy thermal oxidation.

The electronic excitation process has been studied by varying the electron energy and observing the relative efficiency of the electron-induced oxidation process. A resonance at about 10 eV electron energy has been discovered, suggesting that electron attachment, followed by O-O bond scission, is responsible for the activation of adsorbed O_2 molecules, leading to SiO_2 formation even at 90 K.

IV.B.4.3 SUMMARY

It has been shown that both silicon carbide and silicon dioxide thin films may be grown at room temperature and below by means of electron impact on adsorbed precursor molecules. In the case of methylsilane precursor, a highly hydrogenated amorphous silicon carbide thin film was produced. In the case of molecular oxygen precursor, a high quality silicon dioxide film was produced. It is believed that dissociative electron attachment processes for the activation of surface species are responsible for both of the thin film growth processes investigated.

In addition, new insight into the mode of chemical bonding of the -SiH_3 functional groups to covalent solid surfaces has been obtained, and this may be useful in many areas of semiconductor surface chemistry.

IV.B.5 Optically Induced Switching of Electric Field Domain Configurations for Multi-Quantum Well Optoelectronic Devices

Principal Investigator: Professor Ilan Gravé
Department of Electrical Engineering
University of Pittsburgh

Students: Mr. S.W. An
Ms. M. El-Ganayni

IV.B.5.1 INTRODUCTION

The objective of our work is the study of electric field domains in superlattices and multiquantum well systems, and the observation of an all optical switching between different domain configurations.

The application of an electric field to quantum confined structures adds an element of complexity to the system and allows for a larger versatility for applications and devices, since many of the material's properties are influenced by such an applied field. In particular the absorption spectrum and the index of refraction are strongly dependent on the strength of the applied field. Thus, the control of electric field patterns along the superlattice region can be very important and useful.

Since the first studies of superlattices, and similar artificially-made low-dimensional quantum-confined structures, it was realized that the application of an electrical field along the carrier transport direction will not result in a uniform distribution of the field along the periodic structure. The system, instead, settles in a configuration where a number of quantum wells and barriers (or superlattice periods) are under a high-field domain, while the rest of the superlattice is under low-field domain, screened from the effect of the applied field. Moreover, each period under high-field takes on a well-defined voltage drop, which aligns the first excited subband (or energy level) in one quantum well with the ground state subband in the adjacent well. In this way, even if the superlattice miniband conduction has been disrupted by the electrical field, the system still provides a favorable transport path, by allowing resonant tunneling between aligned energy subbands at opposite sides of the superlattice barriers. In the low-field region, transport is achieved through ground state to ground state tunneling. When the electric field is increased, additional quantum wells fall under an expanded high-field region, while the low-field region shrinks and is eventually quenched.

Observation of the formation and expansion of high field domains along a superlattice region can be made by recording the electrical characteristics of the samples, i.e. the current versus voltage curves at low temperatures: a series of negative differential resistance oscillations can be observed. These correspond to the resonant alignment of excited subbands of additional quantum wells entering the high-field domain, as discussed above. Recently, optical techniques have been employed to monitor the formation and expansion of high field domains along quantum-confined structures[1]. A new technique, intraband photocurrent spectroscopy at thermal imaging wavelengths, was used to study field configurations along more complex samples, designed to include a few stacks of different quantum wells grown in series. This tool proved

very effective in characterizing the field configurations along the region of interest (Figure 1). Even more importantly, these studies showed that, when variable (rather than uniform) superlattices were used, a richer, more involved interplay of field configurations could take place[2]. Not only did field domains form and expand along the multi-quantum well region, but they were also observed to readjust or switch to different spatial patterns along the samples, for some critical applied fields. This immediately called for the possibility of applications for switching devices. Moreover, many additional puzzling phenomena were observed, such as the possibility of a high-field domain nucleating from the "wrong side", i.e. the cathode, contrary to the rationale of the screening effect[3]..

IV.B.5.2 ACCOMPLISHMENTS AND SIGNIFICANCE

We have started an effort to model the static behavior of field domains in multi-stack samples. This task is more demanding than modeling simple superlattice structures, and it requires different considerations for unipolar or bipolar samples.

We have designed samples and experiments for observing optically induced domain switching in two different configurations (unipolar and bipolar samples):

1. Using n^+-i-n^+ patterns, in a design suitable for intersubband multicolor infrared detectors: The optical switching can be induced in a number of ways. The simplest scheme plans to modulate the availability of free carriers in the sample. These free carriers are essential to provide the space charge accumulation needed at the boundaries of domains. The doping level can be designed in such a way to induce nucleation of high field domains within different stacks of quantum wells for differently-doped samples. Based on this scenario, illumination can generate additional carriers and enhance the availability of space charge, thus favoring a different nucleation pattern, i.e., forcing an optical switching. The samples for this experiment have been designed and we are expecting to grow them by MOCVD at Pitt or by external collaborators in the near future. The material adopted for the first experiment is the GaAs/AlGaAs system. We have adapted our cryostat and optics to the mid-infrared band, since the experiment will be performed in this spectral region (7-12 μm.) We have purchased a beam condenser to be used in the Materials Research Center FTIR for as-grown sample characterization.

2. Using n^+-i-p^+ patterns, in a design suitable for interband multicolor modulators: Here the sample is undoped in the quantum wells, which are located between n and p contacts. For moderate external bias, only photogeneration can provide the space charge needed to sustain domain boundaries. Here bipolar transport is present, after the generation of electron-hole pairs, and the modeling requires different considerations.

While these samples can perform as multi-color modulators controlled by an applied electric fields, they can also be suitable, in principle, for all optical switching. This requires the choice of a constant applied bias and the variation of light intensity to provide different stable domain configurations.

We have characterized three-stack multi-quantum well samples grown by MBE with low temperature photoluminescence (Figure 2) and electrical measurements (Figure 3). The quantum wells are designed in a stepped/asymmetric geometry to enhance the quantum confined Stark effect. These results show a good fit between our design and the actual excitonic peaks, as well as a strong sensitivity to light. Effects of the electric field on the photoluminescence are also studied, since they can give important clues on the presence, expansion and rearrangement of domains in the samples.

Absorption measurements as a function of applied field and optical power will complete, in the near future, the characterization of the present samples. A second optimized design will be then used for the experimental implementation of optical domain switching.

IV.B.5.3 SUMMARY

We have designed samples for the observation of optically induced switching of electric field domains along a multi-quantum region. Two different experiments are being prepared in the interband (near infrared) and intersubband (mid-infrared) regime. The first interband sample has been characterized by electrical and optical measurements. Features in the I-V curves where observed as well as a modulation of the photoluminescence efficiency as a function of the electric field. All these tend to confirm the presence of high-field domains in the sample, and allow a study of transport and distribution of charge along the multi-quantum well region.

Our cryogenic systems and our optics have been expanded to allow for mid-infrared measurements, as needed for the additional experiment aimed at the observation of all-optical switching of domains with mid-infrared probing light (intersubband infrared detector configuration.)

IV.B.5.4 REFERENCES

1. "Optical studies of electric field domains in GaAs-AlGaAs superlattices", H.T. Grahn, H. Schneider, and K. von Klitzing, Phys. Rev. B **41**, 2890 (1990).
2. "Voltage-controlled tunable GaAs/AlGaAs multi-quantum well infrared detector", I. Gravé, A. Shakouri, N. Kuze, and A. Yariv, Appl. Phys. Lett. **60**, 2362 (1992).
3. "Control of electric field domain formation in multi-quantum well structures", A. Shakouri, I. Gravé, Y. Xu, A. Ghaffari and A. Yariv, Appl. Phys. Lett. **63**, 1101 (1993).

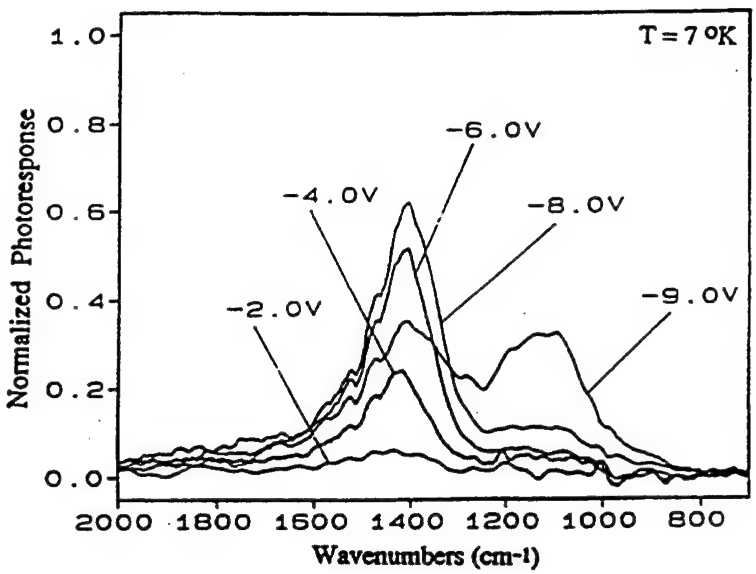

Figure 1: Electrical switching of high field domains monitored with photocurrent intersubband spectroscopy.

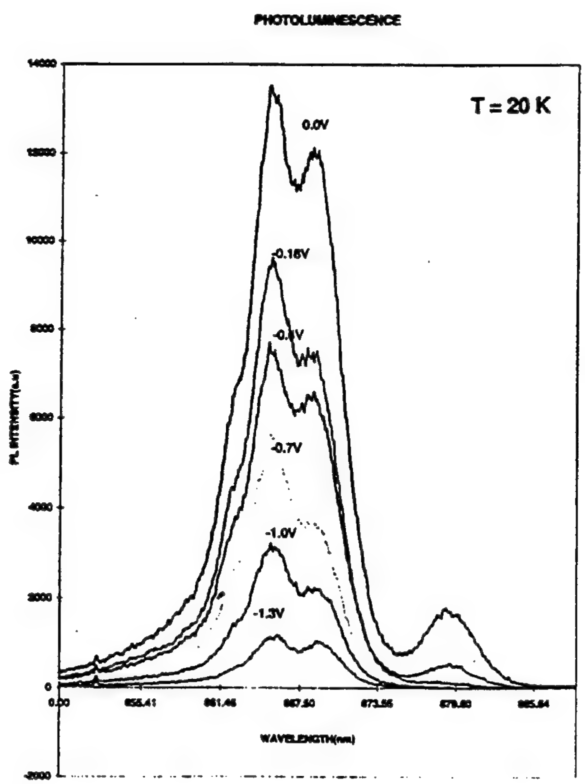

Figure 2: Photoluminescence of a p^+in^+ sample at low temperature, for different applied voltages.

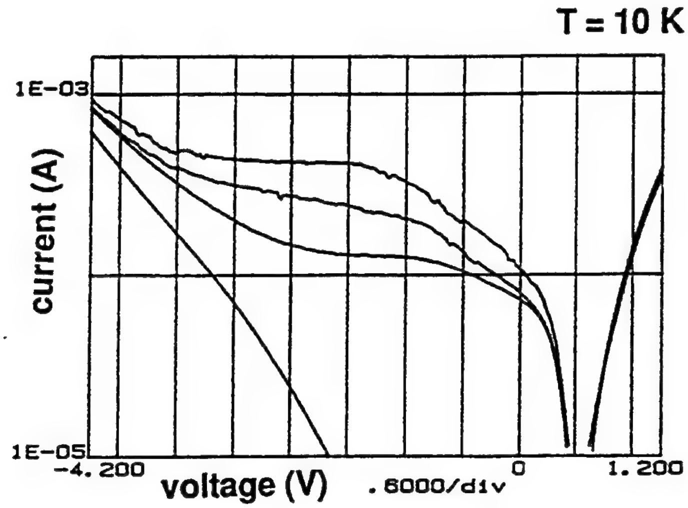

Figure 3: I-V characteristics of a p^+in^+ sample at low temperature, in the dark and with illumination at different wavelengths and constant power.

IV.B.6 Inverse Design of New Materials

Principal Investigator:	Professor D. Beratan Chemistry Department University of Pittsburgh
Other Faculty	Dr. P. Wipf Chemistry Department University of Pittsburgh
	Dr. S. Risser Department of Physics E. Texas State
Students:	Dr. Ch. Kuhn Mr. R. Kondru

IV.B.6.1 INTRODUCTION

Much of new materials design is discovery driven. For example, high temperature superconductors were discovered and developed in the laboratory by luck, profound insight, and/or divine intervention. After the fact, theoreticians have attempted to build *consistent* and *predictive* models. The goal of this research program is to develop a new theoretical strategy that will *target a particular materials property and instruct the synthetic chemist as to what molecular structure should be synthesized to optimize that property*, Figure 1. This strategy is known as an "inverse" approach because it is *property* rather than structure driven. The method has *not* been applied to any materials science problem in the past. We believe that its use could open up a number of important areas of materials science to the rational design of new structures. In areas of materials science in which the intrinsic property itself is understood but the key high performance materials are not forthcoming, this method could have a deep impact. The one year seed project described here involves the development of the inverse design strategy and application to optical and electro-optical materials development. Establishment of these methods should allow the procurement of follow-on funding to support applications of this research.

A broad challenge in materials chemistry is to choose a given property and to design a material that "optimizes" this property (linear or nonlinear optical property, conductivity, band gap, band width, etc.) based upon a set of constraints (molecular size, types of atoms, etc.). In the context of nonlinear optical materials and electron transfer biocatalysts, we have devised rather broad based transferable structure-function relationships. Yet, these problems were solved, essentially, by finesse rather than by applying a somewhat more universal theoretical strategy. The first part of this project was aimed at developing new "inverse" strategies for materials design.

During the course of this project a second, related, challenge associated with optical properties was undertaken. It is often the case that a promising organic natural product is

isolated, but its synthesis in the lab is hampered by the lack of knowledge of the handedness of the multiple chiral centers in the structure. We have sought to develop methods to compute the sign and magnitude of the optical rotation angle in molecules with multiple chiral centers.

IV.B.6.2 ACCOMPLISHMENTS AND SIGNIFICANCE

A. Inverse Design

We have performed exploratory research that uses several inverse and direct design strategies to optimize molecular structures[1]. We have analyzed constrained and unconstrained optimization approaches, based upon Lagrangian multiplier and other methods. Inverse strategies are familiar in many areas of science and engineering[2]. As a specific example, we have analyzed transition oscillator strengths and electronic first hyperpolarizability in few-orbital systems with constrained and unconstrained optimization strategies. Strategies have fallen into two main categories: 1) inverse optimization through the wave function atomic orbital coefficients (constrained optimization), 2) direct optimization of the molecular Hamiltonian through Monte Carlo sampling of parameter space. We are currently investigating methods that allow the inclusion of common chemical "subunits" as part of this strategy, and are analyzing methods of introducing a high degree of constraint to the optimization process in order to guarantee chemically sensible bonding patterns. These strategies were applied to materials science by us for the first time (to our knowledge). As we gain knowledge of the general aspects of these strategies we will apply them to more specific materials design issues.

B. Molecular chirality

The synthesis of promising organic natural products is often hampered by the lack of knowledge of the handedness of the multiple chiral centers in the structure. For a molecule with N chiral centers, there are 2^N possible configurations, and it is often quite difficult to determine the absolute configuration in the absence of an x-ray crystal structure. We are developing molecular quantum mechanical methods that could allow one to narrow the range of likely structures, by computing the sign and magnitude of the optical rotation angle in molecules with multiple chiral centers.

Simple useful qualitative rules exist to describe the optical activity in structures with weakly interacting chiral centers. Unfortunately, these rules are not entirely reliable as the interaction between centers increases. We are developing methods that will lead to the well known additivity relations when interactions are sufficiently weak, but will also describe the less trivial case of interacting chiral centers. The problem, of course, is one of developing these predictive quantum mechanical models.

The perturbation theory expression associated with the optical rotation angle is well known[3]. In order to develop intuition for this relation, and to study a simple case of interacting chiral centers, we developed the "particle-in-a-twisted-box" model for optical activity (and optical rotary dispersion). We have analyzed how box geometry and interactions between chiral units of the twisted box influence the magnitude and sign of the optical activity[4]. Having developed a qualitative framework for the effects from this model, we are now pursuing molecular orbital (semi-empirical Hartree-Fock) strategies to make quantitative predictions of these effects. While

some software exists to compute these quantities at the neglect of differential overlap level, it has proven to be full of "bugs," which we are now removing. We also plan the application of a "divide-and-conquer" *ab initio* strategy to this problem, which could - in principle - produce more reliable predictions.

IV.B.6.3 SUMMARY

In the last year we have initiated a "seed" project associated with the development of design and interpretative guidelines for new materials. We have focused on (1) both inverse and direct strategies for molecular Hamiltonian development, in order to suggest molecules with promising characteristics and (2) the prediction of optical rotation angles in organic molecules with multiple chiral centers. Significant progress was made in both areas and are described in recent publications[1,4]. The research in both areas is continuing and follow-on funding in these areas is being sought.

IV.B.6.4 REFERENCES

1. C. Kuhn and D.N. Beratan, *J. Phys. Chem.* 100, 10596-10599 (1996).
2. (a) L.F. Caudill, H. Rabitz, A. Askar, Inverse Problems 10, 1099 (1994). (b) R.G. Newton, *Inverse Schrodinger scattering in three dimensions*, Springer-Verlag 1989. (c) H.J.S. Dorren, E.J. Muyzert, R.K. Snieder, Inverse Problems 10, 865, 1994.
3. P.W. Atkins, *Molecular Quantum Mechanics, 2nd edition*, Oxford Press, New York, 1983.
4. R. Kondru, S. Lim, P. Wipf, and D.N. Beratan, *Chirality*, in press.

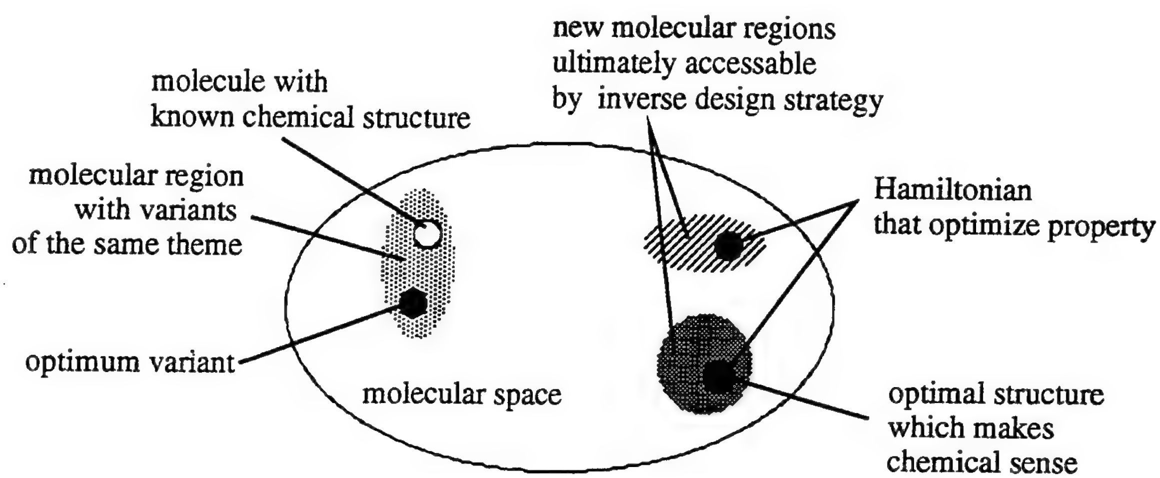

Figure 1: Conceptual view of the inverse molecular design strategy. Note that the goal is to move away from structures that differ in only trivial ways from existing structures, yet to enforce constraints such that the structures resulting from the optimization make chemical sense.

IV.B.7 Theory of Interacting Macroions with Application to Colloid Crystal Assemblies

Principal Investigator:	Professor R.D. Coalson Department of Chemistry University of Pittsburgh
Other Faculty Participants:	Professor S.Asher Department of Chemistry University of Pittsburgh
	Professor A. Duncan Department of Physics Univ. of Pittsburgh
Students:	Mr. J. Zahorchak, Ms. M. Kurnikova Mr. A. Prabaharan

IV.B.7.1 INTRODUCTION

The properties of systems of highly charged colloid particles are largely determined by electrostatic interactions between the particles. Characterization of these interaction forces is made difficult by the presence of a mobile cloud of ions that screen the colloid charges. Although approximate force laws have been devised in the past[1], the validity of these approximations is questionable at high colloid charge and number densities[2]. Thus a more advanced treatment of inter-colloid interactions is necessary in order to successfully model them.

Given an accurate inter-colloid pair potential, molecular dynamics and monte-carlo simulations of a variety of structural and dynamical properties are useful. These include characterization of the stability of colloid crystals and their response to external perturbations (e.g., heating and shearing). An understanding of such properties is valuable in guiding the design of colloid crystalline devices, e.g., optical filters, chemical sensors, etc.

IV.B.7.2 ACCOMPLISHMENTS AND SIGNIFICANCE:

<u>Advances in the Theory of Intermacroion Interactions</u>

With AFOSR-MRC support 1991-1994 we developed a powerful and flexible Lattice Field Theory (LFT) of inter-colloid forces for precisely this purpose[3]. In the last funding year the theory has been generalized to include multipolar species in the ionic atmosphere[4]. This is important for proper determination of the dielectric boundary between low dielectric colloid ($\epsilon \cong 3$) and high dielectric solvent ($\epsilon \cong 80$).

Models and Simulations of Colloid Crystal Stability

During the last 12 month period we have performed the first full scale MD simulation of photothermal compression dynamics[5] (cf. Figure 1). In addition we devised a simple analytical model of the pressure exerted by a colloidal crystal due to electrostatic repulsion between the members of the array. Analytical theory and full MD simulation agree well, and are consistent with known experimental results[2]. Both simulation and our analytical model can be extended, for example to the case where the colloid crystal is embedded in a polymer gel.

IV.B.7.3 SUMMARY

We have developed a practical methodology for computing the interaction forces between highly charged colloidal particles in electrolytic solutions. We have then utilized these force fields to carry out extensive molecular dynamics simulations of colloid crystal arrays which are relevant to the design of optical filters, chemical sensors, etc.

IV.B.7.4

1. A.K. Sood in Solid State Physics, v. 45, ed. H. Ehrenreich and D. Turnbull (Academic, NY 1991).
2. P. Rundquist, S. Jagannathan, R. Kesavamoorthy, C. Brnardic, S. Xu, and S.A. Asher, J. Chem. Phys. 94, 711 (1991); R. Kesavamoorthy, S. Jagannathan, P. Rundquist, and S.A. Asher, J. Chem. Phys. 94, 5172 (1991).
3. (a) R.D. Coalson and A. Duncan, J. Chem. Phys. 97,5653(1992); (b) A.M. Walsh, and R.D. Coalson, J. Chem. Phys. 100,1559(1994); (c) N. Ben-Tal and R.D. Coalson, J. Chem. Phys. 101,5148 (1994).
4. R.D. Coalson and A. Duncan, J. Phys. Chem. 100,2612 (1996).
5. J.C. Zahorchak, M.G. Kurnikova and R.D. Coalson, "A Molecular Dynamics Study of Photothermal Compression of Colloidal Crystals", submitted J. Chem. Phys (1996).

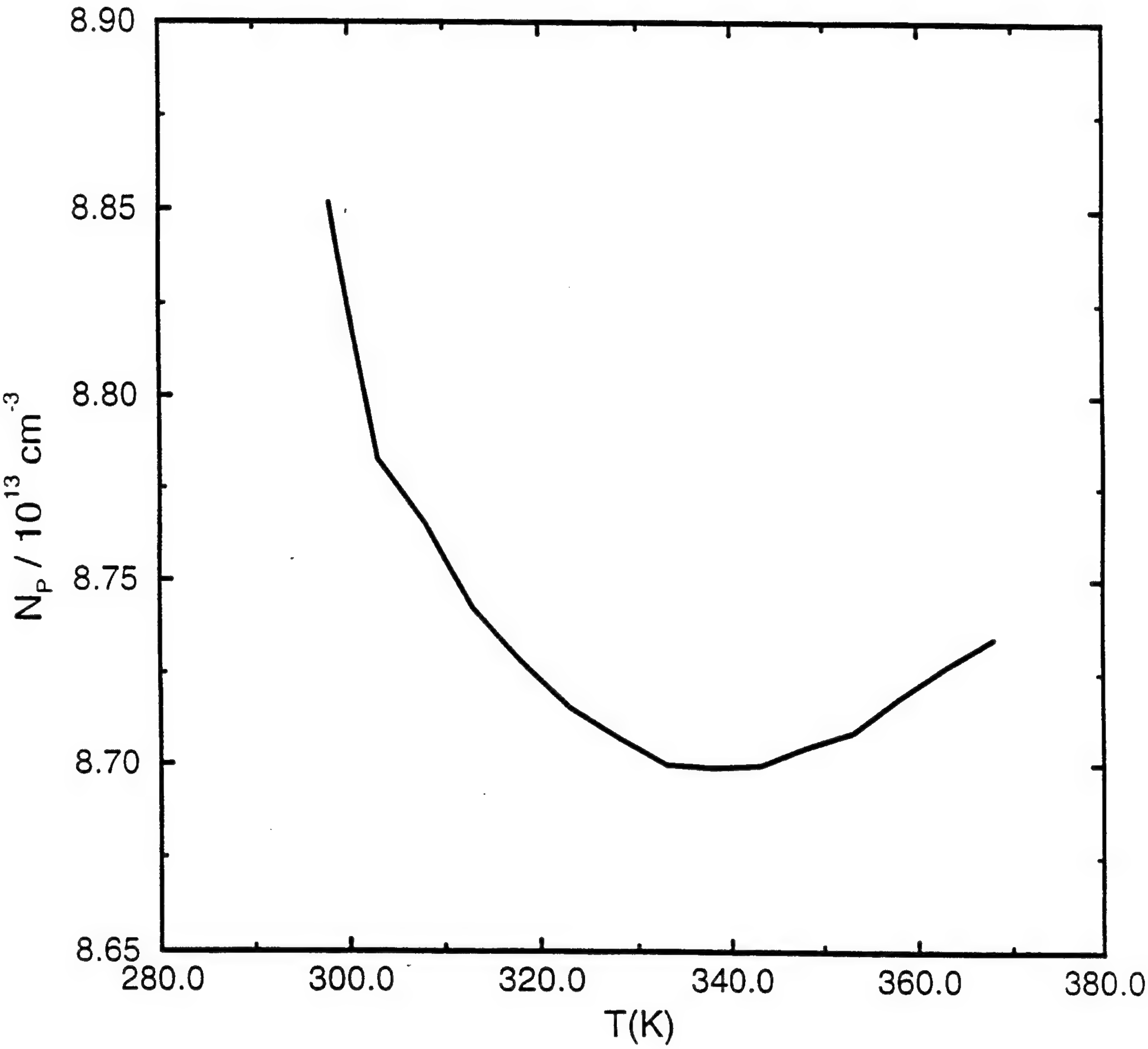

Figure 1: Colloid Crystal Density vs Temperature obtained from Molecular Dynamics Simulations in Ref. 5. Note that initial expansion is followed by lattice contraction at elevated temperatures.

IV.B.8 Determination of Carrier Concentration in n-Type 4H and 6H SiC

Principal Investigator:	Professor W.J. Choyke Department of Physics and Astronomy University of Pittsburgh
Other Faculty Participants:	Professor R.P. Devaty Department of Physics and Astronomy University of Pittsburgh
	Professor D. Langer Department of Electrical Engineering University of Pittsburgh
Students:	Mr. G. Rutsch

IV.B.8.1 INTRODUCTION

Silicon carbide is attracting increasing interest as a semiconductor material for use in high power and high frequency electronics. It is necessary to be able to determine material parameters accurately in order to be able to use the material in devices. One of the most important material characteristics is the free electrical carrier concentration. Characterization methods are well established for the commonly used materials of silicon and gallium arsenide and are often uncritically applied to silicon carbide even though the material is different in many important aspects. The most important one is incomplete impurity ionization at room temperature so that small changes in temperature around room temperature can lead to changes in free carrier concentration. The two most common techniques to determine carrier concentration are capacitance-voltage (CV) and Hall effect measurements. Especially the results of capacitance voltage measurements have often been suspicious at the high and low ends of the doping range. Since capacitance voltage measurements however require comparatively less effort than Hall measurements, it is important to establish under which circumstances capacitance voltage measurements yield results of sufficient accuracy. The overall goal of this study is thus to establish under which circumstances CV and Hall measurements correspond, and how the material characteristics proper to SiC influence both. Recently we have concentrated on determining the significance of the Hall scattering effect; a second order effect that perturbs Hall measurements.

IV.B.8.2 ACCOMPLISHMENTS AND SIGNIFICANCE

Present State of the Investigation

We have constructed a setup for performing Hall and CV measurements between 90 and 800K. We have recently been able to acquire a used electromagnet that provides a higher magnetic field (up to 0.75 T compared to 0.35 T) that is also more stable. Our capacitance

bridge can perform measurements form 5Hz up to 13 MHZ with a bias up to 42 V. Both Hall and CV measurements are routinely performed.

Temperature Dependent Hall Measurements

While testing the setup in the Hall effect configuration, the measured activation energies for the most common n-type dopant in SiC, nitrogen, in the 4H modification of SiC were found to be higher than expected. The electrical activation energy of impurities in semiconductors is usually observed to decrease by Bardeen's rule from a maximum at low concentrations to zero, a metallic state, proportionally to the cube root of the dopant concentration. Optical measurements consistently give a maximum activation energy. It was thus very surprising to electrically determine activation energies that are higher than those determined optically by up to thirty percent. Careful scrutiny of our apparatus and analysis methods did not lead to the detection of any irregularities. In fact, these abnormal values have been measured by at least two other groups[1,2]. An exchange of samples led to very close results.

The Hall Scattering Factor

Impurity activation energies are determined by fitting the neutrality equation to a set of carrier concentrations measured as a function of temperature. This equation contains several material parameters. These are the density of states effective mass, the number of equivalent conduction band minima, and the Hall scattering coefficient. While the first two have been measured by cyclotron resonance techniques, and independently calculated using band structure theory and can thus be considered known, the Hall scattering coefficient was not. The Hall scattering coefficient r_H enters into the relationship between the measured Hall coefficient R_H and the free carrier concentration n by $R_H = r_H / (n e)$, where e is the electron charge, and has been known to vary in other materials between approximately 0.7 and 1.4 depending on temperature and impurity content of the material. Theory[3] predicts that r_H approaches unity in the limit of high magnetic fields, so that $r_H(B) = R_H(B) / R_H(\infty)$, assuming n does not vary with field. According to energy dependent relaxation theory[1], the crossover between low and high field limits of r_H is $\mu_D B \approx 1$, where μ_D is the drift mobility. We have measured the Hall scattering coefficient in 4H SiC and 6H epitaxial layers.

Measurement Setup

The highest room temperature mobility observed in 4H silicon carbide is 948 cm^2/Vs. It is higher at low temperatures. In our laboratory, we have a superconducting magnet that this capable of providing 9T, so we can only hope to observe saturation of the Hall scattering coefficient at low temperatures where $\mu B > 1$. This magnet originally served in a far infrared light absorption experiment. A new sample holder insert was constructed that allows electrical measurements from liquid helium to room temperature with accurate temperature measurement (Figures 1, 2). A commercial insert proved inadequate for this experiment. Temperature stability to 30 mK has proven to be crucial to obtain reliable data especially at low temperatures, because the Hall scattering coefficient is a relatively small effect (< 40%) modifying a primary effect that varies exponentially versus 1/T. The sample is mounted on a sapphire disk with a mica insulated copper holder to insure good thermal contact and has two thermal shields to

prevent thermal gradients from forming and to impede heat flow into the liquid helium reservoir cooling the superconducting magnet (Figure 2). The instrumentation is a Keithley high resistivity Hall effect measurement setup augmented by a high sensitivity voltmeter.

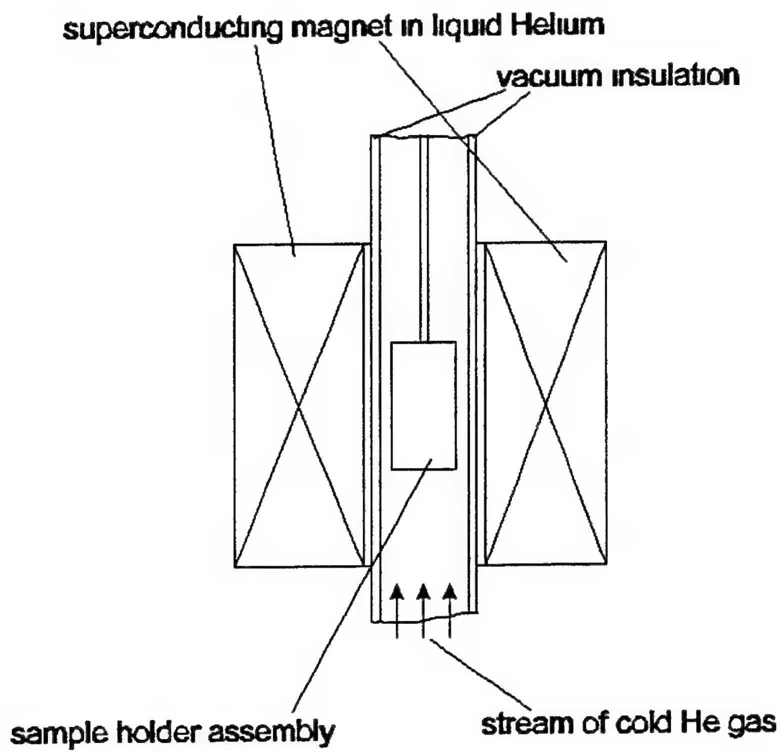

Figure 1: Sample holder assembly in the superconducting magnet

The Hall coefficient R_H, as measured by the van der Pauw technique, varies with magnetic field in all samples. Since high field saturation was not observed even at 9 T, the normalizing factor $R_H(\infty)$ was replaced by either the value of a minimum in the measurement of R_H *versus* B if one was observed at high fields, or the value of R_H at $B = 9$ T to obtain the curve for a representative 4H SiC sample shown in Figure 3. We interpret the upturn observed at the highest fields as field-induced freeze out of the conduction electrons[4]. We observe an inflection point in the measured r_H as a function of B curves that is located approximately where $\mu B = 1$ consistent with theory. In 4H SiC, the observed Hall scattering factor is larger than unity consistently at the lowest temperatures, smaller than one at high temperatures, and varies between 0.92 and 1.21. The data scatter is significant at low fields because the signal is pro-

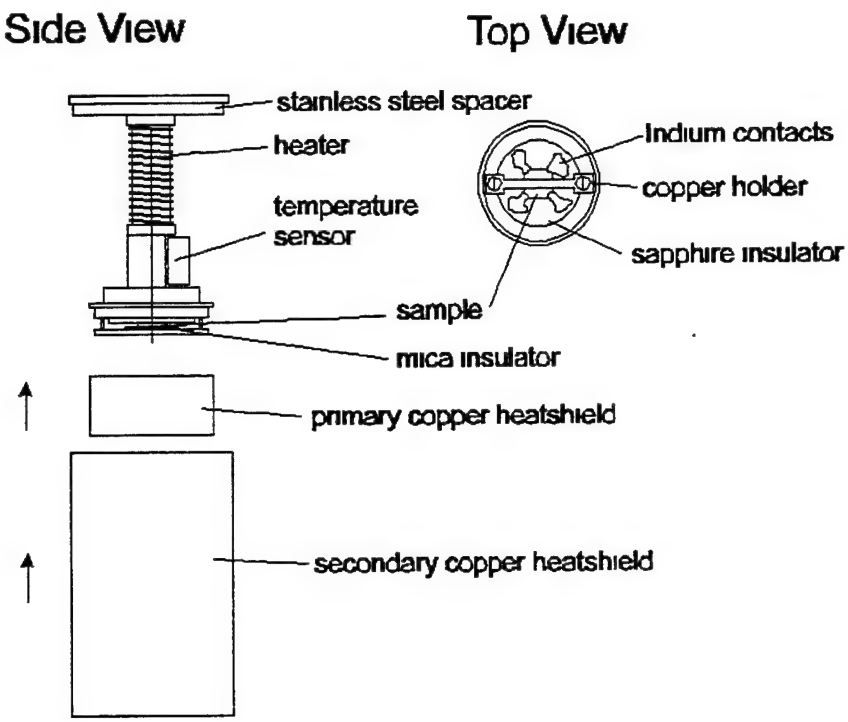

Figure 2: Sample holder assembly

portional to the magnetic field strength and the Hall scattering coefficient is proportional to a small difference between two large numbers.

A comparison of uncorrected (assumed $r_H = 1$) low field Hall data with data corrected with the measured Hall scattering factor reveals that low field measurements lead to an overestimation of N_D - N_A and activation energies in 4H SiC. The difference in activation energies is not large enough to explain the difference between values obtained from optical and Hall effect experiments which is as high as 15%.

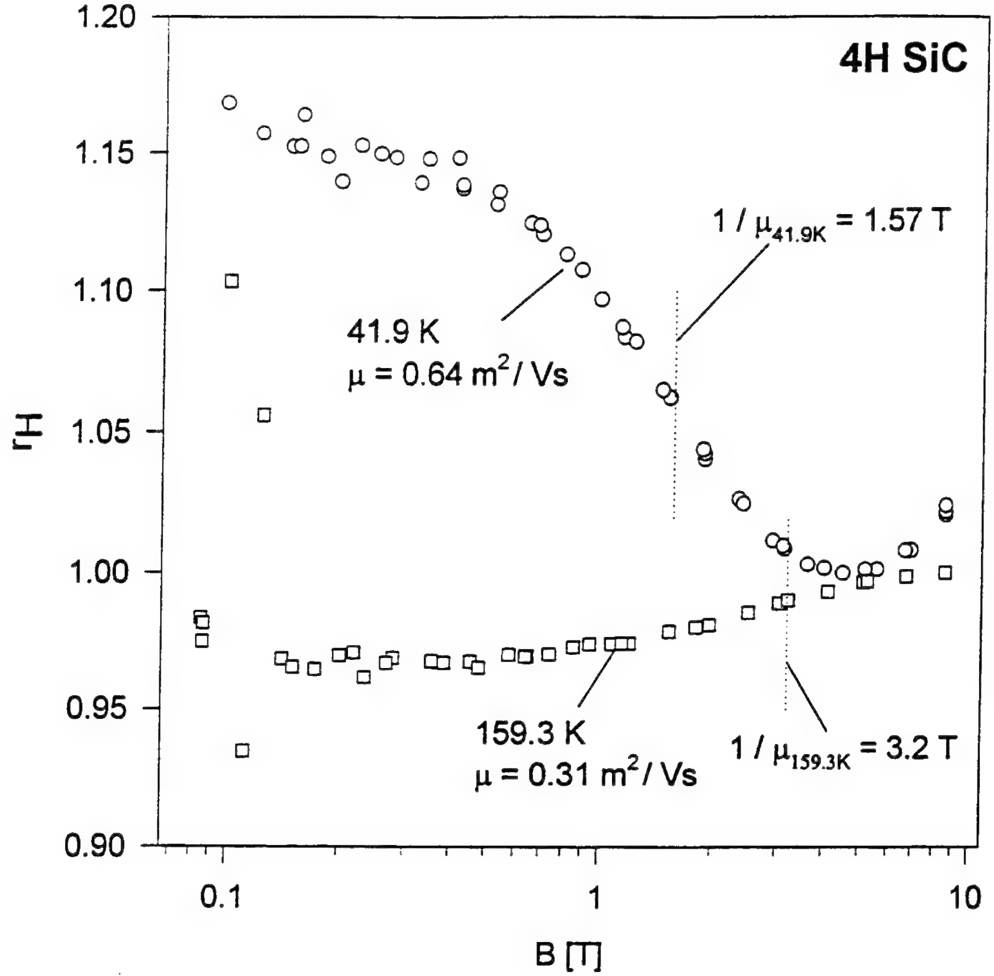

Figure 3: Hall scattering factor r_H, as a function of magnetic field in Tesla of a 4H SiC sample with n(295K) = 5.9 10^{15} cm^{-3} at 41.9K and 159.3K.

Present and Future Work

We are currently performing a similar study in 6H SiC. The only samples with sufficient mobility to be able to observe saturation of the Hall effect are n-type epitaxial layers on p-type substrates. The samples investigated so far proved to be unsuitable do to excessive substrate current leakage at low temperatures.

CV measurements will then be performed on these and further samples. Theoretical modeling of the electron mobilities and Hall scattering factor in 4H SiC is also under way.

REFERENCES

1. A. Itoh, *Control of Electrical Properties of 4H-SiC Grown by Vapor Phase Epitaxy for Power Electronic Application*, Ph.D. Thesis, Kyoto University, 1995.
2. T. Troffer, University of Erlangen-Nürnberg, private communication.
3. P. Blood, J.W. Orton, *The Electrical Characterization of Semiconductors: Majority Carriers and Electron States*, p. 120, Academic Press, London, 1992.
4. J. Appel. *Z. Naturforsch.* 11a, 689, 1956.

IV.C CATALYSIS

IV.C.1 Catalytic Materials for Air Pollution Abatement

Principal Investigator: Professor W. Keith Hall
Department of Chemistry
University of Pittsburgh

Other Faculty Participants: Dr. E.A. Lombardo
Visiting Professor
University of Santa Fe, Argentina

Students: Dr. X. Feng

IV.C.1.1 INTRODUCTION

There is a perceived need for catalysts that will reduce NO to N_2 in the presence of O_2. Such catalysts will be required for the lean -burn engines of the future, and for diesel applications. Suitable catalysts for the selective reduction in the presence of excess O_2 (the SCR process) have been discovered during the last decade, but their useful lifetimes and durability are generally inadequate for commercial application. The underlying problem is that these are zeolitic catalysts and, like other aluminosilicate materials, are unstable in high temperature steam. Yet they must function in these conditions because of the H_2O produced in combustion processes.

Our previous work has focused in three areas: (a) the materials science of the catalyst; (b) the nature and function of the catalytic sites, and the possible intermediates that form thereon, and (c) the reaction mechanism(s) operative in SCR. The first has been directed towards characterization of the changes in composition and structure of the catalyst occurring in the presence of the reacting gases, and the accompanying effects on catalytic activity and selectivity. The second has involved physical characterization of catalysts of varying composition and the changes that occur as a function of pretreatment using various probe molecules in spectroscopic examinations. Physical tools employed include TEM, XRD, IR, UV-Vis, EPR and MAS-NMR spectroscopies as well as measurements of changes in the stoichiometry of the labile oxygen involved in the redox reactions. The third has been directed towards understanding the chemistry occurring during the reaction.

IV.C.1.2 RESEARCH OBJECTIVES

The goals of our work were (a) to develop catalysts that are both sufficiently active for the SCR process and sufficiently durable for practical application; (b) to establish boundary conditions under which these catalysts may be operated for 100,000 miles (or 2500 hrs @ 40 mph) without serious deterioration and (c) to isolate the sources of catalyst deactivation.

IV.C.1.3 ACCOMPLISHMENTS AND SIGNIFICANCE

Research under this program has: (a) led to the discovery of a way to prepare a catalyst that is sufficiently durable to be potentially useful for industrial practice[1-3]: (b) provided understanding of ways in which damage to the zeolite structure and its active centers can occur; and (c) suggested ways to prevent it. In Figure 1 a comparison is made of overexchanged FeZSM-5 with the benchmark CuZSM-5 catalyst on which most of the research in this area has been carried out. It is shown that (a) the former is intrinsically more active than the latter and much more resistant to poisons (H_2O and SO_2). Moreover, it was found that the selectivity for N_2 formations vs. combustion was greatly enhanced by added H_2O over this catalyst.

Interestingly, it was discovered that catalysts prepared from the Na^+ form of the zeolite in a way designed to avoid putting hydrogen on the base-exchange sites were much less susceptible to dealumination and consequently to lattice breakdown than those made from HZSM-5. Hence, our CuZSM-5 catalysts (made from NaZSM-5) were much more durable than those reported by Montreuil et al[4], who studied a 67% exchanged preparation made from HZSM-5. We suppose that the fairly large fraction of the base-exchange capacity of their catalyst that was charge-compensated by bridging OH groups (Brønsted sites) can account for this discrepancy.

In experiments made without added H_2O the exiting gases contained about 1% H_2O. Tests were made with CuZSM-5 starting with about 55% conversion of the NO to N_2 (Fig. 1). When about 20% H_2O was added to the feed stream the conversion dropped to about 3%; on removing the added H_2O the activity was restored to its initial value showing that the poisoning was reversible. When an FeZSM-5 catalyst was tested in a similar experiment, no poisoning by up to 20% H_2O was observed. Further, introduction of 150ppm of SO_2 to the feed had no effect whereas the CuZSM-5 catalyst was irreversibly poisoned (see Figure 1). The times employed in these experiments were equivalent to the Federal mandate for practical application to motor vehicles (100,000 miles or 2500 hrs @ 40 mph). So far we have explored only one feed stock. We anticipate possible complications when olefins are used rather than the cleaner burning paraffins. Moreover, in the course of our research we have learned that the preparation variables are extremely critical in obtaining a good catalyst. For example, NaZSM-5 prepared by the template free method yielded superior catalysts to those made using templates. Not all of our preparations were equally good. In a search for uncontrolled variables, we have discovered that pretreatment with O_2 at 500°C may lead to formation of Fe_3O_4 or Fe_2O_3 coupled with partial or complete deactivation. This may be contrasted with the data of Fig.1 where stability is maintained for long periods of time under typical SCR conditions. It is our objective to understand ageing in the SCR process in scientific terms and to use this information to develop still more superior materials for this purpose.

IV.C.1.4 SUMMARY

Our most significant accomplishments:

- The discovery of the advantages of using oxylate salts for base-exchange.
- The establishment of procedures and techniques of assaying the effects of steam on zeolite structure and stability.

- The establishment of boundaries where (subject to further testing) a particular preparation may be usefully employed, and where it cannot.
- The discovery that control of chemical composition has a profound effect on durability and the development of a much superior composition of enhanced stability and activity, viz., overexchanged FeZSM-5.
- The finding that the SCR reaction is seriously inhibited by excess H_2O vapor pressure over CuZSM-5 catalysts whereas it is not over FeZSM-5. Such water would be present in combustion streams from the fuel burned to produce energy.
- The use of Mössbauer spectroscopy to study the redox behavior of the system and the forced segregation of oxide phases.
- The indication that other materials may function satisfactorily as catalysts without serious inhibition.

IV.C.1.5 REFERENCES

1. U.S. Patent Application Serial No. 08/634, 233 entitled "Improved Catalyst for Purifying the Exhaust Gas from Combustion in an Engine and Methods of Making the Same," recorded July 22, 1996.
2. X. Fend and W.K. Hall, "On the Unusual Stability of Overexchanged FeZSM-5," Catal. Lett., 41, 45 (1996).
3. X-Feng and W.K. Hall, "FeZSM-5: A Durable SCR Catalyst for NO_x Removal from Combustion Streams,: accepted by J. Catal., on 11/18/96. Paper presented at 212th Meeting, the American Chemical Society, Orlando, FL, August 1996.
4. R.A. Grinsted, H.W. Jen, C.N. Montreuil, M.J. Rokosz and M. Shelef, Zeolites, 13, 602 (1993).

Comparison of FeZSM-5 with CuZSM-5

a.

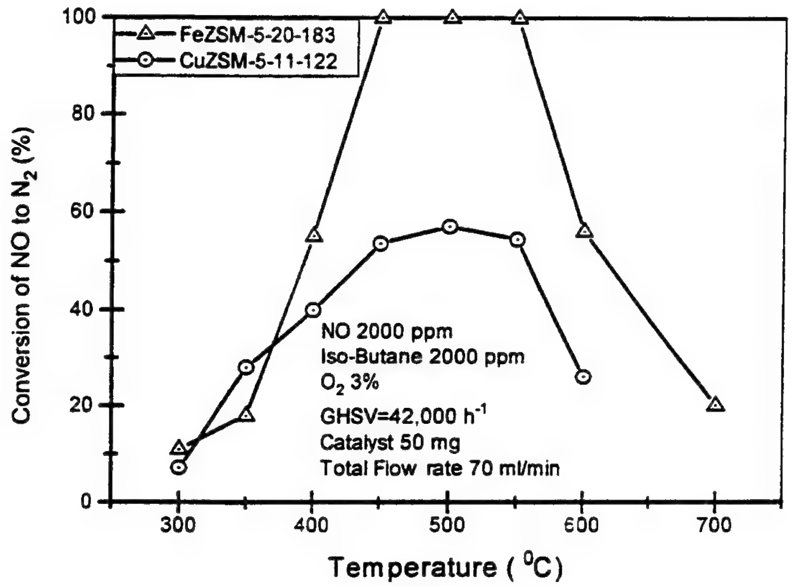

Durability Test of FeZSM-5 over 2500 hr

b.

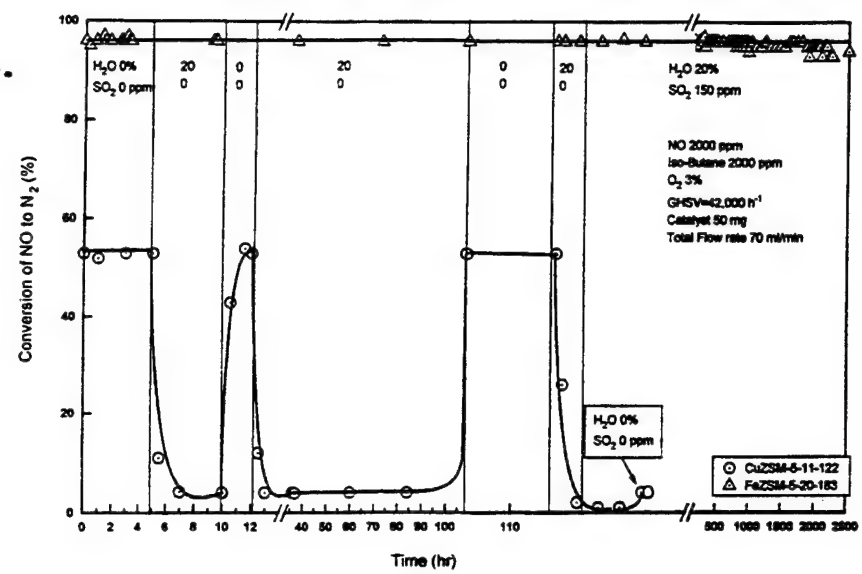

Figure 1: In the top graph the FeZSM-5 catalyst is twice as efficient as the CuZSM-5 between 450-550°C. In the lower graph at 500°C, the FeZSM-5 catalyst is stable and shows no poisoning by steam nor SO_2 during 2500 hr of operation. The CuZSM-5 catalyst however was only half as efficient, and was poisoned by both H_2O and SO_2.

IV.C.2 Hydroxyapatite and Fluorohydroxyapatite for the Oxidative Catalytic Decomposition of Nerve Gases

Principal Investigator: Professor N.G. Eror
Materials Science and Engineering Department
University of Pittsburgh

Other Faculty Participants: Dr. W. K. Hall
Department of Chemistry
University of Pittsburgh

Dr. J. d'Itri
Department of Chemical Engineering
University of Pittsburgh

Student: Mr. T. Palucka

IV.C.2.1 INTRODUCTION

Previous work by our group has shown hydroxyapatite (HA) to be an effective catalyst for the oxidative decomposition of the nerve gas simulant dimethyl methylphosphonate (DMMP). A typical nerve gas is a fluorine-containing phosphonate ester having the general composition $R_1R_2FP{=}O$, where R_1 and R_2 are alkyl or alkoxy groups, and R_1, R_2, F, and O are all bonded to the central P atom. In DMMP, R_1 and R_2 are CH_3O groups, and F is replaced by a CH_3 group, yielding a chemical formula of $(CH_3O)_2CH_3P{=}O$. The reaction of interest is:

$$(CH_3O)_2CH_3PO + \left(\frac{x}{2}+\frac{15}{4}\right)O_2 \rightarrow 3CO_2 + \frac{9}{2}H_2O + PO_x$$

Complete oxidation to CO_2 and H_2O is desired for protection of human beings; the period during which all DMMP is converted to these products is thus called the "protection period." When oxidation of DMMP is less than complete, or where hydrolysis takes place, less desirable products such as carbon monoxide, methanol, and dimethyl ether may be obtained. The PO_x species tends to remain on the surface and acts as a poison; it can react with water to form H_3PO_4.

Samples of HA and fluorohydroxyapatite (FHA) can be synthesized with surface areas greater than 200 m^2/g. These samples differ from low surface area (<50 m^2g) samples in total pore volume. High surface area samples lose active surface area by two means: 1) coverage by phosphorus-based poisons; and 2) closing of pores due to thermal sintering. The amount of dimethyl ether generated during the reaction increases with increasing surface area for unplatinized HA samples.

Platinum (or some other transition metal) must be a component of any practical catalyst system for the decomposition of nerve gases. When platinum is present, the desired reaction products of CO_2 and H_2O are obtained; when the active platinum surface area is covered by

poisons, the catalyst reverts to the behavior of unplatinized HA and FHA samples, yielding methanol and dimethyl ether as products.

IV.C.2.2 ACCOMPLISHMENTS

The amount of methanol generated by apatite samples containing no platinum increases linearly with fluorine substitution when a pretreatment temperature of 773 K is used. For a 573 K pretreatment temperature, this methanol increase is only observed above 50% fluorine substitution. (See Figures 1 and 2).

Figure 3 shows the percent DMMP conversion versus time for the 139 m^2g HA series, (HA139, 1.2PtHA139, and 2.4PtHA139), with protection periods of 0.6, 2.1, and 10.1 hours, respectively. It is interesting to note the similar protection periods for the PtHA sample (10.5 hours) and the 2.4PtHA139 sample (10.1 hours). The fact that the 2.4PtHA139 sample had approximately 1.7×10^{19} Pt atoms on the surface versus 5.7×10^{17} for the PtHA sample suggests that there is a limit to the number of surface Pt atoms which can be effective in this reaction; however, since the surface bonding mechanisms are unclear at this point (do DMMP molecules bond to the catalyst through both the Ca^{2+} surface sites and Pt^{2+} surface sites, or is Pt only active in the dissociation of O_2 molecules?), it is difficult to calculate any limit of effective Pt surface coverage.

The addition of 1.2 wt. percent Pt to the 236 m^2g FHA sample (77FHA236) (to yield the Pt77FHA236 sample) produced some interesting results. Figure 4 shows the DMMP conversion versus time plot for this run, together with that for the 77FHA236 sample itself and a 1.2 Pt/Al_2O_3 sample with a surface area of 213 m^2g. The protection period of about 1.5 hours for the Pt77FHA236 sample showed no increase over the 77FHA236 sample, but the rate of deactivation was markedly reduced by the addition of Pt. Indeed, at 20 hours the sample was converting at approximately 70%; at 49 hours a conversion of 30% was still being obtained. The 1.2 wt % Pt on γ-Al_2O_3 sample had a protection period of approximately 15 hours, but had deactivated to less than 20% conversion after 29 hours. In terms of reaction products, the Pt77FHA236 sample converted all of the DMMP to CO_2 during the protection period; the rate of CO_2 formation dropped slowly after that, until it finally disappeared approximately 30 hours into the run. This is in contrast with all the other PtHA or PtFHA runs, in which CO_2 production fell far short of 100 percent conversion and dropped rapidly to zero after the protection period. Methanol was the only other product, slowly climbing to a maximum of 20 percent carbon conversion at 31 hours into the run.

While the protection period of the Pt77FHA run was unexpectedly short, possibly due to poorly dispersed Pt, the slow deactivation period is of interest, since it might provide some clues as to how to render these catalysts less susceptible to poisoning. The fact that poisoning was rapid on the Pt26FHA, Pt52FHA, Pt79FHA, and Pt99FHA runs seems to rule out any effect due to interaction of Pt with the F^- in the FHA. Further studies are necessary to determine the mechanism of this slow poisoning effect.

The results of the reaction studies indicate that HA or FHA samples by themselves only serve to adsorb the DMMP through the lone pair of electrons on the P==O: group; the bonding site is most likely a surface Ca^{2+} ion (Figure 5). This is followed by the dissociation of a

methoxy side group through adsorption to another surface site, which provides the additional proton to convert the methoxy group into methanol, which leaves the surface as a reaction product. It is apparent that the O_2 molecules do not participate in the reaction to give oxidation products when no transition metal is deposited on the surface. The fact that oxidation does take place in the presence of Pt suggests that the Pt serves to dissociate the O_2 molecules into O^{2-} ions, which then react with the surface methoxy groups to yield the desired reaction products CO_2 and H_2O. This is a simplified scheme; it is also possible that DMMP may adsorb to a Pt site. Fundamental adsorption studies need to be done on the Pt/HA system.

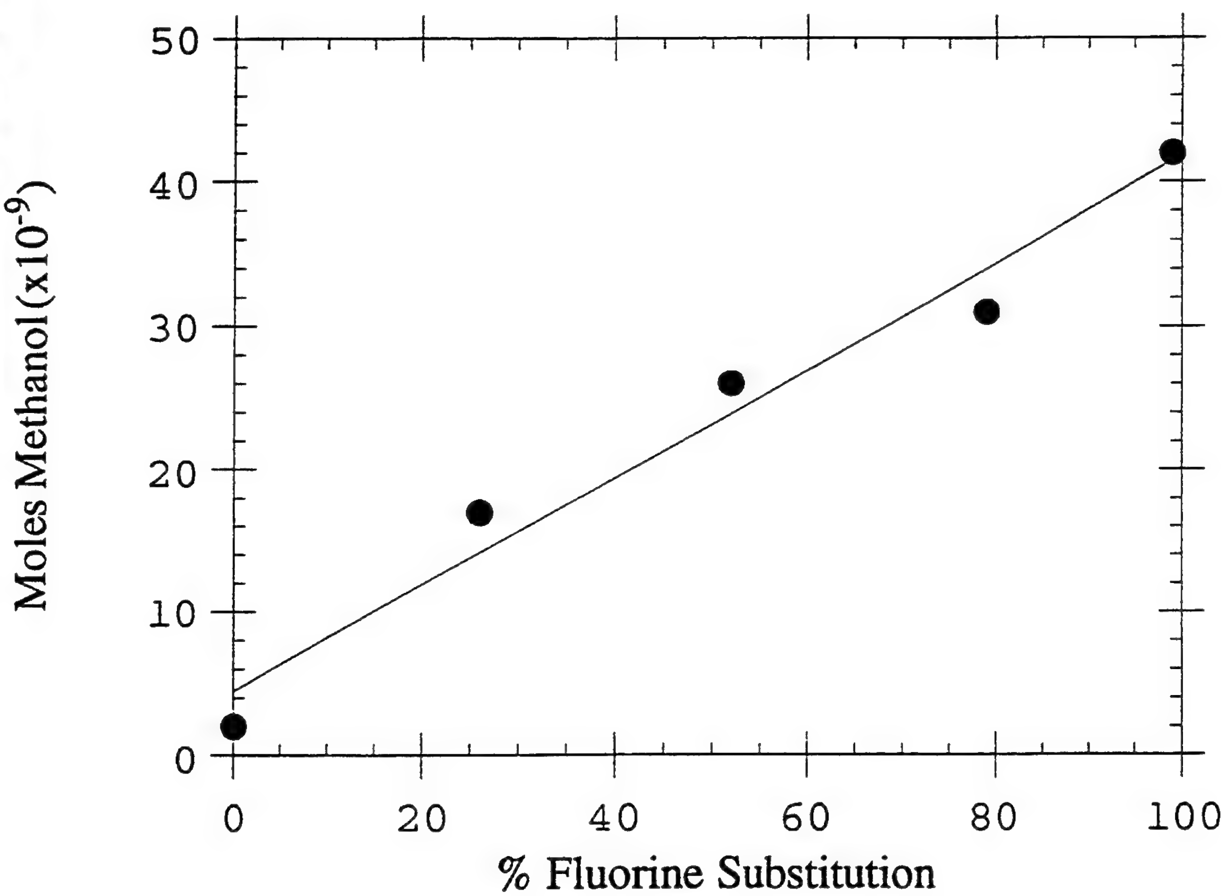

Figure 1 Amount of methanol generated versus percent fluorine substitution for the complete low surface area HA/FHA series of samples run with a pretreatment temperature of 773 K

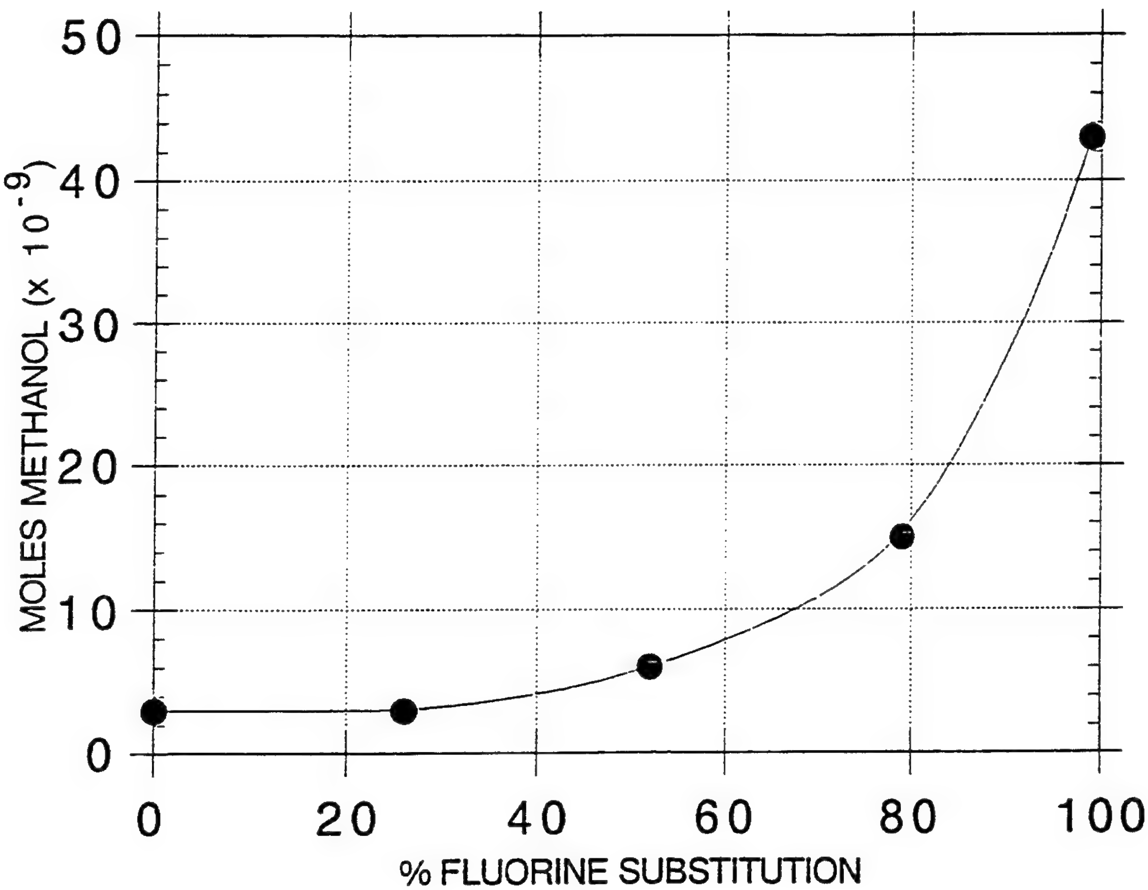

Figure 2 Amount of methanol generated versus percent fluorine substitution for the complete low surface area HA/FHA series run with a pretreatment temperature of 573 K

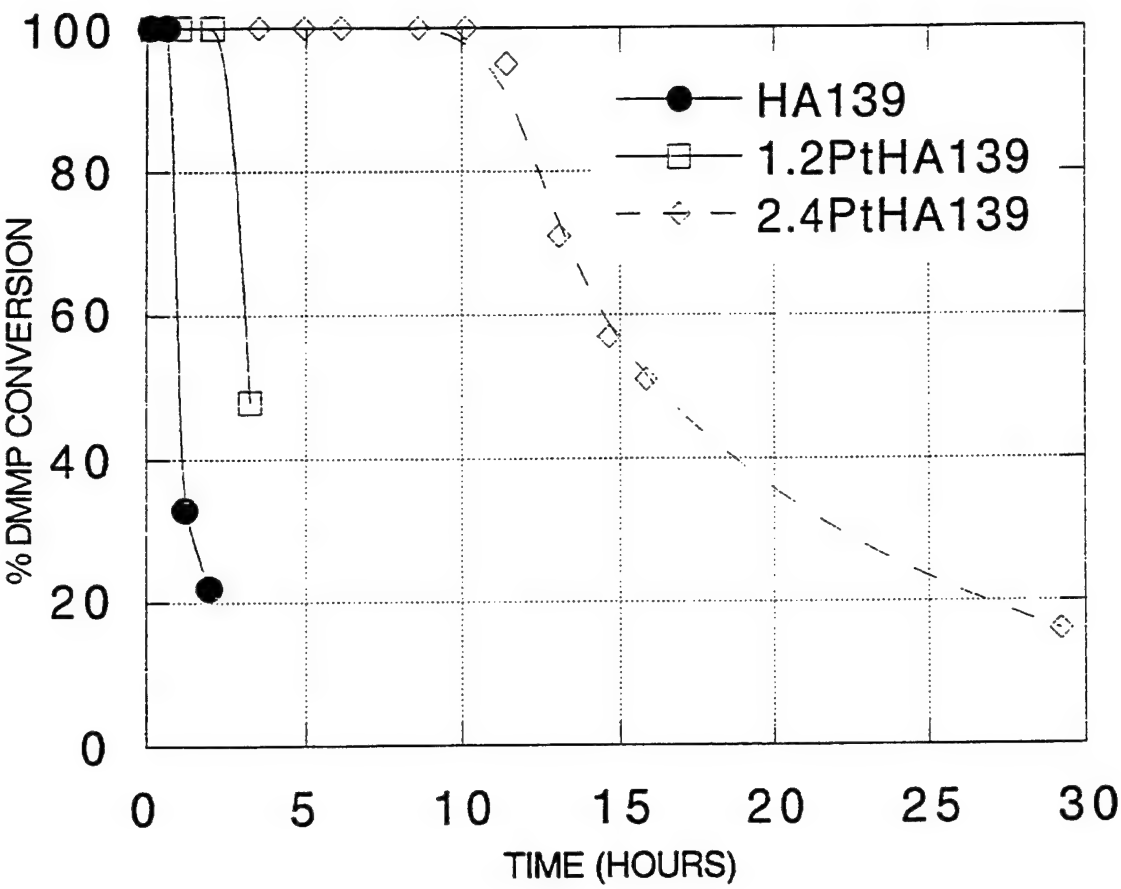

Figure 3 Percent DMMP conversion versus time for the HA139, 1.2PtHA139, and 2.4PtHA139 series of samples

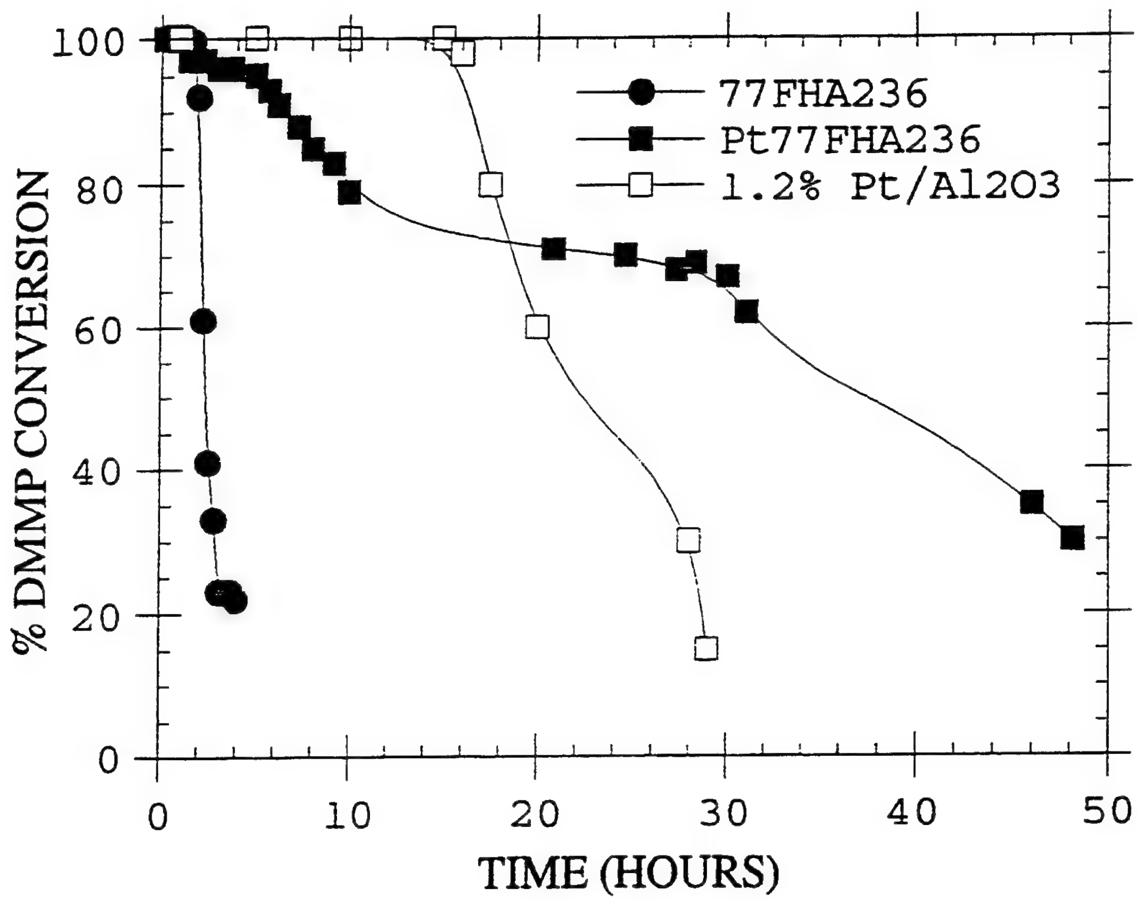

Figure 4 Percent DMMP conversion versus time for the 77FHA236, Pt77FHA236 and 1.2%Pt/AL_2O_3 series of samples run at a temperature of 573 K

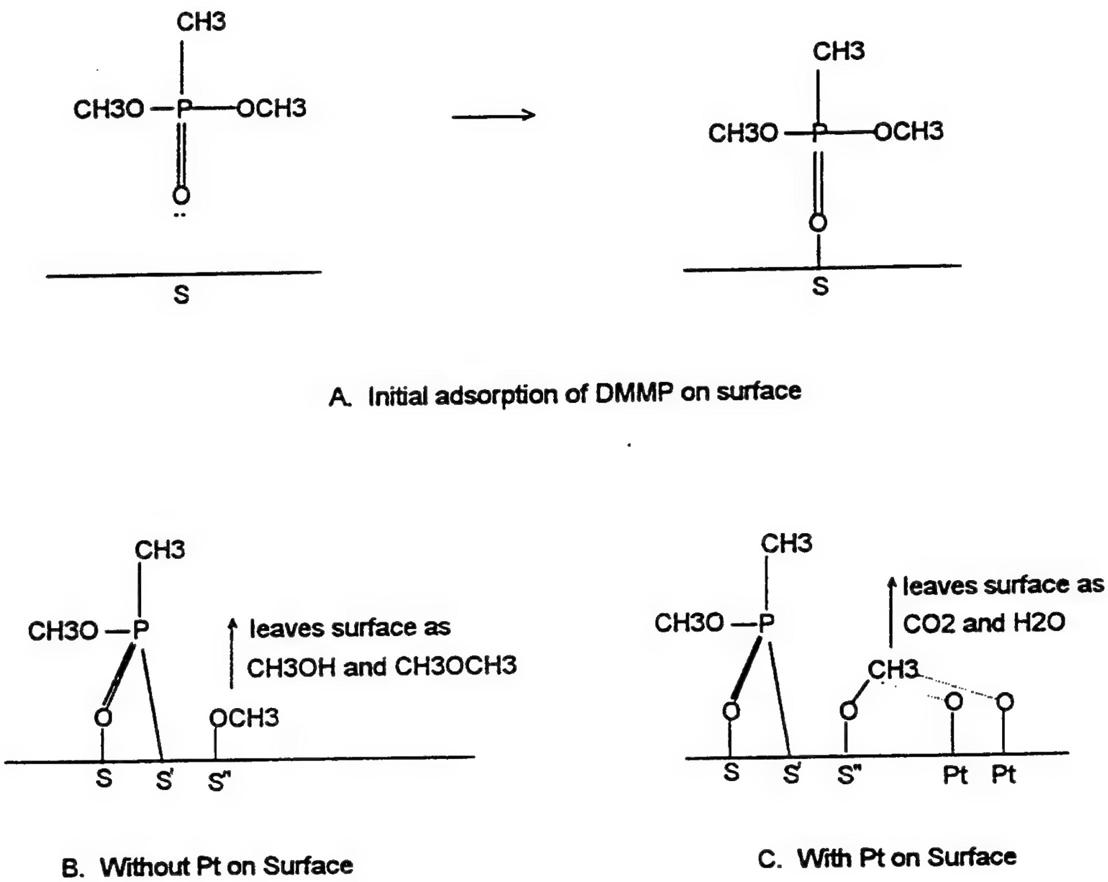

Figure 5 Proposed reaction mechanism for decomposition of DMMP

IV.C.3 Dechlorination of Chlorofluorocarbons

Principal Investigator: Professor Julie L. d'Itri
Chemical and Petroleum Engineering Dept.
University of Pittsburgh

Other Faculty Participants: Dr. W. Keith Hall
Chemistry Department
University of Pittsburgh

Students: Mr. K. Early

IV.C.3.1 INTRODUCTION

The primary starting materials for the production of CFC alternatives have been CFCs themselves[1]. The successful synthesis of HFCs requires highly selective catalysts to replace chlorine atoms in specific locations with hydrogen atoms. The catalyst of choice for these reactions is palladium particles supported on various high surface area materials such as alumina, activated carbon, and aluminum fluoride[2]. The limited stability of these catalyst results in a decrease in catalytic activity with time on stream and, under some conditions, an increase in the undesired partially chlorinated or fully dehalogenated molecules. Our approach to understanding the factors which affect catalytic activity and selectivity is to combine reaction investigations with physical and chemical characterization studies to provide a detailed picture of the surface chemistry.

The objective of this research program is to probe the fundamentals of CFC hydrodechlorination reactions to produce HFCs and then proceeds to use this understanding for the rational design of new catalytic materials with improved performance and selectivity. Particular focus is centered on establishing the factors which affect catalyst lifetime. The reaction of interest has been the hydrodechlorination of CF_3CFCl_2 to form CF_3CFH_2. The primary objectives are listed below:

(1) Prepare a series of catalysts in which either the metal particle size is varied or the type of support material.

(2) Establish the rate expression, kinetics parameters (E_{act}, k_o), and reaction mechanism for the hydrodechlorination of 1,1-dichlorotetrafluoroethane.

(3) Determine the change in catalyst composition and structure as a function of time on stream.

(4) Tailor existing catalysts to stabilize reaction performance.

IV.C.3.2 ACCOMPLISHMENTS AND SIGNIFICANCE

During the past year we have applied a combination of reaction kinetics investigations and characterization of catalysts by FTIR spectroscopy to investigate the hydrodechlorination of CFCs' using Pd supported on Al_2O_3 and fluorinated-Al_2O_3 (fluorination of 10% or less). Similar to the hydrodechlorination of CF_2Cl_2, the selectivity to the desired product (CF_3CFH_2) is higher for Pd/F-Al_2O_3. At early time on stream the Al_2O_3 catalyst is more active than the fluorinated alumina; however, the activity rapidly decreases. Correspondingly, the concentration of hydroxyl groups at the surface of the alumina decreases during the early stages of the reaction. These results suggest that the reaction chemistry can be separated into two distinct regimes: early time on stream during which both the support and the metal participate in the reaction and long time on stream during which the metal is responsible for the catalytic activity. Figure 1 shows the FTIR spectra for the hydroxyl region for a 1 wt% Pd/Al_2O_3 catalyst. The fresh catalyst (a) shows a high concentration of hydroxyl species. The reaction consumes the surface hydroxyl species as seen in the decrease in intensity of the observed peak (b). This change is irreversible; re-reducing the catalyst does not result in an increase in the intensity of the hydroxyl peaks (c).

Experimentation directed at understanding the reaction mechanism has shown that high H_2 partial pressures are needed to avoid deactivation, and steady state is obtained after ~5 h time on stream. Under these conditions (H_2/CFC feed ratio = 20) the reaction is zero order in H_2 partial pressure and positive (0.65) order in 1,1-dichlorotetrafluoroethane partial pressure. Three main products are formed: 1,1,1,2-tetrafluoroethane, 1-chloro-1,2,2,2-tetrafluoroethane, and 1,1,1-trifluoroethane, with approximately 85% selectivity towards the desired CF_3CFH_2. The apparent activation energies associated with the formation of each product range from 52 to 68 kJ/mol. Given that these activation energies are similar in value, we are speculating at this time that the major products share a common rate limiting step. This hypothesis is currently being tested through kinetics modeling. More importantly, all three major products have a non-zero rate of formation in the limit of zero conversion, the implication of which is that all are primary products. The kinetics results are consistent with a reaction mechanism involving a carbene intermediate.

One of the more exciting aspects of the research to date is the possibility of a carbene intermediate. We are presently exploring this aspect of the reaction chemistry by FTIR. The impact of this finding is quite significant in that we now can explore routes to favor carbene coupling reactions - thus, the opportunity exists to convert chlorinated materials into high value compounds such as olefins.

IV.C.3.3 SUMMARY

Our primary accomplishments over the MRC grant period have been:

(a) To develop a detailed understanding of the role of the Al_2O_3 support in the hydrodechlorination of CF_3CFCl_2.

(b) Identify primary and secondary products in the reaction network which has been useful in probing the reaction mechanism.

(c) Develop a reaction mechanism which consists of elementary dehalogenation steps of a surface halocarbon species. Hydrogenation and subsequent desorption of the species at any stage of dehalogenation is the last step in the reaction; viz., readsorption and reaction does not occur.

IV.C.3.4 REFERENCES

1. Manzer, L.E., Rao, V.N.M. Adv. Catal., 1993, 39, 329.
2. Cognion, J.M. Figueras, F., Tournigant, D.J. Catal. 1993, 141, 21.

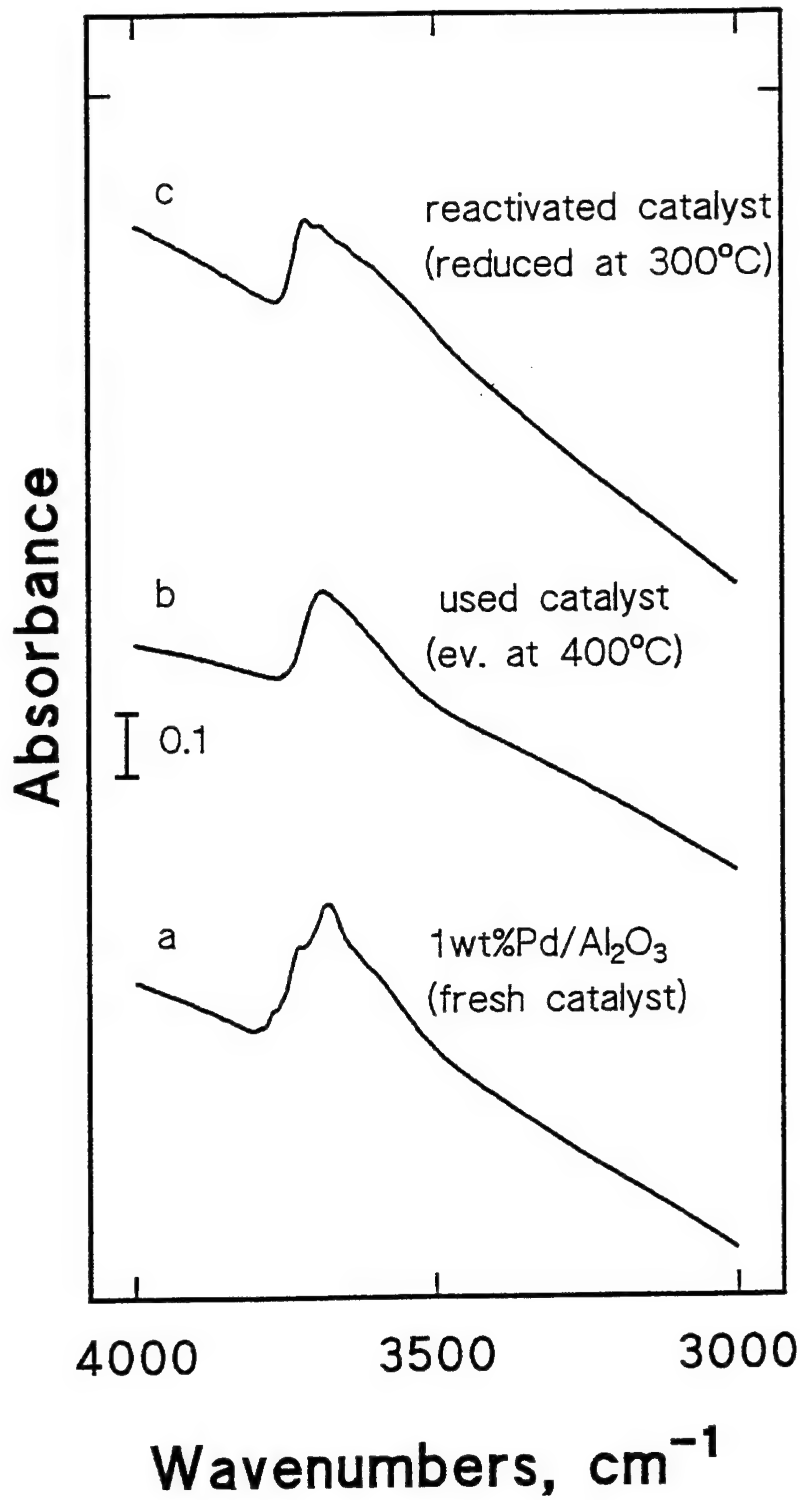

Figure 1. IR-Spectra of the OH-region indicate the irreversible consumption of isolated OH-groups during the reaction.

IV.C.4 Transition Metal Catalysis and Catalysts

Principal Investigator: Professor N. John Cooper
Chemistry Department
University of Pittsburgh

Student: Ms. P. Secrest

IV.C.4.1 INTRODUCTION

The objective of this project is to develop an improved understanding of unitary mechanistic steps which are components of important catalytic sequences. We have focused on the stereochemistry of insertions of simple unsaturated ligands into metal hydride and metal alkyl bonds, as monitored by determining their impact on the stereochemistry of the metal center at which the insertion is taking place.

The significance of this work is that stereochemical control of insertion mechanisms is at the heart of many industrially important catalytic reactions, including chiral hydrogenation and the use of metallocene catalysts to prepare stereoregular polypropylene, but that the intimate details of the mechanistic steps can only be studied in the discrete complexes in which the reactions can be monitored spectroscopically.

The stereochemistry of the insertions is followed by carrying out the reactions at a chiral metal center in a complex which has been rendered diastereotopic through the introduction of a chiral substituent on a cyclopentadienyl ligand. The stereospecificity of the reaction is then determined by following the reaction by ^{1}H NMR, and the absolute stereochemistry is established by X-ray crystallographic determinations of the absolute stereochemistry of the metal center in the starting material and the product. The principle of the experiment is illustrated in Scheme 1:

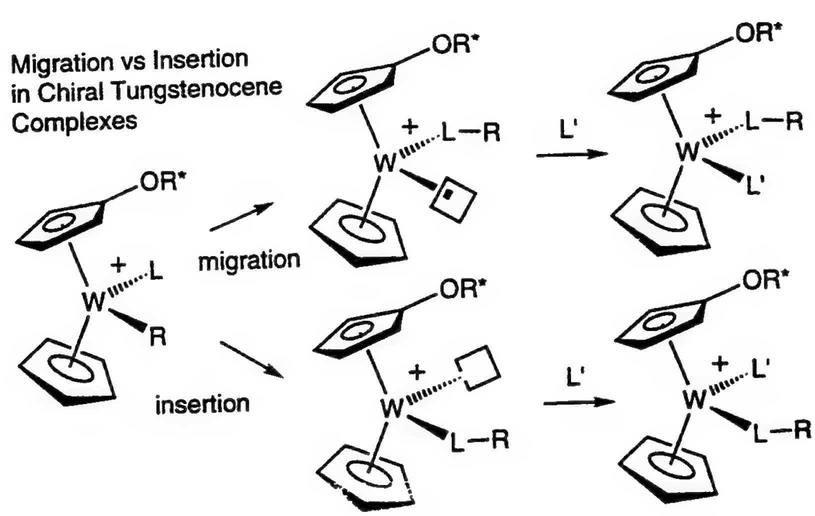

IV.C.4.2 ACCOMPLISHMENTS AND SIGNIFICANCE

In earlier work we had used the addition of a chiral alkoxide with aryl and isopropyl substituents to a cyclopentadienyl ligand in an electrophilic tungstenocene complex to generate a chiral metal center with sufficient stearic discrimination at the metal center to allow the use of NMR as probe of subsequent changes in the stereochemistry at the metal[1].

We have now used this system to determine the stereochemistry of alkylidene/alkyl insertion in the tungstenocene environment by monitoring thermolysis of a single diastereomer of the tungstenocene phosphonium alkyl $[W(\eta^5\text{-}C_5H_5)(\eta^5\text{-}C_5H_4OCHPh^iPr)(CH_2PMe_2Ph)CH_3]^+$. This acts as a labile source of the methylidene methyl complex $[W(\eta^5\text{-}C_5H_5)(\eta^5\text{-}C_5H_4OCHPh^iPr)(CH_2)CH_3]^+$, which then generates a transient 16-electron alkyl complex by alkylidene/alkyl insertion; β-elimination finally generates the observed alkene hydride product $[W(\eta^5\text{-}C_5H_5)(\eta^5\ {}_5H_4OCHPh^iPr)(CH_2CH\ {}_2)H]^+$. NMR and structural studies have established that this sequence occurs with the stereoselectivity shown, implying that the alkylidene/alkyl insertion really involves migration of the alkyl group on to the electrophilic unsaturated carbon of the alkylidene ligand as shown in Scheme 2:

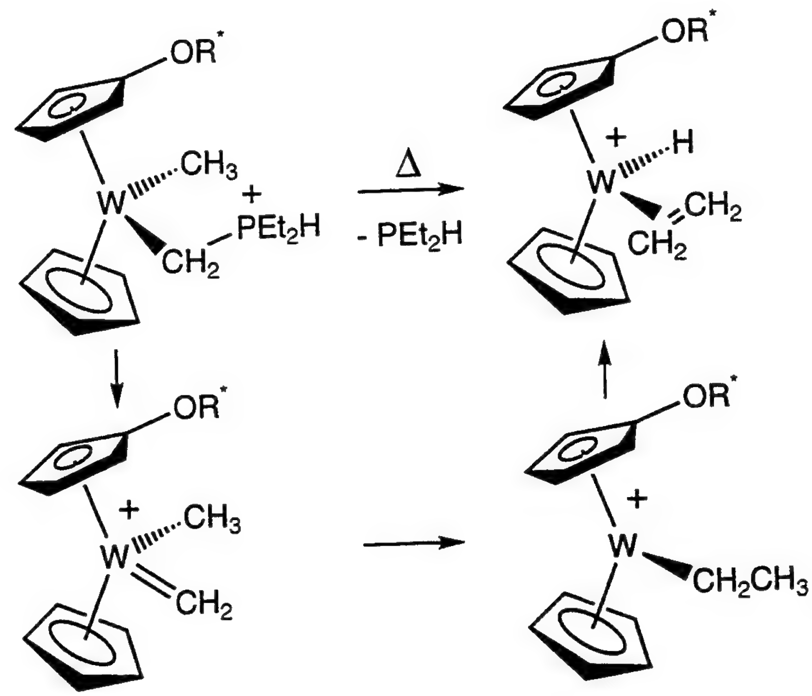

Alkylidene alkyl insertion is well established as unitary step in the Fischer-Tropsch reduction of CO to hydrocarbons, and these experiments constitute the first experimental determination of the stereochemistry of the insertion step.

IV.C.4.3 SUMMARY

Mechanistic studies have established that alkylidene/alkyl insertion in a tungstenocene complex occurs by a migratory mechanism in which the alkyl group moves from the metal to the electrophilic unsaturated carbon.

IV.C.4.4 REFERENCES

1. Nally, J.P., Glueck, D., Cooper, N.J., J. Amer. Chem. Soc. 1988, 100, 4838.

V. NEW INSTRUMENTAL CAPABILITIES

During the period of this grant the following new capabilities were developed at the Materials Research Center.

- Attachments for an existing Atomic Force Microscope have been purchased and are now in use, these attachments include: scanners to permit observations over a larger range of magnifications, scanners to permit observations in liquids, magnetic force capabilities, and a Tektronics color printer.

- A Frequency-Doubled Argon Laser has been purchased and has been installed on a microwave chemical vapor diamond deposition unit at Westinghouse Science and Technology Center.

- Dual arm and parallel beam collimator accessories for the XRD powder machines have been installed. Capabilities have been developed to measure residual stresses in thin films by using four different stress measurement methods.

- A YAG Pulsed Laser has been purchased and installed for measuring the non-linear properties of organometallic compounds.

- A mass spectrometer has been purchased and installed for some of the studies on catalysts.

- A unique infrared pyrometer has been obtained capable of measuring emissivity corrected temperatures and eliminating the impact of radiation originating from surrounding sources hotter than the target.

VI. EXTERNAL AND INTERNAL INTERACTIONS

VI.A Industrial Collaborations

Numerous interactions with industry and other organizations have taken place due to MRC funded research. Additionally cross disciplinary research between numerous faculty has been established or continued. Examples of some of these interactions are described below.

High Performance Materials

- S.A. Asher has been collaborating with Westinghouse and Argonne National Laboratory using in-situ UV Raman Spectroscopy of diamond films. A graduate student is working at Westinghouse on a Master's research program on diamond films.

- F.S. Pettit has joint efforts with Kennametal, Inc. to investigate the wear of diamond films on cutting tools. A Masters' thesis has been completed on the wear of diamond films.

- G.H. Meier has collaborative research with NASA Lewis and Howmet on the effects of sulfur on the oxidation resistance of superalloys.

- G.H. Meier has joint research with the Max Planck Institute für Metallforschung on the use of transmission electron microscopy to study thin oxide layers and the regions of alloys immediately beneath oxide scales. Dr. Ekart Schumann from the Max Planck Institute für Metalloforschung is now at the University of Pittsburgh to perform research with Dr. Meier.

- G.H. Meier and F.S. Pettit have performed research with Dresser-Rand to investigate the effects of oxygen-SO_2 gas mixtures on the mechanical properties of Waspaloy.

- G. Meier and N. Birks have studied the combined erosion-oxidation of hard coatings with Praxair. This has been the topic of a senior project thesis.

- F.S. Pettit has collaborative efforts with WPAFB on the oxidation of Ti-22Al-23Nb at temperatures between 500° to 900°C in oxygen, air, and oxygen plus water vapor.

- G.H. Meier has joint research with Westinghouse Science and Technology Center on the oxidation of superalloys in conjunction with thermal barrier coatings.

- N. Birks is working with the president of Sophisticated Metals of Butler, PA. This is a small firm that specializes in the production of relatively small heats of superalloys. The president, Jim Patterson, is a part-time graduate student on the low sulfur project.

- RMI Titanium Alloys donated the near γ-TiAl for A.J. DeArdo's thermomechanical processing investigations.

- E. Beckman has generated additional funding for his MRC grant project from the Pittsburgh Tissue Engineering Institute, and has recently also signed a contract with RIK Medical Co. of Boulder, CO to investigate generation of microcellular polymer spheres. Finally, he has begun a collaboration with Norsk Hydro (Oslo, Norway) to generate microcellular thermoplastics using CO_2.

- J. Blacheré has been doing collaborative X-ray diffraction on cobalt thin films for hard drive applications with Seagate Recording Media.

Optoelectronics

- D. Langer and J. Falk have had contacts at Wright Laboratories, and MIT Lincoln Laboratory.

- W.J. Choyke works with many people all over the world on SiC, in particular with Northrup-Grumman (formerly the Westinghouse SiC group).

- J. Cooper and M. Hopkins have discussed their new azophenoxy dyes with 3M.

Catalysts

- For Professor K. Hall, the MRC research project is a supplement to an ongoing research program on the development of new durable catalysts. He has worked with and been supported by Air Products and Chemicals Co, the Ford Motor Company, and more recently by Alcoa Technical Center.

- Dupont Company is an industrial collaborator for the dechlorination project of J. d'Itri.

VI.B **Seminars and Workshops**

"Frontiers in Materials Science -1995"

The MRC Symposium, "Frontiers in Materials Science -1995," was held November 8-9, 1995, at the University of Pittsburgh. Illuminating talks were given by twelve distinguished speakers on a range of ground-breaking topics.

VI.C **MRC Industrial Lecture Series:**

A monthly series of lectures have been held in which the invited speakers were mostly senior technology officers from local industry. These lectures are designed to inform the faculty about the high tech work being conducted nearby and also the challenges and opportunities in the materials field. This forum provides opportunities for contacts between the faculty and the local industry.

VII. CURRENT PUBLICATIONS FOR MRC RELATED RESEARCH

Publications for 1994-1995

J. M. Aigler, M. Houalla and D.M. Hercules, "Photoreduction Study of Model Mo/SiO_2 Catalysts," J. Phy. Chem., 99, 11489, (1995).

S.A. Asher, S.Y. Chang, A. Tse, L. Liu, G. Pan, Z. Wu, and P. Li, "Optically Nonlinear Crystalline Colloidal Self Assembled Submicron Periodic Structures for Optical Limiters," Mat. Res. Soc. Symp. Proc. Vol. 374, Materials Research Society (1995).

D.A. Berztiss, F.S. Pettit, and G.H. Meier, "Anomolous Oxidation of Intermetallics", in High-Temperature Ordered Alloys VI, J. Horton, I. Baker, S. Hanada, R. Noebe, and D. Schwartz, eds., MRS, p. 1285 (1995).

R.W. Bormett, S.A. Asher, R.E. Witkowski, W.D. Partlow, R. Lizewski and F. Pettit, "UV Raman Spectroscopy Characterizes CVD Diamond Film Growth and Oxidation," J. Appl. Phys., 77 (11), 5916-5923 (1995).

S.Y. Chang, L. Liu, and S.A. Asher, "Creation of Templated Complex Topological Morphologies in Colloidal Silica," J. Am. Chem. Soc., 116, 6745-6747, (1994).

F. Dettenwanger, E. Schumann, R. Rühle, J. Rakowski, and G.H. Meier, "The Effect of Nitrogen on the Oxidation of TiAl", in High-Temperature Ordered Alloys VI, J. Horton, I. Baker, S. Hanada, R. Noebe, and D. Schwartz, eds., MRS, 1995, p. 981.

J. Engelhardt and W.K. Hall, "Peculiarities Observed in H-D Exchange Between Perdeuterioisobutane and H-Zeolites," Journal of Catalysis, 151, 1-9 (1995).

J. Goldwasser, C. Scott, M. J. Perez Zurita, M. Houalla and D. M. Hercules "Effect of the Preparation Method on the Surface Coverage of Mo/Al_2O_3 Catalysts," Letters, 32, 273, (1995).

H.J. Grabke and G.H. Meier, "Accelerated Oxidation, Internal Oxidation, Intergranular Oxidation, and Pesting of Intermetallic Compounds", Oxid. Metals, 44, 147 (1995).

D.W. Langer and Y. Maeda, "Electric Field Dependent Refractive Index of Quantum-Well Structures: Their Measurement and Applications," Jpn. J. Appl. Phys., 34 ,Suppl. 34-1, 173-175 (1995).

K. Stoppek-Langner, J. Goldwasser, M. Houalla and D.M. Hercules, "Infrared and CO_2 Chemisorption Study of Mo/ZrO_2 Catalysts," Letters, 32, 263, (1995).

K.Y. Lee, M. Houalla, D.M. Hercules and W.K. Hall, "Catalytic Oxidative Decomposition of Dimethyl Methylphosphonate over Cu-Substituted Hydroxyapatite," Journal of Catalysis, Vol. 145, 223-231 (1994).

W. Li and A.C. Balazs, "Cluster Formation in Grafted Polymers with Interactive End-Groups," Molecular Simulations, 13, 257 (1994).

D.B. Lukyanov, G.A. Sill, J.L. d'Itri and W.K. Hall, "Comparison of Catalyzed and Homogeneous Reactions of Hydrocarbons for Selective Catalytic Reduction (SCR) of NOx," J. Catal., 153, 265 (1995).

T.P. Palucka, N.G. Eror, and T.A. McNamara, "Oxidative Catalytic Decomposition of Toxic Gases Using Hydroxyapatite and Fluorhydroxyapatite," in Synthesis and Properties of Advanced Catalytic Materials, ed. by D. Nagaki et al., Materials Research Society, (1995).

T.P. Pollagi, S. J. Geib and M. D. Hopkins, "Synthesis and Structures of Extended-Chain Metal-Alkylidyne Complexes: Conjugated Polymers Composed of Alternating Organic and Transition-Metal Subunits", J. Am. Chem. Soc., 116, 6051-6052 (1994).

J.M. Rakowski, F.S. Pettit, G.H. Meier, F. Dettenwanger, E., Schumann, and M. Rühle, "The Effect of Nitrogen on the Oxidation of γ-TiAl, Scripta Met. et Mater., 33, 997 (1995).

V. Sazo, L. Gonzalez, J. Goldwasser, M. Houalla and D. M. Hercules, " Surface Coverage of Mo/Al_2O_3 Catalysts," Surface and Interface Analysis, 23, 367 (1995).

Yan Shi, J. Falk and R. Patel,"Highly Nonlinear Semiconductor-Metal Composites," Bull. Amer. Phys. Soc.,Vol.39, p.93, A24-8 (1994)

T.C. Stoner, K. D. John, W. P. Schaefer, R. E. Marsh and M. D. Hopkins,"Synthesis and Characterization of $M_2(CCR)_4(PMe_3)_4$ Dimetallapolyynes," J. Cluster Sci., 5, 107 (1994).

R.L. Thompson, M.D. Hopkins, S. Lee and N.J. Cooper, "Thermal and Photochemical Disproportionation of the Oxo-Bridged Dimer $[\{W^V(\eta^5\text{-}C_5H_5)_2(CH_3)\}_2(\mu\text{-}O)][PF_6]_2$," Organometallics 14, 4, 1969 (1995).

A.S. Tse, Z. Wu, and S.A. Asher, "Synthesis of Dyed Monodisperse Poly (methyl methacrylate) Colloids for the Preparation of Submicron Periodic Light-Absorbing Arrays," Macromolecules, 28, 6533-6538 (1995).

F. Yousuf and J. Falk, "GaAs/AlGaAs Multiple-Quantum Well Plasmon Modulator," paper CN-6, p.18, Fall Meeting of Ohio Section of Amer. Phys. Soc. (1995).

Publications for 1996 - 1997 (submitted or published)

S.A. Asher and G. Pan, "Crystalline Colloidal Array Optical Switching Devices," in Nanoparticles in Solids and Solutions (J.H. Fendler and I. Dekany, eds.) NATO ASI Series Vol. 18, pp. 65-69, Kluwer Academic Publishers, Dordrect (1996).

S.A. Asher, J. Weissman, H.B. Sunkara, G.Pan, J. Holtz, L. Liu, and R. Kesavamoorthy, "Novel Optically Responsive Diffracting Materials Derived from Crystalline Colloidal Array Self Assembly", *Polymers for Advanced Optical Applications*, S.A. Jenekhe and K.J. Wynne (eds.), in press (1997).

H.A. Brison, T.P. Pollagi, T.C. Stoner, S.J. Geib and M.D. Hopkins, "Polymeric Self-Assembly of Organometallic Donor–Acceptor Compounds. Synthesis and Structure of $[W(\int CC_6H_4\text{-4-Donor})(OBu^t)_3]_\infty$," Chem. Commun., 1263 (1997).

R.D. Coalson and A. Duncan, "Statistical Mechanics of a Multipolar Gas: A Lattice Field Theory Approach," J. Phys. Chem., Vol. 100, p. 2612 (1996).

F. Dettenwanger, E. Schumann, J. Rakowski, G.H. Meier, and M. Rühle, "Development and Microstructure of the Al-depleted Layer of Oxidized TiAl", Materials and Corrosion, 48, 23 (1997).

M. Eberhardt, M. Houalla and D.M. Hercules "Analysis of the Surface of Reduced V/Al_2O_3 Catalysts," J. Catal., in press.

X. Feng and W.K. Hall, "Overexchanged FeZSM-5 - A Remarkable SCR Catalyst for Automotive Pollution Abatement," Submitted to Catalysis (1996).

N. Gross, E. Zhulina, and A.C. Balazs, "The Behavior of Grafted Polymers in Restricted Geometries Under Poor Solvent Conditions," J. Chem. Phys., 104 (1996) 727.

J.H. Holtz and S.A. Asher, "Highly Responsive Hydrogels and Polymerized Crystalline Colloidal Arrays", Macromolecules, submitted (1996).

J.H Holtz, R.W. Bormett, Z. Chi, N. Cho, X.G. Chen, V. Pajcini and S.A. Asher, "Applications of a New 206.5 nm CW Laser Source: UV Raman Determination of Protein Secondary Structure and CVD Diamond Materials Properties," (Accepted for publication in Applied Spectroscopy).

M. Hua, R. Mutschler, C.I. Garcia, A.J. DeArdo, "Duplex Structure from the Massive Transformation in a Near γ-TiAl Alloy", submitted to Scripta Met.

P. Jernakoff, J. R. Fox, and N.J. Cooper, "Electrophilic addition of CCl_4 to a Cyclopentadienyl ligand in the Tungstenocene Carbonyl $[W(\eta^5\text{-}C_5H_5)_2(CO)]$ to give $[W(\eta^5\text{-}C_5H_5)(\eta^4\text{-}C_5H_5\text{-exo-Ccl}_3)(CO)\,Cl]^{1}$",J. of Organometallic Chemistry, 512, 175-181 (1996).

K.D. John, T.C. Stoner, and M.D. Hopkins, "Ground-State and Excited-State $C\equiv C$ Stretching Frequencies of Dimetallapolyene Redox Congeners, Evidence for Metal→Alkynyl π-Backbonding", Organometallics, accepted for publication.

Z. Karpinski, K. Early, and J.L. d'Itri, "Catalytic Hydrodechlorination of 1,1-dichlorotetrafluoroethane by Pd/Al_2O_3", accepted in Journal of Catalysis.

Z. Karpinski, J.L. d'Itri, "Hydrodechlorination of 1, 1-dichlorotetrafluoroethane on supported Palladium Catalysts: A Static-Recirculation Reactor Study," submitted to Catalysis Letters.

C. Kuhn and D.N. Beratan, "Inverse Strategies for Molecular Design," J. Phys. Chem., Vol. 100, 25, 10595-10599 (1996).

D. Langer, "Fast Quantum-Well Modulator with Low Phase Distortion," accepted for presentation at XXIII Int. Conf. Physics of Semiconductors, Berlin July 1996.

L. Liu, P. Li, and S.A. Asher, "Fortuitously Superimposed Lattice Plane Secondary Diffraction in Crystalline Colloidal Arrays", J. Am. Chem. Soc., 119, 2729-2732 (1997).

D.B. Lukyanov, G.A. Sill, J.L. d'Itri and W.K. Hall, "On the Role of Free Radicals in the Selective Reduction of Nox," Proc. 11th Int. Congr. Catal., Baltimore, June 1996.

Y. Lyatskaya, D. Gersappe, N. Gross, and A.C. Balazs, "Designing Compatibilizers to Reduce Interfacial Tension in Polymer Blends," J. Phys. Chem., 100, 1449 (1996).

G.H. Meier, "Research on Oxidation and Embrittlement of Intermetallic Compounds in the U.S", Materials and Corrosion, 47, 595 (1996).

C. Mennicke, E. Schumann, J. Le Coze, J.L. Smialek, G.H. Meier, and M. Rühle, "SEM-and TEM-Studies of the Oxidation of FeCrAl", to appear in Microscopy of Oxidation 3.

V.I. Merkulev, J.S. Lannien, C.H. Munro, S.A. Asher, V.S. Veerasamy and W.I. Milne, "UV Studies of Tetrahedral Bonding in Diamond-Like Carbon, Phys. Rev. Letters, 78, 4869 (1997).

G.A. Miller and N.J. Cooper, "Synthesis and Characterization of $[\{W(\eta^5\text{-}C_5H_5)_2(CH_2CH_3)\}(\mu\text{-}O)\{W(\eta^5\text{-}C_5H_5)(O)\text{-}(CH_2CH_3)\}]PF_6$, a Mixed Valence Oxo Alkyl Dimer in Which d^0 and d^2 Tungsten Center are Connected by an Asymmetric Oxo Bridge" , J. Organomet. Chem, 528, 151 (1997).

V. Pajcini, C.H. Munro, R.W. Bormett, R.E. Witkowski and S.A. Asher," UV Raman Microspectroscopy: Spectral and Spatial Selectivity with Sensitivity and Simplicity," (Accepted for publication in Applied Spectroscopy).

G. Pan. R. Kesavamorthy, and S.A. Asher, "Optically Nonlinear Bragg Diffracting Nanosecond Optical Switches", Phys. Rev. Lett. -78, 3860-3863 (1997).

F.S. Pettit and G.H. Meier, "Processing Issues Related to Environmental and Intermetallics", pp. 379-390, in Processing and Design Issues in High Temperature Materials, N.S. Stoloff and R.H. Jones, editors, TMS, Warrendale, PA (1997).

T.P. Pollagi, S. J. Geib and M. D. Hopkins, "Redetermination of the Crystal Structure of 1,4-Diphenylbutadiyne," Acta Crystallogr. C, 52, in press (1996).

J.M. Rakowski, G.H. Meier, F.S. Pettit, F. Dettenwanger, E. Schumann, and M. Rühle, "The Effect of Surface Preparation on the Oxidation Behavior of Gamma TiAl Base Intermetallic Alloys", Scripta Mater., 35, 1417 (1996).

S. Rondon, M. Houalla and D.M. Hercules, "Characterization of Mo/C Catalysts," J. Phys. Chem. in press (1996).

C. Sarioglu, C. Stinner, J.R. Blacherè, N. Birks, F.S. Pettit, G.H. Meier, and J.L. Smialek, "The Control of Sulfur Content in Nickel-Base Single Crystal Superalloys and Its Effects on Cyclic Oxidation Resistance" Superalloys 1996, R.D. Kissinger, D.J. Deye, D.L. Anton, A.D. Cetel, M.V. Nathal, T.M. Pollock and D.A. Woodford, eds., TMS, p. 71 (1996).

C. Sarioglu, J.R. Blacherè, F.S. Pettit, and G.H. Meier, "Room Temperature and In-Situ High Temperature Strain (or Stress) Measurements by XRD Techniques", to appear in Microscopy of Oxidation 3.

E. Schumann, F. Dettenwanger, J. Rakowski, G.H. Meier, F.S. Pettit, and M. Rühle, "TEM Investigations Concerning the Effect of Nitrogen on the Oxidation of TiAl" to appear in the Proceedings of the 4th International Symposium on High Temperature Corrosion, Les Embiez, France (1996).

P. Secrest, S.J. Geib and N.J. Cooper, "Conversion of Dimeric, Diamagnetic $[Mo^{v}_2O_3(NSC)_8]^{4-}$ into Monomeric, Paramagnetic $[Mo^{V}O(NCS)_5]^{2-}$ through Photolytic Ligand Redistribution", Inorg. Chem. 36, 0000 (1997).

C. Singh, E. Zhulina, D. Gersappe, G. Pickett, and A.C Balazs, "A Jumping Micelle Phase Transition," submitted to Macromolecules (1996).

R.A. Stoehr, "Modeling the Influence of Fluid Flow on the Development of Porosity and Microstructure in Castings," accepted for presentation at the 35th Annual Conference of Metallursits to be held in Montreal in August 1996 and accepted for publication in the conference proceedings. Being reviewed for publication in the Canadian Metallurgical Quarterly.

H.B. Sunkara, J.M. Weisman, B.G. Penn, D.O. Frazier, and S.A. Asher, "Design of Intelligent Mesoscale Periodic Array Structures Utilizing Smart Hydrogel" Polymer Preprints 37,453-454 (1996).

A.S. Tse, Z. Wu, S.A. Asher, "Synthesis of Dyed Monodisperse Poly(methyl methacrylate) Colloids for the Preparation of Submicron Periodic Light-Absorbing Arrays," Macromolecules 28, 6533-6538 (1996).

T.L. Utz, P.C. Leach, S.J. Geib, and N.J. Cooper, "Synthesis Derivatization, and Structural Characterization of $[Mn\{CN(2,6\text{-}Me_2C_6H_4)\}5]^-$, a Five-Coordinate Isonitrilate Complex Containing Mn(-I)" Chem. Commun., 847, (1997).

T.L. Utz, P.A. Leach, S.J. Geib, and N.J. Cooper, "Formation of the 1,4-Diazabutadien-2-yl Complex [Mn(CNPh*)4{C(=NPh*)}] Through Methylation of a Mn (-I) Isonitrilate", Organometallics, in press.

J.M. Weissman, H.B. Sunkara, A.S. Tse, and S.A. Asher, "Thermally Switchable Periodicities from Novel Mesocopically Ordered Materials," Science,274, 959-960 (1996).

J. Xu, W. J. Choyke, and J. T. Yates, Jr., "Amorphous SiC Film Formation on Si(100) Using Electron Beam Excitation", submitted to Applied Surface Science (1997).

J. Xu, W. J. Choyke, and J. T. Yates, Jr., "Role of the $-SiH_3$ Functional Group in Silane Adsorption and Dissociation on Si(100)," submitted, J. Phys. Chem (1997).

J. Xu, W. J. Choyke, and J. T. Yates, Jr., "Electron Beam Activation of the Oxidation of Si(100)- Enhanced Oxidation Kinetics and the Observation of an Excitation Resonance," to be submitted to Journal of Applied Physics.

J. Xu, W. J. Choyke, and J. T. Yates, Jr., "Enhanced Silicon Oxide Film Growth on Si(100) Using Electron Impact", submitted to J. Appl Phys. (1997).

J.C. Zahorchak and R.D. Coalson, "A Molecular Dynamics Study of Photothermal Compression of Colloidal Crystals," J. Chem. Phys., to be submitted.

B. Zhang, W.R. Bennett, C. Gao, G.C. Rauch and J.R. Blacheré, "CoCrTa/CoCrPtTa Double-Layer Films for Magnetic Recording," submitted to Intermagn. 1996.

E. Zhulina, C. Singh and A. C. Balazs, "Forming Patterned Films with Tethered Diblock Copolymers," submitted to Macromolecules (1996).

E. Zhulina and A.C. Balazs, "Designing Patterned Surfaces By Grafting Y-Shaped Copolymers," Macromolecules 29 (1996) 2667.

E. Zhulina, C. Singh and A.C. Balazs, "Tethered Diblock Copolymers in Selective Solvents", submitted, Macromolecules.

C.D. Zuiker, A.R. Krauss, D.M. Gruen, J.A. Carlise, L.J. Terminello, S.A. Asher, and R.W. Bormett, "Characterization of Diamond Thin Films by Core-Level Photoabsorption and UV Excitation Raman Spectroscopy," Mat. Res. Soc. Symp. Proc., 437, 211-218 (1996).